THE EFFECT OF SURFACE ROUGHNESS ON THE REFLECTED RADIANCE OF BARE TERRAIN : MEASUREMENTS, MODELLING AND INVERSION STUDIES

By

Maxim Shoshany (M.A.)

submitted in fulfilment of the

requirements for the degree of

Doctor of Philosophy

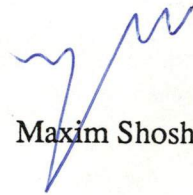in the Department of Geography and Environmental Studies

University of Tasmania,

Hobart, Australia,

August, 1989

STATEMENT

This thesis contains no material which has been accepted for the award of any other higher degree or graduate diploma in any tertiary institution and, to the best of my knowledge and belief, this thesis contains no material previously published or written by another person, except where due reference is made in the text of the thesis

Maxim Shoshany

ACKNOWLEDGEMENTS

ABSTRACT

Bare terrain surfaces have attracted little attention in albedo and remote sensing studies despite their large representation in desert and semi-arid regions of the world. It is the aim of this thesis to investigate the interaction of solar radiation with the Earth's bare surface structure in two stages. The first stage investigates the effect of surface structure on the incoming and outgoing flux using measurements of the Bidirectional Reflectance Distribution Function (BRDF) for various surface types. The second stage developes a methodology for the extraction of roughness information from the BRDF.

Theories describing the effect of facets orientation and multiple reflections on the reflected radiance field are reviewed and discussed. Two major deficiencies are identified: firstly, there is a lack of radiometric data for rocky and stony terrain; secondly there is a lack of measurements which examine the contribution of multiple reflections to the reflected radiance.

A methodology was developed to measure the contribution of secondary reflection (where the first reflection occurs outside the sensor field of view) to the upwelling radiance. In agreement with published models, results showed that the contribution can be high (30%) in certain geometrical configurations. However, unlike other model results, the role of anisotropic reflections via the particulate nature of the surface was found to be of prime importance.A simulation model was developed and it supported the experimental findings.

A study of the BRDF in relation to surface properties was conducted in arid land near Fowlers Gap Research Station, New South Wales. New apparatus was developed to take accurate Hemispherical Directions Radiance Measurements (HDRM). A digitizer for three dimensional in situ roughness measurements was also developed. More than 100 hemispherical data sets were collected for various illumination conditions and surface types: dunes, desert stony pavements and rocky terrain slopes. In general it was found that most of the surfaces exhibited an anisotropic reflection, combining a major component of backscattering with a weaker component of forward scattering.

The BRDF of the different surface types in relation to their roughness properties as determined by the field digitizer is then examined.

The main hypothesis in this research concerns the inverse process of determining the microstructure of the surface from the directional distribution of reflected radiance. It states that given several sets of directional reflected radiance measurements, it should be possible to derive the roughness characteristics of the surface.

The question whether the BRDF has a one-to-one correspondence with the surface microstructure is then addressed. A technique was developed to simulate a wide range of microelements and their BRDF. Results from the simulation show a significant number of cases of equifinality in which a variety of microstructures exhibit the same BRDF. Analysis of these cases suggests that there are many distinctively different combinations of structural properties which can balance the effect of structure on the reflected radiance field . A comparison of field measurements with the simulated cases confirms that BRDF equifinality must be considered in remote sensing applications where there is a need to derive surface properties such as roughness, microstructure and texture from satellite data.

Analysis of the microstructures which exhibited equifinality revealed that they have similarity in their roughness properties. Two parameters are then introduced for characterizing the surfaces' roughness in relation to their reflectance properties. On the basis of the simulation data a method is derived for determining the roughness parameters from reflectance data in certain viewing angles. The assessment of the results showed a moderate to high accuracy which varied with the sun zenith angle.

TABLE OF CONTENTS

CHAPTER 1 : INTRODUCTION

CHAPTER 2 : SOLAR RADIATION AND SURFACE
MICROSTRUCTURE: INTERACTION, DISTRIBUTION AND
INTERPRETATION

CHAPTER 3 : SECONDARY REFLECTION EFFECT ON SENSOR
RESPONSE FOR A V SHAPED VALLEY

CHAPTER 6 :THE EQUIFINALITY OF BIDIRECTIONAL REFLECTANCE DISTRIBUTION FUNCTIONS OF VARIOUS MICROSTRUCTURES

CHAPTER 7 : THE ROUGHNESS SIMILARITY OF EQUIFINAL MICROSTRUCTURES

CHAPTER 8 : THE DETERMINATION OF SURFACE ROUGHNESS PARAMETERS FROM REFLECTANCE DATA: AN INVERSION PROCESS

CHAPTER 9 : SUMMARY AND CONCLUSIONS

LIST OF FIGURES

LIST OF TABLES

LIST OF MAPS

' His radiance is upon Earth and Heaven '   (Psalms)

CHAPTER 1 : INTRODUCTION

1.1. Motivation

This thesis concerns the interaction of solar radiation in the short wave and near infrared spectral regions with natural bare terrain. It aims to understand on one hand, how surface roughness modulates the directional distribution of reflected radiance, and on the other hand, how indicative this distribution is of surface roughness properties.

Desert regions represent a large proportion of natural bare terrain. They are constantly under the influence of various climatological, geomorphological and vegetation processes. Many of these processes are best monitored using remote sensing techniques which, to a large extent, require detailed knowledge of the interrelationship between solar radiation and surface roughness.

Arid and semi-arid regions occupy 31% of the Earth's land surfaces and 80% of the Australian continent ; 12.8% of the world's population live in desert regions and they provide an important proportion of its resources (Mitchell ,1981). A desert environment is dynamic in responding to and influencing climate. A typical rainfall regime may consist of short rain periods of a few hours' duration, followed by hot dry spells lasting for a few weeks. Grasses and herbs can appear within days of a rain event and dry quickly during the subsequent long periods of high insolation. The runoff and flooding which follow the short rain periods have a major effect on the desert landforms. Large masses of coarse sediments are transported and deposited in new areas on mountain footslopes, in the flood plains and on alluvial fans.

Over long time spans (of years) the pattern and distribution of the more drought resistant vegetation may change due to anthropogenic activities and / or global climatic changes. Landforms may change due to the cumulative effect of wind and 'insolation'

growing evidence of desertification in the arid and semi arid regions of the world (Otterman, 1974). In the Australian deserts, desertification due to overgrazing results in deterioration of perennial shrubs (which are highly drought resistant) and consequently creates massive soil erosion (Pickup and Nelson, 1984). The development of gully erosion which is typical in these conditions (Williams, 1981) further accelerates the soil loss.

An investigation of surface albedo variation during the Sahel drought period of 1967-1974 by Norton et al. (1979) and similar studies for the Sinai and Negev areas by Otterman and Fraser (1976) and by Otterman and Tucker (1985) revealed a marked increase in surface albedo during the desertification process. Such rise in albedo is suggested by Henderson-Sellers and Hughes (1982) to be instrumental in decreasing annual rainfall. Rockwood and Cox (1978), on the basis of previous studies, discuss the possible effect of albedo change on the atmospheric circulation.These effects over such vast regions of the world together with the general importance of albedo as a climatic parameter (Hummel and Reck, 1979 ; Henderson-Sellers and Hughes , 1982) emphasize the need to study incoming and reflected radiation distributions in relation to surface properties. A further initiative is provided by the fact that the surface albedo is regarded to be indicative of other surface properties such as drought. Remote sensing is an ideal tool to monitor the desert environment given its size and the dynamic nature of its vegetation and landform distribution.

There are numerous studies in the field of satellite imagery which focus on the study of desert terrain. Proper interpretation of satellite data requires an assessment of the following processes (Duggin, 1985; Teillet, 1986): the passing of radiation through the atmosphere to the surface, its reflection from the surface and the passing of the reflected quantity through the atmosphere to the sensor. Several studies have reported on the need for ground level studies to assess the limitations of remote sensing systems as a result of their spectral, temporal, spatial and radiometric resolution (Forshaw et al., 1986; Justice and Townshend, 1981; Dozier and Strahler,

1983). One of the most interesting subjects of this assessment is the effect of the spatial resolution on the information content and its accuracy. One type of investigation concerns the size of pixels relative to the size of the elements (trees, houses.. etc.) contained in the scene (Jupp et al., 1988) and their heterogeneity (Markham and Townshend, 1981). Other investigations study the relationship between remote sensing data and the data collected at ground level . These studies must overcome two problems, firstly a sampling problem and secondly a problem of compatibility between the two data sets. A sampling problem may result if surface data are not representative of the satellite sensor field of view . Curran and Williamson (1985) claimed that it is not necessarily correct to assume that data collected at ground level are more accurate than that provided by the satellite. They argue that there are inaccuracies involved in sampling large areas in great detail. Examples of these difficulties are given in the measurements of leaf areas for an area of a few square kilometers (which represent the NOAA pixel size) or the need to sample soil moisture over large areas within a short span of time, which only allows for a small variation in soil moisture within the time of measurements. However, more severe is the problem of compatibility of the two data sets where the determination of surface property is dependent on the scale of measurements. For example the determination of surface roughness is scale dependent . This problem is illustrated in sand dune environments where it is necessary to decide whether it is the roughness at the particle scale or at the ripple scale which have the dominant effect on the reflected radiance . Thus, relating remote sensing data to surface roughness requires an understanding of the way that reflected solar radiation is related to surface roughness.

Rough surfaces frequently reflect solar radiation in an anisotropic way, with the intensity of the reflected energy varying with viewing direction. It is anticipated that the study and modelling of the directional distribution of reflected radiance in relation to the surface roughness could assist in deriving better estimates of surface albedo from satellite data. Henderson-Sellers and Wilson (1983) suggested that an accuracy

of +/- 0.05 in surface albedo is needed for climate modelling. On the other hand Kimes et al. (1987) found that albedo estimates from nadir viewing sensors may lead to a 40% error (average desert surface albedo = 0.3). As most of the satellite systems are limited in their off-nadir viewing angles, one way to improve those estimates is through modelling of the anisotropic reflection patterns in relation to surface properties. Alternatively it may be necessary to recommend optimal viewing directions for future remote sensing systems.

The derivation of surface roughness from satellite data is necessary for the study of spatial distribution of landforms and their change, for regional geological study as different lithologies vary in their roughness, and for improving surface material classification by removing the roughness effect. It is anticipated that an assessment of the roughness information that can be derived from reflected radiance and the development of methods for deriving that information may assist in improving the applications of remote sensing data.

To summarise, a study of the relationship between roughness and reflection of solar radiation is relevant to the following research areas:

- the regional study of desert areas ;

- the theory and application of remote sensing;

- climatological studies, mainly regarding surface albedo; and

- the study of natural forms and their mathematical / physical modelling.

The general aim of this study within the framework of various research areas has been presented above . In addition, this chapter defines the terminology and concepts relating to surface roughness and discusses general research objectives.

1.2 Surface roughness: concepts and terminology

'Roughness' is a term that despite its wide usage does not have a general definition. It has been used to quantify the level of deviations (irregularities) from a smooth surface (Hobson, 1973) . However, difficulties arise due firstly to the lack of a common 'yard stick' for measuring the irregularities and secondly to the employment

of more than one statistical or numerical parameters to represent the distribution of irregularities within a specific area. There are three possible approaches to roughness determination :

- form and process oriented approach, where the scale of roughness is derived from information regarding the scale of the processes changing the surface;

- technical approach, where the scale of roughness is determined from the resolution of the measuring apparatus and from limitations regarding the amount of data that can be collected or processed; and

- objective or machine vision approach which is most suitable for remote sensing due to the nature of the data. The usefulness of this approach to the interpretation of roughness is described in the following discussion.

Machine vision methodologies for determining the texture and three dimensional structure of a scene from its images attract growing attention due to their wide industrial applications. Considering the present spatial resolution of most remote sensing systems, the surface represents irregularities of much smaller size. Thus it is not possible to apply those methodologies directly to determine the roughness. However, some similarities may be drawn between roughness and texture. The ambiguity of the term texture is usually regarded as a disadvantage but not so when considering it in relation to roughness ; the term texture is extensively used to describe the size, shape and spatial arrangement (fabric) of detrital sediments (Pettijohn, 1975) . The roughness of bare terrain is largely influenced or determined by the texture of the sediments exposed on the surface. At the same time it is possible to demonstrate that the definition of image texture can be very useful in describing terrain roughness. For that purpose we adopt the definition suggested by Gagalowicz and De Ma (1985, p.290):

" A texture has to be considered as a 2-D information created by the spatial organization of primitives (or basic patterns) that themselves have a random aspect. A texture is a hierarchical structure with two levels in general (it is possible to conceive of even more than two), . . .

. . . deterministic, structural approach corresponds to a macroscopic view of texture (high level): we are interested in the problem of the arrangement of the primitives. The probablistic approach, on the other hand, corresponds to a microscopic view of texture (low level): we are interested in a particular primitive."

It is indeed the case that roughness describe irregularities of three dimensions, however, all other aspects of the above texture definition may also apply to roughness. Natural terrain represents an arrangement of generalized primitives of either facets (tilted smooth planes) or particles (from clay to boulder size) in which each of them may be built of particles and / or facets. The facets or particles may have a deterministic or probabilistic arrangement which will characterise their roughness. In the next chapter the suitability of that definition to describe the roughness in relation to the scale of the radiation interaction will be discussed.

Three wide scale categories are used in this study:

- microscopic scale to represent irregularities of the scale of the radiation wavelength in the short wave and near infrared spectral region;

- mesoscale to represent irregularities much greater than the wavelength and up to the size of a satellite / sensor resolution element, therefore consisting mainly of what will commonly be referred to as terrain roughness ; and

- macroscale to represent forms built of facets of the size of satellite / sensor resolution elements, or greater, therefore relating mainly to the terrain topography.

In their definition of texture, Gagalowicz and De Ma (1985) describe a primitive as denoting a basic pattern in the surface. The term primitive in this definition may be replaced by roughness elements related to forms smaller than the sensor resolution element (mesoscale). As the term 'structure' refers usually to the deterministic form (topography) of a single terrain element (valley, basin , etc.) built of facets of a size within the macroscale category, the 'high level' deteministic structure of the roughness elements is termed in this work as microstructure.

A major part of this work concerns the interaction of radiation with the microstructure of the roughness elements, thus emphasizing the role of the spatial

combination of the facets rather than the elements' size.

1.3 The research objectives

The research objectives as derived from the aims of this study are:

1. To assess and model the effect of roughness properties on the directional distribution of the reflected radiance .

The first objective involves a survey of existing research, an empirical assessment of the roughness effect and the development of models of the relative (normalised) directional distribution of the reflected radiance as a function of the surface roughness. Special attention is given to the modelling of microstructures so that there will be a representation of a variety of surface roughness conditions.

2. To develop an inversion technique which will make possible the derivation of surface roughness from directional distributions of reflected radiance.

Following the level of detail required from the measurements of both the directional distribution of the reflected radiance and the roughness properties of the surface, the limitations of remote sensing systems in terms of their off-nadir viewing capabilities and the costs of their data advocated the use of ground measurement techniques. The findings of this research will be limited therefore to radiances measured at ground level ; further extension of the results to remote sensing applications would require the consideration of the effects of the atmosphere on the reflected radiance which is beyond the scope of this work.

The area of Fowlers Gap Arid Research Station near Broken Hill in western New South Wales was selected as a study site. The description of the area is given in Chapter 5. The research hypotheses and specific research questions are given in Chapter 2 following a description of the existing body of research in this area.

CHAPTER 2 : SOLAR RADIATION AND SURFACE MICROSTRUCTURE: INTERACTION, DISTRIBUTION AND INTERPRETATION

This chapter establishes the theoretical framework of three aspects of solar radiation interaction with the surface microstructure : firstly, the processes of interaction of incoming radiation with the surface microstructure; secondly, the modelling of directional reflectance distributions; and thirdly, the interpretation of surface properties from these distributions.

Despite the fact that this work concerns mainly bare terrain surfaces the discussion covers in some parts vegetated surfaces as well . The primary reason for that inclusion is that there are some similarities between idealized forms (spheres, cones etc.) used to generalize forms of vegetation and bare surfaces and, consequently, similarities in radiation interaction modelling. The second reason concerns the extensive development of research on remote sensing of vegetated surfaces which can be applied to remote sensing of bare terrain.

This chapter is divided into four sections, of which the first three discuss the three aspects of the interaction listed above and the fourth is a discussion of the assumptions and hypotheses made regarding the research objectives.

2.1 The interaction of solar radiation with the surface microstructure

In this section the interaction of solar radiation with the microstructure is described in three parts. Firstly, we discuss the effects of topography and structure on the irradiance at a site. Secondly, the interaction of light with smooth surfaces is described to lay the basis for the analysis and modelling of the interaction of light with rough surfaces which is described in the third part. The patterns of upwelling radiance and their dependence on surface characteristics are presented in the fourth part.

2.1.1 Irradiance on the surface

2.1.1.1 Direct beam irradiance

The slope is a basic attribute of the topography and is of physical importance in defining solar radiation intensities received on the surface . Radiance and irradiance are quantities defined for a projected area. For a unit surface area A , illuminated by parallel colimated beams, the projected area (A') is the "area of cross-section of the incident beam perpendicular to the surface." (Berry, 1923). Other terms found in the literature for the same measure are the actual area or effective area and in a mathematical form it is written:

$$A' = A \cos \theta_i \qquad [2.1]$$

where θ_i is the incident angle between the surface normal and the incident beams. Simple trigonometric equations have been developed for the evaluation of the incident angle in relation to the surface normal. The variables in such calculations are the slope, aspect, latitude, solar inclination and local solar hour. The following equation determines the direct beam irradiance received by any surface tilted at an elevation angle to the horizontal and azimuth angle (Nunez, 1980)

$$E = E_0 \cos \theta_i$$
$$= E_0 (\cos \theta_n \cos \theta_z + \sin \theta_n \sin \theta_z \cos \phi_z \cos \phi_n$$
$$+ \sin \theta_z \sin \phi_z \sin \theta_n \sin \phi_n) \qquad [2.2]$$

where θ_z and ϕ_z are the solar zenith and azimuth angles, θ_n and ϕ_n are the zenith and azimuth angles of the normal to the surface, E_0 is the direct solar beam irradiance on a unit area perpendicular to the beam measured at the bottom of the atmosphere and θ_i is the angle between the direct radiation and the normal to the surface.

Since the sun has a certain pattern of change for its position in the sky which determines the temporal variation and the total irradiance on a tilted plane at the bottom of the

atmosphere, the variation of irradiance with the changing of the sun's zenith and azimuth must be discussed as part of the geometrical / structural effect. Similar expressions for the global direct beam irradiance on a tilted plane are given by Bird and Riordan (1986), Justus and Paris (1985) and Forgan (1983) :

$$E_d= \cos \; \theta_i \;\; D \, E_t \, T_r \, T_o \, T_w \, T_g \, T_a \qquad\qquad [2.3]$$

where E_t is the extraterrestrial irradiance at the top of the atmosphere, D accounts for the sun-earth distance and T_r ,T_a ,T_o, T_w and T_g are the transmittance functions in the atmosphere due to Rayleigh scattering, aerosol scattering and absorption, ozone absorption, water vapour absorption and uniformly mixed gas absorption . All the above transmittance components are proportional to the air mass which is a function of the sun's zenith angle . Thus two sites which form the same sun's angle of incidence according to [2.2] at different times will have different irradiance following the changes in the transmittance components given by [2.3].

When considering the accuracy of estimates of irradiance , it is necessary also to address the question of how accurate or representative is the slope aspect derived from a map, digital terrain model (DTM) or determined from direct measurements.   An average slope and aspect for a portion of the surface may be representative in determining the average irradiance. However, as is discussed later , the spatial distribution of the irradiance on the surface (including the casting of shadows) is dependent on the arrangement of its facets which has an important role in determining the upwelling radiance. As the interaction processes vary with the size of the facets relative to the wavelength of the incoming radiation, attention had to be given to the appropriate modelling of the surface roughness / microstructure.

2.1.1.2 Diffuse irradiance and view factor calculations

In addition to the direct beam radiation there are two sources of radiance incident on a tilted plane which are frequently assumed to be diffuse scatterers. Those sources are radiation from the sky and reflected radiation from the ground. A general form for the diffuse irradiance (E_d : treated as a bulk quantity rather than spectral) in cloudless

conditions following Nunez (1980) is given by:

$$E_d = E_r \ T_{wa} \ T_{da} \ [\ 1 - T_{ws}T_{rs}T_{ds} \ ] \ 0.5 \ F_s + (1 - F_s) \ R \ E_r \qquad [2.4]$$

where T_{wa} and T_{ws} are the transmission coefficients for water vapor absorption and scattering, T_{da} and T_{ds} are the coefficients for dust (aerosol) absorption and scattering , T_{rs} is the coefficient for Rayleigh scattering, R is the reflectance of the surface and F_s is the sky view factor.

A tilted plane receives radiation from source elements according to the proportion in field of view of the radiating source. The structural / geometrical factor which describes the hemispherical fraction occupied by ground elements measured at the center of the radiating object is called View Factor. Davies et al. (1970) defined it empirically "as the ratio of radiation received by the radiometer emanating from a particular source to the total received from all sources (assumed to be radiating at the same rate)". Reifsnyder (1967) took the opposite view and equated the View Factor with flux emitted from a Lambertian surface element (dA_1) to a surrounding object (A_2) relative to the sum of flux emitted to all hemispherical directions (Φ_h):

$$F_{dA_1 \rightarrow A_2} = \frac{d\Phi}{\Phi} = \int_{A_2} \cos \theta_r \ \frac{d\omega}{\pi} \qquad [2.5]$$

where $\cos \theta_r$ is the projected area toward direction r and $d\omega$ is the differential solid angle which a differential portion of A_2 occupies. Since in real conditions different sources emit or reflect different flux densities it is difficult to apply the approach of Davis et al (1970) to the problem of determining the view factor. A detailed geometrical description of the hemispherical field of view at various locations across the surface was required. Basically there are three general methods for deriving the needed view factors: empirical methods which apply fisheye lens photography (Eaton, 1976; Steyn, 1980; Nunez, 1982); methods which apply ancillary data such as DTM (Nunez, 1980); and methods applying model surface elements such as a V shaped valley (Peterson et al. 1985). Knowing all the hemispherical sources radiating into a specific

location the total diffuse irradiance ($E_{d\lambda}$) is given by the following integral (Slater, 1980):

$$E_{d\lambda} = \int_{0}^{\frac{\pi}{2}} \int_{0}^{2\pi} L_{\lambda i} (\theta_i, \phi_i) \cos \theta_i \sin \theta_i \, d\phi \qquad [2.6]$$

where $L_{\lambda i} (\theta, \phi)$ is the incoming spectral radiance from direction (θ, ϕ). In Slater (1980), equation [2.6] describes the incoming radiance from the sky. However, it can be expanded to include diffuse radiation from terrain elements in the field of view. While [2.5] assumes uniform incoming radiance from the sky or the ground, [2.6] suggests that in order to estimate the irradiance accurately it is necessary to model the incoming radiation field for each differential hemispherical sector .

For distant sources such as portions of the sky or major terrain elements (mountains or sea portions for example) their total or average irradiance on the surface can be well defined. However, the radiance distribution at the microstructure scale is difficult to achieve since the change of forms with scale is frequently unknown and therefore it is impossible to determine all the microfacets seen from a location. The assessment of the amount of radiation exchanged between facets of simple microstructures are described later in this chapter.

2.1.2   The reflection from smooth surfaces

2.1.2.1 Specular reflection

The solar flux which travels through the atmosphere and interacts with the Earth's surface can be typically divided into three components (Slater 1980):

$$\Phi_i = \Phi_r + \Phi_t + \Phi_a \qquad [2.7]$$

where i, r, t and a denote incident, reflected, transmitted and absorbed fluxes.

The above equation is suitable to describe any form and scale of interaction: a single specular reflection and 'bulk' reflection when the incident flux escapes the structure of the surface after multiple reflections and transmissions. For laying the basis of the

analysis of structural effects, it is first necessary to describe the very simple theoretical case of light interacting with a perfectly smooth surface.

Consider direct beam radiation incident on a smooth surface subtending an angle θ_i with the normal to the surface. The angle of refraction θ_t is given by Snell's law:

$$\sin \theta_t = \sin \theta_i \ n_1 / n_2 \qquad\qquad [2.8]$$

where n_1 and n_2 are the refractive indices of the two media. It is frequently assumed that the reflected / refracted rays do not leave the plane of incidence and do not alter the frequency of the waves (Mathieu, 1975). Upon interacting with the surface material the reflected radiation is polarized (Egan 1985). As most existing remote sensing systems can not separate the radiation into its polarization planes, the reflectance in natural light is given by the sum of the polarized quantities in the Fresnel equation (Hecth and Zajac, 1974):

$$R = 0.5 \left[\frac{\tan^2(\theta_i - \theta_t)}{\tan^2(\theta_i + \theta_t)} + \frac{\sin^2(\theta_i - \theta_t)}{\sin^2(\theta_i + \theta_t)} \right] \qquad\qquad [2.9]$$

and θ_t is determined by Snell's law.

Thus both the geometry of the refraction and the intensity of the reflected flux are determined by the refractive indexes for each wavelength band. Data provided by Egan(1985) show that the refractive index of the material can change considerably within the shortwave near infrared region. For example, the refractive index of a sample of Saharan desert varied from 1.387 at $\lambda = 0.4\mu$ to 1.605 at $\lambda = 1.105\mu$.

The above discussion was restricted to perfectly smooth surfaces; however, non-smooth surfaces will reflect light specularly if their roughness elements' height (h) is lower than a threshhold defined by Rayleigh criteria (Beckmann and Spizzichino, 1963):

$$h < \lambda / (8 \sin z) \qquad\qquad [2.10]$$

where z is the grazing angle (elevation angle of the reflection direction from the horizon).

From [2.10] it is possible to see that a surface covered with relatively large elements can reflect specularly in very low grazing angles.

Natural bare surfaces are frequently composed of a wide range of roughness elements size where the smaller ones appear on the facets of larger elements in nesting order. For the shortwave and near infra-red spectrum even particles of silt size are larger than the wavelength. It is possible to suggest then that the microfacets of the crystals on the surface of the various particles size may be specular reflectors.

2.1.2.2 Diffuse reflection and scattering at the microscopic scale

Diffuse, Lambertian and isotropic reflection are terms which refer to the scattering of incident flux equally to any direction. In radiance units it is written:

$$L(\theta_r , \phi_r) = const. \qquad [2.11]$$

or in flux units it is written:

$$\Phi (\theta_r , \phi_r) = \Phi (\theta_o, \phi_o) \cos \theta_r \qquad [2.12]$$

where $\Phi (\theta_o, \phi_o)$ is the reflected flux into the direction normal to the surface and θ_r is the exitance angle relative to the normal. The difference between the two expressions is due to the fact that radiance is measured per unit projected area in the viewing direction (Suits, 1983) .

This type of reflection can be observed for many natural surfaces, mainly at viewing angles close to the nadir direction.

There are three types of explanations of the phenomenon of diffuse reflection. The first is based on Grabovski (1914) who suggested that diffuse reflection is formed by internal reflections of the beams which are transmitted through the material and then refracted back into the atmosphere. The second explanation was given by Duntley (1942) by treating the surface as a non-homogeneous medium composed of particles

'suspended' in air . The light incident on the surface undertake multiple reflections upon transmission through the medium and some of those reflections eventually escape back into the atmosphere with a diffuse character. The third approach is based on the assumption that the surface is a finite opaque boundary and that the diffuse reflection is caused by the arrangement of its facets. That approach was first introduced in the Bouguer (1762) hypothesis (according to Berry, 1923) which states that the diffuse reflection is the sum of specular reflections on an infinitesimal number of small mirrors (specular opaque reflectors) oriented equally to all directions. Berry (1923), in support of this hypothesis, proposed an ideal surface composed of a Gaussian slope distribution which may be approximated by slopes on spherical elements. The surface distribution is given as:

$$dA = K \, e^{-(ap)^2} \quad ; dp \cong \frac{K \, dp}{a^2 + p^2} \qquad\qquad [2.13]$$

where dA is the area of microfacets with their normals with slope angle p +/- dp (differential slope interval) , a is their area and K is a constant.

Rense (1950) confirmed Berry's findings and emphasized the correspondence between the proportion of the incident flux reflected into a direction and the relative amount of microfacets which enables specular reflection into that direction. Trowbridge and Reitz (1975) showed, using the Rense (1950) approach, that rough surfaces built of randomly distributed specularly reflecting facets can reflect light in the same manner as an ellipsoid of revolution structure. This argument suggests that there could be an infinitesimal number of facet distributions which will show the same reflection pattern.

These studies omitted the masking and shadowing effects of the surface structure in determining the scattering properties. Such omission might be justified for random roughness patterns primarily as a result of large numbers of structural combinations ; each group of facets with a specific slope and aspect has basically the same probability of being shadowed or obstructed from the light source by other facets, and thus obstruction and shadowing is not expected to change the relative contribution to the hemispherical reflected flux by each portion of the distribution. However, that is not the case with the deterministic structural realizations of spherical or ellipsoid of

revolution, those having the same microfacets directional distributions as the random patterns according to Berry(1923) and Trowbridge and Reitz (1975) . For surfaces built of deterministic elements, it is necessary to assess the potential effects by shadowing or obstructing since they may cause those surfaces to reflect the incident light in a non-isotropic way. By extending the reflectance models to include those structural effects in the microscopic scale, Middleton and Mungall (1952) found that the diffuse reflection pattern is limited to viewing angles smaller than 45° (with respect to the normal) for a surface model which is built of randomly oriented specularly reflecting facets, each of them faced by perpendicular diffusing walls . Torrance and Sparrow (1967) suggested an improvement to the Middleton and Mungall (1952) model and reported a diffuse reflection pattern together with an off-specular reflection component for a surface built of V-groove cavities.

The above mentioned authors were aware of the limitations of the diffuse pattern in describing real reflection distributions for large illuminating and viewing angles. However, it is important to note, firstly, that the directional distribution of the microfacets' orientation is a key component in describing the surface reflection pattern and, secondly, that diffuse reflection is not necessarily linked only to randomly rough surfaces but also to a surface built of deterministic elements. As discusssed previously, the study of reflection from surfaces built of non-random roughness patterns (even with random directional distribution of microfacets) requires the assessment and modelling of the radiation interaction in more detail.

2.1.3 The radiative transfer of solar radiation within the terrain's microstructure

Natural terrain demonstrates an interesting range of boundary types. Frequently its surface is regarded as a finite thin boundary for the interaction of solar radiation; in those cases one separates clearly the processes above and below the boundary . However, most of the real surfaces are quite different; it is extremely difficult to identify a clear boundary for them , or alternatively the boundary is treated as a medium . That reality is well reflected in the treatment of the interaction of light with the terrain surface.There are two main approaches; The first the regards the surface as a porous medium (Figure 2.1a) built of a mixture of air and solid particles. The second treats the

surface as a 'facets' medium (Figure 2.1b) where a continuous surface built of facets fluctuates between two generalized surface boundaries connecting all the extremum points: the upper boundary connects the maxima points of the surface and the lower connects the minima points. The extremum points are determined according to the scale of the analysis.

The incident radiation can be typically divided into three components upon interaction with the surface : that part which is reflected into the atmosphere after one reflection ; that part which is reflected to the sky after multiple reflections; and the radiation which is trapped, by being attenuated and absorbed by the surface materials. Despite the extensive literature that describes the theory of the radiative transfer of solar energy within certain surface structure types, very little experimental data have been published on the effect of multiple reflections of the reflected radiation and on the amount of trapped energy. Two reasons explain this omission: firstly it is extremely difficult to measure them and, secondly, natural surfaces present a problem of nesting scales as the processes of interaction occur at many scales at the same time. Consequently, it is often assumed that the intensities left after the first reflection are negligible. Commonly the effect of structure is analysed at two levels. In the first the main concern is the amount of flux escaping from the structure after only one interaction and, in the second, attention is given also to the exchange processes of radiation within the structure before it is totally attenuated or reflected to the atmosphere.

2.1.3.1 Flux escaping the surface structure after one interaction

Several phenomenological models have been developed for different structural geometries assuming either specular or diffuse reflection . As discussed in the last section, the diffuse pattern of reflection was explained by specular reflections from an infinitesimal number of small mirrors equally distributed to all directions. Other models have been described by Middleton and Mungal (1952). Working with shapes at a microscopic scale and assuming specular reflection, they examined the direct beam radiation reflected from a facet but partly trapped by neighboring vertical facets (Figure 2.2a). They defined a multiplicative factor (M) which estimated the portion (m) of the

A

upper boundary

lower boundary

FACETS   MEDIUM

B

upper boundary

lower boundary

POROUS   MEDIUM
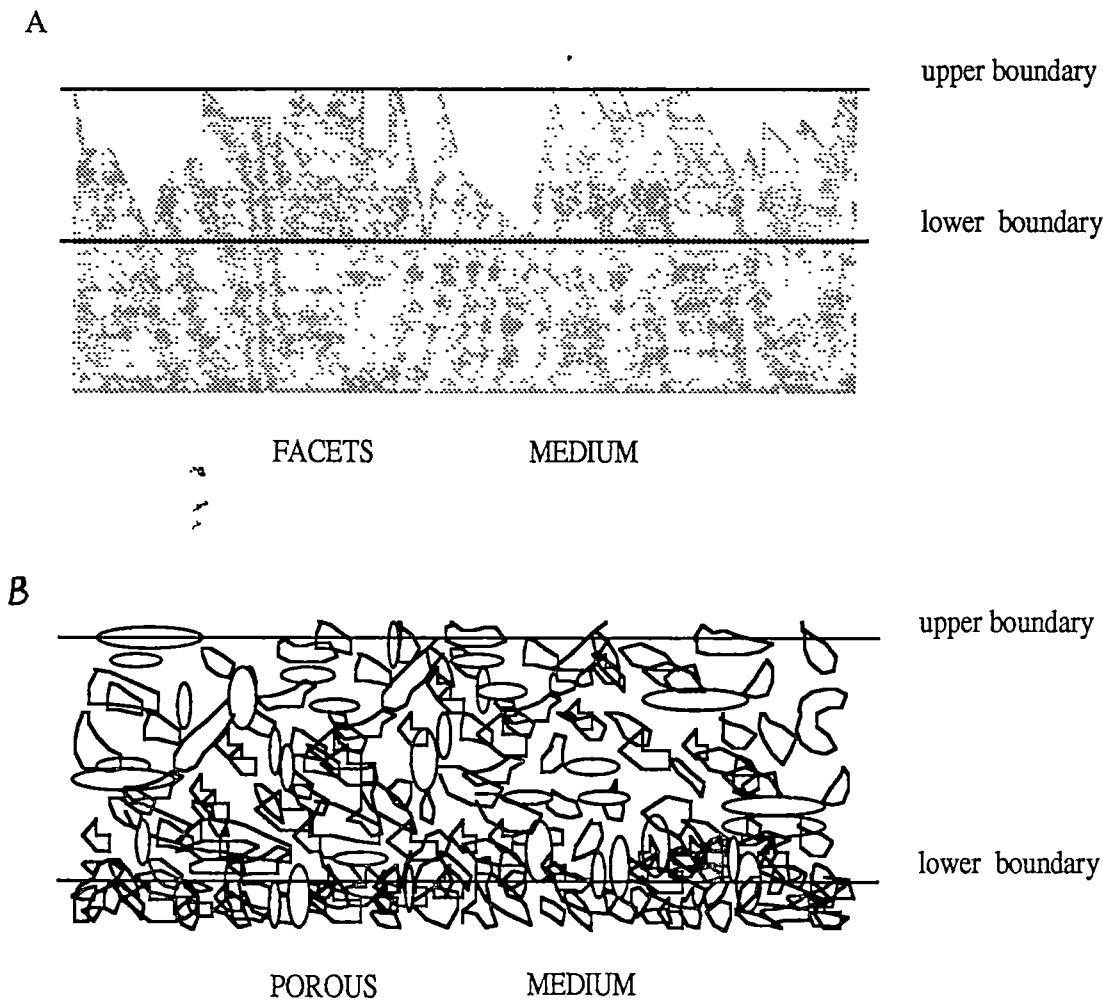
FIGURE 2.1 : Surface boundary as a medium for the interaction of radiation

illuminated facet (l) that reflects the beam back to the sky (i.e. the amount of incoming flux which escapes the structure):

$$M(\theta_n, \theta_r) = \frac{l-m}{l} = 1 - \frac{1-(1-A)^{1/2}}{A} \qquad [2.14]$$

where

$$A = \frac{\sin^2\theta_n - \cos^2\theta_r}{\sin^2\theta_n \ \sin^2\theta_r} \qquad \text{for} \quad \sin^2\theta_n \ne \sin^2\theta_r \qquad [2.15]$$

where θ_n is the facet's slope, θ_r is the angle of the reflected ray in relation to the nadir, l is the facet area and l-m is the reflecting, unobstructed area.

They found that such a multiplicative factor is important in explaining the reflection of snow.The pattern of reflection was basically isotropic for illumination and viewing angles smaller than 45° (relative to the surface normal). Outside those regions, the reflection differed significantly from the isotropic pattern.

An improvement to the model was suggested by Torrance and Sparrow (1967), using a geometrical attenuation factor which accounts for the masking and shadowing that occur within a V - groove cavity structure. This cavity is formed by pairs of facets (from the overall random slope distribution of the facets) with the same slope but opposite aspect (Figure 2.2b).

Thus a new expression was given to A in [2.14]:

$$A = \frac{\sin^2\theta_r - \cos^2[(\theta_r - \theta_i)/2]}{\cos^2[(\theta_r - \theta_i)/2] - \cos[\theta_r - \theta_i] \ \sin^2\theta_r}$$

The application of their model using the modified geometric attenuation factor was found to be in better correspondence with metallic and non-metallic surfaces and explained their off-specular reflection pattern.

In an attempt to derive the total irradiance on facets of ripples' structure, Carroll (1982) calculated the fraction of the direct beam specularly reflected from one facet (i) which is
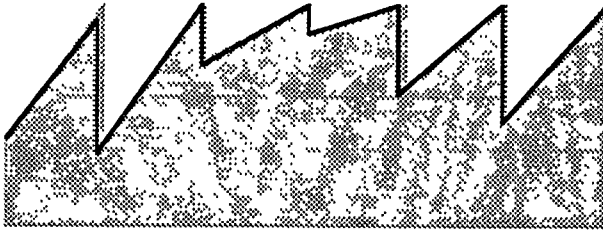
a) Middleton and Mungal (1952) surface model
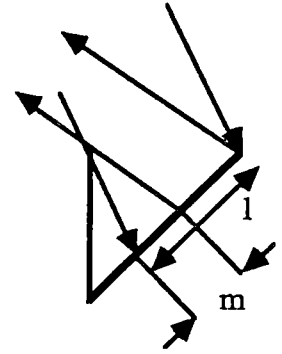
b) Torrance and Sparrow ((1967) surface model
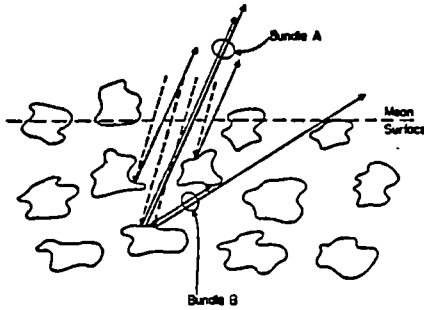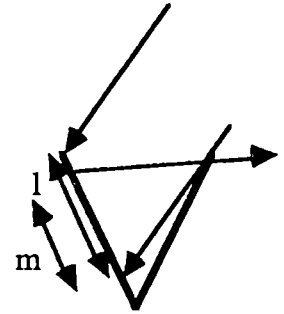
c) Hapke (1963) surface model

$h \sec \theta_i$

$h \sec \theta_i \tan \Omega$
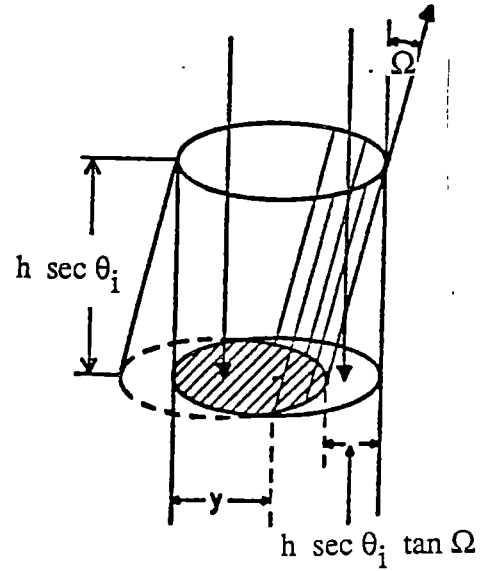
FIGURE 2.2 : Three surface models used for estimating the flux escaping the surface structure

blocked by the second one (j) . The escaping fraction is then given by the reciprocal quantity :

$$M(\theta_n, \phi_n, \theta_s, \phi_s) = 1 - C \, R \, E_1 \cos (\phi_s - \phi_n) \sin \theta_n \qquad [2.17]$$

where $(\theta_n, \phi_n, \theta_s, \phi_s)$ determines the zenith and azimuth angles of the sun and the normal to the ripple facet, and C is a parameter describing whether or not there is flux blocked by facet j .

Hapke (1963, p 4571), in an attempt to understand the Lunar photometric curves, built a model for "materials which have a porous or dendritic or reticulated structure ". This type of surface was visualized as a semi-infinite medium consisting of an irregular arrangement of particles. The reflection pattern is governed by bundles of rays escaping the medium after one reflection from the particles. The geometry of those reflections was formalized by tilted tubes with depth h and effective radius y (Figure 2.2c) which is related to the porosity of the medium. The " fraction of light that is reflected at a given depth h into a direction making an angle Ω with the direction of incidence and escapes unattenuated from the tube (Hapke, 1963; p 4575)" is given by :

$$M(h,\Omega) = \frac{2}{\pi}[\cos^{-1}u - u \, (1 - u^2)^{1/2}] \quad \text{when} \quad 0 \leq u \leq 1 \qquad [2.18]$$

or

$$M(h,\Omega) = 0 \qquad \text{when} \quad u < 0 , \ u > 1$$

where

$$u = (h * \sec \theta_i * \tan \Omega)/2 * y \qquad [2.19]$$

Three types of scattering properties of an individual particle as a function of the phase angle could be chosen in the model for determinig the amount of flux escaping through the imaginative tubes.

In similar work by Egan (1985), the moon's microscopic roughness forms were modelled using a T shaped structure. Both studies reported good correspondence between the moon surface reflection pattern and the reflection pattern predicted for

those structures.

Further recent work by Becker et. al.(1985) introduced a cavity correction factor for the radiation in the thermal infra-red spectrum escaping a rough surface built of blocks and cavities between them.The correction factor is proportional to the phase angle Ω, illumination angle of incidence θ_i, reflection direction θ_r, the azimuth difference between them ϕ, the roughness parameter of the surface (p= cavity radius / cavity depth) and is given by the following expression:

$$M(\theta_i,\theta_r,\Omega,\phi,p,a,b) = \left[\frac{p+a}{p+b}\right]\left\{1+\left[\frac{b-a}{p+a}\right]\exp\left[\frac{-\tan \Omega/2}{p\,(1+A\,\sin\theta_i\,\sin\theta_r\,\sin^2\phi)}\right]\right\} \quad [2.20]$$

where the constants (a,b,A) are adjustable factors and were assumed to be A=b=2 and a=1.

The above work therefore treated the surface structure as composed of two scales, with the reflection from the block's facets a function of the microscopic roughness of the blocks.

Since a detailed description of the surface at the microscopic scale is not available in most of the remote sensing applications, it is generally assumed that the reflection in that scale is isotropic. There were studies which analysed the problem of flux escaping the meso- or macro- structure assuming isotropic reflection at the microscopic scale. There is a major difference between the former approach, characterized by specular reflections, and that required in treating structures built of isotropically reflecting facets. In the first approach, the reflection into a specific direction is dominated by the obstruction / shadowing geometry on the specific microfacets with their normals directed into the mid angle between the illumination and the viewing directions. In the second case, all the microfacets which are not obstructed into the viewing direction or not shadowed reflect a fraction of their incoming flux according to Lambert's law. The problem of following the diffused reflected flux into all hemispherical directions for determining the escaped quantity is different from that described for specular reflection. From every microstructure the flux is escaping in all those directions where there is no

obstruction, and thus there is a need to determine the proportion of the illuminated facet which is seen from each viewing direction. For this reason, most of the studies which assume structures with isotropically reflecting facets calculate the escaping or trapped flux for the integrated hemispherical directions rather than to a specific direction. Examples of these exiting studies involve the radiation balance in urban canyons, where the concern is more in the trapped radiation rather than in its reciprocal quantity (the escaping radiation). Examples of this types of study are given by Nunez and Oke (1980) and others. The main tool for determining these quantities is the technique based on the view factor calculations. A different approach was developed by Otterman(1981) who modelled the radiation reflected from a Lambertian soil with clumps of plants into direction θ_r without interception by the clumps. Those clumps were represented by dark protrusions (thin vertical cylinders) of vertical projection s which intercept the reflected light according to a probability given by exp(- s tan θ). The fraction of reflected radiance which escapes the protrusions is given by:

$$M(\theta_i, \theta_r, h) = 1 - 2 \int_0^{\pi/2} \cos \theta_r \, \sin \theta_r \, [\, 1 - \exp(-s \tan \theta_i)] \, d\theta_r \qquad [2.21]$$

This work was extended later to incorporate randomly distributed horizontal facets (Otterman, 1984, 1985); the obstruction of light transferred in the medium structure was then suggested to be proportional also to exp(-u), where u is the total area of the horizontal facets per unit surface area.

The models described above have a common attribute: they require lengthy equations for treating the flux escaping from a simple surface structure, many times too simplistic to represent the real surface forms. Yet all of them claim good results in predicting the reflectance properties of the surface.It is the complication of this situation which called for the usage of the 'Hotspot' concept by Gerstle and Simmer (1986) and others. That concept is based on the utilization of radiation reflected into the opposite direction of illumination for determining the surface material properties, as in that direction there is minimal effect by the surface structure.

The approach treating the flux escaping after single reflection is many times separated from the approaches considering multiple reflections for two reasons. Firstly, there is the need in remote sensing to simplify the surface interaction models and the assumptions regarding the surface structure. Secondly, it is due to the fact that, in many cases, the radiation intensities left after multiple reflections for surfaces with low reflectivity (as many types of natural terrain are) are claimed to be negligible. In the next section, models which include multiple reflections and predictions made for their effect on the upwelling radiance field are discussed.

2.1.3.2   The radiative transfer of solar radiation within the microstructure

Radiative transfer theories concern the transfer of radiation energy in its different forms through a medium. As discussed earlier, natural surfaces has been treated in two ways, as a porous medium or as a facets medium. In the later, the boundary between the air and the 'solid' earth is frequently treated as a medium by itself since it has the ability to attenuate incident radiation without occupying a closed volume. The main transfer mechanism is scattering or exchange of radiation between neighbouring facets. The exchange of radiation between two facets is a function of the viewing geometry and of their reflection properties. Where surfaces reflect isotropically the exchange of radiation can be modelled through the use of view factors. In the case of specular reflection the process can be followed by simulation models such as the Monte Carlo technique.

A general computational and conceptual framework for modelling radiative transfer within a structure was developed by Van de Hulst (1980). In this approach each component (reflected and transmitted) of each interaction of light on each "slab" of the medium is traced until the radiation incident on the upper boundary is totally reflected and absorbed. The complications arise from the fact that the fractional transmissions and reflections diversify through the medium while progressing back (toward the upper boundary) and forth (toward the lower boundary). For the simple case of two equal

layers the total reflection and transmission is given by the doubling method (Figure 2.3):

R(double layer) = R + T R T + T R R R T + . . .

[2.22]

T(double layer) = T T + T R R T + T R R R R T + . . .

The number of occurrences that have to be considered depends on the reflection and absorption properties of those elements.

Early modelling of the scattering and transmission of light by a heterogeneous diffusing medium were reported by Duntley (1942). Three differential equations describe the internal optics of diffusing materials following the change in height (h=0 at the upper boundary):

$dE_s(h)/ dh = -(A'+B'+F') E_s(h)$

$dE_b(h)/dh = F'E_s(h) - A E_b(h) - BE_b(h) + B E_f(h)$ [2.23]

$dE_f(h)/dh = B'E_s(h) - A E_f(h) - BE_f(h) + B E_b(h)$

where $E_s(h)$ is the direct beam flux density, $E_b(h)$ is the backward (upward) diffuse flux density and $E_f(h)$ is the forward (downward) flux density. The coefficients A, B, F describe the absorption, backward and forward scattering properties of the medium for the internal diffused light. The coefficients A', B', F' describe the absorption, backward and forward scattering properties of the medium for the direct beam light.

Suits (1972) used those differential equations in a study of canopy reflectance by deriving the appropriate coefficients for the absorption and scattering of light by the leaves within the canopy. Later, Davis, Shuchman and Suits (1979) applied the same model to the study of beach sand reflectance.

Two theories for the reflectance of coarse and fine particulate semi-infinite medium were introduced by Emslie and Aronson (1973). Spherical particles with edges and asperities on their surface were assumed to represent the form of the coarse particles.
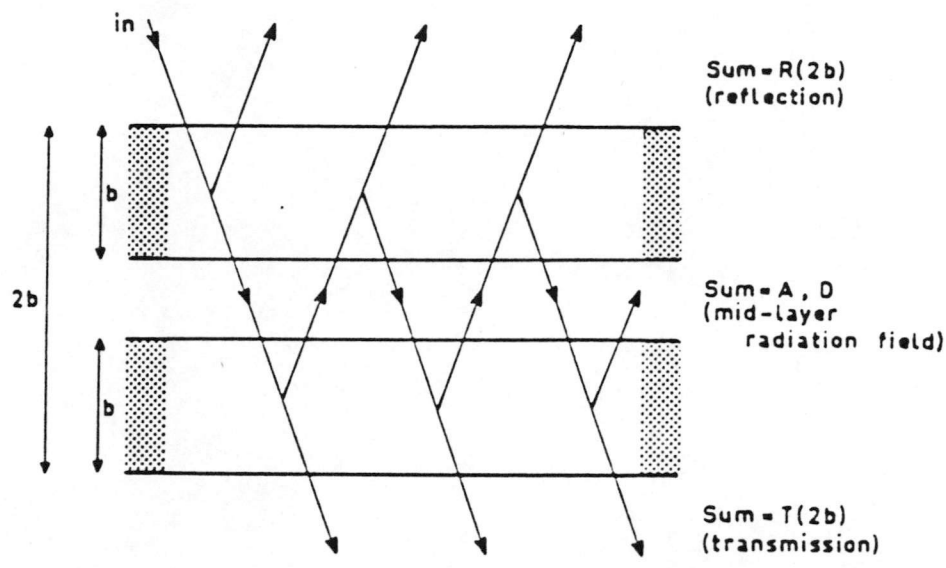
FIGURE 2.3 : An illustration of the Van de Hulst (1980) doubling method
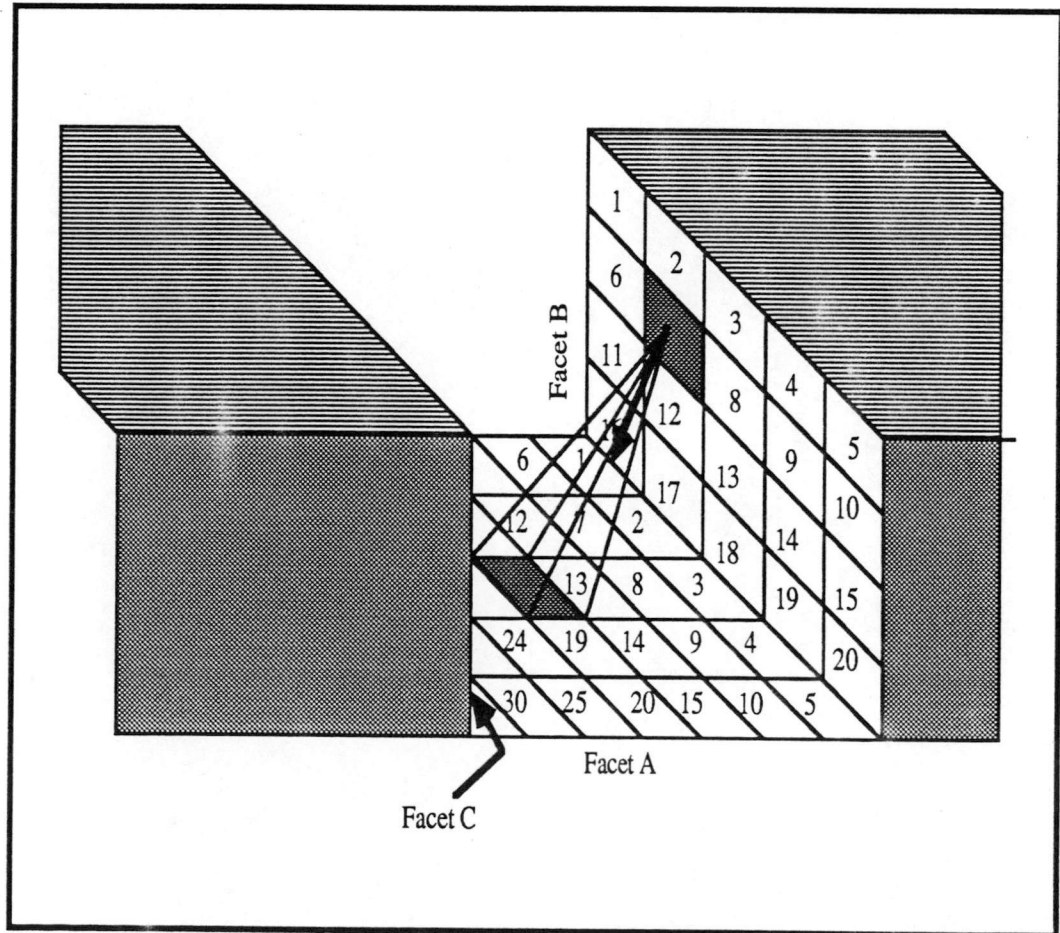
FIGURE 2.4 : The irradiance on a unit surface element from neighbouring facets.

The reflectance of this type of medium is given by:

$$R = 1 + \frac{A'}{S'} - \sqrt{\left[\frac{A'}{S'}\right]^2 + \frac{2A'}{S'}} \qquad\qquad [2.24]$$

where

$$S' = (4 A S_b + 2 S_b S_t + S_b^2) / (4 A + 2 S_t) \qquad\qquad [2.25]$$

and

$$A' = (4 A^2 + 6 A S_t) / (4 A + 2 S_t) \qquad\qquad [2.26]$$

where A, S_b and S_t are respectively the absorption, backward and transverse scattering of a volume of the medium. These three quantities are a function of the particles' density and the absorption, backward and transverse scattering of the individual particles. Unlike the Duntley (1942) model, which involves the gradual conversion of the incident direct beam into scattered radiation while travelling downward through the medium, Emslie and Aronson (1973) relate the scattering and absorption properties to the density of the particles and their optical properties. They claim their model to be much simpler with only little difference in results.

A general computational model for simulating the radiative transfer processes in heterogeneous 3-D scenes was presented by Kimes and Kirchner (1982). The model is based on a rectangular solid subdivided into cubical cells. Each cell is characterized by its own set of optical properties.The transfer of radiation within the structure is through adjacent cells, a fact which simplifies the calculations needed to follow the radiation quantities 'flowing' through the medium. This model was applied mainly for forest canopies. However, it can be used with other types of mediums without major modifications.

In the above mentioned models, multiple reflections were simulated or assumed. However, their effect on the outgoing reflection from the medium is not exactly known.The study of that phenomenon for the case of two or more facets facing each other can throw light on its relative importance.

For the facets type medium, most existing methods were developed for two simple types of cavity structure : the V shaped valley and the rectangular canyon. Basically,

all methods are similar in their approach which can be summarized as follows: the irradiance on each unit area element (Figure 2.4) of each facet (from K facets considered) is the integral of flux received from the elements of the other facets in its field of view according to their irradiance. In mathematical form it is described by:

$$E_{A(1)} = O(A(1))E_{SA} + R \left\{ \left[\sum_{i=1}^{n} E_{B(i)} F_{B(i)->A(1)} \right] + \left[\sum_{j=1}^{m} E_{C(j)} F_{C(j)->A(1)} \right] + \cdots \right\} \qquad [2.27]$$

where $E_{A(1)}$ is the irradiance at element 1 of facet A, E_{SA} is the sun's direct beam irradiance on facet A, $O(A(1))$ is a binary (1 or 0) function denoting obstruction from the direct beam illumination, $E_{B(i)}$ is the irradiance at element i of facet B and $F_{B(i)->A(1)}$ is the viewing factor between the two elements. The irradiance is then the sum of all contributions from elements of facets B,C, D...in the field of view. Since $E_{B(i)}$, $E_{C(j)}$, $E_{D(k)}$... etc. are calculated in the same way, they are approximated in an iterative process assuming, at each iteration, the radiance exitance at an element to be that accumulated before the commencement of the new iteration. Thus, at the first iteration for example $E_{A(1)} = E_{SA}$, then at the second one it is the accumulated value with first reflection from all the elements in its field of view and so on. The number of iterations / multiple reflections is determined according to the contribution at each iteration. Once this contribution is below a certain level the process is stopped. Thus, while in the Van De Hulst (1980) method the process follows the depletion of the incident energy components, here it follows the flux accumulated on the facets.

In the following discussion, studies covering the mutiple reflection are considered in terms of firstly, their specific objectives and, secondly, their predictions of the multiple reflection effect. One of the first attempts was made by Kimes and Kirchner (1981) for a few target area locations (unit area elements). Considering the reflectance of a plane of a V shaped valley, they used a simple simulation model to estimate the error in the reflectance measurements as a result of neglecting multiple reflections. For a [1] surface with an intrinsic reflectance of 0.5, the error was found to be of magnitude 4% for valley planes with a slope up to 20° . Higher values were found for steeper

valleys.

Bruhl and Zdunkowsky (1983) developed a method similar to that described in [2.27] for approximating the effect of multiple reflections on the irradiance on an inclined slope in mountainous terrains and urban canyons. An 8% effect was estimated for snowy surfaces with a reflectance of 0.85.

A model for calculating the multiple reflection effect on the upwelling radiance from V shaped valleys measured by a pyranometer positioned at different heights above the valley floor was described by Peterson et al. (1985). In addition to the exchange of radiation between the two facets they added the effect of the view factor formed by each facet at the sensor. The effect was expected to be considerable for surfaces covered with snow. However, no specific prediction was given.

Cooper and Smith (1985), using a Monte Carlo simulation, calculated the reflection of radiation from a 'row' and 'clump' periodic surface. The radiance was calculated for a sensor positioned at different orientations. They report an increase in the absorption of radiation due to an increasing number of interactions.

Ferencz et al. (1987) developed a method for calculating the 'cross radiation effect' for V shaped and rectangular furrow models. Their method proposes an analytic expression for calculating the irradiance received at an element from its neighbouring facets. According to their analysis of the effect, its magnitude is comparable to that of the direct beam for highly reflecting surfaces.

As there is not a set of experimental data to assess the effect of multiple reflections, extra weight is given to the predictions made by the simulation models. All the studies presented above concluded that the effect of multiple reflection must be considered in remote sensing applications. However, while Peterson et al. (1985) do not specify an exact figure for the multiple reflection effect, both Kimes and Kirchner (1981) and Bruhl and Zdunkowsky (1983) predicted an effect between 4% and 8% for mountainous terrain, Ferencz et al.(1987) predicted the effect to be very high (of the magnitude of the direct beam irradiance) in some cases. Since most of the existing models describe the transfer of light within a medium through multiple reflection (either between neighbouring facets or particles), it is important to determine their effect

empirically.

2.1.4   Discussion

2.1.4.1 Surface models and scale of radiation interaction

The importance of the surface structure in determining the amount of flux reflected and the pattern of the reflection field is well established in the literature. A representative list of structural elements used for analysing and modelling the interaction of light with the surface is given in Table 2.1. Surface structure models differ considerably between those developed for the microscopic scale and those developed at a scale characteristic of surface roughness and topography. The differences can be summarized as follows:

- at the microscopic scale, the surface is modelled by a combination of a directional distribution of microfacets and of a cavity which is formed by pairs of microfacets;

- at the mesoscale, elements with simple geometry (cubes, cones, spheres for example) are positioned on the surface where the element's surface is considered to be rough in their microscopic scale. In some studies the emphasis is on the cavity which is formed between the elements while in other studies the amount of shadow is the main concern.

Generally, it appears that these models are very site specific since they are designed to solve a particular surface/radiation combination. Analysis of radiation interaction with bare surfaces of different geomorphological conditions requires some flexibility in the geometrical-optical modelling to allow some variation in the form of the elements (for example asymmetry, different values of flatness or roundness, etc.). The flexibility in the models is given by allowing these variations without changing the general equations which describe the radiation interaction.

2.1.4.2 The reflection from rough surfaces

Earlier, two 'pure' types of reflection were discussed. Both of them related to smooth surfaces. Specular reflection occurs from facets with roughness elements smaller than a size determined by the Rayleigh criteria and diffuse reflectance from

TABLE 2.1 Surface models

Year	Source	Model description	Scale
1923	Berry	random slope distribution	M
1952	Middleton & Mungal	random facet distribution forming asymetric cavities	M
1963	Backmann & Spizzichino	periodic, random (facets, objects)	M/R
1963	Hapke	porous surface: particles in semi -infinite medium	M/R
1967	Torrance & Sparrow	random facet distribution each in a V groove cavity	M
1973	Emslie & Aronson	spherical particles with edges and asperities on their surface	R+M
1975	Trowbridge & Reitz	average irregularity represented by ellipsoids of revolution	M
1981	Otterman	plane with protrusions	R
1981	Carroll	triangular ripples	M/R
1981	Kimes & Kirchner	V shaped valley	R/S
1983	Bruhl & Zdunkowski	valley	S/M
1985	Cooper et al.	'row' and 'clump' periodic structure	R/S
1985	Becker et al.	cavities between rough blocks	R+M
1985	Peterson et al.	V shape valleys	R/S
1985	Egan	plane with T shape protrusions	M
1985	Norman et al.	cubic elements on a flat plane	R
1986	Li and Strahler	cones on flat plane	R
1987	Ferencz et al.	rectangular and V shaped furrows	R/S
1987	Cierniewski	spherical particles	R

scale:

M : microscopic

R : roughness (micro or meso scale)

S : macroscale (topography)

flat surfaces covered with smooth (specular reflecting) microfacets larger than the wavelength (but much smaller than the size of the generalized facets) which are oriented randomly. In between those 'pure' reflection types there are numerous possiblities which can be divided into two categories. Firstly there is the category of roughness elements of size comparable to the wavelength of the incident radiation. Examples of these size of roughness elements can be found in small facets of crystals under conditions of chemical and physical erosion or where the edges of the crystals themselves appear on the surface.

For the visible and near infrared wavelength, it is hard to find large facets built of particles of the size of the wavelength. Recent research in that area indicates that there is no simple solution for the problem of modelling the interaction of light at this roughness scale. Moreover, Schiffer (1988, p.704) indicates that : ' ... it has been shown that a slight surface roughness may partly invalidate the method of determining optical constants by applying Fresnel's formulas to measure reflectances.'. The modelling of reflectance in that scale is beyond the scope of this work. However, empirical works had shown that an off specular reflection pattern can be expected as reported by Coulson (1966) who also suggested the use of Mie scattering theory for this roughness category.

In the second category, specularly reflecting facets are spatially distributed in various densities and patterns on the surface (represented by the roughness of the surface at this scale). The resulting directional distribution of reflected radiance for a few typical transition stages of the weakening of the reflection into the surface (generalized) specular direction as a result of increasing roughness is given in Figure 2.5 . In this scale category, the reflected radiance field is mainly determined by the unobstructed specular reflections as described in section 2.1.3.1 . The effect of shadows for smooth surfaces with roughness at the microscopic scale is minimal because of the strong specular component. The intermediate reflection patterns were termed off-specular or forward scattering by Coulson(1966), Middelton and Mungal(1952), Torrance and Sparrow(1967), Eaton and Dirmihrn (1979) and others and observed for sand, snow , salt and alkali flats.

Superimposing mixtures of facets with the above described reflection properties on facets of roughness elements much larger than the wavelength of the incoming radiation produces a wide range of reflection properties at the mesoscale. The reflected radiance field in these cases is determined by the processes of radiative transfer of light within the structure and by the dominant effect of the spatial distribution of irradiance in general and shadows in particular. The effect of shadows on the reflected radiance field has not been discussed in this section since it focusses on the processes of radiation absorption , transmission or reflection. However, the effect due to shadowing is described later where the reflected radiance into a direction is considered and related to the mixtures of surface elements viewed in that direction and their irradiance.

Lastly, it is necessary to mention two limitations evident from the literature and relevant to this study. The first limitation concerns the effect of polarization. As indicated by Coulson (1966), Egan (1985) and others, the polarization properties of light are closely related to surface roughness properties. However, at this stage there is no remote sensing system in the shortwave and near infra-red electromagnetic spectrum which provides polarization information . Since the aim is to assist in the development of remote sensing applications for desert areas, the effects of polarization were not included in this study. The second limitation concerns the effect of the atmosphere. In addition to the depletion of the reflected radiance from the surface, the atmosphere also has an adjacency effect where "adjacent terrain can contribute to the the radiance of the observed pixel" (Teillet, 1986, p. 1642) or a " cross irradiance" effect due to multiple reflections between the lower atmosphere and the ground (Singh, 1988). Since these effects have not yet been fully assessed empirically (Singh, 1988) and as this study mainly concerns the processes at ground level, those effects were not included here. However, proper interpretation of surface properties from remote sensing data requires the consideration of the effects .
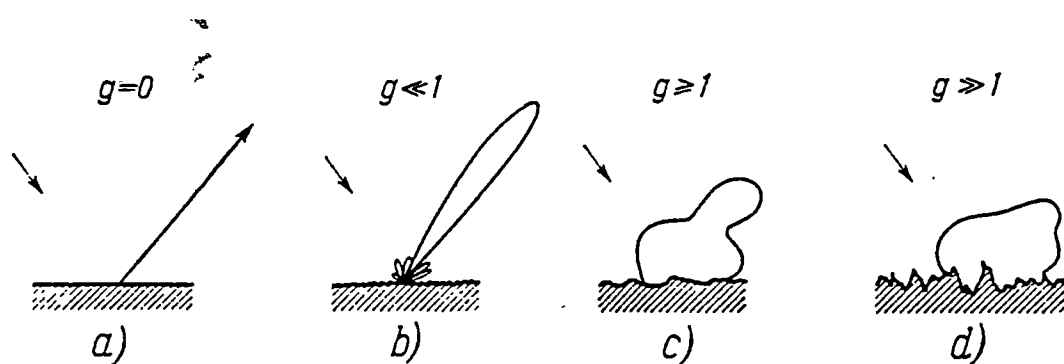
FIGURE 2.5 : The change of reflection distribution with increasing the directional distribution of specularly reflecting facets (source: Beckmann and Spizzichino, 1963). The letter g denotes the level of surface roughness.

2.2 The reflectance of surfaces and its directional distribution.

2.2.1 Albedo and reflectance

In the last section the interaction of incoming flux with the surface structure was described. In [2.9] the reflectance is given by the Fresnel equation for a single episode of direct beam reflection from a perfectly smooth surface. In cases where reflection is spatially integrated over a rough surface, the reflection is the integrated amount of flux which escapes the structure during the whole interaction processes. The spectral reflectance of the surface is given by:

$$R_\lambda = \frac{I_{\lambda r}}{I_{\lambda i}} = \frac{\Phi_{\lambda r}}{\Phi_{\lambda i}} \tag{2.28}$$

where $\Phi_{\lambda r}$ and $I_{\lambda r}$ are the upwelling spectral flux / irradiance and $\Phi_{\lambda i}$ and $I_{\lambda i}$ are the downwelling spectral flux / irradiance.

The reflectance or reflectance factor is dimensionless, it is an important property of the surface and often characterizes its material optical properties (refractive indexes) and its roughness. Attention should be given to the methods used for measuring R in relation to the directional distribution of the incoming and upwelling radiance. In the case, for example, where the surface reflects isotropically the upwelling irradiance can be given by:

$$I_{r\lambda} = L_\lambda (\theta, \phi) \, \pi \tag{2.29}$$

where $L_\lambda (\theta, \phi)$ is the radiance measured at any viewing direction (θ, ϕ).

Similar definitions to [2.28] are found for 'albedo' and 'surface albedo' (Kondratyev, 1969; Swain and Davis, 1978; Henderson - Sellers and Hughes , 1982; Iqbal, 1983 and many others). However, a distinction between albedo and reflectance exists in two areas. Firstly, reflectance relates to a specific wavelength

band, while the albedo gives the integrated value over all the solar spectrum :

$$\alpha = \frac{\int\limits_{.3}^{3.0} \phi_{\lambda r} d\lambda}{\int\limits_{.3}^{3.0} \phi_{\lambda i} d\lambda}$$

[2.30]

Secondly, as albedo is commonly measured using two pyranometers, one directed up and another down, it is regarded as an integrated quantitiy over the whole hemispherical directions while reflectance is more attached to the directionality of the reflected radiance field. Since most of the natural surfaces are not isotropic reflectors , a nomenclature was introduced for describing and modelling the directional distribution of the reflectance.

2.2.2 Anisotropy surface reflection: terminology and measurements
2.2.2.1 Directional reflectance

Several terms have been developed to describe non-isotropic reflection patterns from a complex structure. A 'directional brightness' term was formulated by Minnaert (1941). The term directional reflectance appears in the work of Middleton and Mungal (1952) . Hapke and Van-Horn (1963) measured the directional reflectance using a method relating reflectance from a sample surface to reflectance from a Lambert surface in the same direction.. Following the same method, Coulson (1965) detemined directional reflectance as the ratio of radiation intensities:

$$R(\theta,\phi)= L(\theta,\phi) / L_{Lambert}*\pi \qquad sr^{-1} \qquad [2.31]$$

where $L(\theta,\phi)$ is the reflected radiance in the zenith and azimuth angles (θ,ϕ) , recorded from a sample surface and $L_{Lambert}$ is the reflected radiance from a standard Lambert surface of 100% albedo in any direction. The numerator of [2.31] refers to

a radiance (W m^{-2} str^{-1}) whilst the denominator is an irradiance (W m^{-2}) and therefore the directional reflectance is in units of sr^{-1}.

Since one of the main areas of application for the directional reflectance concept is in determining the surface albedo, a substantial amount of work has tried to link the few directional reflectance measurements to the albedo by using an anisotropy correction factor. Examples of such work are given in Salomonson and Marlatt (1968, 1971) and Brennan and Bandeen (1970), Otterman (1981), Eaton (1976) and others.

2.2.2.2 The anisotropy of bare terrain surfaces: existing data.

Bare surfaces exhibit a wide range of anisotropy reflectance patterns. In Table 2.2 those patterns are generally described by the type of change of reflectance in the backward and forward directional regions. The majority of the measurements are taken at ground level and limited mainly to soil surfaces since the motivation in many of these studies is the need to understand soil reflectance as a background for vegetation measurements. A detailed description of the surface morphology was not reported and thus it is difficult to explain the differences in the reflectance patterns found. The general trends in the data are as follows:

- most of the bare surfaces exhibited a strong backscattering peak; and

- the anisotropy was found to decrease significantly with increasing sun elevation angle.

The main contradiction appears between the work reported by Coulson (1966) and Chen and Rao (1968) and those works reported by Kimes et al. (1984), Walthall et al. (1985) and Norman et al. (1985). The first group found a secondary peak at the forward direction while the second found the reflectance data to decrease to a minimum in that region.

It should be noted that the peak in the forward direction was found to be shifted from the specular direction downwards to low grazing angles.

Another area of conflicting results concerns the reflectance in the directional region between the horizon (in the backward direction) and the illumination direction: some studies report a constant high level of reflectance while others report a decreasing

TABLE 2.2 Directional reflectance pattern for bare surfaces: existing data

AUTHOR	SURFACE TYPE	METHOD	BACKWARD DIRECTION	FORWARD DIRECTION	REFLECTANCE PATTERN
Hapke & Van Horn (1963)	corrugated rocks	Laboratory	-	-	isotropic
	porous medium	- " -	strong peak	-	-
Coulson (1966)	desert sand	- " -	strong peak	strong peak	minimum reflectance at nadir, anisotropy decreases with increasing sun elevation
	black loam agglomerates 20μ to 4 mm	- " -	strong peak	secondary peak	
Chen & Rao (1968)	desert sand	- " -	strong peak	secondary peak	minimum reflectance at -25° anisotropy decreases with increasing sun elevation
	soil	- " -	strong peak	secondary peak	minimum reflectance at -30° anisotropy decreases with increasing sun elevation
	white sand	- " -	weak peak	weak peak	mainly isotropic pattern
Brennan & Bandeen (1970)	desert sand	Aircraft	weak peak		mainly isotropic
Eaton (1976)	Alkali flats	ground measurements	strong peak	strong peak	strength of backward peak weakens rapidly with increasing sun elevation
	salt flats	- " -	moderate peak	-	
	ploughed fields	- " -	strong peak	minimum	
	top dune	- " -	minimum	strong peak	
	bottom dune	- " -	moderate peak	moderate peak	
Kimes et al. (1984)	bare soil	- " -	strong peak	-	weakening peak with increasing sun elevation
Walthall et al. (1985)	rough soil	- " -	strong peak	minimum	
Norman et al. (1985)	rough soil	- " -	strong peak	minimum	weakening peak with decreasing roughness and increasing sun elevation

Note : negative degrees = θ_v - 180°

level with a decrease in the viewing elevation angle.

The lack of sufficient data for bare terrain is, to a large extent, due to instrumental difficulties encountered in constructing a device to collect detailed hemispherical reflectance data from a target area within a short time interval (Deering and Leone, 1986). Existing satellite sensor systems are even more limited in their range of off nadir viewing angles, spatial resolution and temporal cover. The tendency has been to collect data mainly over flat homogeneous areas, not covering wide mountainous regions and stream beds which are characterized by large spatial variability of surface morphology.

2.2.3 The Bidirectional Reflectance Distribution Function (BRDF)

Natural terrain exhibits quasi specular reflections, backscattering and a wide range of angular distributions of reflected radiances. As a result there is need for detailed quantitative measurements and modelling of these phenomena.

Nicodemus et al. (1977, p.2) extended the directional reflectance concept to distribution functions which "... not only exhibit a continuous distribution, from the pure delta-function spikes of highly specular propagance through gradually broader and flatter peaks to the smooth flat curves of isotropically diffuse propagance, but also show a variety of distorted shapes that do not fall directly between the two extremes ". The Bidirectional Reflectance Distribution Function (BRDF) is given by the following expression :

$$f_r\,(\theta_i,\,\phi_i;\,\theta_r,\,\phi_r) = dL_r\,(\theta_i,\,\phi_i;\,\theta_r,\,\phi_r;\,E_i)\,/\,dE_i\,(\theta_i,\,\phi_i) \qquad sr^{-1} \qquad [2.32]$$

where $dL_r\,(\theta_i,\,\phi_i;\,\theta_r,\,\phi_r;\,E_i)$ is the differential reflected radiance reflected into direction $(\theta_r,\,\phi_r)$ from the sum of reflected radiance due to differential irradiance $dE_i(\theta_i,\,\phi_i)$.

The above definition to the BRDF relates to a generalized homogeneous uniformly irradiated flat surface in the sense that the spatial distribution of the irradiance on the

surface and the reflected radiance are both depending only on direction (Nicodemus et al., 1977). In other words, the viewed target area has to be large enough relative to the microtopography to ensure that the reflected radiance into a specfic direction is not changing with a shift of the center of the sensor field of view within the area of facet with the same surface properties.

The BRDF uniquely determines the albedo of the surface and contains the signature of the surface properties such as material and microstructure. Accordingly, the applications were developed into two not independent areas, the study of solar energy balance and the interpretation of surface properties from reflectance data. The importance of the BRDF in remote sensing applications is well reflected by the quantity of research undertaken in this area. However, a full description of the BRDF for natural scenes cannot be practically achieved by measurements as indicated by Hugli and Frei (1983). Consequently the BRDF was developed by either phenomenological modelling where interaction models are developed for surfaces of known (or assumed) properties, or empirical modelling by interpolating the full hemispherical distributions from limited directional incoming/reflected radiance data. The methodologies developed in these two areas in relation to bare terrain surfaces are described in the following sections.

2.2.3.1 Phenomenological modelling of BRDFs

Most natural terrain in the roughness scale is heterogeneous: it exhibits a mixture of spatial elements. In this section the heterogeneity is confined to elements much smaller than the sensor IFOV. With modifying slightly the general scheme for describing the reflected radiance from heterogeneous scenes given in Duggin (1986),

the differential reflected radiance $dL_r(\theta_i, \phi_i; \theta_r, \phi_r; E_i)$ can be expressed by the following weighted sum:

$$dL_r(\theta_i, \phi_i; \theta_r, \phi_r; E_i) = \Sigma\, dL_{r1}(\theta_i, \phi_i; \theta_r, \phi_r; E_i)\, W_1$$

$$+ dL_{r2}(\theta_i, \phi_i; \theta_r, \phi_r; E_i)W_2 + \ldots\ldots + dL_{rn}(\theta_i, \phi_i; \theta_r, \phi_r; E_i)\, W_K \qquad [2.33]$$

where W_K is the weighting factor which accounts to the fraction of IFOV filled by target element K and $dL_{rK}(\theta_i, \phi_i; \theta_r, \phi_r; E_i)$ is the differential radiance reflected from that element into direction (θ_r, ϕ_r) from differential irradiance dE_i .

The contribution of multiple reflections to $dL_{rK}(\theta_i, \phi_i; \theta_r, \phi_r; E_i)$ is not specifically mentioned; however, practically and theoretically as long as those contributions originate from the same differential irradiance $dE_i(\theta_i, \phi_i)$, they should be included. Assuming isotropic reflection from each surface facet element the differential reflected radiance from an element K is given by:

$$dL_{rK}(\theta_i, \phi_i; \theta_r, \phi_r; E_i) = E_K R / \pi \qquad [2.34]$$

where E_K is the irradiance received on facet K (given in [2.27]) and K is the index of facets characteristic of the microstructure of the roughness of the surface (scene).

The obstruction of a facet element in the viewing direction is given by $W_K = 0$ (its obstruction from an illumination direction is accounted for in [2.27]).

Those spatial elements are the facets of a characteristic microstructure, the shadowed areas, the background or spatial elements of different spectral properties. Different spatial elements receive different amounts of radiation according to their orientation and the shadowing or obstruction from direct beam radiation occurring in the structure. Kriebel (1976) stressed the importance of the distribution of the irradiance on the surface as a main source for anisotropy. There are numerous studies in the area of canopy reflectance which utilize functions which describe the directional distribution of the leaves (treated as facets) as a major parameter for modelling the directional distribution of reflected radiance. Whilst the optical properties of leaves, their size and directional distribution can be derived or assumed (Verhoef (1984), Strebel et al.(1985), Gerstl and Simmer (1986) ,Goel and Grier (1988) , Grant

(1987)), the facets of bare terrain have to be derived empirically for each surface type separately . To date , the problem of determining the characteristic surface facets empirically has not been resolved in the area of geomorphology.

The three dimensional arrangement of facets for simple microstructure elements of the surface in relation to their reflectance properties have been studied both for bare and vegetated areas. A list of those microstructures appears in Table 2.2. Special attention was given to shadowing of the different microstructures for example by Egbert and Ulaby (1972), Otterman (1981), Singh and Cracknell (1985), Li and Strahler (1986) , Ranson et al. (1986), Ranson and Daughtry (1987) and Danson (1988) for forest canopies and by Norman et al.(1985) and Cierniewsky (1987,1989) for bare surfaces.

Norman et al. (1985) modelled the soil aggregates as blocks casting shadows (Figure 2.6). The relative bidirectional reflectance distribution function of soil surfaces built of those aggregates is given by :

$$R(\theta_i, \phi_i ; \theta_r, \phi_r) = (1- A_1- A_2- A_3- A_s) E_4+ A_1E_1+ A_2E_2 + A_3E_3 + A_sE_s \qquad [2.35]$$

where the As (Figure 2.6) are the relative viewed area of each block's facet (A_s is the shadowed area) from each viewing direction and the Es denote the irradiance in each of the viewed areas.

Cierniewski (1987 p.98, 1989) with the view that " the amount of reflected direct beam energy in the visible and near-infrared range from anisotropic soil surfaces is strongly correlated with the shadowed area per unit area of soil fragments" developed a set of equations which enables the calculation of the proportion of shadowed area cast by spherical particles in the viewing direction for any illumination direction.

The main purpose of Cierniewski's studies (1987,1989) was the calculation of the hemispherical reflectance of soils rather then developing their BRDF. An extension of the model to describe the BRDF is possible but also requires attention to the
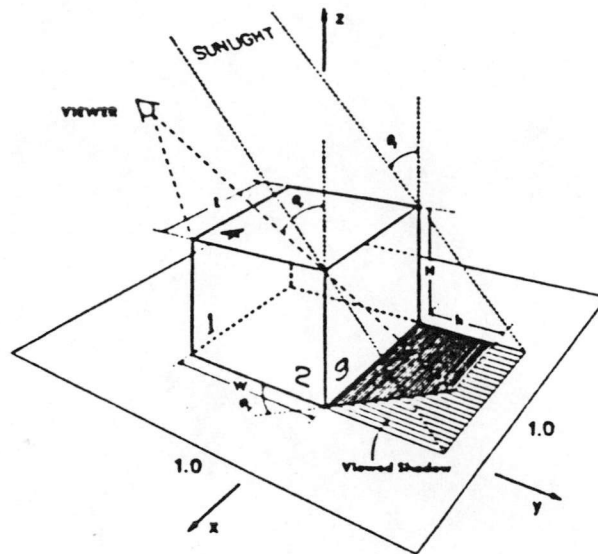
FIGURE 2.6 : Scene components derived by Norman et al. (1985) for soil aggregates modelled by a block element.
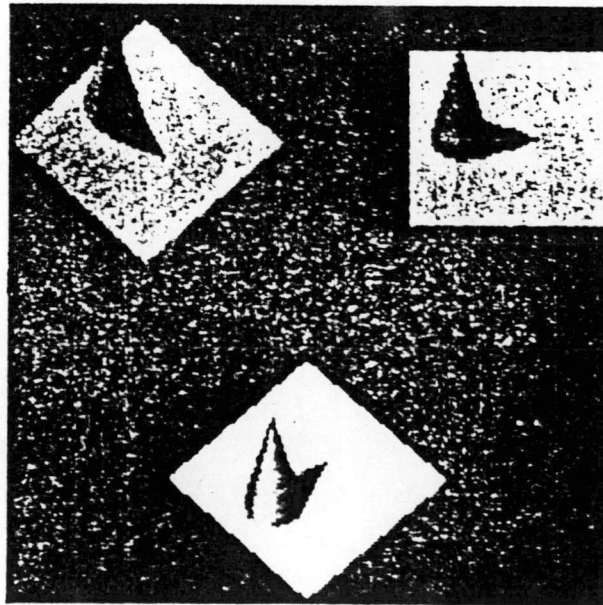
FIGURE 2.7 : Scene components derived by Li and Strahler (1986) for forest canopy modelled by cone elements.

distribution of the irradiance on the illuminated areas of the spheres.

Li and Strahler (1986) modelled the directional reflectance factors (DRF) of conifer forest canopy by modelling individual trees as cones distributed on a spectrally contrasting plane (Figure 2.7). The DRFs are then the area weighted sum of the reflectances of four scene components:

$$R(\theta_i, \phi_i ; \theta_r, \phi_r) = K_g G + (1 - K_g) [(C_c / A_c) K_c C + K_t T + K_z Z] \qquad [2.36]$$

where the Ks are the relative areal proportion in the viewing direction occupied by the different components ; c and g denote sunlit canopy and ground while z and t denote shaded canopy and ground respectively ; G, C, Z and T are the reflectances of those components; C_c / A_c accounts for the overlapping between crowns and the shadowing of crowns by other crowns. The Ks are functions of the illumination and viewing angles : $\theta_i, \phi_i , \theta_r, \phi_r$.

Both models given by [2.35] and [2.36] assume isotropic reflection from each of the structure components and the area of the different scene components is used as a weighting factor. While in the first each component is characterized by its irradiance, in the second, the components are characterized by their reflectances. The difference between the models represents differences in approaches for vegetated versus bare terrain.

Following the above equations ([2.34] to [2.36]), it is possible to indicate under the assumption of isotropic reflection that the effect of microstructure is limited to determining the relative proportions of the components in the sensor field of view. Thus, the effect is not scale dependent. The same observation was made by Norman et al. (1985) and Jupp et al. (1986).

2.2.3.2 Parametric and empirical modeling of BRDF

For the cases where the properties of the surface are not fully known or where it is not possible to assume a representative microstructure as a subject for the solar

radiation interaction, there is wide usage of empirical functions for modelling the BRDF. In these models a major consideration is given to the illumination / viewing geometry, sun angle of incidence, off-nadir viewing angle and phase angle.

For modelling the anisotropic reflectance of lunar surfaces Minnaert (1941) formulated the following expression:

$$L(\ \theta_i, \theta_r\ ) = C\ \cos^k\theta_i\ \cos^{k-1}\theta_r \qquad\qquad [2.37]$$

where $L(\ \theta_i, \theta_r\ )$ is the reflected radiance into direction θ_r due to illumination from direction θ_i, k is a roughness/ structure parameter and C is a constant representing mainly the reflectance of the surface material. When k=1 the surface is a smooth Lambertian reflector, while most of the natural surfaces have k values between 0 and 1 (Justice et al. (1981). The rationale behind this function is that reflected radiance is influenced mainly by the amount of shadows in the field of view which is supposed to be small at large off nadir viewing angles and relatively large at the nadir direction. Justice et al. (1981) claim that [2.37] is inappropriate for k > 1, where there is a high specular component. It may be concluded therefore that the Minnaert model treats the roughness as elements built of isotropically reflecting facets.

A detailed analysis of a few models based on the Minnaert method is given in Teillet et al. (1982). In an attempt to reduce the topographic effect in forest areas, they proposed a semi-empirical correction factor (C.F) which accounts for the anisotropy of the target area according to the angular relations formed by the illuminating angle, reflection angle and the surface slope and aspect :

$$C.F = \left[\frac{\cos(\theta_r - \theta_n)}{\cos\theta_r} \right]^{1-n} \left[\frac{c + \cos^k\theta_i}{c + \cos^k\theta_{in}} \right] \qquad\qquad [2.38]$$

where k, the 'Minnaert constant', n and c are determined empirically for each spectral band and surface type, θ_{in} is the sun angle of incidence relative to the normal to the

tilted surface of slope θ_n and θ_i is the sun's zenith angle. Teillet et al. (1982) found that the Minnaert models in their different form have had a limited success in improving the classification of forests, and thus a limited success in modelling their anisotropy.

Other methods incorporate the phase angle (Ω: the angle between the sensor viewing direction and the illumination direction) as a variable of the model. Pinty and Ramond (1986,1987) derived an analytical expression for the BRDF of two surface categories, "land" and "desert" , which differ in their k value :

$$f_r = R_o \; \cos^{k-1}\theta_i \; \cos^{k-1}\theta_r \, [\; 1+ (1- k^2) \cos^2\Omega] \qquad [2.39]$$

The model was found appropriate for describing the BRDF of "land" and "desert" surface types for the relatively large pixels utilized in their study.

Walthall et al. (1985) proposed an empirical model based on the observation that the shape of the contours of the reflectance distribution of many vegetated and bare surface types is similar to the shape of a mathematical form called the "limacon of Pascal", and developed the following modification of the limacon equation:

$$f_r \, (\phi_i, \theta_r, \phi_r) = a \; \theta_r^2 + b \, \cos(\phi_r - \phi_i) + c \qquad [2.40]$$

where a, b, c are coefficients derived by the least square method for each sun zenith angle.

Recently, a non-parametric approach was introduced by Dymond (1988). The essence of this approach is the mapping of known radiance values into multidimensional space where each dimension represents an independent variable. Unknown radiance values are then interpolated in that space following the nearest neighbour scheme. The variables in this work were mainly geometrical: $\cos\theta_i$, $\cos\theta_r$

or cos Ω. The advantage of this scheme is that no assumption is made regarding the form of the function describing the reflectance distribution from radiance received at any incoming direction. Dymond (1988) showed that using this method it is possible to gain an insight into the nature of variation of the reflectance with each of the angular components. The method does not provide a general numerical description of the surface BRDF, but it does suggest that a detailed description of the reflectance distribution can be achieved by interpolating between known values.

2.3 The derivation of surface properties from reflectance data

2.3.1 Inversion techniques

In previous paragraphs, the processes which determine the anisotropic reflection were discussed. The inversion techniques, which have been developed in remote sensing, are aimed at recovering the surface properties from reflectance data. In most cases, those properties relate to the spatial combination of the different types of surface elements. There are two distinct methods of accomplishing this objective: firstly, the method for deriving surface properties from the statistics of the spatial variation exhibited in one or a few images; and secondly, a method for deriving surface properties according to the similarity between a set of directional reflectance data derived from a model which links surface properties to the directional reflectance distribution and a set of reflectance data measured from a target. The distinction between image and directional reflectance data is somewhat artificial since images (specially multiple images) may provide directional distribution data. More important is the distinction between images of high resolution, where the surface objects are at the size equal to or higher than the sensor spatial resolution element and those of low resolution (objects smaller than the spatial resolution element). As discussed by Strahler et al. (1986) the derivation of surface properties of surface objects from low resolution data is difficult to achieve. Surface roughness is certainly a property in this last category. In the following text, we will describe a few of the existing studies of both inversion methods.

The first method emphasizes the importance of the information regarding the

composition and structure of heterogeneous scenes. Li (1985) modelled a coniferous forest as a plane covered by cones of different size and densities. The average reflectance (S) of a forest pixel is a combination of four reflectance components:

$$S = (A_g \, G + A_c \, C + A_{sg} \, Z + A_{sc} \, T) \, / \, A \qquad [2.41]$$

where G, C , Z and T are the reflectance vectors of background, crown, shadowed background and shadowed crown respectively, and A_g, A_c , A_{sg} and A_{sc} are their areas which sum to A as the total area of the pixel. Rearranging the components and substituting some of them by geometric terms yields:

$$S = G - Gm\Gamma + Xm\Gamma \qquad [2.42]$$

where X is the average reflectance of a cone and its associated shadow, m is the ratio of the squared cone radius to the pixel's area, and Γ is a dimensionless geometric form parameter describing the cone and its shadow.

Rearranging equation [2.42] gives :

$$m = \frac{G - S}{\Gamma (G - X)} \qquad [2.43]$$

since Γ was assumed to be constant , equation [2.43] establishes firstly that m can be derived from reflectance data and secondly that (V(m)) the variance of m for a timber stand should be equal to the variance of the reflectance. Li (1985) showed that (V(m)) can be given approximately by the following:

$$V(m) \cong (\omega \, R^2 + \omega \, M + M) \, (R^2) \qquad [2.44]$$

where ω is an assumed value derived from the coefficient of variation of the cones's radius, M is the mean of m and V(m) is determined from the reflectance data. Thus,

it is possible to derive the average squared crown radius (R^2) and then since

$$(\omega R^2 + \omega M + M)(R^2) = (\omega + \omega N + N)(R^2)^2 \qquad [2.45]$$

it is possible to derive also N the mean number of trees witin a pixel.

The above method was applied to a Landsat scene and found to give good predictions for R^2 and N. Similar work was carried out by Jupp et al. (1986) for a semi-arid eucalypt woodland in Australia. However, since this environment was found to be more complex the inversion was not fully developed. Instead some relations between the scene components and the reflectance were discussed.

The use of the scene variance as a measure of the composition of the scene's elements and their structure was further developed by Woodcock et al. (1988). They included the scene's variogram which, in general terms, characterizes the covariance between scene elements as a function of the distance between them . Two measures of the variogram (Figure 2.8) are suggested to correspond to the composition of the elements in the scene; the height of the sill is related to the density of the elements while the range is related to the size of the elements. Since the scene's elements are larger than the surface elements (trees), part of the information is masked. This masking effect on the variogram is called regularization. Techniques for exploring the 'punctual' variogram of the 'real' spatial distribution from regularized (empirical) variograms are discussed in Woodcock et al. (1988) and Jupp et al. (1988). The use of a simple scene model to bridge the gap between these variogram types was explored by relating the variograms explicitly defined for a disc model to those defined for coniferous forest scenes simulated by Li (1985) . Good correspondence was found to exist between the variograms empirically defined for the forest scenes with and without shadows and those of the disc model . The disc model based variogram did not correspond as well with variograms of Thematic Mapper (TM) scenes of residential and forest areas. However, the potential of the techniques was found to be promising in revealing some characteristics of the spatial distribution of the elements and their size.

A different type of study was reported by Danson (1988) . He found it possible to derive structural information for forest stands from the spectral information gathered using Daedalus Airborne Thematic Mapper data. The work covered one type of forest (Corsican pine) and it is not clear whether the relations hold in all forest types or if there is a need to develop them empirically for each . However, it was found for the specific forest type that the role of shadow was important in the red and near infrared but not in the middle infrared.

It has to be added in this regard that the study by Li (1985) and other more empirical studies such as that reported by Ranson et al. (1986) stressed the importance of a large difference in reflectance properties between the trees and the background to allow the structural (shadow) effect to be best pronounced.

The early need to develop the second type of methods, those linking surface properties to the reflectance distribution was mainly derived from attempts to study the surface conditions on the Moon and the Mars. Those studies are well represented by the work done by Minnaert (1941) and Hapke and Van Horn (1963) .

Another type of work concerns the development of methods for surfaces and radiation wavelength which emphasize the specular reflection component . Rense (1950) claimed that there is a one-to-one correspondence between the directional distribution of the facets and that of the reflected radiance. On the basis of similar argument Cox and Munk (1954) interpreted the roughness of the sea surface from statistics of the sun's glitter. Trowbridge and Reitz (1975) used Rense's method for showing that the surface of an ellipsoid of revolution can have the same facets and reflectance distribution as surfaces of random or Gaussian facets distribution. The same principles were applied for the determination of surface roughness from the reflection pattern in the radar wavelength (Shcaber, 1975; Schultejann, 1985).

For composite surfaces built of diffuse reflectors such as forest canopies and bare terrain in the shortwave and near infra-red spectrum, the relations between the reflection pattern and the surface are not as straightforward as those described in the former case.
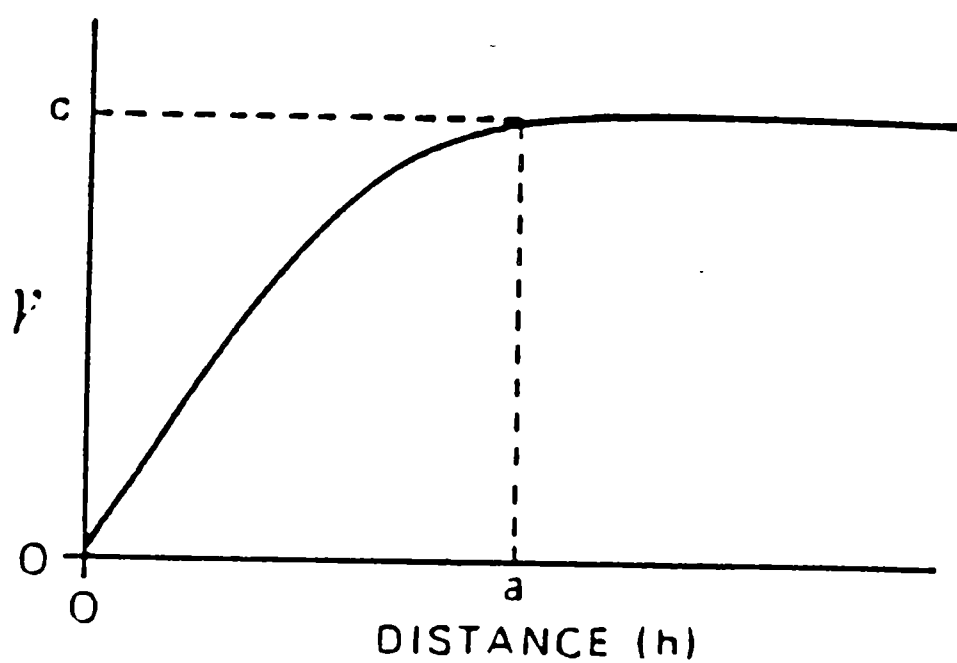
FIGURE 2.8 : The sill and range of the scene's variogram (after Woodcock et al. (1988)).

Smith et al. (1980) based on Minnaert (1941) suggested a method for estimating the Minnaert constant (k) from the reflected radiance into a sensor (Landsat) positioned in the nadir direction recorded over forest areas with different slope and aspect. The radiance into the nadir direction is given by:

$$L_{nadir} = L_{normal} \; \cos^k \theta_{in} \; \cos^{k-1} \theta_r \qquad [2.46]$$

where L_{nadir} is the scene (Landsat) reflected radiance, L_{normal} is the radiance reflected from an isotropic reflector when the illumination is from the direction of the normal to the surface.

A linear equation is then formed:

$$\log(L_{nadir} /\cos \theta_r)= \log L_{normal} + k * \log(\cos \theta_{in} * \cos \theta_r) \qquad [2.47]$$

and an approximation of k can be given by regression analysis on the two known

elements : $\log(L_{nadir} /\cos \theta_r)$ and $\log(\cos \theta_{in} * \cos \theta_r)$. The data set was collected over pixels which were identified accurately in the Landsat image and given

slope and aspect values for the calculation of θ_{in} and θ_r .

In the above model k which can be interpreted as the surface roughness, is predicted from the anisotropy of the reflected radiance field. The same technique was applied also by Eyton (1989) for deriving Minnaert constant k , this time as representing the surface scattering properties of snow surfaces.

For more detailed modelling of the interaction of radiation in crop and forest areas, Goel and Grier (1986, 1988) developed an inversion technique based on Duntley's equations (see equation [2.23]). The radiance per unit depth of the canopy is given by:

$$dL / dh = (u \, E_b(h) + v \, E_f(h) + w' \, E_s(h)) / \pi \qquad [2.48]$$

where $E_s(h)$ is the direct beam flux density, $E_b(h)$ is the backward (upward) diffuse

flux density and $E_f(h)$ is the forward (downward) flux density . The parameters u, v and w' are dependent upon the canopy parameters: r_L the leaf hemispherical reflectance, t_L the leaf hemispherical transmittance, H the average area of the leaf projections into a horizontal plane, V the average area of the leaf projections into a vertical plane, the solar zenith angle , the view zenith angle and the azimuthal difference between the sun and viewing directions . Other canopy parameters are the ground cover and row azimuth direction.

The canopy reflectance R at the top of the canopy (h=0) is given by π L divided by the irradiance at h=0. The inversion technique for estimating the canopy parameters from reflectance data involves

a least squares fitting of the canopy reflectance model to the real reflectance data using an objective function F of the following form:

$$F = \sum_i (R_i - R_i')^2 \qquad\qquad [2.49]$$

where R_i and R_i' are the measured and estimated reflectance values respectively for a particular illumination and viewing angle from available data sets.

The estimated canopy reflectance is given by an iteration process which determines each of the radiative transfer components in [2.48] according to models linking the canopy parameters to the flux travelling up and down within the canopy. The values given to the canopy parameters are changed in the iterative process until the estimated and measured reflectance values best fit. The inversion model provided good estimates of the canopy parameters from reflectance data in the near infrared spectral band measured with an Exotech Model 100 radiometer for 40 to 60 hemispherical viewing directions at 18 different sun illumination directions.

In another recent work by Nilson and Kuusk (1989), an inversion technique similar to the one suggested by Goel and Grier (1986, 1988) was applied to a canopy reflectance model developed for a homogeneous plant canopy. The canopy reflectance model was based on statistical modelling of the leaf area orientation and of the gaps between trees.

The soil reflectance term in their model was derived using Walthall et al.'s (1985) method (described in the last section).

The two types of inversion methodologies discussed above are of limited use in their application in the study of bare terrain forms, mainly since they assume that the surface objects (tree crowns for example) have a specific form. However, it is anticipated that some of the principles of the techniques developed would be of major importance in the development of inversion techniques for bare terrain.

2.3.2 Optimal viewing / illumination angles for determining surface properties

The objectives of determining optimal viewing / illuminating geometries vary greatly and concern a wide range of physical properties of the sensor , the target and the atmosphere between them. Kimes et al. (1984) define two contrasting applications: those that concern minimum variation from the nadir direction, therefore reducing unwanted effects, and those utilizing the maximum variation of reflectance, so as to provide additional information about surface properties. For passive systems like those used in the shortwave and near infrared spectral region, the direction of illumination is a predetermined parameter which is not controllable. However, it may be used in limited applications in the design of a data acquisition system which exploits low or high sun elevation angles. Some research was directed into the evaluation of off nadir viewing angles despite the fact that there is limited availability of off-nadir viewing data from remote sensing platforms following technical and practical problems involved in providing such data.

For terrain targets of the mesoscale structure, the roughness of the surface is a major reason for their anisotropic appearance. Applications which try to minimize the effect of surface structure / roughness can be divided into two strategies: firstly, those utilizing the nadir and off-nadir viewing angles on a plane perpendicular to the sun's azimuthal plane for low sun zenith angles (Hugli and Frei ,1983; Kimes et al., 1984; Kimes et al., 1987); and secondly, there are applications of the 'hot spot' which view the target within the same direction of the illumination (Gerstl and Simmer,1986 ; Jupp et al.,

1986). While the nadir region was found to be of limited success (Hugli and Frei, 1983 ; West and Stohr, 1985; Dymond, 1988) the second strategy received limited attention .

However, there is a need to utilize the extended range of off-nadir viewing angles in deriving the surface structure / roughness properties, in improving the discrimination and classification of heterogeneous targets (Duggin, 1986), and in developing a comprehensive data set for surface BRDF.

2.4 Discussion

This chapter has reviewed the existing literature in three different aspects of the radiometry of bare terrain. As stressed in the introduction, the lack of studies over bare terrain has emphasized the need to learn from the developments in radiometry of vegetated surfaces. In this section we discuss the differences and limitations set on the applications of methods and models of vegetated surfaces to bare terrain.   The deficiencies found in the body of research were mentioned throughout the review and are summarized here as well. Finally, the major hypothesis of this study will be presented together with the specific research questions.

2.4.1 The limitations of applying models for vegetated surfaces to bare terrain

Bare and vegetated surfaces are both complex systems significantly different from each other. The modelling of their structure for remote sensing and albedo studies requires some generalization of their complexity. It is the similarity between the generalized geometries which allows the application of similar models. However, there are some severe limitations. Those limitations are a result of the following differences:

- Spectral: many of the models for vegetated surfaces emphasized the role of the contrast between the vegetation and the 'background' in deriving the vegetation properties (NDVI - (Normalized Difference Vegetation Index)) for example). For bare surfaces such contrast between the elements and the background does not necessarily exist.

- Facets : for vegetation it is possible to define characteristic facets: leaves, their optical properties , size distribution, etc., while for bare terrain there are not such widely recognized characteristic facets. The problem of determining such characteristic facets for bare terrain is still to be addressed in geomorphological studies.

- Shape of elements: vegetation elements : trees, shrubs tend to exhibit characteristic form, whilst bare terrain exhibits a wide range of shapes: flatness, roundness, etc.

- Patterns: crops exhibit directionality, natural vegetation does not (in the common cases). Bare terrain exhibits patterns of microtopography and directionality which is a result of the transportation of the surface material through mass movement, wind action or by runoff .

2.4.2 Areas of deficiencies in current radiometric research of bare terrain

From the review of the various models and methods, several deficiencies have been noticed and mentioned throughout the text. Those deficiencies can be summarized as follows:

- Surface modelling : existing surface models represent a unique geometrical-optical solution without much flexiblity which could allow the extension of the models to a family of geometries.

- Multiple reflections : existing predictions do not fully agree on the extent of the effects due to multiple reflections and there are no experimental procedures available for measuring the effects.

- BRDF for rocky bare terrain : existing data was collected mainly over flat homogeneous terrain and there is no data for bare rocky terrain which could, in theory, exhibit large spatial variations.

- Inversion techniques for rough surfaces: most of the existing inversion tehniques were designed to derive vegetation characteristics from reflectance data. These techniques cannot be utilized directly for bare terrain due to the limitations described in the last section.

2.4.3 Research hypotheses and questions

This work's objective is to investigate the relationship between the surface structure and its reflectance properties. Existing theories, reviewed in this chapter indicated the important role that the surface structure has in determining the reflectance. The first hypothesis which is derived accordingly states that:

Surfaces built of different microstructures will form different BRDFs. In other words, the first hypothesis suggest a one to one correspondence between the surface structure and its directional reflectance distribution.

However, as indicated by the following examples this is not necessarily the only logical conclusion that can be made on the ground of the existing body of knowledge:

- At the microscopic scale, it was shown by Berry (1923) and Trowbridge and Reitz (1975) that randomly rough surfaces can have the same directional distribution of facets as deterministic smooth forms like a sphere and an ellipsoid of revolution and consequently have a similar reflection pattern . It is possible to suggest, then, that there are infinitesimal combinations of the directional distribution of microfacets which, following the same principle, will form the same reflection pattern. In this situation , each spatial arrangement of the microfacets forms a specific structure and therefore many structures may form a similar directional reflection distribution.

- At the meso and macro scales, it was shown that the reflection pattern from a very simple structural element was very similar to that found from real surfaces while real surfaces exhibit large variability of shapes at different scales.

- The flux transferred within the structure after multiple reflections was suggested in some cases to be of the same magnitude as the direct beam irradiance, and thus able to mask the effect of the shadows which are a major expression of structure.

- Norman et al. (1985, p.662) suggest that the effect of the shape of the soil aggregates " is not likely to be very dramatic" . They also pointed out there that the relative size of aggregates does not cause the BRDF to differ .

Following the above observations it is possible to state an alternative hypothesis:

BRDF does not have a one to one correspondence with the surface microstructure.

This thesis is therefore developed on the basis of 'multiple working hypotheses' (Haines-Young and Petch, 1983). For resolving the contradiction proposed by the two hypotheses we have specified five research questions:

1. What is the role of multiple reflections in determining the reflectance field ?

2. What is the level of anisotropy of bare terrain forms ?

3. What is the level of sensitivity of the BRDF to changes in the surface microstructure ?

4. What is the information regarding surface properties that can be derived using an inversion technique ?

5. Are there optimal viewing angles where the effect of the structure on the reflectance is more pronounced ?

These questions are addressed in the following chapters:

- Chapter 3 develops the methodology, describes the instrumentation to measure the multiple reflection effect and provides an assessment of the effect.

- Chapters 4 describes the methodologies and apparatus developed for measuring the directional distribution of reflected radiance from bare desert terrain and the roughness properties of those surfaces.

- Chapter 5 provides a description and analysis of the data collected in the arid environment near Fowlers Gap Research Station in western New South Wales.

- Chapter 6 develops a simulation model for a wide range of surface microstructures and analyses the similarity between their BRDFs.

- Chapter 7 develops roughness parameters according to the similarity between microstructures having similar BRDF.

- Chapter 8 develops a parametric reflectance model for bare surfaces characterized by their roughness and an inversion technique for this reflectance model.

- Chapter 9 summarises and discusses the answers to the above questions with their implications for the present and future research in the areas of remote sensing and albedo studies of desert areas.

CHAPTER 3 : SECONDARY REFLECTION EFFECT ON SENSOR RESPONSE FOR A V SHAPED VALLEY

In the last chapter we discussed existing studies concerned with the effect of multiple reflections between surface facets on the reflected and absorbed radiation (Section 2.1.3.2). Even though most of these studies concluded that the omission of the effect may lead to considerable errors in determining the surface reflectance, there was disagreement about the magnitude of the effect. The aims of the study reported in this chapter are firstly to provide an empirical assessment and secondly to gain an insight into the problems involved in determining the multiple reflections effect.

Consideration was given to the determination of an appropriate term to signify the case of multiple reflections between facets in the mesoscale size category. A secondary reflection effect (SRE) can be defined as occurring when solar radiation is received at a detector after two or more interactions with the Earth's surface. It can be categorized into two types (Figure 3.1) : Firstly a SRE is termed internal when the first and second reflections occur within the sensor field of view (FOV).Secondly, an external SRE occurs when the secondary reflection originates from a first reflection outside the sensor FOV. The differentiation between the two types of SRE was necessary for representing two different implications of the effect, firstly in determining the surface reflectance for facets in mountainous terrain and secondly for understanding the interaction of light with the surface roughness. A major reason concerned the anticipation that a methodology may be developed more easily for measuring the external SRE than for the internal effect. Furthermore, understanding the external SRE will also aid the understanding of the internal type of effect.

This chapter is divided into four sections. The first section describes the development of an experimental procedure for measuring the external SRE in a V shape valley configuration covered by sand . The second section describes the development of a simulation model for gaining more insight into the processes involved. The third section reports on the comparison between the simulation and experimental results.
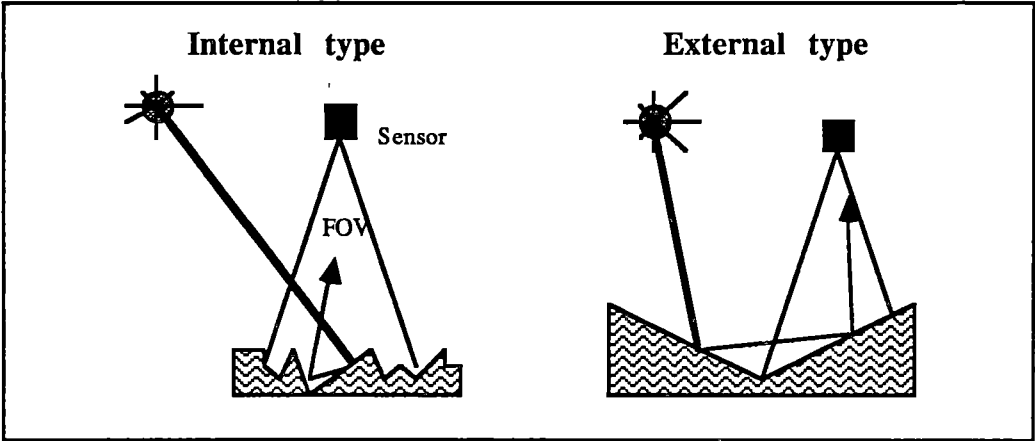
FIGURE 3.1 : External and internal types of secondary reflection.
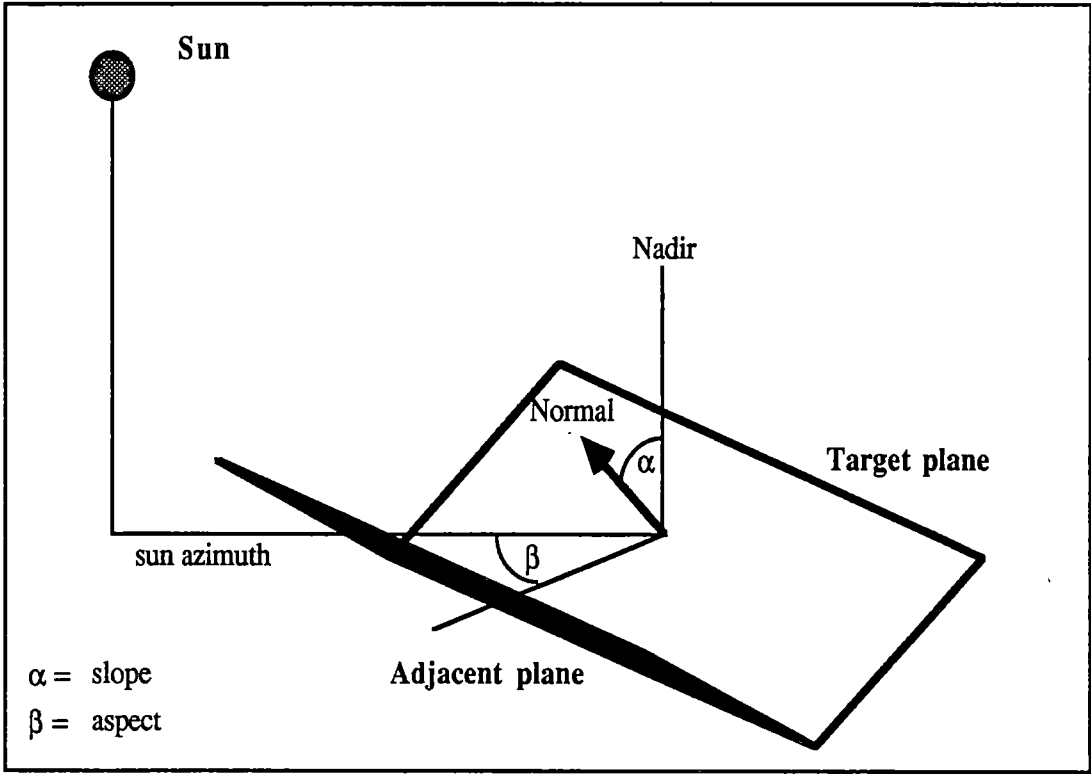
FIGURE 3.2 : Valley planes illumination geometry.

The fourth section discusses the implications of the results for this study in particular and for remote sensing applications in general. A major part of this work was also described in Shoshany (1989 A).

3.1 An experiment for measuring the external secondary reflection effect.

The difficulty in measuring secondary reflection stems from the inseparability of the reflected radiance into its primary and secondary reflected components. In this work a method was devised to prevent the external type of SRE without changing the geometry of the scene. The experiment was held on a hardware model of a V shaped valley (Figure 3.2), where the valley's tilted planes (80x40 cm in size) were covered by a thin layer of sand. An eight channel Delphi radiometer (Ellis and Nankivell 1985, Belliss 1986) was mounted 3.2 m above the target plane, viewing its central part from the nadir direction with 1° FOV. Measurements of the reflected radiance from the target plane were taken repeatedly whilst the sun's zenith changed from 50° to 20° and other parameters were varied as follows:

1. Valley plane's slope - 10°,20° and 30°.

2. Valley plane's aspect relative to the sun azimuth (see Figure 3.2) - 0° ,20° ,40° ,60° ,90° ,120° ,140°,160° and 180° .

3. Sand types- fine (0.1mm) calcium carbonate sand and coarse quartz sand(1.0 mm) .

4. Spectral bands- Landsat MSS band 4 (0.525 to 0.613 μ), band 5 (0.609 to 0.701 μ), band 6 (0.713 to 0.820 μ) and band 7 (0.787 to 1.033 μ) simultaneously.

For each combination of these parameters, two successive measurements of reflected radiance were taken, once when the target plane received secondary reflection from the adjacent plane and once when such secondary reflection was prevented by covering the adjacent plane with a black cloth (Figure 3.3). A full set of measurements for nine valley plane aspects and for a single valley slope angle was acquired within 5 minutes, thus allowing only a limited range of sun zenith angle.

Radiometer

reflected
radiance with
external
secondary
reflection

Adjacent plane

Target
plane

a

reflected
radiance
without
external
secondary
reflection

Sun's
direct beams
on the adjacent
plane are totally
absorbed by the black
cloth

b
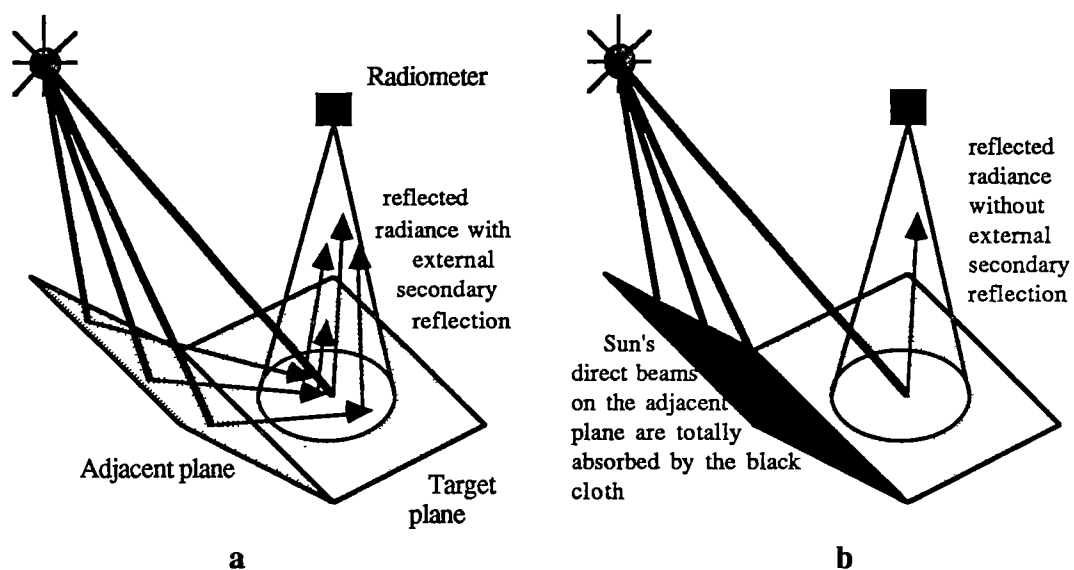
FIGURE 3.3 : A method for measuring the secondary reflection effect (not to scale): **a** indicates the configuration for measuring L" while **b** indicates the configuration for measuring L'.

The experimental secondary reflection effect (SRE_e) is then given by the following ratio:

$$SRE_e = (L'' - L') / L' \qquad [3.1]$$

where L' is the reflected radiance when the secondary reflection was not allowed, and L'' is the reflected radiance when it was allowed. An alternative way to quantify the SRE is by calculating it in terms of reflectances. However, one should take into consideration that, in that case, there is a need to determine accurately the true irradiance at the target, which was not possible in this experiment and is very difficult to achieve in remote sensing applications. The difficulties involve, in the general case, the need to make measurements of reflected and incident radiation simultaneously (Duggin and Philipson, 1981) and, in our experiment, the need for the use of a second radiometer (not available to us) and its assembly in the valley configuration without causing disturbance to the secondary reflection measurements. Moreover, assuming that the irradiance is not changing between two successive measurements of L'' and L', the SRE will be the same if we replaced the radiances in [3.1] by reflectances.

The data collected represent the SRE for the central part of the target plane. However, the SRE is expected to vary as the irradiance from the adjacent plane onto the target varies with the valley planes' slope and aspect and its position across the target plane .

Experimental data exhibited a wide range of SRE effects with values from 0.0 to 0.35. With certain sand types, the effect was found to be relatively low in most cases, while in others the magnitude of the SRE varied greatly between the geometrical configurations.

The reflected radiance and SRE of coarse quartz sand (Figures 3.4 and 3.6) exhibited the following trends:

- **Differences between band 4 and band 7** : the change in reflected radiance with target plane aspect is much more pronounced in band 7 than in band 4 as a result of larger contribution of the sky irradiance in band 4 than in band 7 . The effect of secondary reflection for band 4 is smaller than that of band 7 , both in absolute radiance
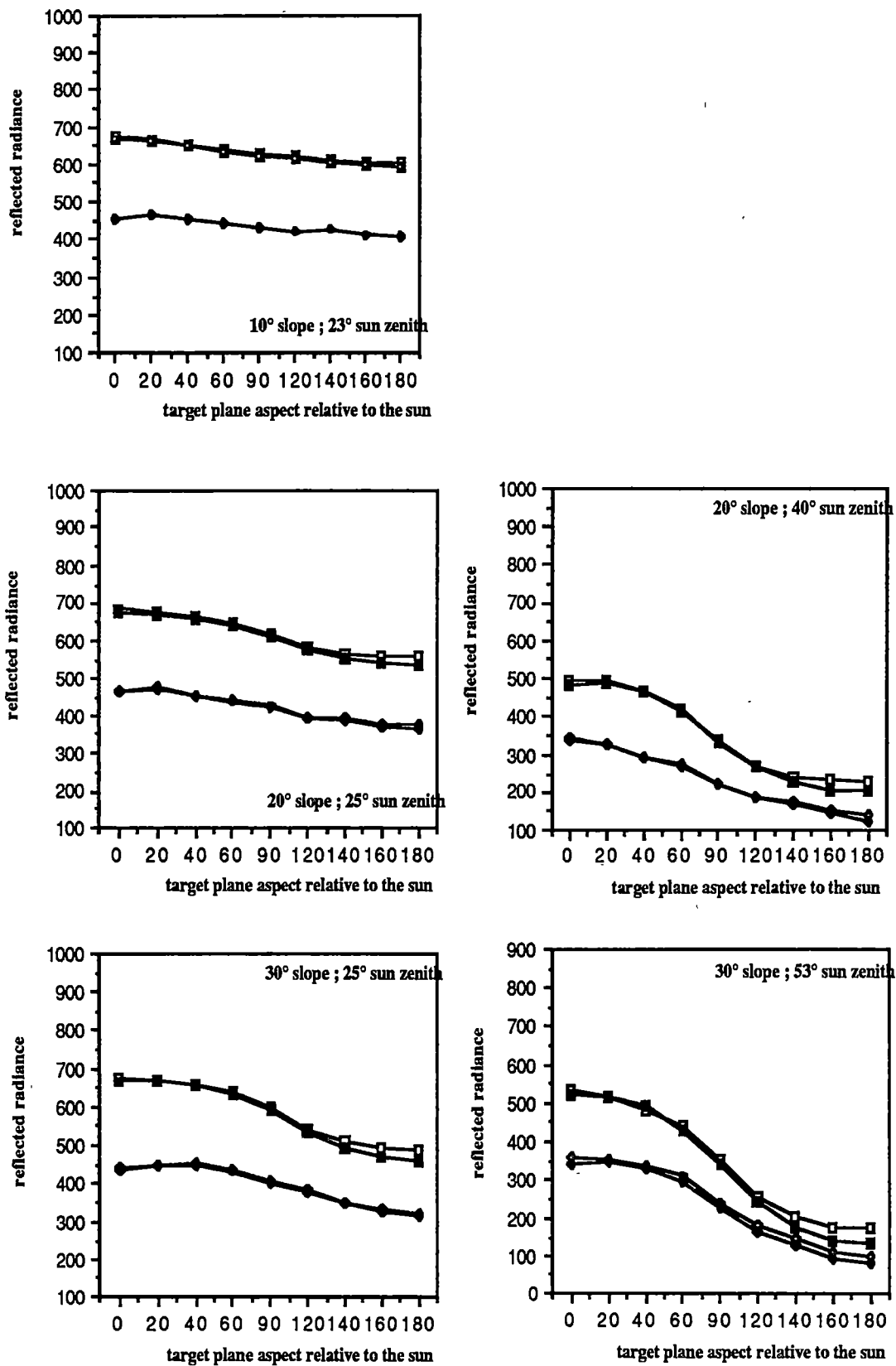
FIGURE 3.4 : Reflected radiance (μW cm^{-2} sr^{-1}) from coarse quartz sand.

Diamonds : band 4 data (empty= L" ; black= L')

Squartes : band 7 data (empty= L" ; black= L')
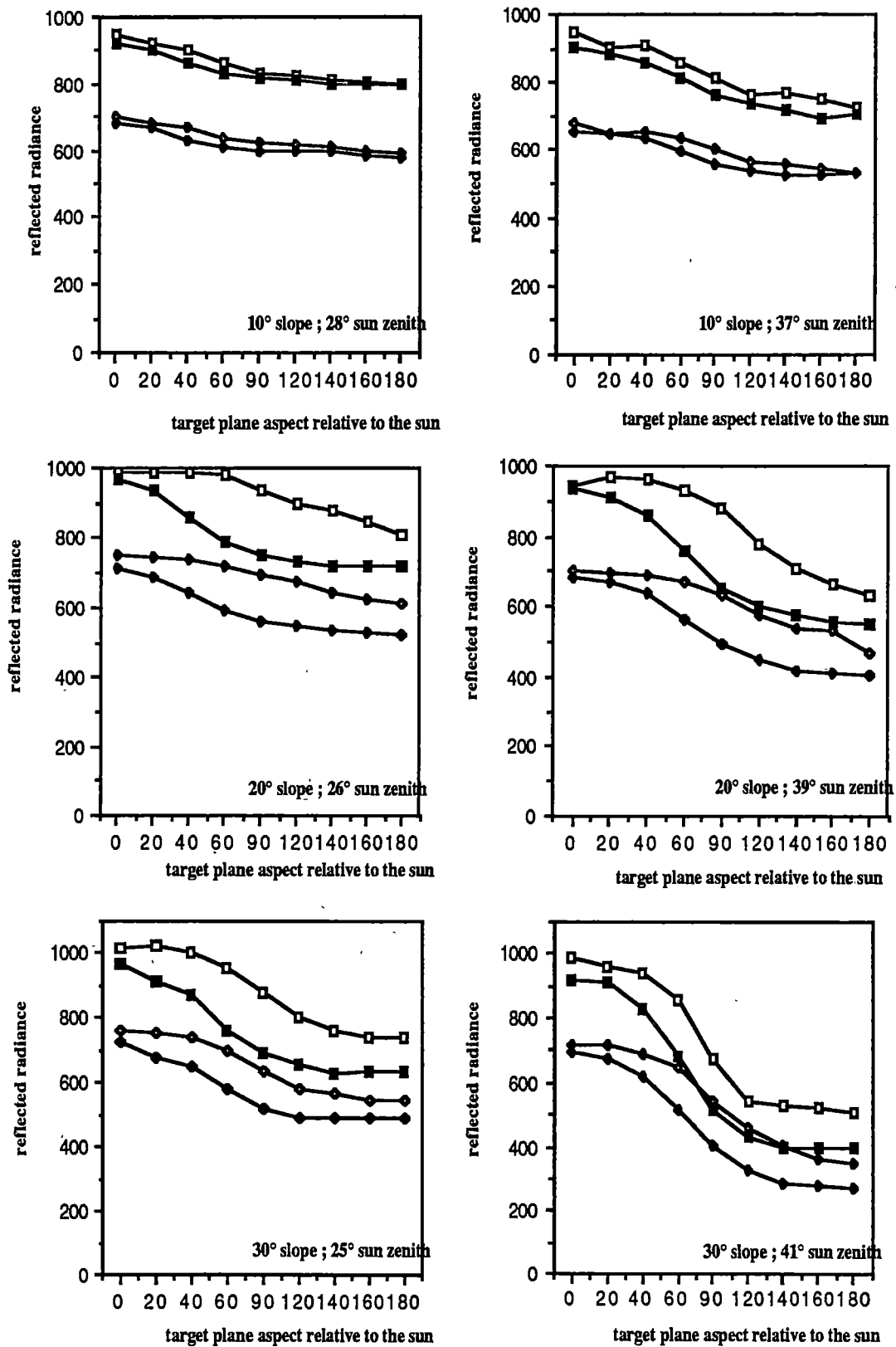
FIGURE 3.5 : Reflected radiance (μW cm^{-2} sr^{-1}) from fine calcium carbonate sand .

Diamonds : band 4 data (empty= L" ; black= L')

Squartes : band 7 data (empty= L" ; black= L')
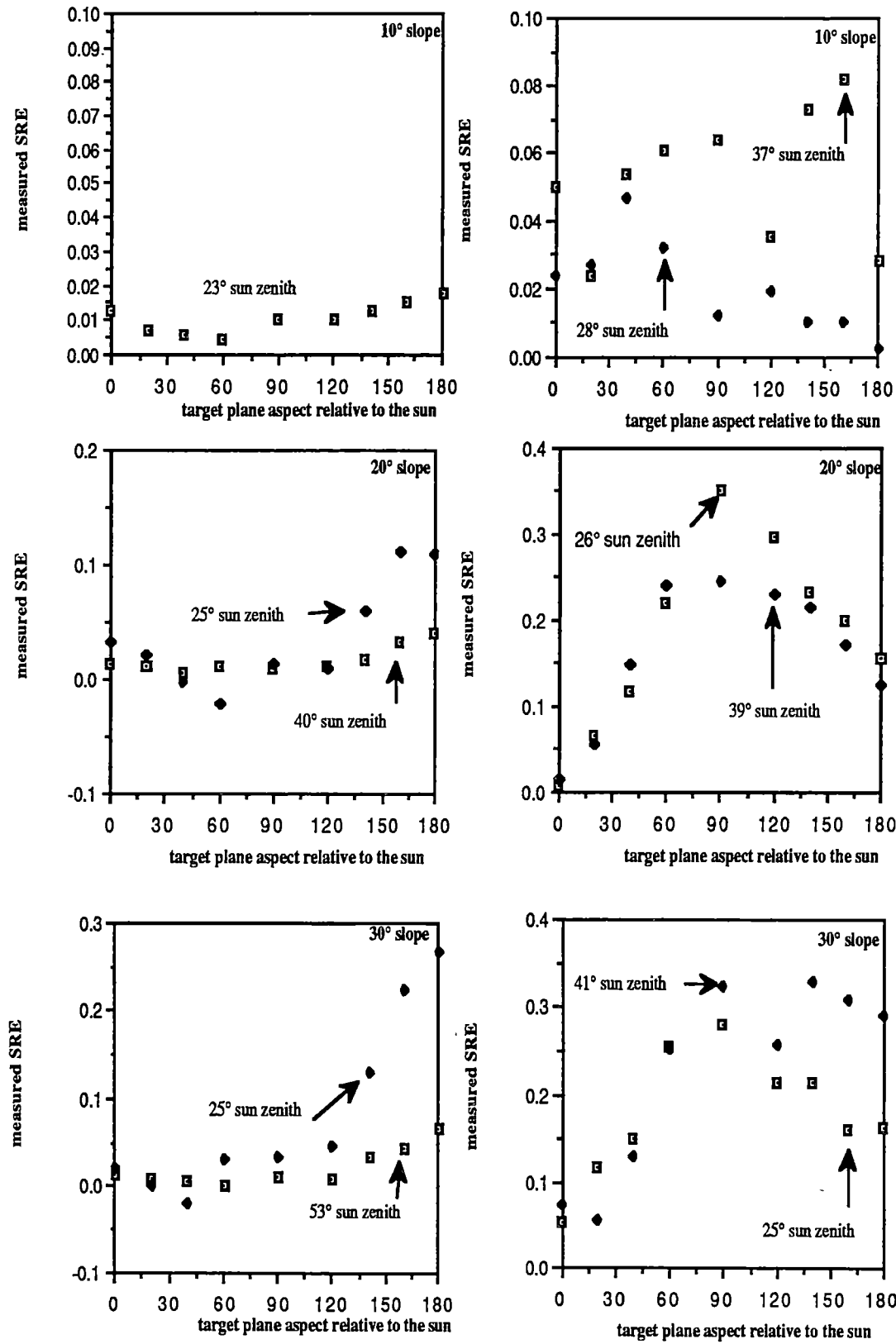
FIGURE 3.6 : Secondary reflection effect measured for the coarse and fine sand.

Left : coarse quartz data ; Right : fine calcium carbonate data.

terms (L" - L') and in SRE values.

- **Reflection pattern:** was basically isotropic as the change in the reflected radiance in band 7 correlates very well (R^2 =0.99) with the change in the cosine of the sun angle of incidence.

- **SRE pattern:** The SRE was at maximum when the target plane aspect was at 180° and decreased to nearly 0.0 at 60° .

- **SRE change with valley plane slope:** maximum SRE of 0.02 was found for 10° slope, maximum SRE values of 0.035 and 0.105 were found for 20° slope and to maximum values between 0.055 to 0.265 for 30° slope.

- **SRE change with sun angle of incidence** : the maximum SRE increased as the angle of incidence decreased.

This findings do not agree with the level of SRE predictions made by Ferencs et al. (1987). This could be explained by the fact that Ferencs et al. (1987) assumed that the surface is smooth, i.e. that all the points on the target area are viewed by the sensor and receive reflected flux from all the adjacent plane at the same time. It is possible to suggest that the SRE is low as a result of obstruction: some of the area seen by the sensor does not receive flux from the adjacent plane and some of the target surface area which receives flux from the adjacent plane is not seen by the sensor . Since most of the natural surfaces are rough, these experimental results suggest that the SRE is expected to be relatively low for valleys of slope lower than 20° with rough surfaces and isotropic reflection pattern. The SRE can be expected to be moderate to high for valley slopes greater than 20° and a small sun angle of incidence on the adjacent plane.

The reflected radiance and SRE of fine calcium carbonate sand exhibited a remarkebly different patterns from those found for the coarse quartz sand (Figures 3.5 and 3.6):

- **Differences between band 4 and band 7** : the change of reflected radiance in band 7 with varying the target plane's aspect is more pronounced than that found in band 4 (for the reasons discussed above). There is no major difference between the SRE found in the two bands.

- **Reflection pattern:** the reflected radiance without SRE exhibited a nonisotropic

reflection pattern with a pronounced backward scattering represented by the nearly constant radiance when the target plane is facing the sun and a steep decrease in reflected radiance with increasing the target plane aspect. On the other hand, the rate of decrease of reflected radiance including SRE with increasing the target planes' aspect was reduced dramatically.

- **SRE pattern:** the secondary reflection contribution in absolute terms (L" - L') showed minimum contribution at target plane aspect of 0° , maximum contribution at 90° and moderate contribution at 180°. The SRE (Figure 3.6) increased from nearly 0 to maximum at 90° and then slightly decreased toward 180°.

- **SRE change with valley plane slope:** the SRE increased with the valley planes slope from maximum of 0.07 at 10° slope, through 0.25 at 20° slope and 0.3 at 30° slope.

- **SRE change with sun angle of incidence:** there was no major change apart from the SRE found at 10° target planes slope which fluctuated considerably and therefore raised questions regarding their representativeness.

The SRE found for fine calcium carbonate sand is high and cannot be explained using the existing simulation methods, firstly since it does not correspond with the level of SRE predicted by Kimes and Kirchner (1981) and Bruhl and Zdunkowski (1983) and, secondly, because it was not associated with isotropic reflection from the adjacent plane. It is difficult to make any suggestion with regard to the obstruction effect of the surface roughness on the SRE found for the fine calcium carbonate sand. One should consider that the fact that the calcium carbonate sand particles are smaller does not mean that the surface is smoother than that of the quartz sand. The only difference that can be taken into account is that of the nonisotropic reflection. In the next section we will test whether a simulation model based on an anisotropic reflectance pattern may explain the experimental results.

3.2 A simulation model for reflection from particulate surfaces

The objective of the simulation model is to provide an independent assessment of the SRE behaviour found experimentally. The model simulates the process in which

flux is transferred within the V structure, with emphasis on the way in which incident rays interact with surface particles. To simulate the reflection from fine calcium carbonate sand particles with low transmissivity, the bulk reflectance can be assumed to be formed by external reflections on the surface of the particles (Davis et al 1981), which are assumed to have a relatively high reflectance factor of 0.5. The surface model is assumed to be built of spherical, opaque particles, covering the valley planes, and forming an array of 80x40 cells. Two possible related effects were not included in the simulation: firstly, that of multiple reflections between adjacent particles; and secondly, the combined effect of the obstruction of some of the surface areas viewed by the sensor from the adjacent plane and the obstruction of surface areas receiving secondary reflection from the sensor. An inclusion of both of the effects would result in great complication for the simulation model since, firstly, there is a need to determine the exact form of the particles and their spatial arrangement and secondly, since there will be a need to calculate the viewing and obstruction geometries for each surface point for many directions (formed from different locations on the adjacent plane relative to the target area). The effect of multiple reflections between particles (internal SRE) is expected to be of the form of an additive term which may be partly responsible for the anisotropic reflection pattern of the surface. As our method is based on establishing a phase function which will simulate the surface anisotropy reflection, it is believed to account for the multiple reflections between particles. Considering that the obstruction effect is not changing with varying the target plane azimuth, its effect on the SRE can be assumed to be in the form of a multiplicative factor, and thus it is not expected to change the azimuthal pattern of SRE. Following the experimental procedure, only the target's central particle (cell) is considered.

The amount of incident flux which is reflected by a spherical particle into a target (Figure 3.7), is proportional to $d\Phi$ (after Emslie and Aronson 1973):

$$d\Phi = \Phi_0 * R * (\sin\theta 1 - \sin\theta 2) * d\delta \qquad (W) \qquad [3.2]$$

where Φ_0 is the incident direct beam flux, R is the reflection factor, and $d\delta$ represents

target

2*θ1

2*θ2

0.5

Φo

θ2 θ1
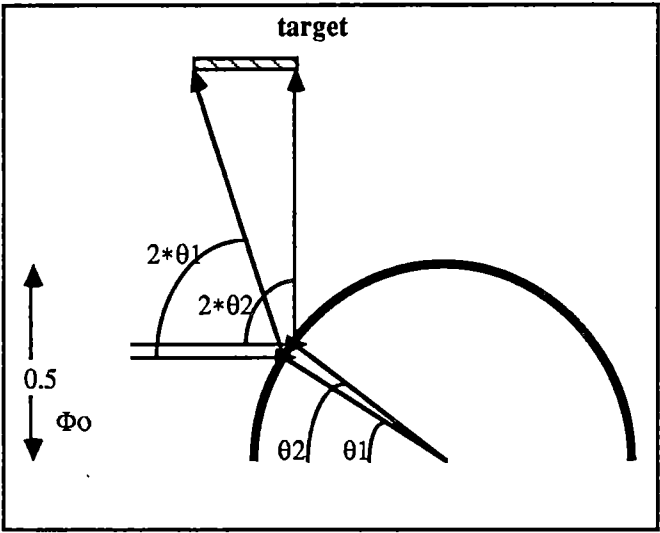
FIGURE 3.7 : The scattering of the sun direct beam from a spherical particle.

the differential width of the beam. The above expression is correct for perfectly smooth spherical particles.

In the presence of edges and asperities on the sphere surface, the shading and interception of reflected light is proportional to the local angle of incidence ($\bar{\theta}$). A simple expression which accounts for such an effect can be described by equation 3.3, where PF is a dimensionless weighting factor which modulates the reflected flux:

$$PF = (1 + \cos 2\theta) / 2 \qquad\qquad [3.3]$$

The values given by this function when 2θ equals 0, 90 and 180 are 1, 0.5 and 0 respectively. A description of such strong backscattering and weak forward scattering is reported in many works, for example in Coulson et al.(1965) .The radiance which is reflected into the sensor, after a first reflection of the sun direct beam with the target plane is given by:

$$L'_m = \cos \theta_t \ * \ d\Phi_{t->s} \ * \ PF_{t->s} \ / \ d\omega \qquad\qquad W \ m^{-2} \ sr^{-1} \qquad [3.4]$$

where $\cos \theta_t$ is the projected area of the target plane toward the sun, the subscript t->s denotes reflection from the target plane to the sensor and $d\omega$ is the solid angle formed by the sensor.

As can be seen in Figure 3.7 the spherical particles act as scatterers, the scattered light is then received on the target's central cell from a wide range of angles formed by the adjacent plane. For this reason and following considerations with regard to the obstruction effect (described above), it is assumed that the second reflection will approximate to an isotropic pattern.

The radiance received by the sensor after secondary reflection is given by:

$$L''_m = L'_m + \cos \theta_a \ * \ [\Sigma_{j=1}^{n} \ d\Phi_{aj->t} \ * \ PF_{aj->t}] \ * \ R \ / \ \pi$$

$$(W \ m^{-2} \ sr^{-1}) \qquad [3.5]$$

where $\cos \theta_a$ is the projected area of a cell on the adjacent plane toward the sun , n is

the number of cells on the adjacent plane and the subscript aj->t denotes reflection from cell j on the adjacent plane to the central cell on the target plane. The radiances L'_m and L''_m are then normalized by dividing them by the predicted radiance for sun zenith angle of 0.0 .

The SRE derived from model calculations is given by:

$$SRE_m = (L''_m - L'_m)/ L'_m \qquad [3.6]$$

The simulation is of the form of a phase function where the phase angle (the angle between mutual incident and reflected beams) is an essential parameter . In real applications the phase function is not known, but, using multiple viewing angles that function can be constructed.

3.3 Assessment of model predictions

The assessment of the model performance is made by comparing it with the experimental data. However it should be mentioned that perfect agreement cannot be expected as the model ought to give an independent estimate based on the assumptions made regarding the shape of the particles, the shape of the phase function and the pattern of the second reflection from the particles into the sensor. To enable comparison between them, the two data sets were normalised by the reflected radiance (measured and predicted) into the direction normal to the surface where the sun angle of incidence was equal to 0.

Model and measurements show broad agreement in trends (Figures 3.8 and 3.9). The correlations found between the two data sets are as follows:

- A very good correlation (R^2 between 0.94 and 1.00) between reflected radiances without secondary reflection.

- A moderate to good correlation (R^2 between 0.53 and 0.91) between reflected radiances with SRE.

Results from the simulation support the experimental findings that secondary reflection can be important when the surface is reflecting with an anisotropic pattern
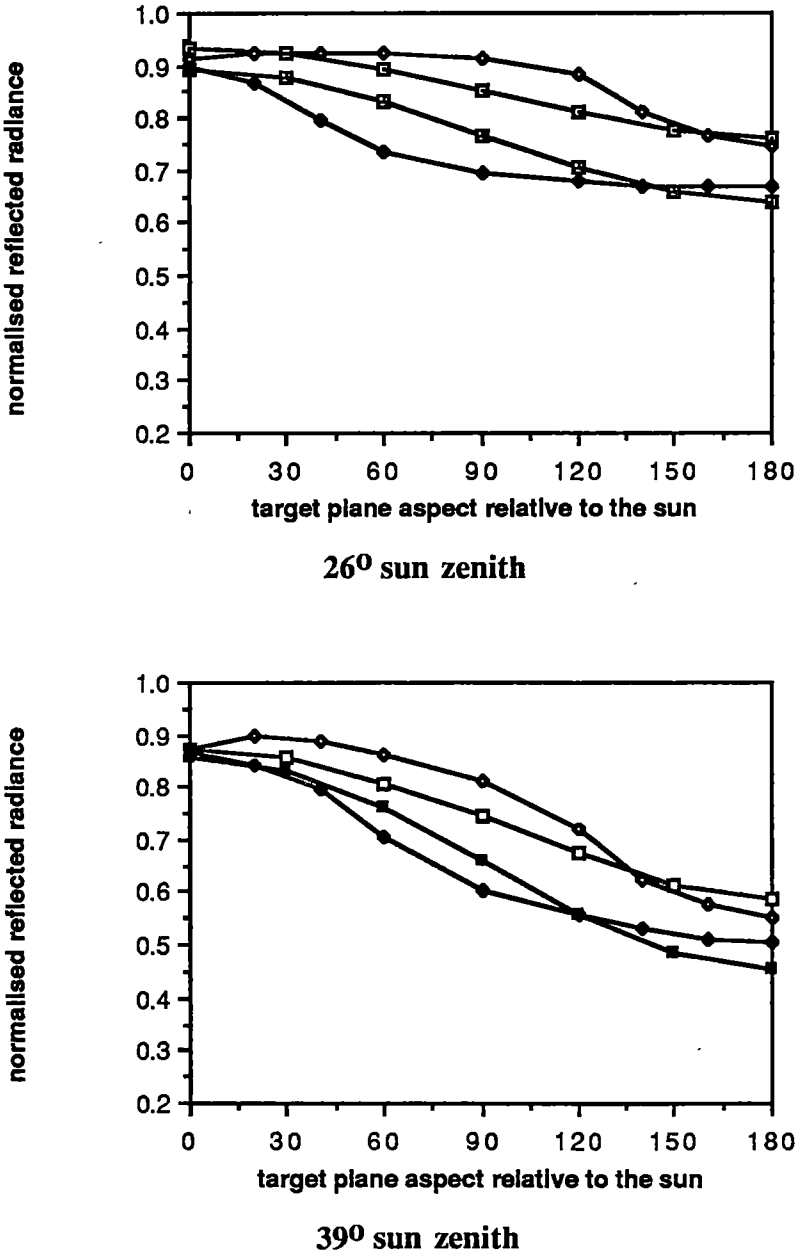
FIGURE 3.8 : Experimental versus model data for 20° valley planes slope.

Diamonds : experimental data (empty= L" ; black= L')

Squartes : model data (empty= L" ; black= L')

25⁰ sun zenith

41⁰ sun zenith
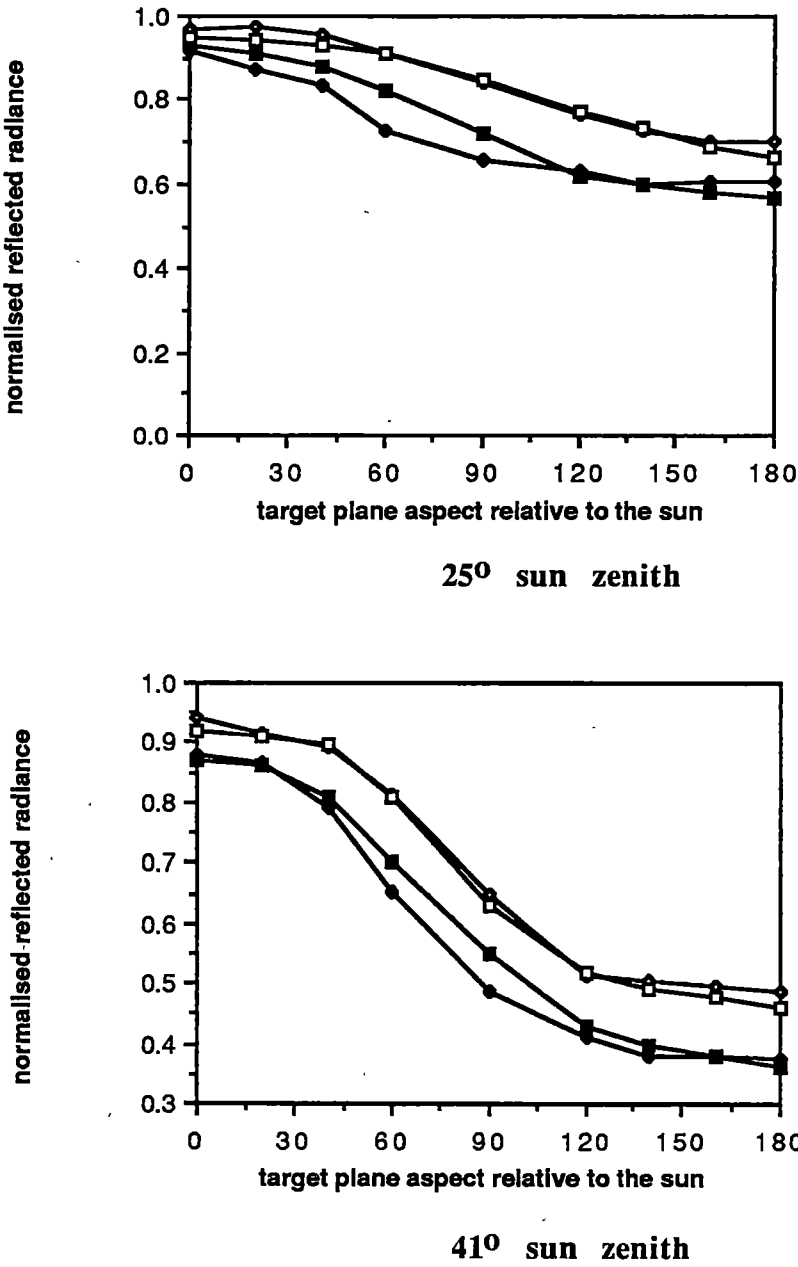
FIGURE 3.9 : Experimental versus model data for 30⁰ valley planes slope.

Diamonds : experimental data (empty= L" ; black= L')

Squartes : model data (empty= L" ; black= L')

and that those effects tend to reduce the variation in reflected radiance with changing valley azimuth. Minimum effects were found for both data sets when the target plane is facing the sun. However there is a discrepancy with regards to the maximum effect.

The model predicts maximum SRE when the target plane faces away from the sun, thereby receiving a relatively high reflection from the adjacent plane which is facing the sun. In contrast, the experimental data show a maximum SRE when both planes are facing a direction perpendicular to the sun direction and thus are equally illuminated.

It is suggested that the differences between the experiment and the simulation regarding the location of maximum secondary effect may be due to some inaccuracies involved in the measurements method or due to several linked unknowns such as the exact shape of the particles and their orientation on the tilted planes, the true reflection factor and the effect of multiple reflection between particles. Further analysis of model / measurement deviations should concentrate on the tendency of the model to overestimate the L_e' radiance, and to underestimate L_e'' for target plane aspect of 0^0 to 130^0 (the subscript e in denotes experimental measurements). Model results also tend to underestimate L_e' radiance, and to overestimate the L_e'' for target plane aspect of 130^0 to 180^0. On the basis of these observations it can be suggested that an underestimated forward component of L' for the region of 90^0 to 180^0 adjacent plane aspect (with the corresponding changes in the angle of incidence) would produce an underestimation of the SRE for the region of 0° to 90° target plane aspect, thus emphasizing the possible role of forward reflections in determining the SRE and the need for more empirical data on the real scattering functions of the surface particles.

The simulation model presented in this study was found to be in general agreement with the experimental results with regard to the level of the secondary reflection and the general trends of change of the reflected radiance from varying the target plane aspect both with and without secondary reflection. The reported simulation model was successful since the anisotropy of the surface acted as an amplifier of the reflection from the adjacent plane to the target plane and by that, it overcame the obstruction effect. In other words, there are two negating factors. One is related to the obstruction effect due to the surface roughness which reduces the SRE. The other is related to the

amount of flux reflected from the adjacent plane to the target plane relative to the direct beam flux on the target plane. This amount is controlled by three parameters : the slope of the valley planes, the sun angle of incidence on the valley planes and the anisotropy level of the surface. The SRE will increase with certain combinations of these factors and therefore may be approximated by several models and not only the one presented in this study. Such different combinations might explain why the SRE was found to be relatively high for valley planes covered with coarse quartz sand with slope angle of 30° or 20° only when the sun angle of incidence was low (Figures 3.4 and 3.5).

3.4 Discussion and conclusions

This work developed from the absence of experimental procedures for the assessment of secondary reflection effects and of a simulation model for the prediction of that effect for anisotropic reflecting surfaces. A proposed experimental procedure and simulation process for the assessment and modelling of the external SRE of a V shaped valley have been presented in this work. The valley strucure represents a common case where two facets face one another and therefore exchange radiant flux. For sand surfaces with dunes and ripples of various scales as well as for ploughed fields, it is a morphological and radiometrical reality . The interaction of light in the hardware model is comparable to that which occurs in nature between two facets of a ripple. Thus it can be claimed that this technique provides a means of simulating real world processes and exploring the parameters that control those processes. The understanding of external SRE is an essential step prior to addressing the problem of internal SRE. The proposed simulation technique can be applied to the analysis of internal SRE where the structure of the surface is explicitly defined and where the scattering properties of the surface are well known. However, for the other cases where the surface microstructure is described only by a roughness measure, a different approach is needed.

The amount of energy exchanged between the facets depends on the solar irradiance on those facets, on their scattering properties, and on their reflective power. When the facets are large and separated by large distances (several hundred meters) the scattering properties in the atmosphere may become important and possibly reduce the effect of

secondary reflection. Therefore, as the pixel size in remote sensing systems tends to decrease, the SRE is expected to increase. More empirical data using the proposed experimental technique is needed for the full assessment of external SRE. On the basis of limited experimental and simulation data, one can draw three conclusions :

1. The SRE depends on the surface roughness, the valley planes' slope and aspect, the sun angle of incidence and the surface anisotropy level. As discussed earlier, certain combinations of these factors may result in a relatively high SRE.

2. For reducing the effects of external SRE on the surface BRDF, it is recommended that the BRDF be measured when the slopes are facing the sun (target plane aspect of 0 relative to the sun direction).

3. The SRE reduces the variability in the reflected radiance from rough surfaces. Therefore it must be taken into account when there is a need for reducing the topographic effect .

The significance of the SRE results, which were obtained in this study with regard to the research hypotheses and questions outlined in Chapter 2, is that the secondary reflection may reduce but not totally mask the effect of the surface roughness microstructure . Thus, the SRE does not provide an explanation or evidence in support of the second hypothesis that the BRDF is insensitive to the microstructure.

CHAPTER 4 : METHODOLOGY AND APPARATUS FOR FIELD MEASUREMENTS

A study of the interaction of radiation with naturally rough surfaces requires the collection of detailed radiometric data of mainly the directional distribution of the reflected radiance and of detailed roughness measurements for the same field sites. As discussed in Chapter 1, ground level measurements had to be taken because of limitations related to viewing directions and spatial resolution of current remote sensing systems and the costs of existing data (from SPOT or the Daedalus ATM scanner for example) which were beyond the research budgets available for this study . However, it was found that there is no readily available apparatus for collecting ground level radiometric and roughness data within short time spans. Fast acquisition of such data was required for various reasons: to limit the variation in irradiance conditions while measuring the distribution of reflected radiance from a site, for optimal utilization of the limited number of clear days and for administrative and budget considerations which limited the possible length of the field work.

The objective of this chapter is to give a description of the methodologies and apparatus developed for measuring the radiometric and roughness properties of bare terrain surfaces. It is therefore divided into two parts which cover the radiometric and the roughness measurements.

4.1 The apparatus for Hemispherical Directions Radiance Measurements (HDRM): description and operation.

4.1.1 Existing systems

The review of existing systems for acquiring detailed radiometric data is limited to systems built for field measurements. There were some systems built for laboratory measurements, and some of the data collected utilizing those systems is described in Table 2.2. However, most of those systems are not suitable for field measurements which provided a considerable technical challenge.

The basic equipment for ground measurements of integrated hemispherical incident and reflected radiance is the pyranometer. Surface albedo may be obtained by measuring the incoming and reflected global radiation (Monteith, 1962; Nunez et al., 1972). The first attempt to differentiate the incoming or reflected radiance into its directional components was made by using a fish-eye lens in conjunction with pyranometer data. Reifsnyder (1967) and Stein (1980) calculated the view factor of different sources radiating into a location within a forest canopy , a terrain valley or an urban canyon. The main disadvantage of this technique is that the view factor cannot be directly converted to radiances.

The Multisensor pyranometer (Hamalinen, 1985; Slaen, 1983) provides an improved method for direct measurements of the directional upwelling / downwelling radiance. This instrument is built of 25 sensors at the same spectral band (0.3 to 2.5 μ) organised in four azimuthal planes and 30° off-nadir angle intervals . Within ten minutes (which is the integration time for each sensor), the irradiances measured from all of the sensors can give a detailed description of the radiance field. A slightly different approach, where the hemispherical downwelling and upwelling radiances are measured by four moving pyranometers, was described by Valko (1983).

Studies of the surface solar energy balance using satellite data require a different approach. The albedo is derived from the BRDF of the surface which is extrapolated from directional reflectance measurements using sensors with a narrow field of view (FOV). Detailed ground measurements of the directional reflected radiance field are then necessary for modelling the relation between the albedo and discrete measurements in a narrow FOV. Eaton (1976) and Eaton and Dirmhirn (1979) describe one of the first detailed measurements of upwelling directional reflectance. A Nimbus medium resolution infrared radiometer (MRIR) with 2.86^O FOV and a TIROS radiometer with 5.0^O FOV were used to acquire the data. The main objective of this work was to develop a correction factor to make possible the estimation of albedo from reflected radiance measurements into the nadir direction . A Portable Apparatus for Rapid Acquisition of Bidirectional Observations of the Land and Atmosphere (PARABOLA) which provides a very fast (30 sec.) acquisition of the full spherical field of directional

radiance in three different spectral channels was described by Deering and Leone (1986). All the above mentioned sensor systems were built for measurements over flat homogeneous surfaces as different patches of the surface are seen from each viewing direction but assumed to describe the same scene. In mountainous terrain and areas of dense drainage, or over alluvial fans and stream channels those assumptions do not hold. Deering and Leone (1986, p.3) were aware of that limitation:

'Creating an instrument that would look at the same "study plot"

or ground target area while measuring the reflected radiance

for all view zenith and azimuth directions was desired, but it

was recognized that with the aforementioned constraints such

an engineering feat might not be practicable. The obvious

implication of the present system is that the sample target

area must be (or assumed to be) spatially homogeneous over

the range of viewing angles critical to a given study and or

spatially replicated sampling may be required. '

For full coverage of the hemispherical reflected radiance field from a target area there is a need to relocate the instrument at 24 different positions relative to the target, one per azimuthal interval (15°). Such relocation will reduce the azimuthal and viewing angle accuracy, will reduce the speed by a factor greater then 24 and most of all, will potentially create a disturbance in surface conditions where the instrument is mounted on a truck or on a tripod.

There are few studies which address the problem of multi - angle viewing of a target surface. For measuring microwave scattering and emission, Chang and Shiue(1980) mounted four radiometers on a truck crane lift so that the all four radiometers observed the same surface area. Here too, there was a need to relocate the truck at different positions toward the target. A good solution to the problem was introduced by Shibayama et al. (1986). A hand-held radiometer Mark II (Tucker et al. , 1981) was mounted on an apparatus so that it was positioned with an angle toward the target area and rotated around the center with that fixed angle. Because of its structure the change of viewing angle between every turn had to be done manually, and consequently the

acqusition of hemispherical sets of five zenith angles in eight azimuthal planes was very slow (30 minutes). An added difficulty relates to the supporting base of the equipment being present at the center of the target area. Shifting the radiometer off centre reduces the possibility of the supporting structure appearing in the radiometer FOV, but at the same time it increases the dispersion of the FOV around the centre. However, more serious is the potential disturbance to the surface by the supporting structure. For vegetated surfaces that interference could be minimal. However, in the case of bare surfaces in general and for sand areas in particular it can cause substantial disturbance to the surface conditions which extends far beyond the center. Another limitation concerns the difficulty of moving the apparatus between sites. Given these limitations, it was the objective of this work to design and make a sensor system that would:

- minimize the dispersion of FOVs from a wide range of off-nadir viewing angles and maximize their overlap;

- complete acquisition of a hemispherical data set in a time span of a few minutes;

- minimize the disturbance to surface conditions; and

-be highly mobile and easily transportable.

4.1.2 A design concept for the HDRM.

The design concept used a combination of mechanical and electronic systems (sensors and data logging). Observing a target from hemispherical directions means theoretically that a sensor has to rotate around the target along profiles on the envelope of a 'hypothetical' hemisphere with an arbitrary radius. However, as noted by Deering and Leone (1986), such hypothetical viewing configuration is very hard to achieve for technical reasons. Therefore the apparatus for Hemispherical Directions Radiance Measurements (HDRM) which was constructed (Figure 4.1) aimed at limiting the spread of the sensor FOV over the surface area rather than providing 'spot' measurements. One of the major constraints was the need for rapid acquisition of data to ensure that there was only limited variation in the irradiance conditions while acquiring the reflected radiance data over a large number of hemispherical directions. This constraint implied that such rotation should be controlled mechanically and

FIGURE 4.1 : The apparatus for Hemispherical Directions Radiance Measurements (HDRM).
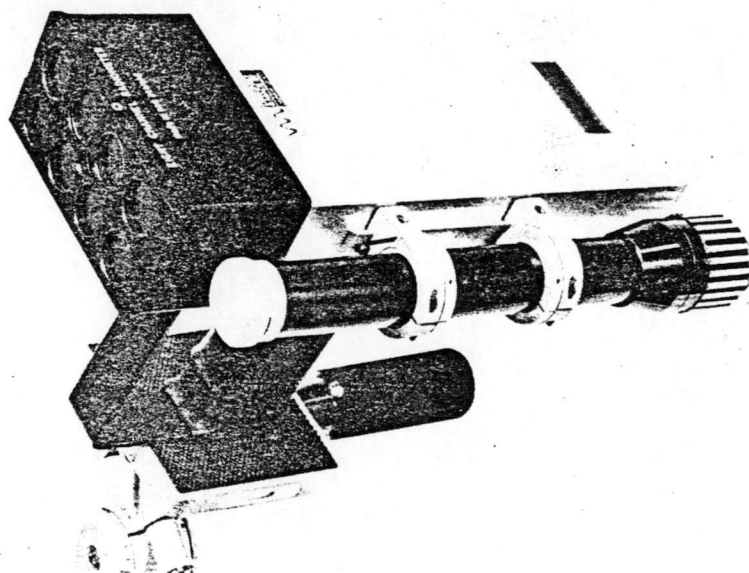
FIGURE 4.2 : The Delphi eight channel hand held radiometer

monitored electronically rather than manually. As it is difficult to achieve mechanical control along a nonlinear profile, the design here was based on the geometry of a triangle with one side of variable length. The radiometer which is positioned perpendicularly at the end of one of the fixed length sides will change its viewing angle toward the surface according to the change of the angle θ_1 at the corner of the triangle (Figure 4.4). In that setting, it is possible to measure both the upwelling and downwelling hemispheres by rotating the radiometer by 180^0. As discussed earlier, that solution would not provide a perfect spot target (the centres of the different FOVs will not converge on the centre of the target area), but it will provide a substantial amount of overlapping between the FOVs. Such an approach is justified when the target area can be assumed to be homogeneous and the microrelief amplitude is smaller than one half of the FOV, or when there are multiple measurements (samples) of the reflected radiance into each direction.

The components of the HDRM apparatus (Figure 4.1), which was built on the basis of the varying triangle principle, are the mechanical system for driving the rotation of the triangular frame (and changing its geometry), the sensor system for the acquisition of radiance data and the micrologger for controlling the operation and storage of data. The HDRM's three components, the operational considerations and the data preprocessing are described in the following sections.

4.1.3 The sensor system

The sensor system was based on an early model (1985) of the Delphi radiometer (Figure 4.2) designed and built by the Department of Scientific and Industrial Research (DSIR) of New Zealand (Ellis and Nankivell, 1985). The Delphi is a hand held battery powered radiometer with the following features:

1. Eight sensors (channels) built of Silicon detectors and multilayer interference filters in the short wave and near infrared region: 400-1100 nm.

2. Narrow (1^0) FOV and wide (20^0) FOV for radiance measurements.

3. Flat plate cosine receptor for irradiance measurements.

4. Scan (all channels scanned and stored within 4 sec) and one channel continuous

TABEL 4.1 Delphi channels: nominal center wavelength, measured band widths and half-power points (from Ellis and Nankivell (1985))

Channel Number	Nominal Centre Wavelength (nanometres)	Equivalent Square Bandwidth (measured)	Half - Power Points Lower	Upper (nanometres measured)	Comments
0	500	22.69	493.8	514.7	
1	550	85.20	525.4	612.9	MSS band 4
2	650	84.19	609.4	701.3	MSS band 5
3	650	157.05	575.9	762.2	GMS
4	670	30.17	659.4	686.1	
5	750	104.78	713.7	820.3	MSS band 6
6	950	238.23	786.7	1033.7	MSS band 7
7	780	20.07	770.0	787.9	

reading modes.

5. LCD display with a range of 0 to 9999 digits.

The spectral characteristics of each sensor are given in Table 4.1. As a result of storage limitations, only four sensors which follow the Landsat MSS bands were used.

The Delphi radiometer was designed to be operated manually. However, its ability to monitor each channel continuously, enabled us (with technical assistance provided by the Central Science Laboratory of the University of Tasmania) to design an interface with the C 21X Micrologger (Campbell Scientific Inc., 1985). This combination of the Delphi and the C 21X provided a data acquisition rate and storage capabilities which met the data acquisition requirements. The C21X measures the DC output voltage (in microvolts) which is transferred continuously from the sensors to the Delphi's storage and display unit. The conversion from voltage to radiance is done in two stages. In the first stage a microvolts reading is converted to instrument digits and, in the second stage, the digits are converted to radiance. The equations for conversion from microvolts to digits were determined experimentally. For several targets which represented a wide range of reflected radiance intensities, and two readings of microvolts and instrument digits were recorded. A linear regression between the two readings revealed a perfect correlation (R^2 of 1.0) for all four channels used (Figure 4.3). The high accuracy of microvolts measurements by the C21X ensured that there would not be significant loss of information. The conversion from radiometer digits to radiance was done using the calibration constant which were supplied by the Department of Scientific and Industrial Research (DSIR) of New Zealand. During the three years of operation in field and laboratory conditions, the Delphi kept its calibration and there was no significant degradation of the detectors. This was confirmed by a factory check after the field program. An unfortunate mistake in assembling the radiometer caused a change in the gain and offset of band 4 which influenced the irradiance reading mainly at very low illumination conditions.

A wide FOV of 20° was chosen for the Delphi radiometer, thereby ensuring a sufficient large target area to characterize the surface microrelief . The measurements of all the radiometer channels were completed within 8 / 256 of a second , so that it can
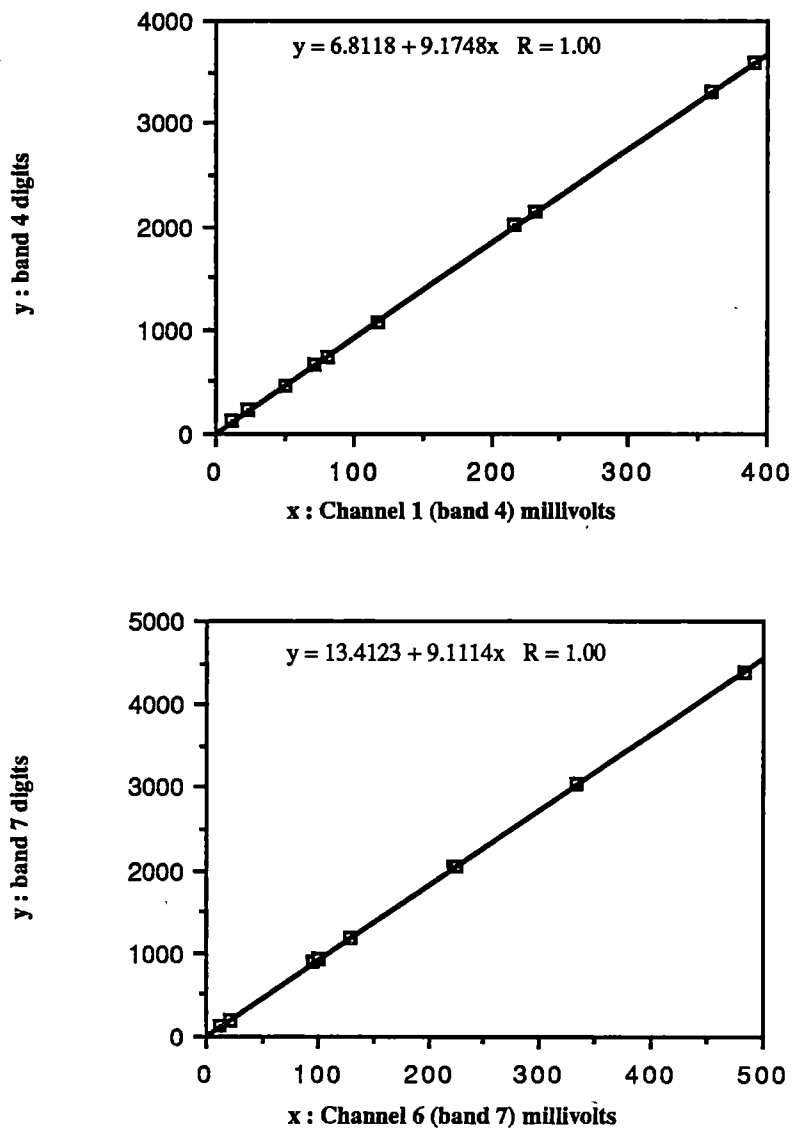
FIGURE 4.3 : The conversion from millivolts measured by the C 21X to the Delphi digits .

be assumed that all the four sensors were viewing the same scene. The cosine receptor was used for measuring the direct and diffuse irradiance on the surface. An obstruction disk successively blocked the direct rays of the sun on the Delphi sensor arranged at a plane parallel to the surface. The procedure allowed the measurement of the total and diffuse irradiance incident on the sensor (and on the surface).

4.1.4 The mechanical system

As described earlier, the mechanical system works on the basis of the geometry of a triangle with one side of varying length. Varying the triangle side length is achieved by the rotation which is needed for positioning the radiometer in different azimuthal directions toward the target.

Thus , both zenith and azimuth view angles are derived from the same rotation, a fact which is a major contributor to the simplicity of the system, its drive and its control. A coarse thread of 0.5 cm with a total length of 25 cm was used for varying the length of the vertical side of the triangle.The other two sides of the triangle (Figure 4.4) are fixed at the time of operation but their length could be adjusted according to the requirements. The thread is connected to a chain drive and a potentiometer (MET ONE wind direction sensor) for driving and measuring the azimuthal change. The triangle and drive construction can be mounted on any platform for transport between sites and for conducting measurements. Due to the requirement of minimal disturbance to the sites it was mounted on a bipod construction which had to be light enough for two people to carry .

The bipod frame itself was assembled in the field and its parts could be adjusted to form different height according to the requirements. However, the maximum dimensions were limited by the weight and total length which could be transported in a practicable manner.

A crucial part of the apparatus is the drive system. It was needed for three reasons: to make possible remote operation with minimal effect by the operator on the target irradiance, to help in overcoming the changes in rotation resistance due to gravitational forces acting with / against the direction of rotation, and to enable an electric motor to
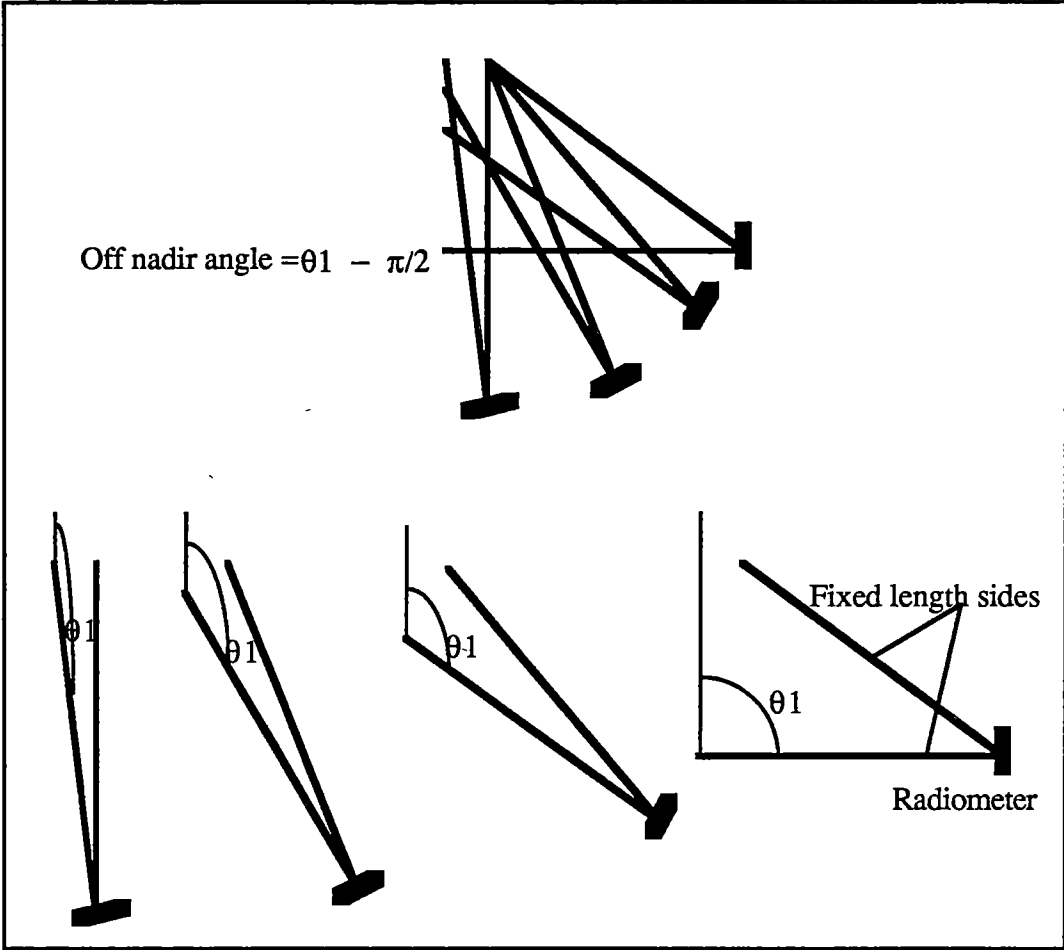
FIGURE 4.4 : The triangular geometry for varying the off-nadir viewing angle.
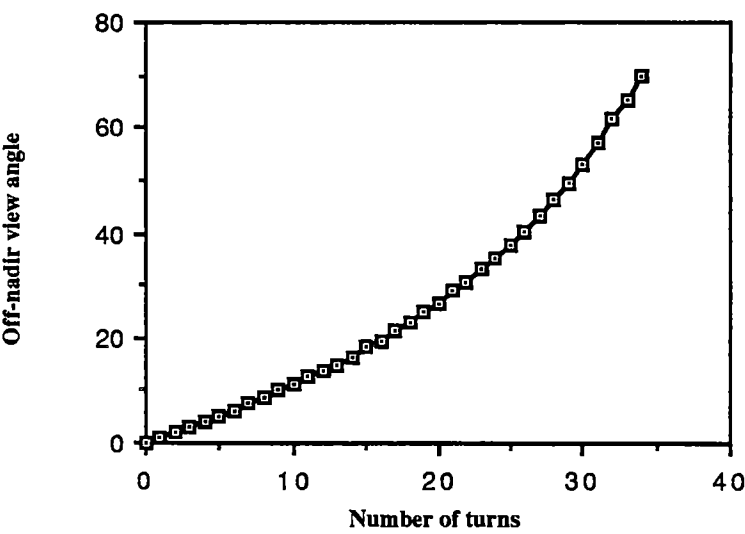
FIGURE 4.5 : The off-nadir viewing angle as a function of the number of turns.

be used in future operations.To fulfill these objectives, a gear box was used which transferred the rotation from the vertical plane to the horizontal and which reduced the rotation ratio by 2 to 1 (and therefore gaining an extra force to overcome changes in the gravitational force).

4.1.5 Pixel configuration and operational considerations

The size of the target area and of the FOV ground pixel are primarily a function of the height of the bipod and secondly of the length of the triangle sides.The height was set to be 1.80 m as a result of weight considerations (50 kg total weight for the bipod and triangular construction plus the radiometer data logger and accessories needed for running the operation).The considerations concerning the length of the triangular sides are more complicated. As their length decreases the target area increases and at their minimal length the target area configuration is similar to that of the PARABOLA system (Deering and Leone, 1986). Increasing the triangle side length decreases the target size but increases the amount of overlapping in the FOV pixels. The maximum off-nadir angle was $65^{o,}$ and this angle ensured that the target area would not extend beyond the distance defined by the distance between the two feet of the bipod. Changing the off-nadir angle from 0° to 65° required 34 turns; the rate of the angular change is not linear (Figure 4.5) starting with 1° per turn and finishing with 5° at the 34th turn. Such resolution is useful, firstly, for identifying accurately pixels which are shadowed by the apparatus frame and, secondly, since it makes possible several samplings for each viewing direction. The data are then aggregated into 5° intervals at the preprocessing stage. For operational considerations the rotation rate could not be kept constant ; the cable from the radiometer to the micrologger was wrapped around the central pole and thus there was a need to control it manually so that it would not appear in the sensor FOV and would not be damaged by the thread. As a result of this manual control of the cable, which required slowing down the rotation in some portions of the circle, a turn was completed in 5 to 10 seconds (the whole hemispherical set between 170 to 340 seconds) . As a result of the time control on successive measurements (there was also a minimal azimuthal distance control), there

TABLE 4.2 HDRM sensor FOV footprint change with number of turns
along one azimuthal plane

no. of turns	a	b	c	x
1	0.1213	0.1209	0.1211	-0.4066
2	0.1208	0.1214	0.1211	-0.3915
3	0.1204	0.1219	0.1211	-0.3767
4	0.1201	0.1224	0.1210	-0.3621
5	0.1198	0.1230	0.1210	-0.3477
6	0.1195	0.1236	0.1209	-0.3333
7	0.1193	0.1242	0.1209	-0.3189
8	0.1191	0.1249	0.1208	-0.3044
9	0.1189	0.1257	0.1207	-0.2897
10	0.1188	0.1265	0.1207	-0.2746
11	0.1188	0.1274	0.1206	-0.2591
12	0.1188	0.1284	0.1205	-0.2430
13	0.1189	0.1296	0.1204	-0.2262
14	0.1190	0.1309	0.1204	-0.2086
15	0.1193	0.1324	0.1203	-0.1901
16	0.1196	0.1341	0.1203	-0.1706
17	0.1201	0.1361	0.1203	-0.1498
18	0.1208	0.1384	0.1204	-0.1276
19	0.1217	0.1412	0.1205	-0.1040
20	0.1228	0.1444	0.1207	-0.0785
21	0.1243	0.1483	0.1210	-0.0511
22	0.1262	0.1531	0.1215	-0.0215
23	0.1287	0.1588	0.1222	0.0107
24	0.1318	0.1660	0.1231	0.0459
25	0.1357	0.1748	0.1244	0.0844
26	0.1408	0.1861	0.1261	0.1271
27	0.1474	0.2006	0.1284	0.1746
28	0.1559	0.2195	0.1315	0.2282
29	0.1672	0.2451	0.1356	0.2894
30	0.1823	0.2805	0.1412	0.3604
31	0.2030	0.3317	0.1489	0.4446
32	0.2323	0.4099	0.1594	0.5473
33	0.2754	0.5385	0.1745	0.6772
34	0.3424	0.7752	0.1968	0.8500

a , b, c : axes of footprint ellipse (short length, long length and half
width respectively)
x: distance from the center

was not a consistent azimuthal interval and slower movement resulted in more measurements per turn. That inconsistency of the azimuthal interval was desirable, since in our opinion, it increases the representativeness of the hemispherical sets .

A set of five equations (Equations 4.1 to 4.5) was developed for calculating the geometrical characteristics of the sensor FOV footprint on the ground. Those include the short axis (a) , the long axis (b) and the half width (c) of the ellipses which are produced by the sensor FOV footprint on the ground and their location relative to the centre of the sampled area (x). Table 4.2 provides the data calculated for the 34 turns using the following equations:

$$h = h_m - ((l_1^2 - (l_2 * \cos \theta)^2)^{1/2} - lu) \qquad [4.1]$$

$$a = (\tan \theta - \tan(\theta - \beta)) * h \qquad [4.2]$$

$$b = (\tan(\theta + \beta) - \tan \theta) * h \qquad [4.3]$$

$$c = h * \tan \beta / \cos \theta \qquad [4.4]$$

$$x = h * \tan \theta - l_h \qquad [4.5]$$

where h is the height of the sensor above the ground, h_m is the minimal height when the radiometer is in 90° off-nadir angle (30 cm); l_1, l_2 and l_u are the sides length of the triangle (40, 44 and 17 cm respectively; θ is the off-nadir angle and β is the half power of the sensor FOV (=10°); and l_h is the horizontal distance of the sensor from the target area centre.

The location of the FOV footprint in the target area is measured from the cross axes of the ellipse to the center of the target ; x gets a negative value for the cases where the ellipse cross axes is 'before' the target's centre and positive values where it is away from the centre.

The azimuthal interval was a result of operational considerations: the maximum number. of storage locations allowed for 20 data points per turn and thus 680 data points in one

hemispherical set per spectral channel. The number of data locations per turn dictated an azimuthal interval of 18°, and the representative reflected radiance was then the average of the readings made along this interval. The actual amount of data which was acquired was determined by the sampling controls of the C21X (0.1 sec. time control and 6° azimuthal control) and thus it is a function of the rate of rotation : slow rotation will ensure that three readings will be averaged in each azimuthal interval , while quick rotation will result in one or two readings per azimuthal interval. It was important to provide more than one reading per azimuthal interval (which will then be further aggregated also into 5° off-nadir angle intervals) for increasing the representativeness of the data and to reduce the effect of the points -spread function (PSF) in the field of view (Duggin, 1986).

To save rewinding time between two successive sets, the starting off-nadir viewing angle had to be alternately 0^0 and 65^0 . The reverse ordered sets (from 65^0 to 0^0) are sorted back at the preprocessing stage.

Each data record in a hemispherical data set consists of exact time (given by the C21X), azimuth (given by the MET ONE wind direction sensor) and four spectral channels . From the azimuthal data, it will be possible to calculate the off nadir angle subtended by the radiometer toward the target. The time data is needed for controlling the operation in differentiating between hemispherical sets and identifying discontinuities within each set. The total and direct beam irradiance at the site were measured immediately before or after each hemispherical set using the diffuse plate arrangement. In addition to the HDRM data , the sun's azimuth (using a compass), the sun's zenith angle (using an inclinometer) and the local time were recorded before each hemispherical set .

4.1.6 Self shadowing

Two self shadowing configurations were considered in the designing process of the HRDM. In the first, the sun direction is perpendicular to the HDRM long axis, thus leaving the central part of the target clear of shadows. In the second configuration, the sun direction coincides with the HDRM long axis, thus creating a narrow (2 cm) shadow across the target area. The second configuration was found to be preferable for two
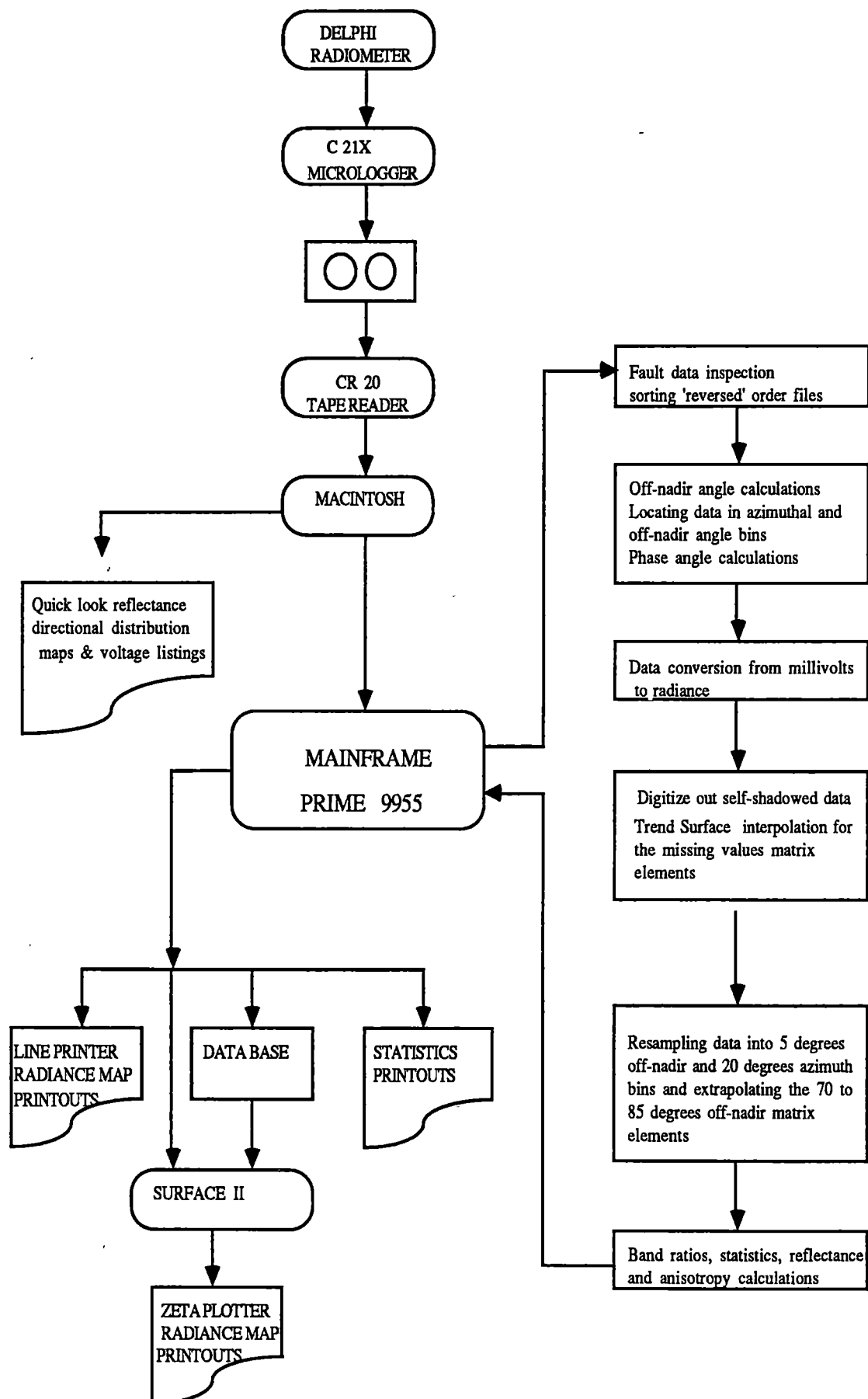
FIGURE 4.6 :   Flow diagram for the processing stage.

reasons:

1. The exact location of the shadow is known .

2. The shadow is minimal as the projected area of the HDRM into that direction is minimal too.

There are two types of self shadowing effects in the second sun-HDRM configuration.The first is an azimuthal effect where the frame shadow appears in the FOV of the sensor for readings made close to the sun's azimuth (or opposite to that direction). The second type refers to the off-nadir angles between 21° and 33°, where the sensor FOV includes the central area of the target with the frame shadow. Both these types of self shadowing effects are removed by interpolation at the processing stage.

4.1.7   Data processing

This section describes the preparation of data for mapping the directional variation of the reflected radiance, calculating the sites' hemispherical reflectance and further processing according to the research objectives. The processing procedures (Figure 4.6) are divided into three stages: input, processing and output.

The input stage starts at the end of the acquisition stage when the hemispherical sets which are stored on a cassette tape are transferred from the recorder to a Macintosh microcomputer using a CR 20 data reader. A listing of the voltage data and maps of the directional distribution of the raw voltage data are thus made possible for first inspection of the data immediately after acquisition. At the end of the field work, data were transferred from the Macintosh to the University of Tasmania mainframe computer - Prime 9955.

The processing stage included eight sequential stages:

Initially, data were inspected so as to remove faulty records. Hemispherical sets which were acquired in a reverse mode were sorted so that all the data sets followed the same direction of rotation (from 0^0 to 65^0 off-nadir view angle).

In the second stage, the off nadir angle and azimuth were calculated from the azimuthal (rotation) data for each record and it was then located in the data matrix. The time
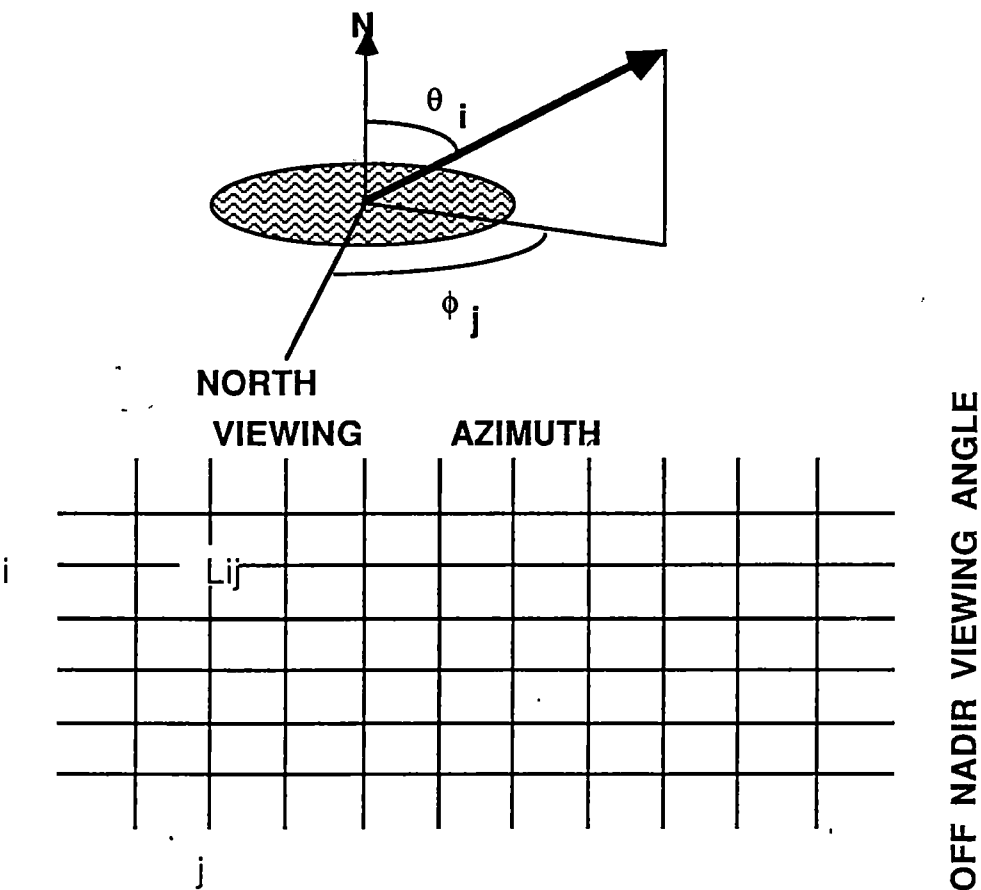
FIGURE 4.7 : The data matrix structure for a hemispherical set stored in the data base.
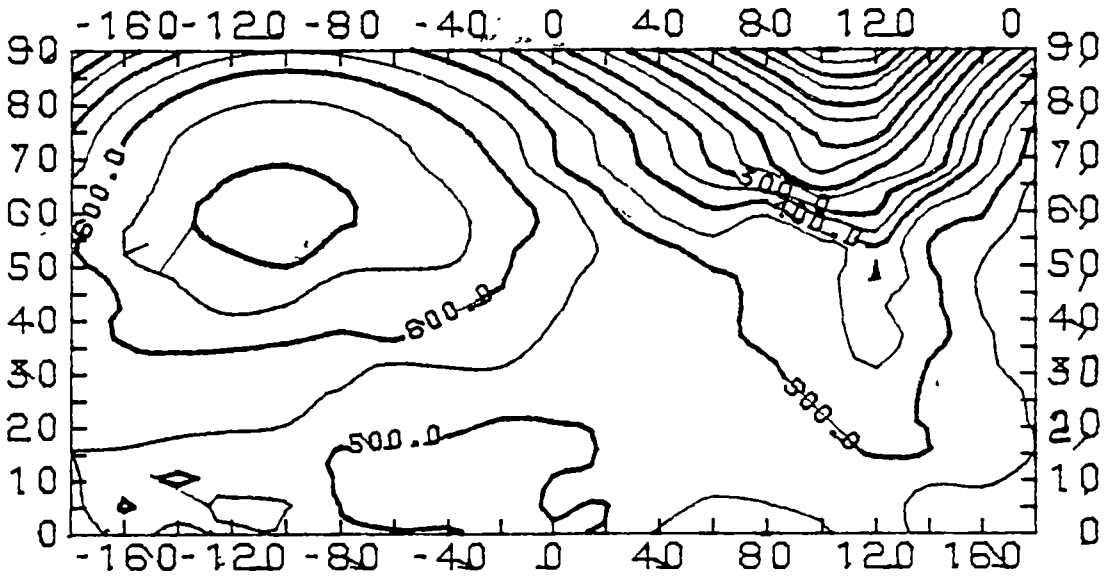
FIGURE 4.8 : The reflected radiance map for a hemispherical set (band 7) measured over sand.

Units : $\mu W\ cm^{-2}\ sr^{-1}$

information was removed from the records and replaced by the phase angle (angle between illumination and viewing directions).

In the third stage, data were converted from microvolts to radiance using the equations for conversion from microvolts to radiometer units and then using the DSIR calibration constants for conversion to radiance.

In the fourth stage the data matrix was displayed in an array of 34 off-nadir angle bins and 18 azimuth angle bins.The matrix elements with self shadowing effects were digitized out and a Trend Surface Analysis was applied to each spectral band separately using the Mather (1975) algorithm for the remaining array elements. Using the trend equation the correct radiance for the self shadowed elements and for the missing elements were interpolated.In the fifth stage the matrix (Figure 4.7) which represents a hemispherical data set was rearranged by aggregating the data into bins of 5^0 off-nadir angle interval and the matrix elements from 70^0 to 85^0 were extrapolated from the trend equations (they were not included in the band ratio calculations or statistics). Each hemispherical set therefore is composed of 235 directions between 0^0 and 65^0 off-nadir angle (one nadir direction plus 13 x 18 off-nadir directions).

In the sixth stage we calculated six band ratios (7/5, 7/4, 7/6, 6/5, 6/4 and 5/4) for each record, the statistics of the hemispherical (average, variance, standard deviation, skewness and kurtosis) and the hemispherical reflectance factor following Eaton and Dirmhirn (1979) it was given by:

$$R_\lambda = \frac{\sum_{\theta_r=0^\circ}^{90^\circ} \sum_{\phi_r=0^\circ}^{360^\circ} L_\lambda(\theta_r,\phi_r) \cos\theta_r \sin\theta_r \, \Delta\theta_r \, \Delta\phi_r}{E_\lambda} \qquad [4.6]$$

where λ is the wavelength which correspond to the spectral bands, E_λ is the total spectral irradiance measured using the diffuse plate mounted on the Delphi radiometer and $L_\lambda(\theta_r, \phi_r)$ is the reflected radiance into the direction (θ_r, ϕ_r) which is stored in the data matrix. The reflectance values for the off-nadir angles between 70^0 and 90^0

were extrapolated on the basis of the trend surface analysis technique .

The output stage produced various output formats to be used in later analysis : the new data matrix was stored in a data base, the reflected radiance map (Figure 4.8) was produced using the SURFACE II package and a histogram of the radiance frequency distribution and a printout of the statistics were also produced .

4.2 The apparatus for field measurements of surface roughness properties: description and operation.

Existing methods for collecting morphometric data for sediments are, to a large extent, manual. Commonly the three axes and roundness of a sample of particles are measured directly or by digitizing from one or multiple photographs. Examples of digitizing methods are given by Burke and Freeth (1967) and Pryor (1971). In most of these techniques, however, the particles or their photographs have had to be taken into a laboratory, thus limiting the amount of data that can be collected and more importantly allowing the possible loss of spatial information . More recent techniques relying on the Quantimet 720 image analyser are mainly used for size analysis rather than three dimensional modelling of the form of the particles. The third dimension can be derived using a stereo pair, but the contouring process and the digitizing of those contours add major components of manual work, processing time and data storage.

Following the need for fast measurements of surface roughness properties immediately after the radiometric measurements, it was concluded that it was necessary to develop a field digitizer allowing measurement of facets and particles from fine gravel size at a relatively high resolution (2 mm) and with data storage in a computer compatible format. In addition, it needed to be capable of processing the data for providing immediate parametrization of their texture and form. For practical reasons it was required that a field digitizer would be light, simple to operate and have large data storage and fast computing abilities. Budget and time constraints required that the equipment would be better constructed using commercially available parts. The description of the roughness digitizer and its operation is given in this section and also in Shoshany (1989 B).

FIGURE 4.9 : The digitizer and micrologger in working position in the field.

4.2.1 Design and operational considerations

The design concept of the digitizer (Figure 4.9) involved developing a system to measure and record hand movement whilst following the outline of pebbles or facets . The task of digitally recording such 3-D movement in a spherical coordinate system can be made possible by using three potentiometers. Two MET ONE (model 024A) wind direction sensors (Campbell Scientific, Inc. 1982) provide measurements of the azimuth and inclination (height) of the digitizing head (Figure 4.10). A third potentiometer provides measurements of the distance of the digitizing head from the center of the coordinates system. By applying DC voltage to the three potentiometers the three output voltage readings determine the position of the digitizing head. Due to time constraints and development complications, however, the third potentiometer was not operational at the time of the field work . As will be shown later that shortcoming did not affect our roughness measurements.

A C 21X micrologger (Campbell Scientific, Inc. 1985) facilitates the electronic and the processing aspects of the operation. The first aspect includes the excitation and measurement of an output voltage. The second aspect concerns the programmability of the C21X which allows the control of the operation using the control switch, data processing and output of the results using a printer or on a cassette tape. The above described components were then assembled together with a supporting framework, a digitizing device and operator's control switch (Figure 4.10).

A major concern was the resolution of the apparatus, which is defined by three parameters. These are the electrical resolution given by the micrologger and the potentiometers, the distance of the digitizing head from the centre of the coordinates system and the rate of data acquisition. The main source of error is in the azimuth and inclination angles readings since they are the most influenced by the second parameter . An angular accuracy of the magnitude of +/- 0.18° was determined for those angular readings . Thus the spatial resolution (e_r) of the digitizer is determined by:

$$e_r = \text{(distance of digitizing head from the center in mm)} \times 0.00314159 \qquad [4.7]$$
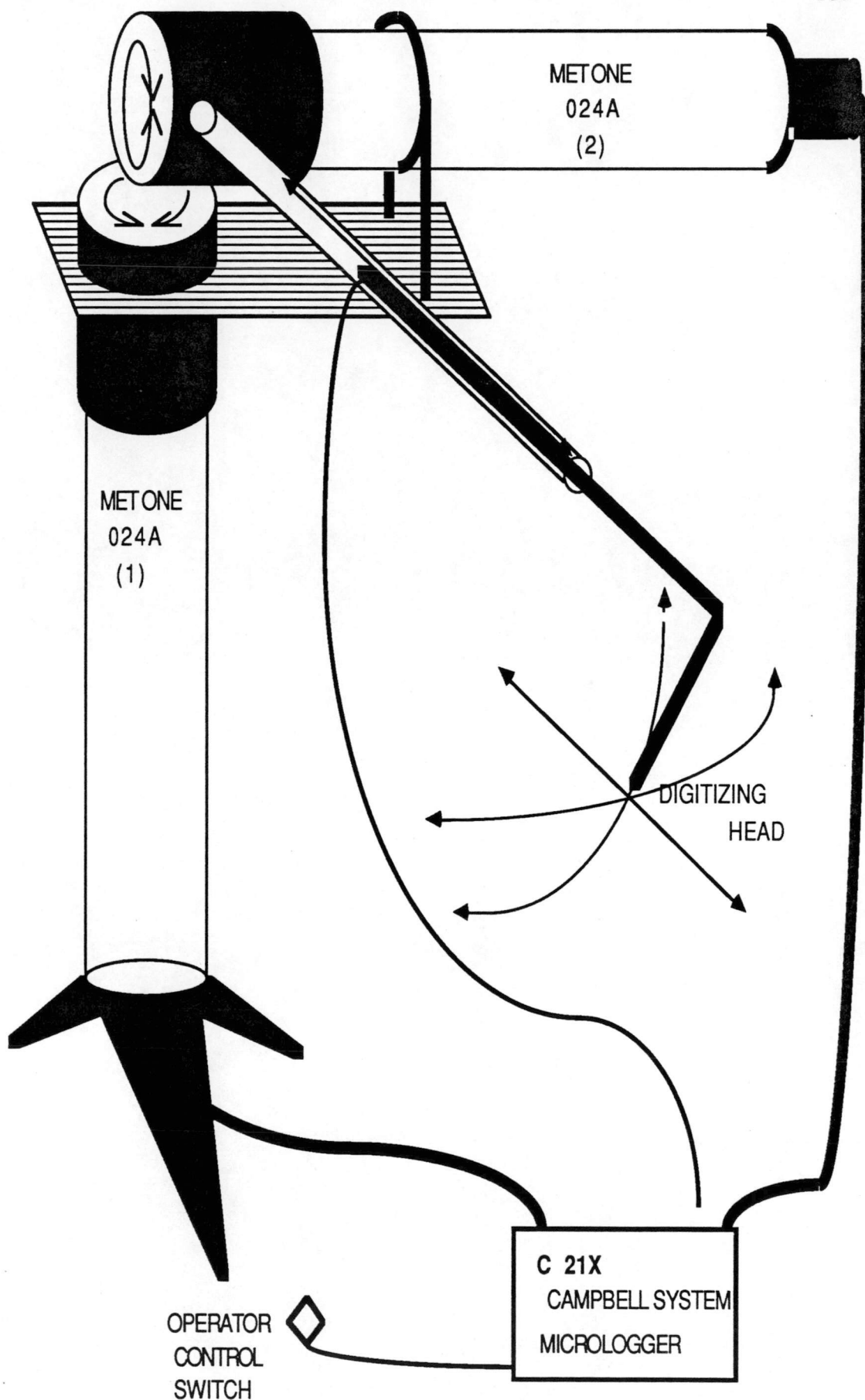
FIGURE 4.10 : A schematic diagram of the digitizer and its components.

By using a higher ratio (greater than the 1:1 ratio used here) of the number of MET ONE revolutions required to complete a full cycle of 360°, it would be possible to increase the accuracy level.

The effect of the data acquisition rate on the accuracy level depends on the rate of movement of the digitizing head by the operator and the sampling rate of the micrologger. As the maximum rate of the C21X is 80 samples per sec. there will not be any serious loss of accuracy as long as the operator maintains a slow to moderate pace of movement.

Basically, there are two options of operation: the first suits measurements of textural attributes for a single clast while the second suits applications of pattern and microtopograhic measurements. Option 1 involves the change of the digitizing head position so that it is possible to close polygons around a clast. After the completion of three polygons in three orthogonal planes, a full parameterization of the clast's texture is carried out. Results are then stored and the statistics for a sample of clasts can be calculated. Option 2 makes possible the determination of absolute coordinates for any point on the exposed surface in the digitizing space. By recording the coordinates of the digitizer location and the machine units for 0 azimuth (North) and 0 inclination it is possible to calculate the true coordinates for every point at the processing stage.

Data acquisition in the two options can be controlled by the operator's switch either to digitize individual points or to collect data continuously while the digitizing head is moved across the surface.

Two programs for the C 21X micrologger were developed to facilitate the required applications in each of the options. The roughness digitizer which was built from the components described above was found to be useful for field operations. It was light (9.5 kg) and simple to operate using the control switch. It had an unlimited final storage and an intermediate storage (for processing) of more than 2500 points. The data transfer to a computer was simple using a tape reader.

4.2.2 Field measurements of the roughness properties

In Chapter 1 we defined roughness in accordance with Gagalowicz and De Ma's
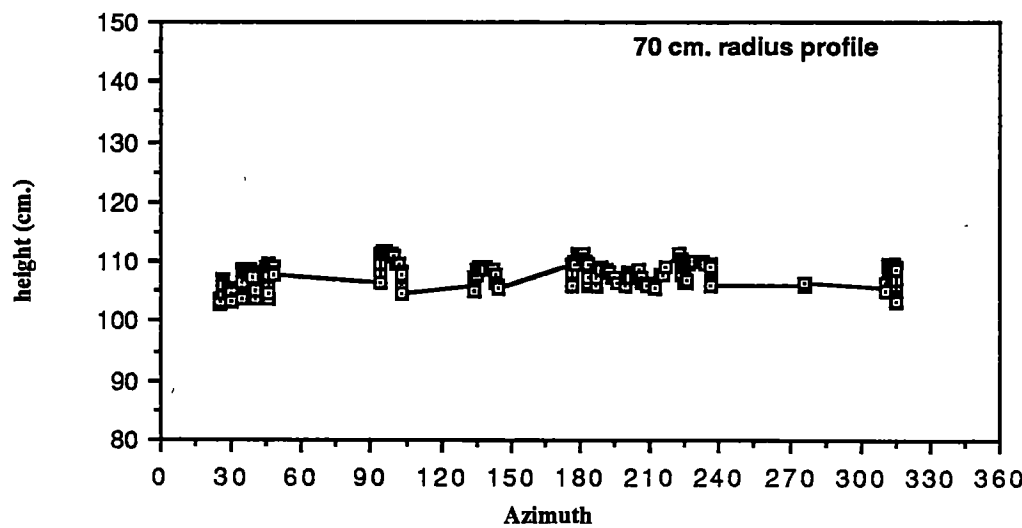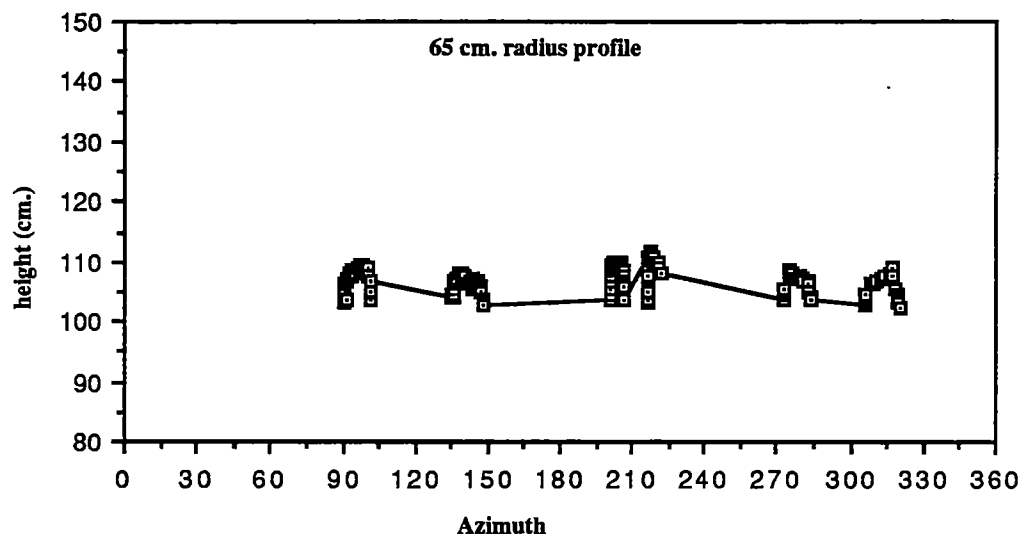
FIGURE 4.11 : The roughness sampling along two typical circular profiles.

(1985) definition of texture. The roughness of natural bare terrain is perceived as a spatial arrangement of generalized primitives of either facets (tilted smooth planes) or particles (from clay to boulder size) when each of them may be built of particles and / or facets.The objective of our field measurements was to characterize those primitives of the surface roughness. In the case of stony desert terrain the roughness can characterized by the particles and the area of exposed soil between them. The following parameters were considered as essential descriptors of site roughness :

- Percentage of stony cover as the percentage of the area from an oblique view which is covered by rock fragments. If there is more than one type of rock fragments (for example: quartz and quartzite particles), then each type of percentage cover is measured separately.

- Average and directional distribution of the distances between particles. To reveal whether there is some directionality in the spatial pattern, the distances between pebbles were measured along circular profiles. The directionality was examined by searching for orthogonal directions with minimum and maximum distances respectively.

- Particles size and shape. According to methods developed by sedimentologists (as reviewed in Pettitjohn, 1976), we calculated the following parameters:

   - The size of particles in three axes : length, width and height where each of the axes was

   characterized by three measures of the distribution, the 50, 70 and 90 percent size (the 50% size for example is the size of the particles in the sampled area of which 50% of the particles are smaller than it). As a general size measure, the average of the three axes measures was calculated for each pebble.

   - The sphericity of the pebbles was calculated using Zingg's measure:

$$\sigma = \sqrt[3]{\frac{IS}{L^2}}$$ [4.8]

   where L , I and S are the length, height and width of the pebble.

   Figure 4.12 provides a shape classification scheme for the pebbles in two dimensions given by I/L and S/I, and isolines of sphericity according to [4.8].

   - The roundness of the pebbles is expressed by (Pettijohn, 1975):

$$P = \dfrac{\displaystyle\sum_i^N \dfrac{r_i}{R}}{N}$$ [4.9]

where r_i are the individual radii of the corners of the pebbles, N is the number of the corners and R is the radius of the maximum inscribed circle of the pebble. There are six roundness classes (Lewis,1984) described in Figure 4.13 : very angular, angular, sub angular, sub rounded, rounded and well rounded.

For achieving such detailed characterization of the particles /pebbles and of the distances between them, there was a need to provide a representative sample of the site. Following accuracy considerations of the roughness digitizer, it was decided to sample the roughness along three circles with 65, 70 and 75 cm radius from the centre of the target area. The circle radii were chosen to be of +/- 10 cm from the 70 cm radius to ensure that the resolution between the circles would have only limited variation (2.0 +/- 0.3 mm). An example for the two circles for a model site built of dense parallel rows of pebbles is given in Figure 4.11. Thus, following the roughness along those three circles, it is possible to measure the distance between the pebbles and to provide data for the calculations of shape for each of the pebbles immediately following its digitization. The data stored for each site contains, for each pebble, the shape parameters , its location in spherical coordinates and its distance from the previous pebble.
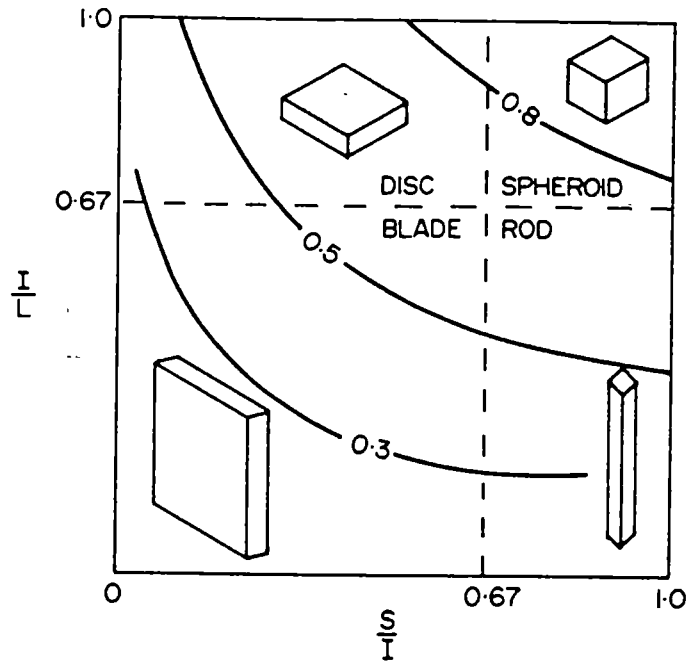
FIGURE 4.12 : A shape classification scheme for the pebbles in two dimensions given by I/L and S/I, and isolines of sphericity, where L , I and S are the length, height and width of the pebble (from Lewis, 1984).
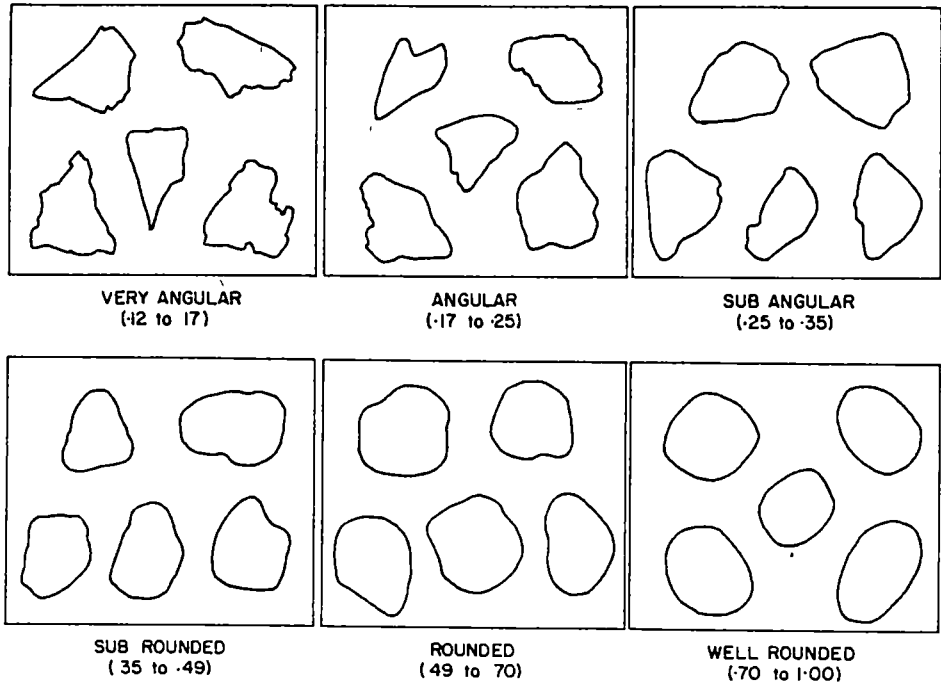
FIGURE 4.13 : Six roundness classes (from: Lewis,1984).

CHAPTER 5: THE RADIOMETRY OF BARE DESERT TERRAIN IN RELATION TO SURFACE PROPERTIES : FIELD DATA.

The objective of this chapter is to describe the data gathered during the field work and discuss interelations between surface roughness and reflectance properties. Section 5.1 provides a geographical description of the region and discusses the suitability of the area near Fowlers Gap Arid Zone Research Station for the field work according to the thesis objectives. Sections 5.2 and 5.3 describe the radiometric data gathered using the HDRM apparatus with special reference to the anisotropy level of the reflectance distribution, the hemispherical reflectance factors and band ratios' variation. The above optical properties are discussed in relation to the mineral composition, degree of stone cover and the size of the pebbles determined for sites in stony desert plains and on stony desert slopes. Section 5 provides a short description of the model sites which were measured mainly to provide reference data for comparison with simulation results.

Section 5.5 examines the main features of the data in relation to existing knowledge, to the regional study of landforms and to the research objectives given in Chapter 2.

5.1 The area of Fowlers Gap

5.1.1 Regional description

Fowlers Gap Arid Zone Research Station is located about 110 km north of Broken Hill in Western N.S.W (Map 1).

GEOLOGY : the area (Map 2) is composed of four stratigraphic units (Beavis and Beavis, 1984) :

- Precambrian metamorphic rocks which form the Barrier Range block in the northeastern structural part of the Adelaide Geosyncline (Sullivan, 1972). Topographically , the area is hilly and characterised by gentle slopes and wide valleys. The rocks in this block comprise quartzites, limestones, dolomites, quartz and shales. The appearance of quartz rocks in the area is due to quartz veins which strongly

LOCATION

o Bourke   Grafton o

• FOWLERS GAP

o Broken Hill

NEW SOUTH WALES

Newcastle o

o Hay   Sydney o

Canberra o

SANDSTONE

St

Md

Gh

Sc

Nk

Nn

Fw

Ls

Gh

Oh

7

8

Cn

SILVER CITY HIGHWAY

Oh

12

FOWLERS GAP

13

14

CONSERVATION

Gh

Sc

Fw

Nk

KEY TO LAND SYSTEMS

Cl CALOOLA — Caloola Creek floodouts, with many crabholes and patches of Mitchell grass.

Cn CONSERVATION — Scalded flats between the main river floodouts

Fl FOWLERS — Main river frontages

Fw FARAWAY — High sandstone ranges and low rounded hills.

Gh GAP HILLS — Slopes east of the ranges, with bands of saltbush

Ls LIMESTONE — Rounded hills with saltbush banding crossed by limestone outcrop

Ma MANDLEMAN — Floodout of Fowlers Creek, with many crabholes

Md MULGA DAM — Broad low sandstone ridges with mulga and saltbush

Nk NUNDOOKA — Sandstone ranges with some mulga or casuarinas

Nn NUNTHERUNGIE — Rolling stony country with bands of saltbush and bare areas of light bulldust soils

Oh OLD HOMESTEAD — Stony terraces along Fowlers Creek near the Homestead.

Sc SANDY CREEK — Scalded river flats with saltbush

Ss SOUTH SANDSTONE — Breakaway slopes with saltbush and casuarinas

St SANDSTONE TANK — Broadly undulating stony country with bands of saltbush.

Map 1 : Fowlers Gap region: topography, land systems and location of sites as marked by arrows (source : Corbet et al. (1972)).

L E G E N D

Quaternary	Gravels and Sands
	Sands, clays
Tertiary	Silcrete
Mesozoic	Telephone Creek Sandstone
Devonian	Nundooka Sandstone
	Sandstone
	Quartzite

Coco Range Formation

Sandstone and Conglomerates

Precambrian

Farnell Group

Fowlers Gap Formation

Quartzite

Limestone

Shales

Faraway Hill Quartzite

Sturt Meadow Siltstone

Quartzite

Freislich Quartzite

Western Creek Dolomite

Willyama

Picnic Creek Metamorphics

Phyllonite

Limestone

Quartzite

Butlers Peak

Sandstone Tank

Fossils

Old Sandstone Bore

Freislich Tank Dam

Landing Ground

Homestead

SILVER CITY HIGHWAY

Flowers

Telephone Creek

GAP CREEK FAULT

Fowlers Creek

MAP 2 : Fowlers Gap region : geology (source : Beavis and Beavis , 1982)

intruded the other layers of rocks.

- Devonian sediments (mainly sandstone) which form the Bancannia trough .Topographically the area is a lowland with gentle slopes breaking sharply near Nundooka creek and Picnic creek faults which form also the western boundary of this unit.

- Two units : the Mesozoic sediments (mainly conglomerates) and Quaternary alluvium form the Great Artesian Basin which is a relatively large flat area . The Quaternary sediments are divided into two types, sands and clays in the Sandstone Tank area and gravels and sand on the large plains extending over the eastern part of the region.

CLIMATE : The climate of the Fowlers Gap region can be classified as arid on the basis of the 100 years of recorded measurements for the region and as described using the Thornthwaite, Koppen and Budyko schemes (Bell, 1972).

The mean annual rainfall is 204 mm. It is uniformly distributed through the year with an average of 20 rain days (of more than 0.25 mm/day) per year (Atlas of Australian Resources : Climate, 1986). The situation in Fowlers Gap is similar to Alice Springs where Mabbut (1977) defines the area as only moderately arid in terms of the average rainfall but stresses the importance of periods of extreme conditions in determining the geomorphic processes and the landscape character. There are short periods of high rain intensity which produce high runoff and flooding. The intensity of rain in this region is of a maximum of 1.2 mm /hour for 24 hours (Atlas of Australian Resources : Climate, 1986). These periods of maximum intensity have been termed "wet spells" (Bell, 1972) and the probability of their occurrence ranges from 60% for 7mm per day to 5% for 80 mm per day mainly between December and March. The "dry spells" or annual rainfall of less than 100 mm which correspond to drought conditions occurred in seven years during the period between 1909 and 1968 (Bell, 1968). The amount of incoming solar radiation at noon during December in this area is claimed to be " the highest reached anywhere in the world" (Bell, 1972). This is a result of the relatively long durations of clear sky conditions which are translated to an annual average of 9 hours of bright sunshine conditions per day with on average, 7 hours / day in July and 11 hours / day in January (Atlas of Australian Resources- Climate , 1986). The

relatively high temperatures found in this area are a consequence of these relatively high irradiance conditions. The mean daily maxima range from 17° C in July to 37° C in January and the mean daily minima range from 13° C in July to 21° C in January. Frosts below 0° C occur in this region only about four or five times a year . Bell (1972) indicated that 'the temperature data showed no significant trends or erratic variations with different periods of record'. Therefore the extreme temperature conditions are related to the maximum daily temperatures rather than to extreme daily fluctuations as observed in other arid areas of the world.

The yearly pattern of mean daily relative humidity shows a relatively high value (70%) in July compared to Sydney and other coastal regions. The January value (36%) is a very similar to that recorded in Alice Springs and the general area of the Simpson Desert.

Extreme wind conditions with gusts of 110 to 140 kph occur in this area with a probability of between 1% and 10% in any year.

The climatic conditions described above together with the geological setting, create a highly variable environment both spatially and temporally, having therefore a major influence on the character and evolution of the landscape.

LAND FORMS: Morpho-structurally the region is part of the Australian desert which is grouped under the shield and platform desert type (Mabbut, 1977) . At a continental scale, (Dury, 1967) it is located within the Bulloo- Bancannia drainage basin between the Lake Eyre basin to the north west and the Murray-Darling basin to the south east.

The Fowlers Gap -Calindary area was divided by Mabbut (1972) into five physiographic regions :

- The Barrier Range region which corresponds to the southwestern part of two stratigraphic units: the Barrier Range block which is expressed by uplands comprising rugged gneissic hills with a local relief of up to 150 m and the Bancannia trough which forms lowlands developed on Devonian sandstone rocks. The drainage system in this region is part of the Bancannia drainage with Fowlers Gap and Sandy Creeks forming wide valleys

- Bancannia plains which correspond with the southwestern part of the stratigraphic unit of the Great Artesian basin with alluvial plains in its western part and aeolian sand surfaces to the east.

- Central Ranges and slopes comprise the Koonenberry and Bynguano mountainous areas with the most prominent relief in the centre .This area corresponds to the north eastern part of the Barrier range stratigraphic unit.

- Stony Tablelands and Plains at the northeastern part of the region comprising 'gibber plains broken by tabular uplands with silcrete caps' (Mabbut, 1972).

- Cobham plains in the northern part of the region, consisting mainly of sand dunes and playas.

A further areal classification of the Fowlers Gap region (Corbett et al. , 1972) was provided by the mapping of 31 land systems (Table 5.1 and Map 1). These land systems were identified according to the definition made by Christian and Stewart (1953) as " an area or group of areas throughout which there is a recurring pattern of topography, soils and vegetation". The total area occupied by the individual land systems ranged from 500 ha (Barrier land system) to 224,000 ha (Katalpa land system). The number and variation in the character of the land systems within the relatively small region of the Fowlers Gap - Calindary area reflects the spatial and the temporal variation in the environmental conditions which was outlined earlier. In the following two sections a more detailed geomorphological discussion is given of the specific sites.

SOILS: The soils in the Fowlers Gap area are roughly divided into two major types in the Atlas of Australian Resources- Soils and Land Use (1980): crusty red duplex soils (type Bd3) and shallow loam soils (type cf3). The first type cover about 3% of Australia ; "they are found in arid areas on extensive stony plains, pediments, tablelands and some flood plains ... often covered by partially embedded pavement of gravels, pebbles or stones of silcrete, ironstone, quartzite or other country rock up to 15 cm in diameter." (Atlas of Australian Resources- Soils and Land Use ,1980). The second type covers about 18% of Australia and characterizes mountainous regions with steep slopes in all climatic zones.

TABLE 5.1 : Land system characteristics of Fowlers Gap region (source : Corbet et al. 1972)

Relief Class	Predominant Lithology	Predominant Soil	Predominant Vegetation	Land System
Ranges	limestone	sandy loam	mulga	Teamsters
	gneiss	sand		Barrier
	phyllite	loamy sand	mulga and bluebush	Wonaminta
	quartzite sandstone		mulga and shrubs	Faraway
				Nundooka
Tablelands		silcrete duricrust	mulga	Kara Hill
			acacias and shrubs	Quarry View
		sandy loam	mulga and shrubs	Pulgamurtie
Hills and plains		loamy sand		Flat Top
	dolerite		dead finish and shrubs	Kayrunnera
	sandstone		mulga	Ravendale
Lowlands and foot-slopes			acacias and shrubs	Pulchra
			mulga	Tekum
			saltbush	Oakvale
	shale		casuarinas and shrubs	Cymbric
		loam	shrubs	Nuntherungie
		loamy sand	shrubs	Katalpa
	shale plus aeolian sand		shrubs and pines	Nundora
	limestone	loam	shrubs	Floods Creek
	gravelly alluvium	loamy sand	saltbush	Sandstone Tank
		sandy loam		Gap Hills
Plains	finer-textured alluvium	loamy sand	Mitchell grass	Caloola
			saltbush and grasses	Conservation
				Fowlers
			mulga, whitewood and shrubs	Yancannia
		sand	mulga, shrubs and grasses	Allandy
				Rodges
	sandy alluvium			Nucha
	aeolian sand			Gumpopla
			white pine and grasses	Marrapina
Pans	evaporites and sand		cane grass, lignum, saltbush	Cobham

VEGETATION : The vegetation in the Fowlers Gap area "shows a marked xerophytic character reflecting the harsh arid climate which prevails" (Milthrope, 1972). Most of the area (60%) is covered with different densities of mulga (*Acacia aneura*) mainly in mountain , piedmont and sand terrain. Approximately 30% of the area is occupied by perennial saltbush (*Atriplex vesicaria*) and bluebush (*Kochia sedifolia*) in lowlands and stony desert slopes. Ground- storey communities of different types of grasses and forbs cover large areas on the plains and in flooding areas specially after rainy events. The diversity and density of mainly shrubs and ground storey vegetation communities vary following climatic conditions and stock grazing pressure.

5.1.2 Suitability of the area for the present research

Following the objectives of this work as outlined in chapter 1, it was necessary to identify a suitable area for the research in the vast arid region of Australia. The criteria applied for selecting Fowlers Gap as the study area are:

- It represents arid environments in terms of climate, landforms and sparse vegetation cover. As described in the last section, existing research in this area indicates that it has most of the characteristics of an arid environment. Not least stony areas on the slopes and alluvial plains were reported to have sparse or no vegetation cover. The two soil types in this region are typical of the soil conditions in vast areas of Australia (around 20% of the continent).

- It provides a high probability of 10 to14 clear days within a period of a month, as indicated in the climatic description of the area. The annual average number of hours of bright sunshine conditions is among the highest in the continent. During January and February there are 12 cloudless days per month on average according to the data collected by the Bureau of Meteorology for Broken Hill.

- It provides a variety of arid landforms within a relatively small area . Desert landforms elsewhere frequently occupy large areas, sometimes over hundreds of square kilometers. Therefore transportation over long distances is required to sample sites of different geomorphological character. In the Fowlers Gap region, the large

variation in geological structure and topography created the conditions for the development of many land forms within a relatively small area.

- The area is and has been subject to continuous research activities which gives the opportunity to link this study to past and future studies in remote sensing and related environmental disciplines. Fowlers Gap, a research facility of the University of New South Wales, has been the location for much research in the areas of botany, zoology, geomorphology and geology dating back to the early sixties. These past and present activities provided a detailed description of the region which helped to assess its suitability as a study area. Lately, there has been a growing interest in developing remote sensing applications in this area, which is reflected by the work by Milne and Zhou (1987) and in planned studies of the geology of the region using an ERS-1 microwave scanner in early 1990. As there are some similarities in desert conditions and landforms between Fowlers Gap and Alice Springs, there is also a possibility to link the work done in the two regions.

- It has well equiped facilities necessary for the support of research activities involving the use of sensitive electronic and optical equipment. Fowlers Gap Research Station was able to provide optimal conditions for conducting research activities in a desert environment for the researchers and their equipment.

As a result of the above considerations the main part of the field work was conducted in this area between 17th January and 8th February 1988.

The following three sections discuss the morphometric and radiometric data gathered in areas of stony bare terrain.

5.2 Stony desert plains

Five sites of stony desert pavements were selected on the Quaternary alluvial plains formed in the drainage basin of Fowlers Gap Creek. The drainage basin encompasses the two distinct physiographic regions of Barrier Range and Bancannia Plains (Mabbut, 1972) . In the first region the stony pavements extend over relatively small areas (of dimensions of a few hundred meters) between the creek channels and the footslopes of hills with a local relief of up to 150m. These areas are described in the

Land Systems map (Map 1) as Old homestead unit (Oh) of 'Stony terraces along Fowlers Creek near the Homestead'. In the second region, the stony pavements are found on stable plains between the wide floodplains of Fowlers Gap Creek. These areas are classified mainly as Conservation (Cn) land system and described as 'Stable alluvial plains to 8 km wide between active floodplains; extensively scalded surfaces traversed by sub-parallel ill-defined depressed drainage zones' (Corbett et al. , 1972). The general appearance of the stony pavements is of quartz and quartzite pebbles standing loose or partly protruding above the surface of the typical desert loam soil (Chartres, 1982). The mineral composition of the pebbles and their density is determined by the parent rock underlying the soil zones, the distance from the hilly / rocky slopes and the morphogenetic process. The formation of stony desert plains can be explained by three distinct types of processes (Cooke and Warren, 1973; Mabbut, 1977) : by the deflation of the fine material between the pebbles (leaving them as a desert armour) ; by surface wash where the fine material is removed by runoff; or by upward displacement of stones by the large extent of swelling and shrinking that clay soil exhibits in the wetting and drying cycles. Coarse material may be deposited on the flood plains as a result of washing from steep areas or by flooding events. The variability of environments is well expressed in the landscape in general and in the morphology of the desert pavements in particular. This variability is further evident in the five sampled sites of this surface type (Table 5.2 and Figure 5.1). Each of the sites is distinctly different from the others, despite the relative closeness of their locations. The sites can be characterised as follows :

Site 7 : low (37%) stony cover dominated by small (1.3 cm mean size) quartzite pebbles.

Site 8 : low (35%) stony cover equally divided between large (3.4 cm mean size) quartz and quartzite pebbles.

Site 12 : moderate (47%) stony cover dominated by medium size (2.6 cm mean size) quartzite pebbles.

Site 13 : low (32%) stony cover equally divided between small (1.3 cm mean size) quartz and quartzite pebbles.

Site 14 : High (85%) stony cover dominated by small (1.0 cm mean size) quartz pebbles.

As can be observed in Figure 5.2 the pebbles in those sites clustered mainly on the border between Zingg's disc and spheroid categories. Similarly most of the pebbles appeared to be grouped under the angular roundness category following the Pettijohn (1975) index.

In addition to providing a suitable study area to meet the general research objectives of this thesis, stony pavements added data of interest. Site variability in mineral composition, precentage stony cover and size of the pebbles result in interesting differences in the reflectance field. Another interesting phenomenon to study is their predominantly strong forward component mainly at low grazing angles which is easily observed by the human eye (this phenomenon may be linked to the presence of quartz particles or to the desert varnish that gravel tends to develop in this environment).

The radiometric measurements were conducted using the apparatus and methodologies described in Chapter 4. Each of the sites was sampled at three close locations, 3 meters apart. Data measured at each location included hemispherical integrated irradiance data and detailed directional reflected radiance data . Each location was sampled at four different sun zenith and azimuth angles, for a total of 60 hemispherical sets , each comprising 235 hemispherical viewing directions for four spectral bands (see section 4.1.6 for detailed information on the data structure).

The total amount of data is too large to be fully presented here. To increase the representativeness of the data and reduce its volume, the data collected at the three locations for each site was averaged. The averaging was done by adding the matrices which describe hemispherical sets for the three locations of each site taken within 10 to 12 minutes and then by dividing the resulting matrix elements by three. Full hemispherical data for spectral band 7 is presented in Appendix A. Important characteristics of the data sets will be presented and discussed here as follows:

Irradiance : as all the sites were positioned on flat plains with local slopes of less than 2° and clear sky conditions were sought throughtout the major portion of the field work, the irradiance measurements were found to be stable and consistent with the

TABLE 5.2 : Surface properties for five stony desert plain sites in Fowlers Gap region

Site quartzite	Stony cover (%)	(s*)	pebbles stony cover (%)	quartz pebbles (s*)	quartz stony cover (%)	quartzite pebbles (s*)
7	41	1.1	11	1.2	30	1.0
8	40	2.8	18	2.5	22	3.0
12	36	1.2	18	1.1	18	1.3
13	48	2.4	11	1.8	37	2.7
14	83	1.2	80	1.1	3	1.8

* s : mean size of pebbles in cm.

Note : each site represent an average of three samples.

Site 7

Site 8

Site 12
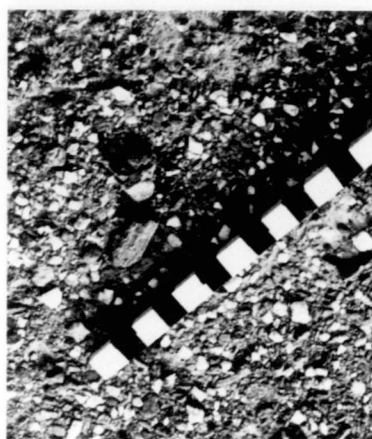
Site 13

Site 14

FIGURE 5.1 : Photographs of five sites of stony desert plains in the Fowlers Gap region (the ruler in the photographs is of 2 cm. intervals)
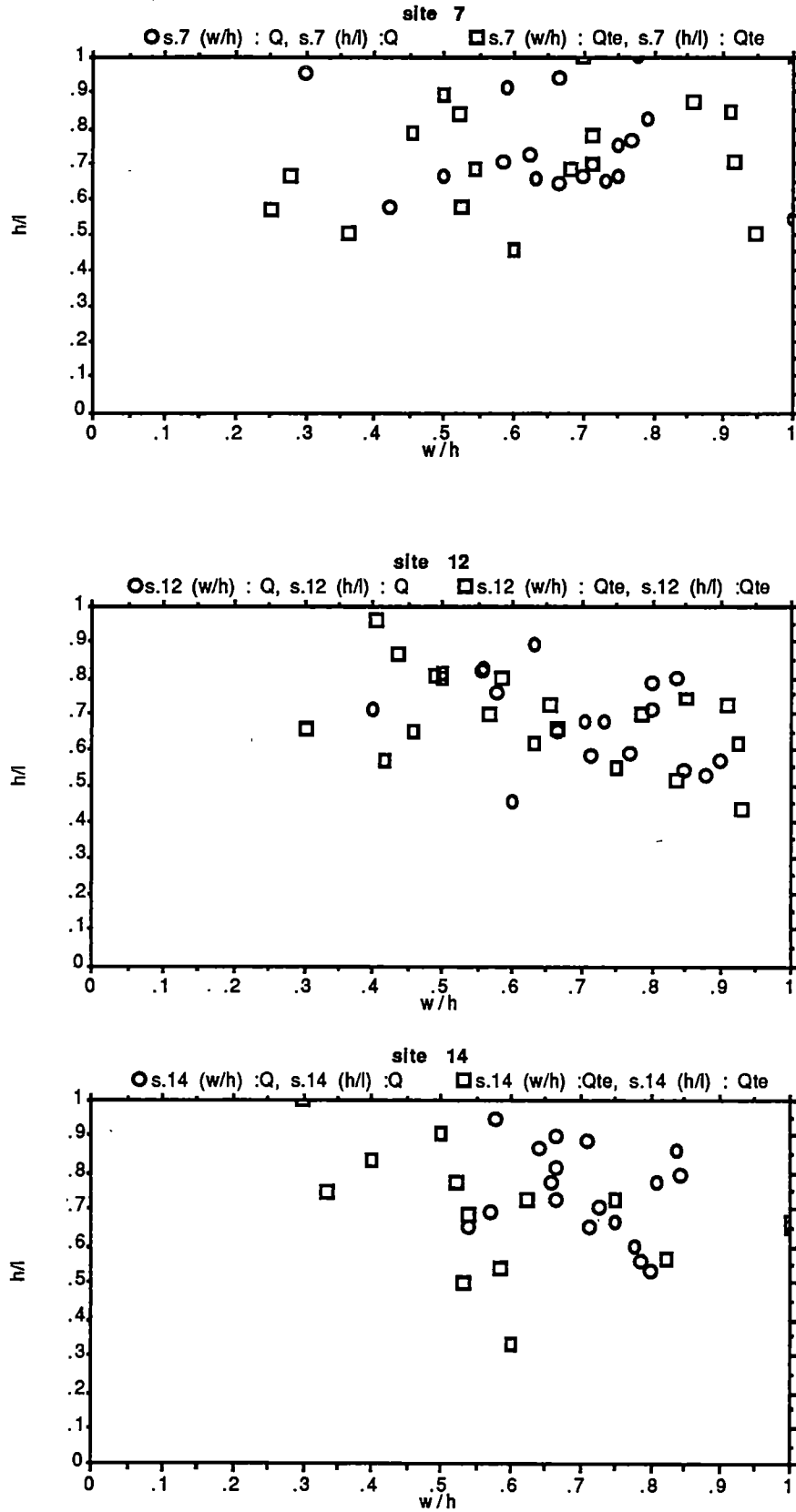
FIGURE 5.2 : Scatter plot of the pebbles of three of the stony plains sites in the two dimensional space formed according to Zingg's axes ratios. (l, h and w are the length, height and width axes respectively).
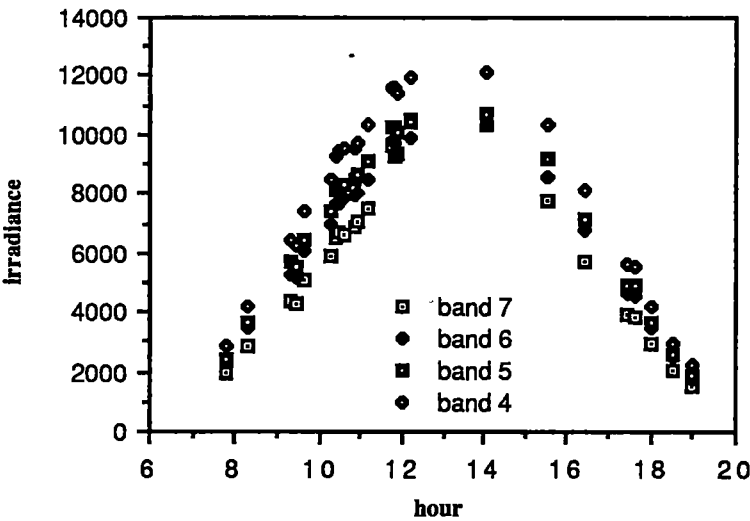
FIGURE 5.3 : Total irradiance (μW cm^{-2}) measured on flat stony plains between the 24/1/88 and 7/2/88.
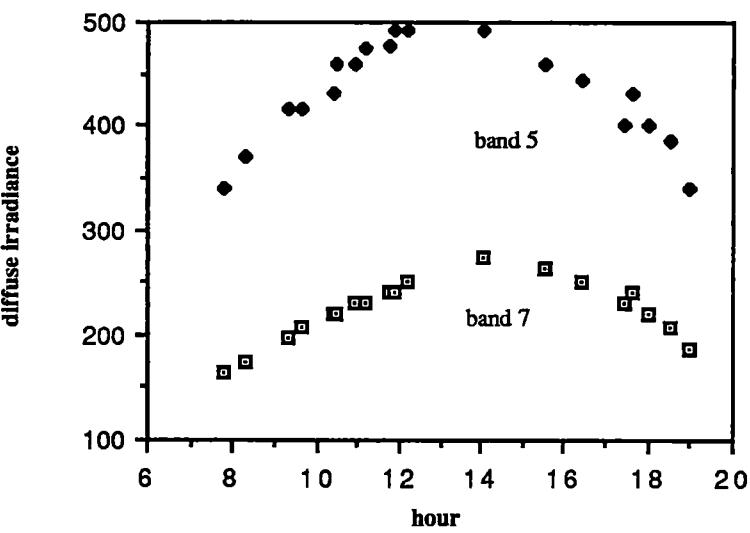
FIGURE 5.4 : Diffuse irradiance (μW cm^{-2}) measured on flat stony plains between the 24/1/88 and 7/2/88.

general daily trends (shown for example in Iqbal (1983)) as shown in Figure 5.3.

The diffuse irradiance (Figure 5.4) comprised between 2% of the total irradiance at solar noon and 12% six hours later in band 7 and between 4.5% and 17.5% in band 5.

Anisotropy level : the pattern of change of reflected radiance in the sun's azimuthal plane (Figure 5.5) serves as the basis for our discussion. The anisotropy is well expressed in these diagrams: it decreases considerably with decreasing sun zenith angle, but even at low zenith angles such as 18° there is still a pronounced level of anisotropy . The absolute difference in reflected radiance between the maximum and the minimum readings ranged between 300 $\mu W/$ cm^2/sr to 70 $\mu W/$ cm^2/sr. The reflected radiance changed from a low average of 300 μW / cm^2/sr at high zenith angles (55°) to high average of 700 $\mu W/$ cm^2/sr at low zenith angles (17°), thus providing an anisotropy factor (ratio between maximum and nadir values) of between 1.50 and 1.05. A combination of a strong backward (viewing angles lower than 90°) and weaker but very well pronounced forward (viewing angles higher than 90°) component was found to characterize most of the directional reflected radiance distributions. These trends can be clearly observed in Figure 5.5. The change in the anisotropy level for all the sites was found to correlate (with correlation coefficient of -0.673) with the change in cosine of the sun angle of incidence. In order to examine whether any of the surface properties may be partially related to the anisoptropy, we calculated the multiple correlation between the anisotropy level and the cosine of the sun angle of incidence with each of the surface properties separately. Results showed that the addition of the surface properties only marginally increased the prediction quality of the anisotropy level by the change in the cosine of the sun angle of incidence.

Hemispherical reflectance factor : the stony pavement sites show a relatively high hemispherical reflectance factor for band 7 and a moderate hemispherical reflectance factor for band 4 . It is well known that the hemispherical reflectance factor varies with the the sun zenith angle as discussed, for example, in Cerniewsky (1987). Figure 5.6 present the hemispherical reflectance factor values found for the stony pavements sites at various sun zenith angles. The trend of an increasing hemispherical reflectance factor with decreasing cosine of the sun zenith angle is well pronounced in
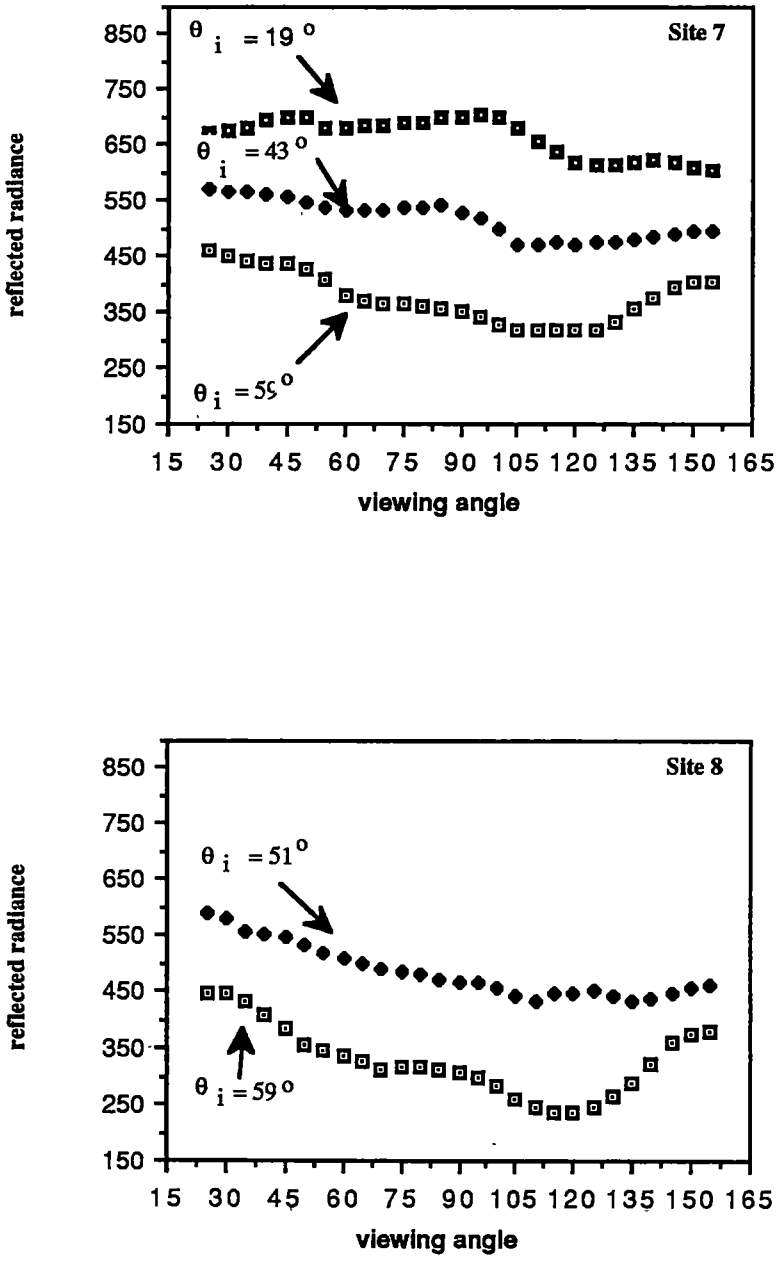
FIGURE 5.5 : Directional distribution of reflected radiance (μW cm^{-2} sr^{-1}) of stony desert plain sites measured along the sun's azimuthal plane at various sun zenith angle (the viewing angle is 0° on the horizon into the sun direction and 180° with the sun direction).
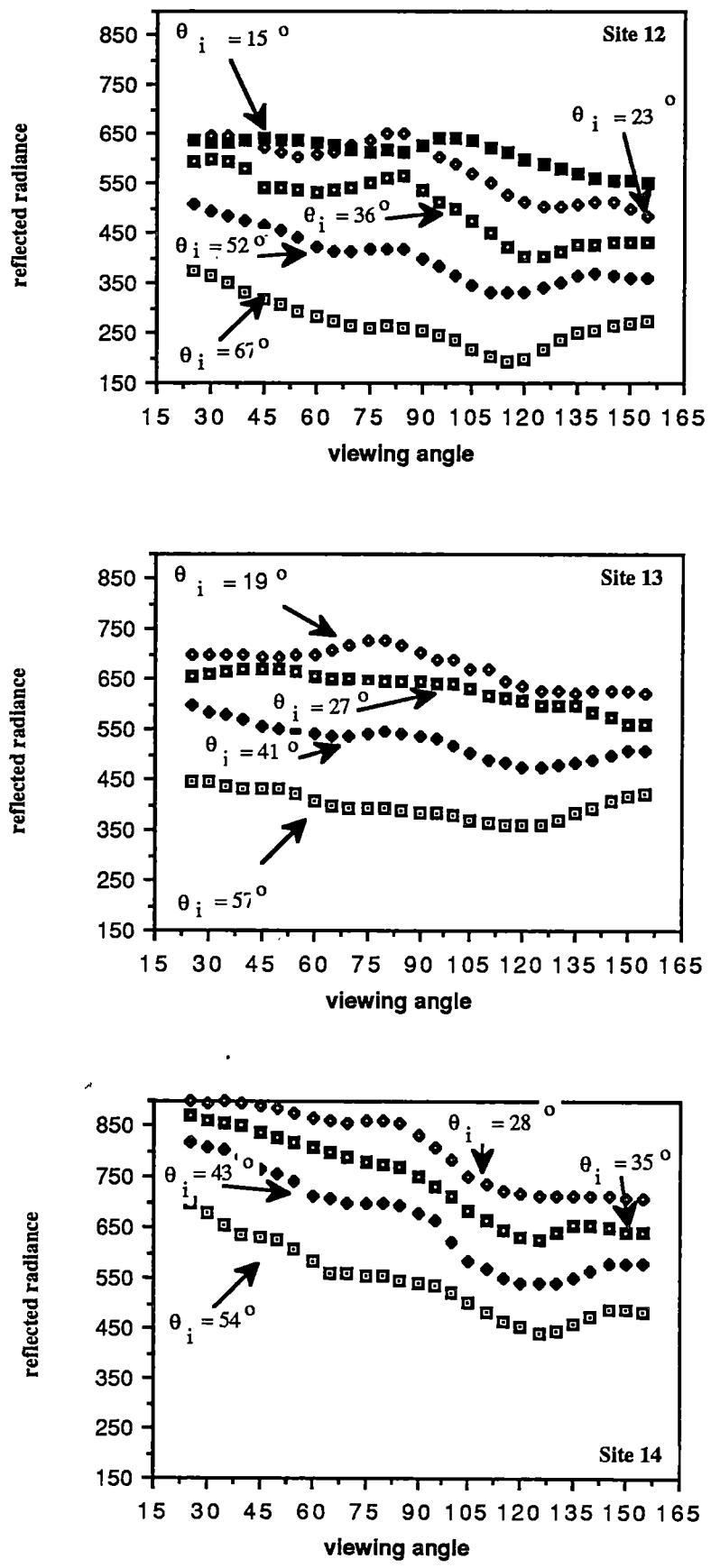
FIGURE 5.5 (continued): Directional distribution of reflected radiance (μW cm^{-2} sr^{-1}) of stony desert plain sites .

band 7 but also expressed in band 4.

Table 5.3 presents the correlations found between the change of the hemispherical reflectance factor values between measurements for all the sites and the change of surface properties between the sites. From the structure of the correlation matrix, it is clear that the hemispherical reflectance factor in band 4 (and also in band 7 at a lower level) has a relatively high correlation mainly with the percentage of area covered by quartz. The two other surface properties with relatively high correlation (positive or negative) with the change in the hemispherical reflectance factor are the quartzite percentage cover and percentage stony cover. However, both properties are highly related to percentage quartz cover.

Band ratios: At each site a series of band ratios (7/4, 7/5, 7/6, 6/4, 6/5 5/4) was calculated for each of the 235 bins of hemispherical directions of reflected radiance. This exercise was repeated for three to five different sun zenith angles. Three of these band ratios (7/5, 6/5, 7/6) had an overall mean value of 0.9, a standard deviation of 0.03 and a very low variation of 0.07. By contrast, a high variation was encountered with band ratios containing band 4 (7/4, 6/4, 5/4). These three band ratios showed an average value of 1.2 and a relatively high variation of 0.3 . As discussed above in relation to the hemispherical reflectance factor of band 4, the band ratios with band 4 are highly correlated with stony quartz cover (Table 5.3).

The significance of these results (within the limitations set by the number of sites) is firstly that it suggests that the percentage quartz cover can be detected from the band ratios including band 4. Secondly, it is possible to claim that the measured surface roughness properties are not a key factor in determining the anisotropy level. Thirdly, as band ratio variation was found mainly between sites rather than between hemispherical sets (of the same site) acquired at different sun zenith angles or between different viewing angles of the same hemispherical sets, then mineral composition is unlikely to be a major determinant of anisotropy.
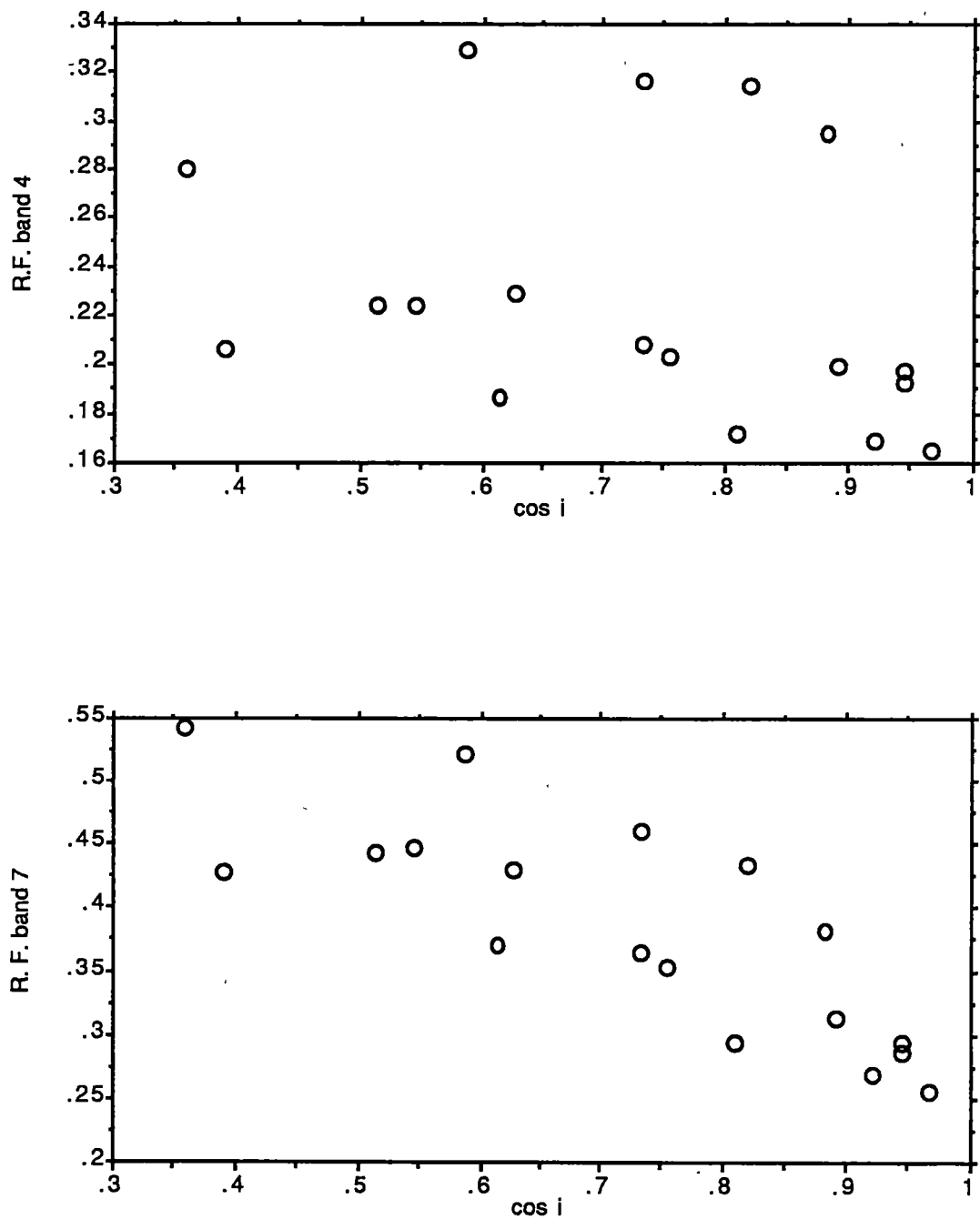
FIGURE 5.6 : The change in hemispherical reflectance factors for all the stony plain

sites with the change in the cosine of the sun's zenith angle in band 4 and band 7.

TABLE 5.3 : the correlation matrix between parameters expressing variation in surface propertries and parameters describing variation in the radiometric characteristics of the different stony plain sites.

Correlation Matrix for Variables: X_1 ... X_9

	cos i	ani. factor	7 / 4 R...	Q cover...	Qte cov...	Q size	Qte size	R.F. ban...
cos i	1							
ani. factor	-.673	1						
7 / 4 Ra...	.069	-.205	1					
Q cover ...	.075	.094	-.967	1				
Qte cove...	-.042	-.305	.892	-.888	1			
Q size	-.373	.111	.341	-.316	.435	1		
Qte size	-.274	.035	.193	-.085	.276	.905	1	
R.F. band 4	-.297	.415	-.95	.892	-.875	-.147	-.045	1
R.F. band 7	-.814	.745	-.592	.458	-.509	.151	.123	.782

Variables:

cos i : cosine of the sun zenith

ani. factor : anisotropy factor

7/4 Ratio : bands ratio 7/4

Q cover : percentage quartz cover

Qte cover : percentage quartzite cover

Q size : quartz pebbles mean size

Qte size : quartzite pebbles mean size

R.F. band 4 : hemispherical reflectance band 4

R.F. band 7 : hemispherical reflectance band 7

5.3 Stony desert slopes

Four sites of stony desert slopes (Map 1) were selected on the broad hills built of Devonian quartzose sandstone rocks unit called Nundooka sandstone in the geological map (Map 2).The area is part of the Barrier Range physiographic region characterized by gently undulating topography with a low vegetation cover of scattered mulga and saltbush. A major reason for selecting this area was the sparseness of its vegetation , as the steeper terrain of the Barrier Range region was densely covered with shrubs at the time of the field work. The area is characterized by low to moderate slopes (up to 12°) with red loamy sandy soil and rock fragments spread with densities decreasing with decreasing altitude. The spatial arrangement of the pebbles suggests that they were moved downhill by surface wash.

The four sites (Figure 5.7) which were sampled in three close locations each were selected along a 150 m profile representing the steepest slope descent from an arbitrary location at the top of the hill. Measurements of the pebbles and the distance between them using the roughness digitizer indicate that the four sites vary considerably:

Site 3 : slope 8°, aspect 345° , 53% stony cover, with 5.4 cm mean pebble size and 0.36 mean sphericity .

Site 4: slope 9°, aspect 350°, 72% stony cover, with 5.7 cm mean pebble size and 0.312 mean sphericity.

Site 5: slope 10°, aspect 0°, 57% stony cover with 5.6 cm mean pebble size and 0.27 mean sphericity.

Site 6: slope 9°, aspect 355°, 44% stony cover with 4.4 cm mean pebble size and 0.228 mean sphericity.

Similar roundness values in the range of 0.4 to 0.45 as defined using Wadell's formula (in Lewis, 1984) were found for pebbles of all sites. Most of the pebbles in the area were classified to be of tabular or disk shape (following Zingg's classification scheme) as indicated in Figure 5.8. This indicates that the pebbles preserve the some of the bedding and faulting planes in the parent rock.

Site 3

Site 4

Site 5

Site 6

FIGURE 5.7 : Photographs of five sites of stony desert slopes in the Fowlers Gap region (the ruler in the photographs is of 2 cm. intervals).
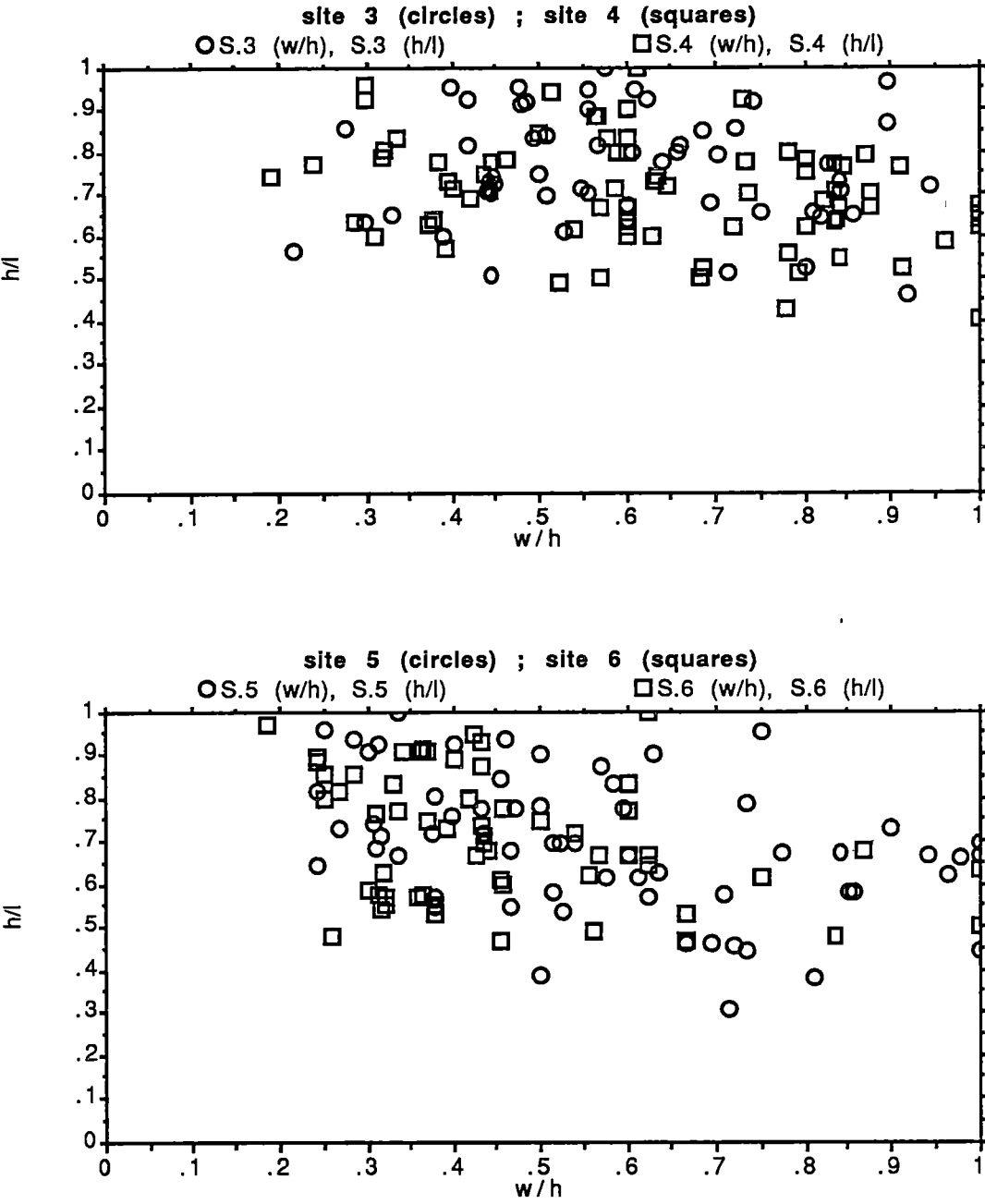
FIGURE 5.8 : Scatter plot of the pebbles of each of the stony slopes sites in the two dimensional space formed according to Zingg's axes ratios. (l, h and w are the length, height and width axes respectively).

The data describing surface properties reveals that there is a marked difference in roughness between sites in terms of percentage stony cover and sphericity of the pebbles with sites 4 and 6 exhibiting the two extreme conditions.

The radiometric properties of the site will be discussed following the same procedure described in the last section :

Irradiance : as all the sites are having similar slope and aspect, a similar level of irradiance was found. Figure 5.9 represents the recorded irradiance for site 4 as a function of the local time. As expected, the irradiance correlates highly with the change in cosine for θ_i indicating that there is no major component of secondary reflection from neighbouring slopes (as can be expected in such hilly topography).

Hemispherical reflectance factors : similar to the findings in the last section the hemispherical reflectance factors increased with decreasing cosine θ_i (Figure 5.10) with band 7 having a much higher correlation coefficient than band 4. This was expected due to the larger contribution of sky irradiance in band 4 than in band 7.

Anisotropy level : the pattern of change of the reflected radiance in the sun's azimuthal plane (Figure 5.11) serves as the basis for our discussion. The anisotropy is well expressed in these diagrams, indicating strong backscattering with very low forward scattering appearing mainly in large sun zenith angles. Anisotropy factors (ratio between maximum and nadir value) calculated for each of the averaged hemispherical data sets provided values between 1.69 and 0.98, while the absolute differences in reflected radiances (in band 7) between maximum and minimum readings ranged between 300 μW/ cm^2/sr and 90 μW/ cm^2/sr. At the same time the reflected radiances changed from an average low of 250 μW/ cm^2/sr to an average high of 650 μW/ cm^2/sr at sun zenith angles close to 55° and from an average low of 600 μW/ cm^2/sr to an average high of 800 μW/ cm^2/sr at sun zenith angles close to 20°.

The anisotropy factor was found to be correlated only with the cosine of the sun zenith angle and there was no indication of any correlation with properties expressing the surface properties (Table 5.4) .
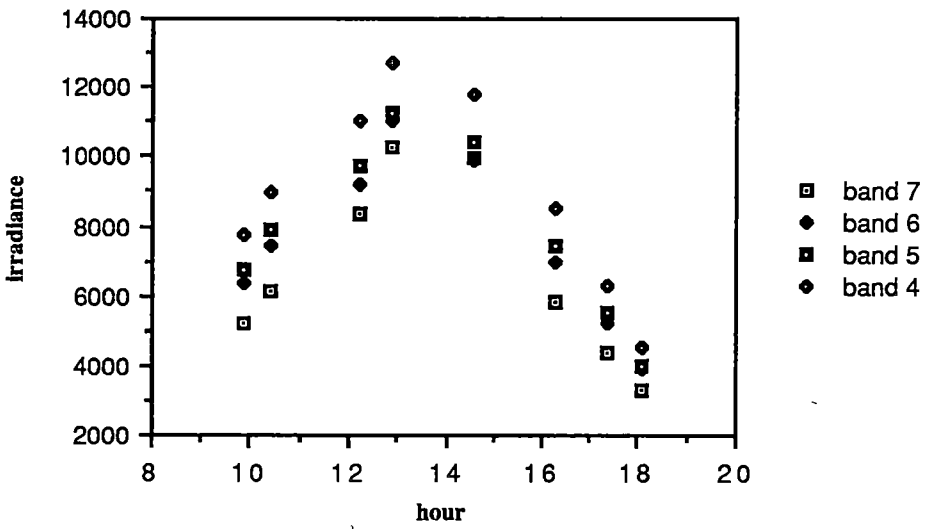
FIGURE 5.9 : Total spectral irradiance (μW cm^{-2}) measured on stony slopes between the 24/1/88 and 7/2/88.
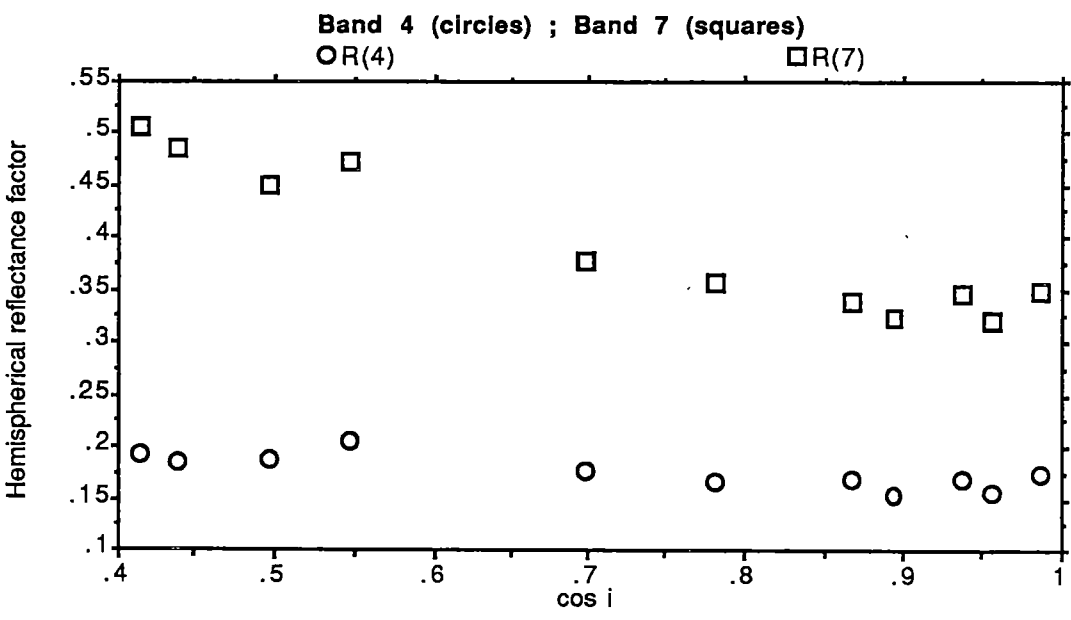
FIGURE 5.10 : Hemispherical reflectance factors for bands 4 and 7 as a function of the cosine of the sun angle of incidence.
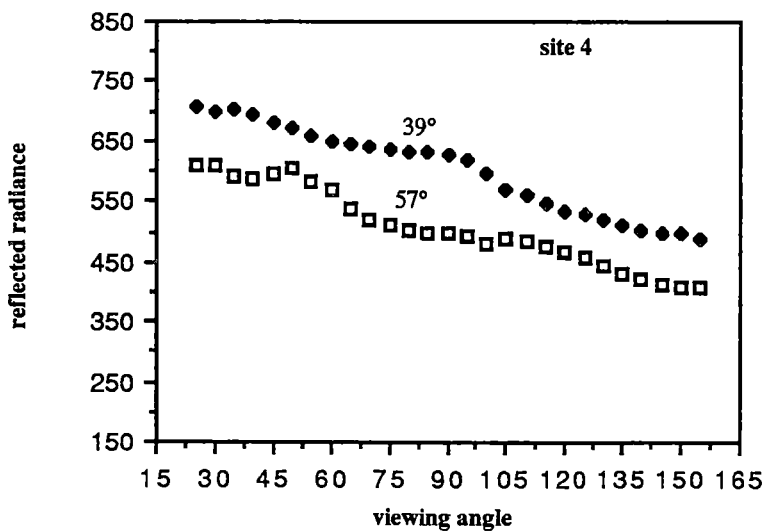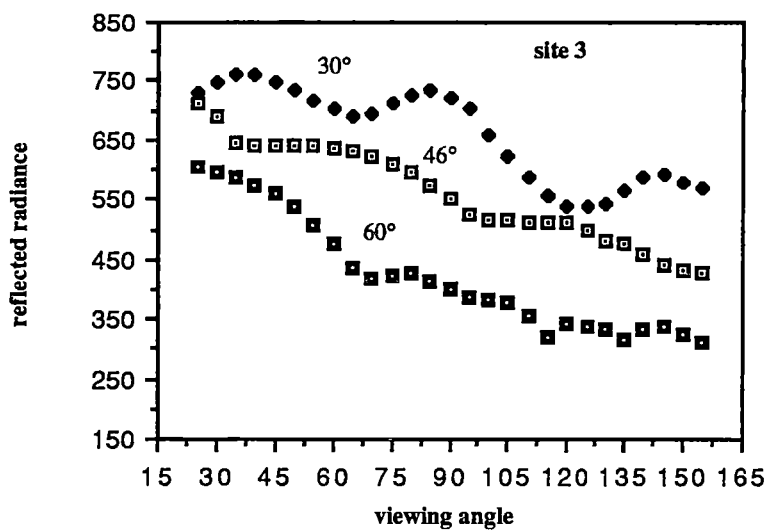
FIGURE 5.11 : Directional distribution of reflected radiance (μW cm^{-2} sr^{-1}) of stony slopes sites measured along the sun's azimuthal plane at various sun zenith angle (the viewing angle is 0° on the horizon into the sun direction and 180° with the sun direction).
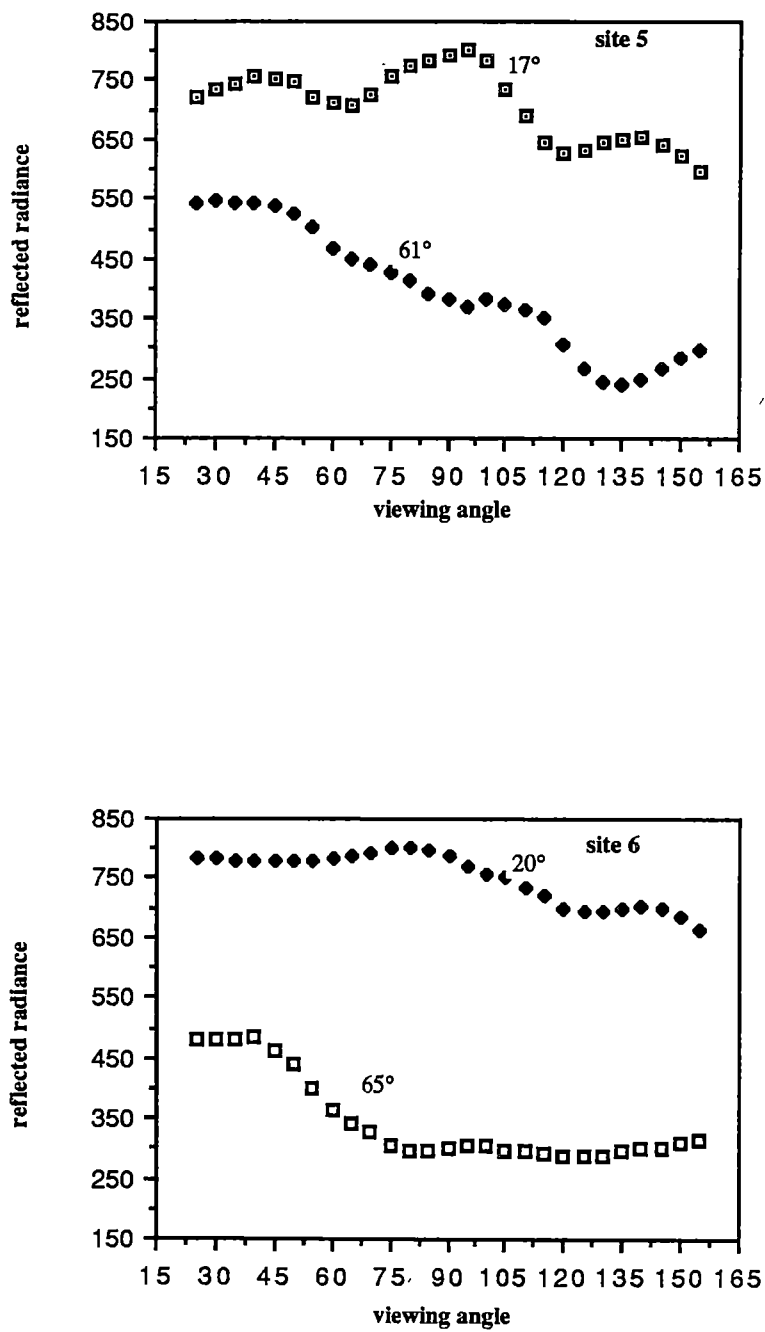
FIGURE 5.11 (continued): Directional distribution of reflected radiance (μW cm^{-2} sr^{-1}) of stony slopes sites measured along the sun's azimuthal plane at various sun zenith angle (the viewing angle is 0° on the horizon into the sun direction and 180° with the sun direction).

Band ratios : the band ratio variation within all the hemispherical data sets was found to be relatively low with average band ratio values of 1.30 and average standard deviations of 0.035 . The band ratio maximum of 1.75 was exhibited by the ratio of 6/4 while the minimum band ratio values of 0.9 were recorded for the ratio 7/6. The variation between the hemispherical data sets of different sites indicated only two possible relations between surface properties and band ratio (Table 5.4): the ratio of 7/6 had a correlation of -0.693 with percentage stony cover and band ratio 6/4 had a correlation of 0.628 with pebble size. Much more data would be needed for establish solid evidence that these two band ratios are indicative of surface roughness properties for this terrain type. The fact that, for the stony plain sites there was no indication at all of such possible relations, limits considerably the significance of these findings.

TABLE 5.4 : The correlation matrix between parameters expressing variation in surface properties and parameters describing variation in the radiometric characteristics of the different sites.

Correlation Matrix for Variables: X_1 ... X_8

	7/4	6/4	R(4)	R(7)	A.F(7)	% S.C	cos i	size
7/4	1							
6/4	-.127	1						
R(4)	.184	-.217	1					
R(7)	.535	-.351	.892	1				
A.F(7)	.56	-.267	.664	.852	1			
% S.C	.2	.556	.12	.06	.041	1		
cos i	-.606	.286	-.8	-.958	-.933	-.158	1	
size	.158	.628	-.093	-.047	.086	.835	-.14	1

variables:

7/4 : bands ratio 7/4

6/4 : bands ratio 6/4

R(4) : hemispherical reflectance factor for band 4

R(7) : hemispherical reflectance factor for band 7

A.F(7) : anisotropy factor for band 4

% S.C : percentage stony cover

cos i : cosine the sun angle of incidence

size : mean pebble size

5.4 Model sites

In order to establish radiometric data for surfaces of clearly different microstructure, all with dominant directionality, we constructed in the natural environment three types of sites: a site of dense rows of pebbles on bare soil, a site with sparse rows of pebbles on bare soil and two sites of artificial sand ripples (Figure 5.12). The first two sites were constructed in the Fowlers Gap area while the sand ripples sites were constructed in the South Arm area near Hobart , Tasmania.

It was felt necessary to collect radiometric data for the model sites in order to allow a comparison between simulated and real BRDFs of simple microstructures. The model sites represented the variability in microstructure which characterizes natural conditions due, for example, to the shape and spatial arrangement of the surface particles in addition to their microstructure as constructed artificially. Such a comparison between BRDFs of semi-artificial microstructures and those of simulated ones will be carried out in the following two chapters.

Since the artificial sites did not represent characteristic surface roughness conditions of specific natural terrain, their radiometric properties are not presented in this chapter. Those properties will be discussed in Chapters 8 and 9 through the comparison with the BRDFs of the simulated microstructures .

Site 1a (355° rows azimuth)   Site 2 (237° rows azimuth)

Sites 17 (340° ripples azimuth) and 18 (243° ripples azimuth)
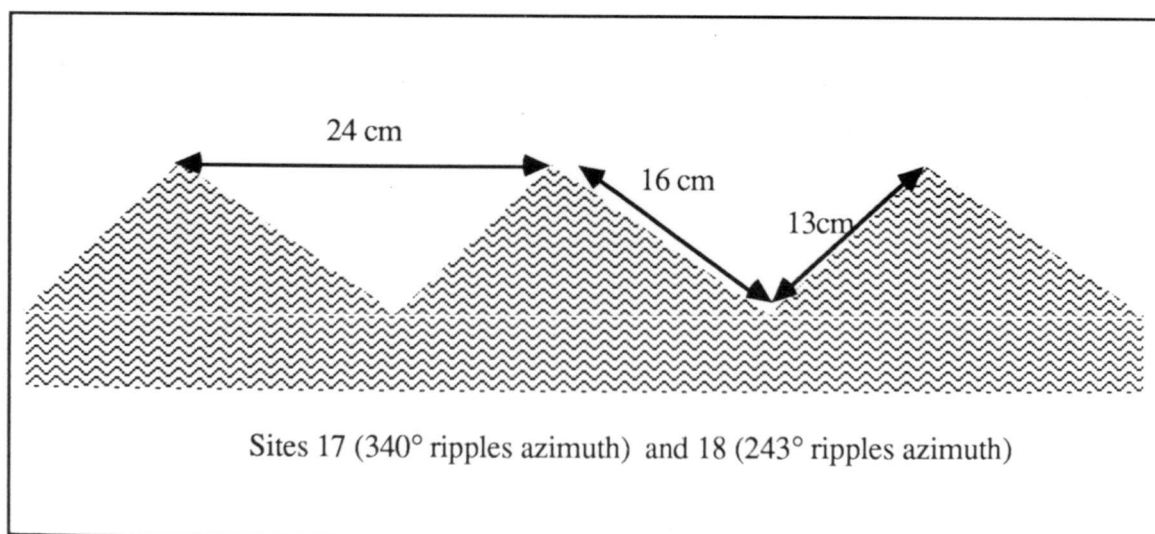
FIGURE 5.12 : Photographs of two model sites of pebbles organized in rows in the Fowlers Gap region and a cross section of the artificial sand ripples sites in the South Arm

5.5 Discussion

The field data collected and reported in this chapter is believed to be of the first of its kind to be collected for bare terrain in Australia and other desert regions of the world in terms of the level of detailed information regarding both the reflectance field and the roughness properties. The level of detail limited the number of desert surface types that could be included in this study, thus limiting its regional significance; however it gave some insights into roughness / reflectance relationships and enabled some conclusions with regard to the research questions and hypotheses.

The general radiometric characteristics of the sites correspond well with the already published data. For example our findings regarding the hemispherical reflectance factors correspond well with those of Otterman and Fraser (1976) and others for other desert environments (Sahara, Sinai). Those factors vary considerably between the wavelength bands : between 0.2 for band 4 to 0.5 for band 7. In support of Coulson and Reynolds' (1972) findings and in disagreement with predictions made by Cerniewsky (1987), we found that the hemispherical reflectance factors increased with the increasing sun angle of incidence .

Band ratios were found to vary between sites following mainly the change in the surface material type. Such variation was indicated by, for example, the ratio of bands 7/4 for changes in quartz percentage cover for the stony desert plain sites . The same band ratio also can be used to separate between the stony desert slopes of the hills built of Devonian quartzose sandstone rocks (with a band ratio values of 1.7) and the areas of stony desert pavements on Quaternary alluvial plains (with a band ratio value of 1.2). Thus, band ratios are valuable for mapping the different landforms; a further extension of band ratio measurements could be used to assist in the mapping of land systems over the entire Australian continent.

A significant level of anisotropy was found for all of the sites and thus stresses the importance of its modelling for albedo studies. Surface roughness properties as determined in the field measurements were not found to influence the level of anisotropy. Those findings are in support of the second research hypothesis that the surface BRDF does not have a one to one correspondence with the surface roughness.

However, two directions of further research appeared necessary before one could reach a more decisive conclusion. Firstly there was a need to increase the range and variety of roughness conditions assessed. It was not possible to test a wider range of roughness conditions through field measurements and, for that purpose, there was a need to assess a simulation model. Such a simulation method is described in the following chapter. Secondly, there was a need to assess which surface roughness properties (if any) which are more related to reflectance. A formalization of such properties might add a new facet to the assessment of roughness / reflectance relationships . That avenue is taken further in Chapter 7.

CHAPTER 6 :THE EQUIFINALITY OF BIDIRECTIONAL REFLECTANCE DISTRIBUTION FUNCTIONS OF VARIOUS MICROSTRUCTURES

The relationship between form and process is at the heart of scientific work. Hypotheses of cause and effect are frequently based on evidence that a new form emerges from an old one through the action of a process. Problems with scientific explanations arise when observations show that a form could evolve from more than one initial form.This situation which is called equifinality has been extensively discussed in a geomorphological context by Haines-Young and Petch (1983) and others.

BRDF equifinality refers to the case presented by the second research hypothesis (in Chapter 2) which suggests that the BRDF has not one to one correspondence with the surface microstructure. On one hand, the Bidirectional Reflectance Distribution Function (BRDF) as a detailed description of the reflectance field for any direct beam irradiance is frequently linked and modelled for specific roughness microstructure (examples of microelements which were used to form BRDF are given in Table 2.1). On the other hand, a few studies and mainly that of Norman et al. (1985) have suggested that there is some level of similarity between BRDFs of different microstructures. The implications of this situation are in two areas. The first is in the interpretation (using inversion techniques) of surface properties from data of directional distribution of reflectance (or of reflected radiance). Another way to look at the interpretation problem is the possibility that one might draw a conclusion from a successful attempt to model the BRDF using simple standard microstructure that this microstructure does represent the surface forms where it is not necessarily right (if there is equifinality). The second area of BRDF equifinality implications concerns the determination of albedo from satellite data. If there is no BRDF equifinality, albedo studies require a detailed modelling of an infinitesimal number of surface types. Alternatively, where there is equifinality, one can determine the surface albedo for

many surface types from the BRDF of a few categories. The potential importance of these two implications justifies a detailed study of BRDF equifinality.

The objective of this work is to assess the extent of equifinality of BRDFs by examining the similarity between BRDFs and a wide range of different types of microstructures. This chapter is structured in the following way: the first section describes a model for simulating wide range of microstructures; the second section describes the equations developed for determining the BRDF for each microstructure; the third section provides a definition for BRDF equifinality, the fourth section assesses the equifinality found between the BRDFs determined for the simulated microstructures; the fifth section assesses the equifinality with field measurements of BRDF; and the sixth section provides a discussion of the phenomenon and its implications.

6.1 The simulation of surface microstructures

To enable the assessment of equifinality of BRDFs, there is a need to form a large number of different microstructures. Practical reasons dictate that a variety of microstructures be developed from elementary structures, so that simple equations account for the geometry of the solar energy interaction with the surface. The simplicity of the elements ought to allow the usage of general expressions for describing the shadowing and obstruction which occur with the change of illumination and viewing angles. Existing methods based on the summation of the interaction processes at discrete point locations within the structure are given by Cooper and Smith (1985) and Ferencs et al (1987).These methods require long processing times when extended to a large number of forms. An approach similar to the one developed by Cierniewski (1987) was adopted in this study with a simpler, more flexible structure which allows asymetry and angularity. A modular unit of five facets (Figure 6.1) was found to fulfil the above requirements and offers a large number of different microstructures . The determination of any specific microstructure from the model was achieved by setting
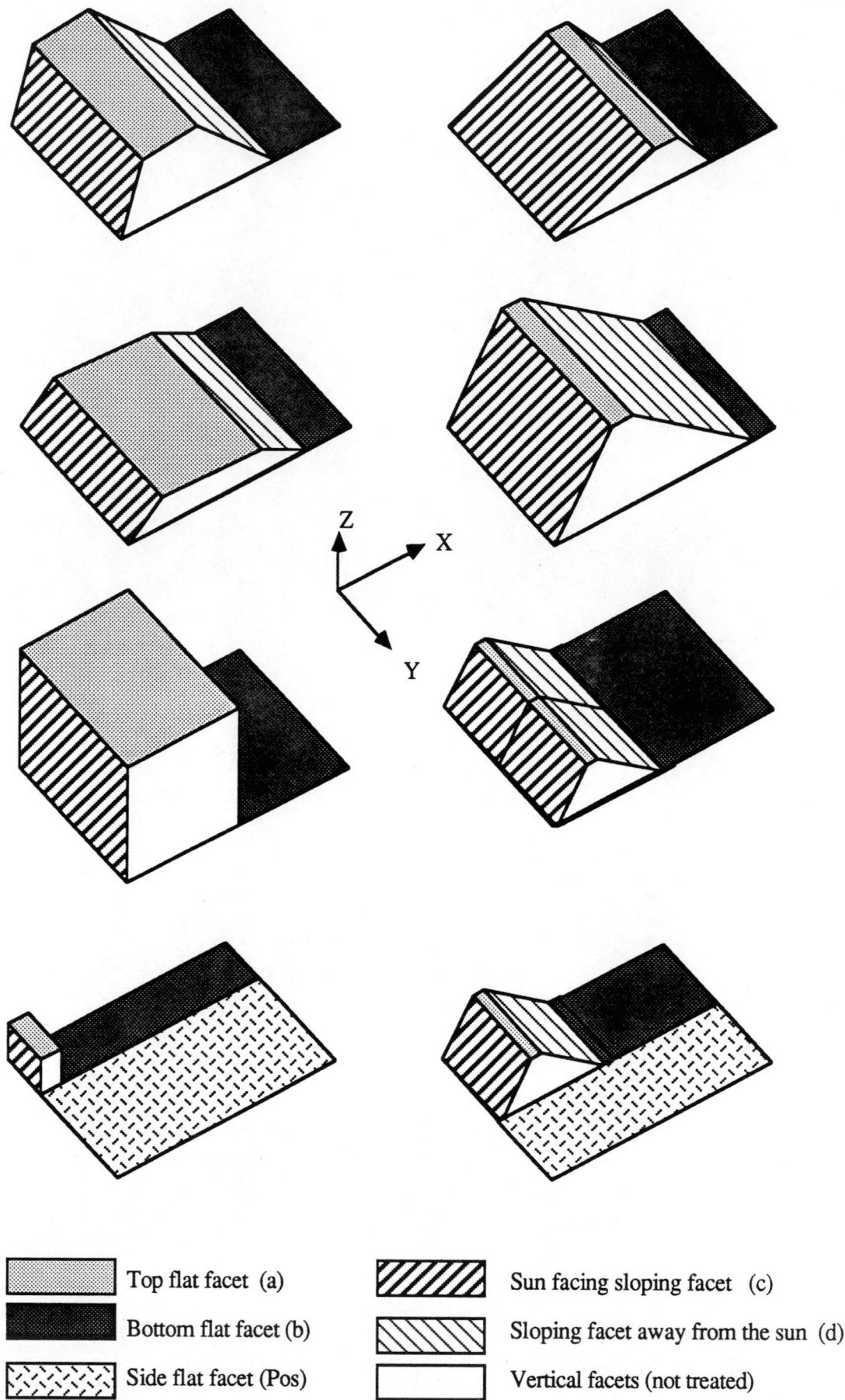
FIGURE 6.1 : Eight microstructures formed by varying the structural parameters.

six parameters (Figures 6.1 and 6.2) :

- height of the element (h).

- length (Pa: in the X dimension) of the top flat facet (a).

- projected length (Pc: in the X dimension) of the first sloping facet (c).

- projected length (Pd: in the X dimension) of the second sloping facet (d).

- length (Pb: in the X dimension) of the flat portion between the two sloping facets (b).

- width (Pos: in the Y dimension) of the flat portion adjacent to the element (side facet).

Each roughness element generated by this scheme occupies a square unit area. The projected dimensions of the facets on to the horizontal X and Y axes therefore sum to 1x1 unit. By changing the relative proportions of each component, one can form numerous elements which represent a wide range of roughness patterns (Figure 6.1). To restrict the combinations to a reasonable number (432), the structural parameters were divided into a few relatively broad categories, parameters h and Pos to four steps (h : 0.25, 0.50, 0.75 and 1.0; Pos : 0, 0.25, 0.50 and 0.80) and parameters Pa,Pb,Pc,Pd into seven steps (Table 6.1). The choice of relatively broad categories ensured that equifinality would not occur as a result of similarity in microstructure.

6.2 The calculation of the BRDF along the sun's azimuthal plane

· A complete description of the BRDF could not practically be achieved for such a large number of forms. Since the most informative part of the BRDF is along the illumination plane, the simulation will be restricted to that plane. Following Nicodemus et al.(1977) the BRDF for any reflection direction (r) and for any solar incidence angle (i) is given by:

$$f_r = dL_r \left(\theta_i, \phi_i ; \theta_r, \phi_r \right) / dE_i \left(\theta_i, \phi_i \right) \qquad \qquad sr^{-1} \qquad \qquad [6.1]$$

were θ and ϕ are the zenith and azimuth angles.

The irradiance comprised 1 unit of direct beam irradiance (on a facet perpendicular to the beams) and an average of 0.07 unit of diffused sky irradiance (E_{sky}) as a representative value which was estimated from field measurements.

TABLE 6.1 : The combinations of parameters: Pa, Pb, Pc , Pd in the microstructure model.

Pa+Pb	Pa			Pc+Pd	Pc		
0.25	0.0625	0.125	0.1875	0.75	0.1875	0.375	0.5625
0.50	0.125	0.25	0.375	0.50	0.125	0.25	0.375
0.75	0.1875	0.375	0.5625	0.25	0.0625	0.125	0.1875
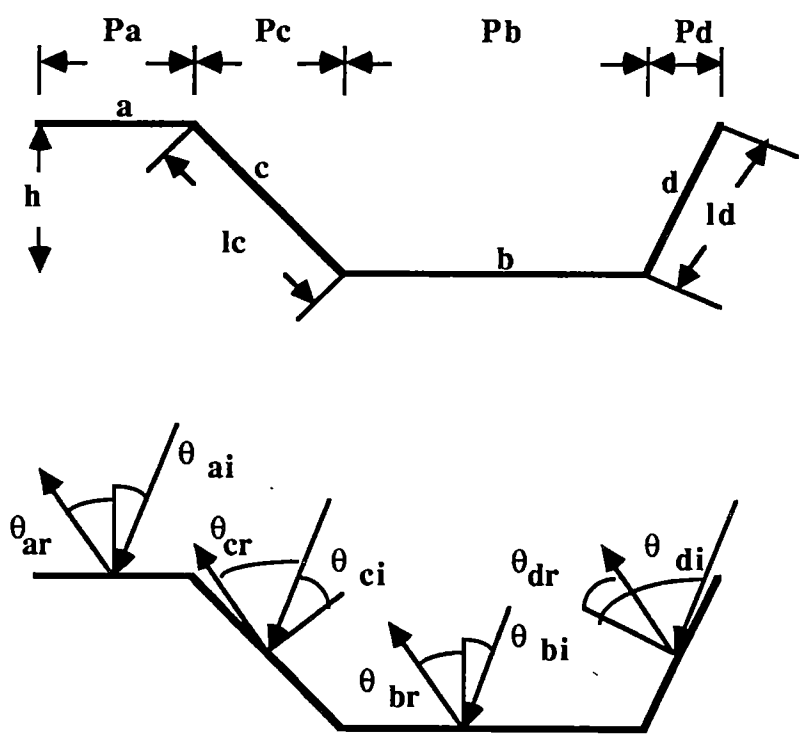
FIGURE 6.2 : The basic microstructure element : a cross-section in the XZ plane.
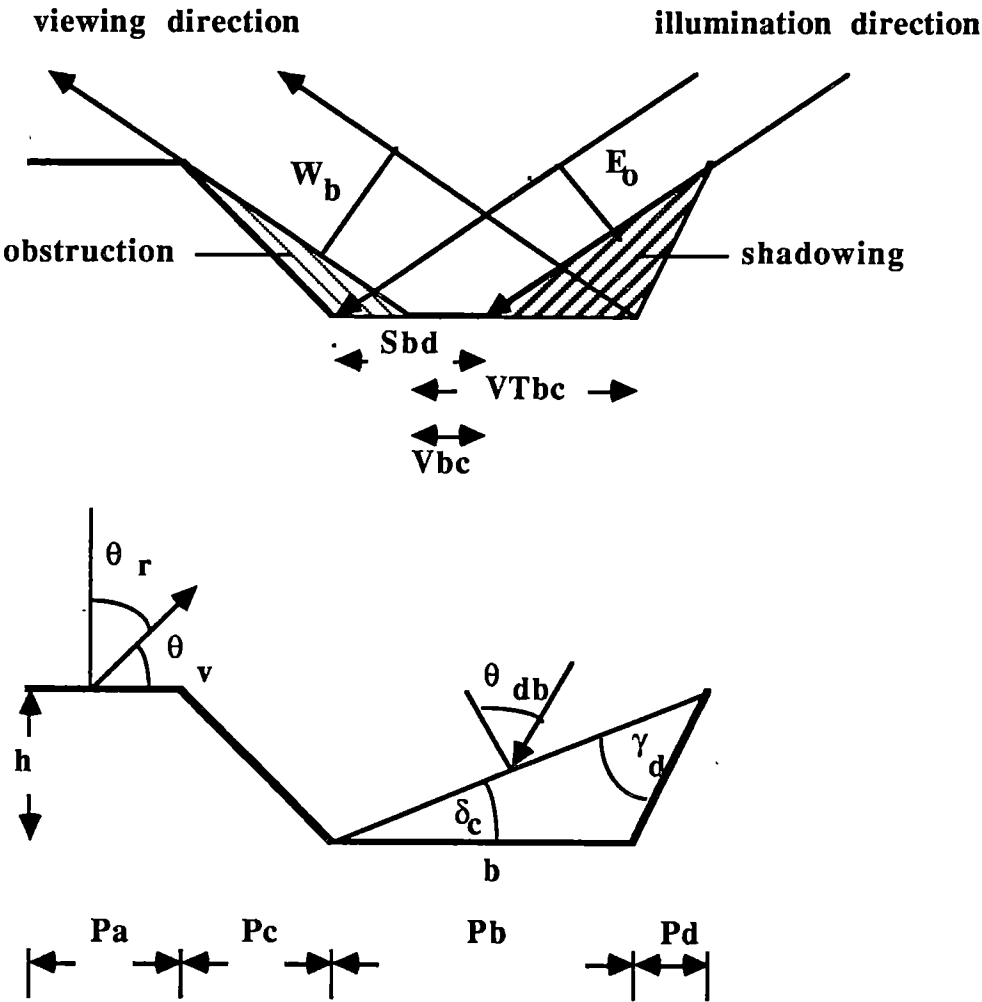
FIGURE 6.3 : The shadowing and obstruction geometries for facet b.

The sky irradiance was included since it is an additive factor (noise) in measurements of reflected radiance in real BRDF measurements which has the potential of increasing the equifinality. The amount of reflected radiance from each facet is formed by three components:

- reflection from direct beam irradiance.

- reflection from diffused sky irradiance.

- reflection from secondary reflection.

Considering the range of illumination directions and the number of microstructures, there were two options : either to allow full range of sun zenith (+/- 90°) and half of the number of the microstructures (since half of the microstructures are the mirror images of the other ones) or to allow only half of the range of sun zenith (from 0° to 90°) and the full number of microstructures. As computationally there is no difference between the two, the second option was chosen since it was found to be slightly simpler in terms of presentation .

Assuming isotropic reflection and an identical reflectance factor for all facets, the differential reflected radiance from each facet into any direction r is determined by the product of two expressions . The first expression gives the fraction of incident flux which contributes to the reflection into the viewing direction . The second weights the contribution of flux from each facet per unit projected area perpendicular to the viewing direction. A set of equations was devised to allow for the obstruction and shadowing occurring at each facet (facet Pos is not included in that stage) for various illumination and viewing angles and for the different component irradiances. Those equations determine 24 parameters which account for the shadowing and obstruction at each facet. As the geometrical / optical principles used for determining each of the parameters are similar for all the facets, we will describe here only the equations for calculating the parameters for facet Pb assuming that the side facet does not exist (Pos = 0) . When the side facet occupies a certain portion of the surface element then the irradiance and the reflected radiance from the other facets are weighted proportionally. Figures 6.2 and 6.3 provide illustration of the geometry of the situation and of the terms used in the following equation.

The flux from direct beam irradiance on the facet Pb ($E_{b(direct)}$) if there is no shadowing is given by:

$$\Phi_{b(direct)} = Pb\ E_o\ \cos\theta_{bi} \qquad [6.2]$$

A parameter Sbb is then calculated to determine whether the facet is illuminated (even partly) or not. This is done by calculating the cosine of the sun angle of incidence (θ_{db}) on the imaginary facet extending from the upper edge of facet d to the lower edge of c, then:

$$S_{bb} = \frac{\cos\theta_{db} + |\cos\theta_{db}|}{2\cos\theta_{db}} \qquad [6.3]$$

where if $\cos\theta_{db} \leq 0$ then $S_{bb} = 0$, otherwise $S_{bb} = 1$. If Sbb = 1 then we have to calculate the illuminated portion of facet b (Sbd); in other words, the portion which is not shaded by facet Pd:

$$S_{bd} = 1 - \frac{l_d \sin\left(\dfrac{\gamma_d - ((\frac{\pi}{2} - \theta_{ib}) - \delta_c) + |\gamma_d - ((\frac{\pi}{2} - \theta_{ib}) - \delta_c)|}{2}\right)}{P_b \sin(\frac{\pi}{2} - \theta_{ib})} \qquad [6.4]$$

Equations [6.2] to [6.4] together account for the flux incident on facet Pb for any direct beam illumination direction. Since the illumination direction is limited to the range of 0° to 90° facet c cannot shadow facet b and therefore there is no need to develop a parameter which will account for such shadowing. The diffuse flux received on a facet either from the sky or from neighbouring facets is derived mainly using a view factor calculated from the centre of the facet. The sky view factor for facet b is given by:

$$VF_{bs} = \frac{\pi - \left[\arctg\left[\dfrac{h}{\frac{P_b}{2} + P_d}\right] + \arctg\left[\dfrac{h}{\frac{P_b}{2} + P_c}\right]\right]}{\pi} \qquad [6.5]$$

The flux incident on the facet from diffuse sky irradiance is given then by the product of facet relative size and its sky view factor. The flux incident on a facet due to diffuse irradiance from the neighbouring facets is derived in similar way, where the flux reflected from the facets is proportional to their direct beam irradiance, the surface reflectance factor. Equations of the type of [6.2] to [6.5] enabled the calculation of the flux incident on each of the facets, the following equations were developed to account for the obstruction of the illuminated area of Pb in any viewing direction along the sun azimuthal plane. The obstruction in the viewing direction is either due to facet Pc or Pd. The proportion of the <u>illuminated</u> area of facet Pb which is <u>not</u> obstructed by facet c from viewing direction θ_v (which corresponds to reflection direction θ_v) is given by:

$$V_{bc} = \frac{S_{bd} \cdot (1 - VT_{bc}(\theta_v)) + | S_{bd} \cdot (1 - VT_{bc}(\theta_v)) |}{2 \, S_{bd}}$$

[6.6]

where $VT_{bc}(\theta_v)$ which is the proportion of facet b which is not obstructed by facet c from viewing direction v is given by:

$$VT_{bc}(\theta_v) = 1 - \left[\frac{l_c \, \sin\left[\dfrac{\gamma_c - (\pi - \theta_v - \delta_d) + | \gamma_c - (\pi - \theta_v - \delta_d) |}{2} \right]}{P_b \, \sin(\pi - \theta_v)} \right]$$

[6.7]

Using similar equations, we calculated V_{bd} and the unobstructed area of any other facet in the sensor FOV from any specific direction v. The above equations provided us with the amount of flux incident on a facet which is not obstructed from the viewing direction. As mentioned before, we assume isotropic reflection from the facets, and therefore for calculating the reflected radiance the flux which contributes into reflection direction r has firstly to be multiplied by the reflectance factor and divided by π steradians. Secondly, we calculated a parameter (Wb_r) which accounts for the fact that radiance is defined per unit area perpendicular to the viewing direction. The parameter Wb_r is a function of the cosine of the reflection angle relative to the normal to the facet and of the portion of the facet seen from that direction ($VT_{bc}(\theta_v)$). Following the

same procedures with similar types of parameters for all the other facets of the microstructure, the differential radiance components for a combination of solar and viewing zenith angles are given by:

Direct beam component

$$dL_{direct} (\theta_i, \phi_i ; \theta_r, \phi_r) = E_0 R(Pa \cos \theta a_i \; Wa_r$$
$$+ Pb \cos \theta a_i \; Sbb \; Sbd \; Vbd \; Vbc \; Wb_r + lc \cos \theta c_i \; Scd \; Vcd \; Wc_r$$
$$+ ld \cos \theta d_i \; Sdd \; VTdc \; Wd_r)/\pi \qquad (Wm^{-2}sr^{-1}) \qquad [6.8]$$

Diffuse sky component

$$dL_{sky} (\theta_r, \phi_r) = E_{sky} R (Pa \; Wa_r + Pb \; VFbs \; VTbc \; VTbd \; Wb_r$$
$$+ Pc \; VFcs \; VTcd \; Wc_r + Pd \; VFds \; VTdc \; Wd_r)/\pi \qquad (Wm^{-2}sr^{-1}) \qquad [6.9]$$

Secondary reflection component

$$dL_{secondary} (\theta_i, \phi_i ; \theta_r, \phi_r) = E_0 R^2 (((lc \cos \theta c_i \; Scd \; VFbc)$$
$$+ (ld \cos \theta d_i \; Sdd \; VFbd))Wb_r \; VTbc \; VTbd$$
$$+ ((Pb \cos \theta b_i \; Sbb \; Sbd \; VFcb) + (ld \cos \theta d_i \; Sdd \; VFcd)) \; Wc_r \; VTcd$$
$$+ ((Pb \cos \theta a_i \; Sbb \; Sbd \; VFdb) + (lc \cos \theta c_i \; Scd \; VFdc)) \; Wd_r \; VTdc)/\pi$$
$$(Wm^{-2}sr^{-1})$$

[6.10]

The differential radiance from that facet is given by:

$$dL_{side} (\theta_i, \phi_i ; \theta_r, \phi_r) = (E_0 \cos \theta a_i + E_{sky}) Pos / \pi \qquad (Wm^{-2}sr^{-1}) \qquad [6.11]$$

and the BRDF (assuming that the sky irradiance adds only noise) for a combination of direct beam irradiance from (θ_i, ϕ_i) and reflection direction (θ_r, ϕ_r) is given by:

$$f_r = (dL_{side} (\theta_i, \phi_i ; \theta_r, \phi_r) + (1-Pos) (dL_{direct} (\theta_i, \phi_i ; \theta_r, \phi_r) + dL_{sky} (\theta_r, \phi_r)$$
$$+ dL_{secondary} (\theta_i, \phi_i ; \theta_r, \phi_r) (1-Pos))) / (E_0 \cos \theta_i) \qquad [6.12]$$

where:

E_0 - the direct beam irradiance on a unit area perpendicular to the beam.

R - the reflectance factor of the surface.

θa_i, θb_i, θc_i, θd_i - the sun angle of incidence on facets a,b,c,d.

Wa_r, Wb_r, Wc_r, Wd_r - the projection of each facet in the field of view of direction r.

Sbb , Sdd - determines if the facet (b or d) is illuminated or not (=1 or 0).

Scd , Sbd - the proportion of facets c and b which is not shadowed by the neighbouring facet d.

VTbd , VTbc , VTcd , VTdc - the proportion of a facet (first subscript) which is not obstructed by a neighbouring facet (second subscript) when viewed from direction e.

Vbd , Vbc , Vcd - the proportion of the illuminated area of a facet (first subscript) which is not obstructed by a neighbouring facet (second subscript) when viewed from direction v.

VFbs , VFcs , VFds - the sky view factors for each facet.

VFbc , VFbd , VFcb , VFcd , VFdb , VFdc - the view factor that a facet (first subscript) occupies from the middle of a neighbouring facet (second subscript).

Equation [6.12] was evaluated for 27 bins (5° each) of viewing angle (from 25° to 155°) , for 9 bins (10° each) of sun elevation angle (from 10° to 90°) and for each of the 432 microelement configurations. A sequence of 27 reflected radiance predictions will be referred to as an 'azimuthal string'. A standardization procedure was applied to the azimuthal strings since, in real remote sensing applications, we do not usually know the reflectance factor of the surface material and the exact irradiance. When the sky irradiance is low (as it is in band 7 for example), the denominator of [6.12] may be assumed to be constant , the differential reflected radiance into direction (θ_r, ϕ_r) may be assumed to be the total reflected radiance into that direction (since there is then only one source) and therefore the normalization of the reflected radiance by the reflected radiance into the normal direction may be expected to be identical to those of equation [6.12] normalised by the reflectance value into the nadir direction. This

normalization procedure makes possible comparison between simulated and real azimuthal strings in real remote sensing applications. Those standardized azimuthal strings may serve therefore as the main tool for assessing the equifinality of BRDF and for deriving structural information from reflected radiance data. The symbol f_r will denote in the text the distribution of normalized BRDF (or reflected radiance) along an azimuthal string. Examples of azimuthal strings for five different microstructures are presented in Figure 6.4. The wide range of anisotropy exhibited by those azimuthal strings exemplifies the important role of the microstructure in determining the reflected radiance field and its relevance to albedo studies.

6.3 BRDF equifinality : definition

Three components of the system of form and process must be considered in assessing equifinality: initial conditions, physical processes and final form. In geomorphology the initial conditions and the final forms relate to the state of the same physical system which changes according to the processes. The case considered here is different: the initial conditions relate to the microstructures which are subject to the interaction of light (process) and the final forms relate to the form of the reflected radiance field (BRDF). That process involves the reflection, shadowing, obstruction and radiative transfer of the incident radiance within the microstructure . The shape of the standardised curve of reflected radiance (azimuthal string) is the manifestation of this instantaneous process. Following Haines-Young and Petch (1983) the BRDF equifinality is defined as follows:

A single azimuthal string is said to exhibit BRDF equifinality when it can be shown to arise from a range of microstructures through the operation of the same causal processes.

The interaction processes may be assumed to be the same when for example the facets reflect isotropically. From a wider point of view, it may be suggested that as
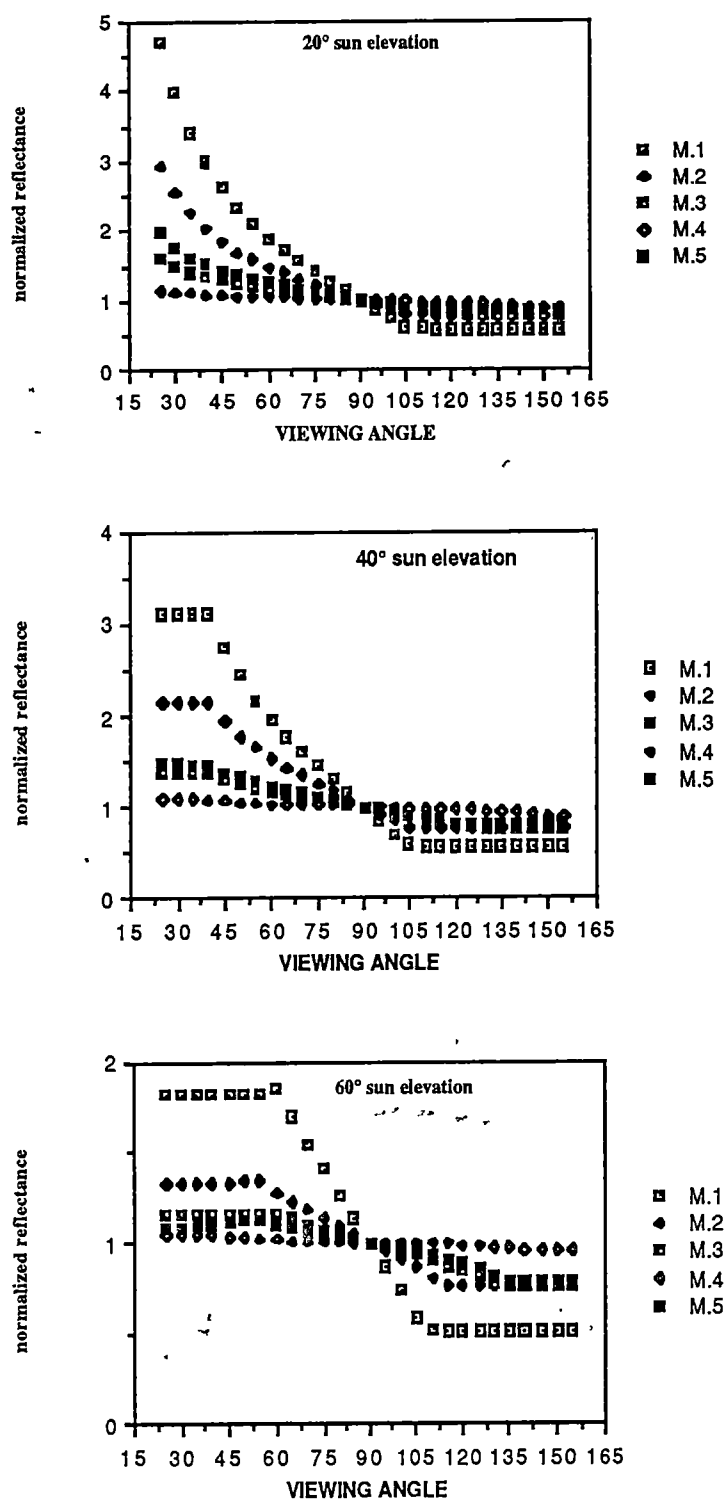
FIGURE 6.4 : Azimuthal strings from simulated radiance for 5 microstructures.

M1 : Pa=0.125 ; Pb= 0.375 ; Pc =0.25 ; Pd= 0.25 ; Pos= 0.0 ; h= 1.0

M2 : Pa=0.125 ; Pb= 0.125 ; Pc =0.188 ; Pd= 0.563 ; Pos= 0.25 ; h= 0.75

M3 : Pa=0.250 ; Pb= 0.250 ; Pc =0.375 ; Pd= 0.125 ; Pos= 0.50 ; h= 0.5

M4 : Pa=0.188 ; Pb= 0.063 ; Pc =0.375 ; Pd= 0.375 ; Pos= 0.80 ; h= 0.25

M5 : Pa=0.563 ; Pb= 0.188 ; Pc =0.063 ; Pd= 0.188 ; Pos= 0.0 ; h= 0.25

long as the ratio between the wavelength of the incident electromagnetic radiation and the size of the roughness elements in the microscopic scale is kept identical, one may assume that the same causal processes determine the surface BRDF.

A major criticism of the equifinality concept in geomorphology is that a lack of precise definitions both for the processes and for the forms could lead to the determination of equifinality where it does not really exist. The same argument can be applied to remote sensing, where it is difficult to determine both the microstructures on the Earth's surface and the exact nature of radiation interaction at the surface. Since we can simulate both the microforms and the process of radiation interaction, this study can provide an objective assessment of the equifinality phenomenon.

6.4 Testing for equifinality with simulated BRDF

The presence of equifinality is tested by comparing all pairs of azimuthal strings .The similarity is measured by the correlation between each pair of azimuthal strings. Such correlation can be described by the following equation:

$$f_{r1} = a_0 + c\, f_{r2} \qquad\qquad [6.13]$$

where f_{r1} and f_{r2} are the two azimuthal strings , c is the slope and a_0 is the intercept of the correlation equation. The quality of the correlation is given by the correlation coefficient r. Perfect equifinality corresponds to unity in both c and r . It is convenient to define a single equifinality measure (EF) which takes into account both c and r :

$$EF = (1 - |1-c|)*r' \qquad\qquad [6.14]$$

where
$$r' = 1 \quad \text{when } r >= 0.85$$
$$r' = r/0.8 \quad \text{when } r < 0.85$$

The equation makes no distinction between positive and negative deviations of c from 1 . For assessing the potential occurrence of equifinality, EF was divided into two categories: high (EF>0.90) and moderate (0.90>EF>0.80) . A category of moderate equifinality was defined since it describes a significant similarity between two azimuthal strings which could be the best achieved in some real situations where the

effects due to inaccuracies in the radiometric measurements and added noise (from the atmospheric path radiance for example) are not negligible . Equation [6.14] gives extra weight to the slope of the equation relative to the correlation coefficient in determining the quality of equifinality. The rationale behind this is that two azimuthal strings may have a very good correlation between them even if the rate of change of their normalized reflectance is quite different. Since the rate of change of the normalized reflectance is an expression of the anisotropy level, two such strings cannot be regarded as equifinal.

An iterative process calculates the EF between every pair of azimuthal strings from the 432 simulated azimuthal strings for each sun zenith angle.The results form a diagonal matrix of order 432 (partly presented in Figure 6.5). Inspection of the matrix suggests that there is a substantial amount of equifinality present in the data. From 93096 tested pairs, between 6429 and 8171 (7% - 8.7%) exhibited high equifinality, and between 4105 and 6791 (4.4% - 7.3%) exhibited moderate equifinality. In other words, for each azimuthal string in our simulation we can expect to find between 48 to 64 equifinal strings.

On the basis of these findings there was a need to consider three types of possible explanations for the equifinality :

1) Existence of dominant structural parameter values: thus, microstructures which were determined with one or two identical dominant parameter values are expected to exhibit equifinality .

2) Similarity in the overall roughness formed by the microstructures. Thus, microstructures which exhibit the same roughness will be radiometrically equifinal. Two roughness measures were used. The first measure relates to the shape of the cavity along the illumination direction:

$$\rho_1 = 0.5 \, h \, / \, (Pb + (Pc + Pd)/2)$$

The second is a planar measure (Hobson, 1972):

$$\rho_2 = A' / \, A$$

where A' is the sum of the areas of the microfacets and A is the area of the generalized plane (1^2 unit).
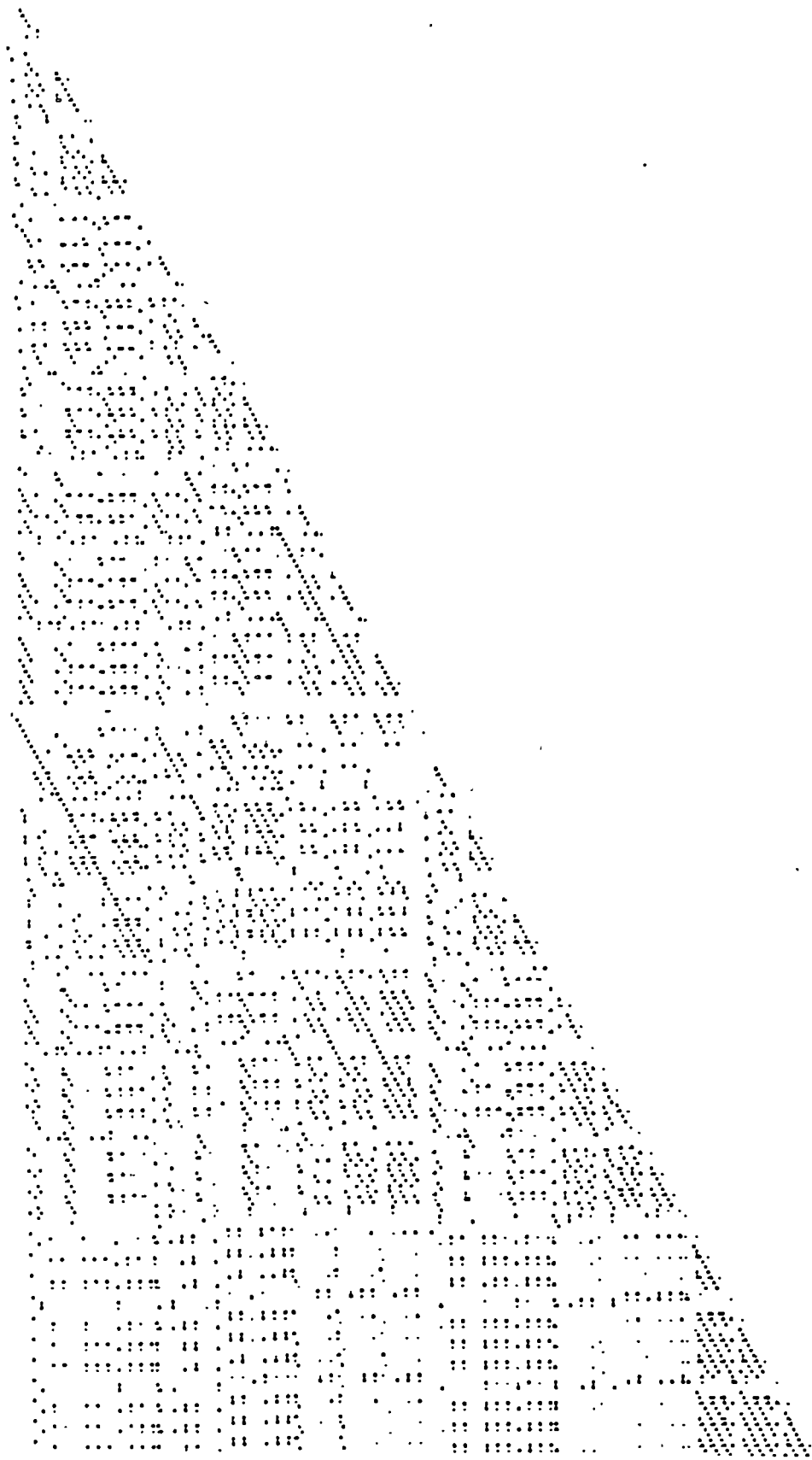
FIGURE 6.5 : A portion of equifinality matrix for all possible combinations of 432 simulated azimuthal strings (black squares denote high equifinality, dots denote moderate equifinality and blank areas denote low (no) equifinality).

3) Existence of different combinations of structural parameters which are not equal in equifinal pairs but balance each other in determining the reflectance field. For example, an azimuthal string of a microstructure with a large Pa and small Pos might be found equifinal to an azimuthal string of a microstructure with large Pos and small Pa since in both cases the total flat area which is not shadowed and/or obstructed is the same.

A technique was developed for assessing the relative weight of each of the first two possible explanations. An array of six binary indices was formed, each binary index denotes by 1 the situation where the two microstructures were simulated using the same parameter value. An example would occur when two microstructures are equal in height or when they have the same roughness value (+/- 10%).The number of occurrences for any combination of the six parameters is then recorded in the array. For example, the binary indices 0 0 1 0 0 0 denote parameter three as identical for both microstructures, while 0 1 1 0 0 1 denote parameters two, three and six as identical . Thus, a sum of 64 different combinations of parameters is tested by identifying the binary combination of structural parameters formed by each pair of microstructures with high or moderate equifinality. The percentage of occurrences for each combination from the high and moderate equifinality cases in four correlation matrices (for sun elevation angles of 30°, 50°, 70° and 90°) is presented in Table 6.2 . The matrix presentation is formed by splitting the microstructure parameters into two groups of three .

The following analysis of the frequencies of combinations of parameters associated with the equifinality cases can provide some possible explanations for that phenomenon:

-There is a relatively large proportion of cases (14% to 25%) where various unknown combinations of non identical parameter values are responsible for the equifinality (0 0 0 0 0 0 combination).

-The proportional width of flat area parallel to the microelement (Pos) is the single parameter (0 0 0 1 0 0 combination)with the highest frequency (average of 19%). That finding was expected as large values of Pos will produce only minor effects from the microelement on the reflected radiance field (which becomes mainly isotropic).

159

TABLE 6.2 : Analysis of equifinality : percentage cases for combinations of structural parameters which were found identical in equifinal pairs of azimuthal strings. Since combinations with less than 1% were given 0% in the table, the matrices do not sum to 100%.

	High equifinality										Moderate equifinality					
Pos	0	0	0	0	1	1	1	1	0	0	0	0	1	1	1	1
R1	0	0	1	1	0	0	1	1	0	0	1	1	0	0	1	1
R2	0	1	0	1	0	1	0	1	0	1	0	1	0	1	0	1
Pa Pc h							30° elevation									
0 0 0	14	3	0	0	19	0	1	0	15	4	0	0	21	1	1	0
0 0 1	5	0	1	0	2	5	0	1	5	0	1	0	2	7	0	2
0 1 0	2	0	0	0	4	0	0	0	2	0	0	0	5	0	0	0
0 1 1	1	0	0	0	0	2	0	0	1	0	0	0	0	2	0	0
1 0 0	2	0	0	0	9	0	0	0	2	1	0	0	6	0	0	0
1 0 1	1	0	0	0	0	4	0	1	1	0	0	0	0	2	0	0
1 1 0	0	0	0	0	5	0	0	0	0	0	0	0	1	0	0	0
1 1 1	0	0	0	0	0	0	0	0	0	0	0	0	0	0	0	0
	Total no. of cases : 6654										Total no. of cases : 6791					
							50° elevation									
0 0 0	15	4	0	0	20	0	1	0	15	4	0	0	20	0	2	0
0 0 1	6	0	1	0	1	6	0	1	6	0	1	0	2	7	0	2
0 1 0	2	0	0	0	4	0	0	0	3	1	0	0	4	0	0	0
0 1 1	1	0	0	0	0	2	0	0	1	0	0	0	0	2	0	0
1 0 0	2	1	0	0	6	0	0	0	2	1	0	0	5	0	0	0
1 0 1	1	0	0	0	0	4	0	1	1	0	0	0	0	2	0	0
1 1 0	0	0	0	0	3	0	0	0	0	0	0	0	1	0	0	0
1 1 1	0	0	0	0	0	0	0	0	0	0	1	0	0	0	0	0
	Total no. of cases : 6430										Total no. of cases : 6310					
							70° elevation									
0 0 0	23	2	0	0	15	0	1	0	16	3	1	0	20	0	2	0
0 0 1	7	0	1	0	0	4	0	1	6	0	1	0	1	6	0	1
0 1 0	4	0	0	0	3	0	0	0	3	1	0	0	4	0	0	0
0 1 1	1	0	0	0	0	2	0	0	1	0	0	0	0	2	0	0
1 0 0	5	1	0	0	5	0	0	0	3	1	0	0	6	0	0	0
1 0 1	1	0	0	0	0	2	0	1	1	0	0	0	0	1	0	0
1 1 0	1	0	0	0	2	0	0	0	0	0	0	0	2	0	0	0
1 1 1	0	0	0	0	0	0	0	0	0	0	1	0	0	0	0	0
	Total no. of cases : 8171										Total no. of cases : 5937					
							90° elevation									
0 0 0	25	2	0	0	11	0	0	0	17	3	1	0	13	0	1	0
0 0 1	8	0	2	0	1	2	0	0	7	0	1	0	1	4	0	1
0 1 0	5	0	0	0	4	0	0	0	3	1	0	0	5	0	0	0
0 1 1	1	0	0	0	0	2	0	0	2	0	0	0	0	2	0	0
1 0 0	4	0	0	0	6	0	0	0	4	1	0	0	6	0	0	0
1 0 1	1	0	0	0	0	1	0	1	1	0	0	0	0	2	0	0
1 1 0	1	0	0	0	7	0	0	0	2	1	0	0	1	0	0	0
1 1 1	0	0	0	0	0	0	0	0	0	0	1	0	0	0	0	0
	Total no. of cases : 6429										Total no. of cases : 4105					

$\rho1$, $\rho2$: planner and cavity roughness measures.
The roughness measures of equifinal pairs were regarded as equal if the deviation between them was less than 10% (+/-).

-The second, most common single parameter is the height (0 0 1 0 0 0 combination) which appears in 7% of the equifinal cases. Clearly, a low height will result in a small effect of the microstructure and therefore should increase the possibility of equifinality.

-Three other single parameters with similar occurrence frequency of 3.5% are: Pa Pc and p_2 (1 0 0 0 0 0 , 0 1 0 0 0 0 and 0 0 0 0 0 1 combinations) .

-Most of the combinations of more than one identical parameter values appear in the column of the Pos parameter. The major combinations of two identical parameters are of Pos with Pa (1 0 0 1 0 0 combination) and of Pos with Pc parameters (0 1 0 1 0 0 combination) which account for 4% of the cases.

It should be noted that as many as 20% of the cases are spread across the rest of the combinations with frequencies less than 1%. The main conclusion from the analysis of BRDF equifinality cases is that there is not one major structural parameter or one combination of parameters which is associated with the majority of the equifinality cases, instead, many combinations are responsible for a few cases.This finding supports the hypothesis that BRDF equifinality is mainly a result of the balancing effects (explanation type 3) occurring when the same effect of one or two microstructure properties on the reflected radiance field is gained from a microstructure with completely different structural properties.

In this part of work, we assessed equifinality between azimuthal strings at the same sun zenith angle, but it was possible to suggest that the level of equifinality will be reduced by searching for the microstructures which reappear in the groups of equifinal microstructures determined at different sun zenith angles. If the equifinallity is associated with combinations of structural properties which are unknown at this stage, then what are we going to compare ? Thus it was necessary first to identify those characteristic combinations and formalise them before that step could be made.

6.5 Testing for equifinality with field measurements of BRDF

As discussed in Chapter 5, the anisotropy level found for the field sites did not correlate with any of the surface roughness properties. This was supporting evidence that there is equifinality. In this section we will assess the BRDF equifinality of

azimuthal strings (those derived from field measurements) in relation to the simulated azimuthal strings. The assessment of equifinality with field measurements of BRDF is important for two reasons. Firstly it serves as a test for the validity of the assumptions used in the simulation regarding the exact form of interaction between the surface and the incident radiation. If the simulated strings correlate well with the measured ones then it validates the analysis of equifinality from the simulated data. Secondly, it provides an opportunity to test the potential effect of equifinality on real remote sensing applications. The assessment procedure here is similar to the one used in the previous section, it is based on the calculations of the correlation between pairs of azimuthal strings . An azimuthal string derived from field measurements of BRDF was compared to simulated azimuthal strings for 432 different microstructures. The real azimuthal strings were obtained from BRDF measurements of the sites described in the last chapter.

Equifinality was found to exist for all the real azimuthal strings; on average, ten simulated strings exhibited very significant correlation ($0.95 < c < 1.05$ and $r > 0.8$) with each of the real ones.That firstly confirms that the simulation model does represent the real interaction of the solar energy with the surface. Secondly, it suggests that the real microstructures found in the field are contained in the family of the simulated forms.

As it is impossible to present the whole data set, only 4 real azimuthal strings are presented here (Figures 6.6 to 6.9), each with their 5 best correlated simulated strings. Those sets represent four different sun elevations from 30° to 70° and two roughness types, pebbles arranged on soil and artificially built sand ripples. The real azimuthal strings in the graphs appear in the x axis while the 5 simulated strings appear as the y axis. The combination of structural parameters for each of the correlated simulated strings is given in the legend. It can be seen that although the lines of correlation cluster together and although each correlation is significantly representing the relations between the simulated and real data, there is some scattering of the points. This scattering is a result of a combination of effects : firstly , the effect of differences

FIGURE 6.6 : The correlation between 5 simulated azimuthal strings and an azimuthal string derived from field measurements of reflected radiance from site 17 of artificial sand ripples at sun zenith of 50^0 and azimuth of 340^0 .

FIGURE 6.7 : The correlation between 5 simulated azimuthal strings and an azimuthal string derived from field measurements of reflected radiance from site 17 of artificial sand ripples at sun zenith of 30^0 and azimuth of 274^0 .

FIGURE 6.8 : The correlation between 5 simulated azimuthal strings and an azimuthal string derived from field measurements of reflected radiance from site 2 of pebbles densly arranged on soil at sun zenith of 70^0 and azimuth of 51^0.
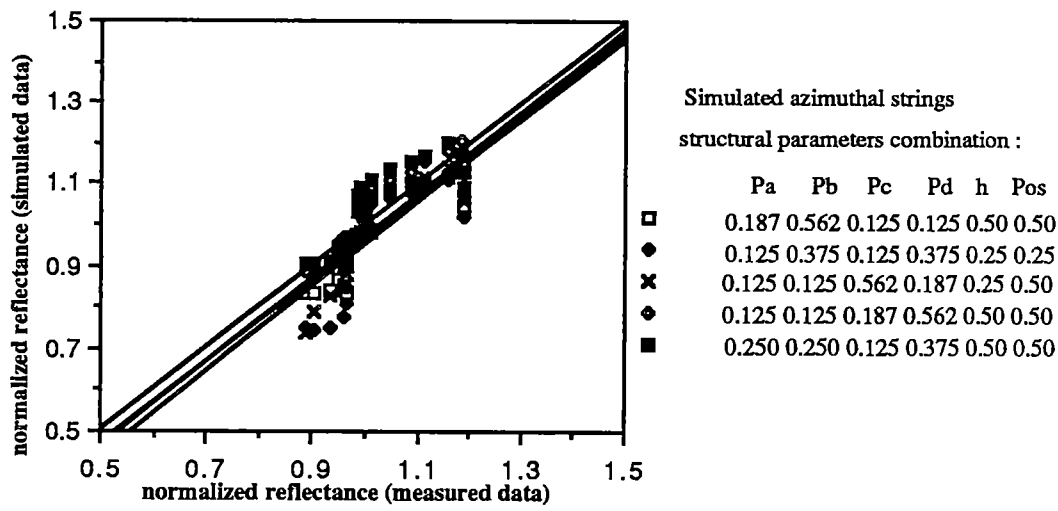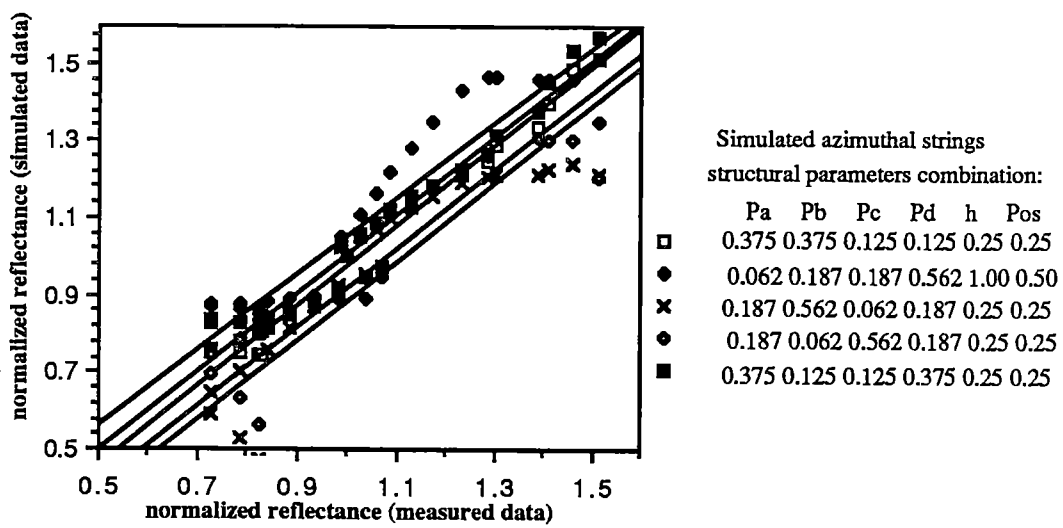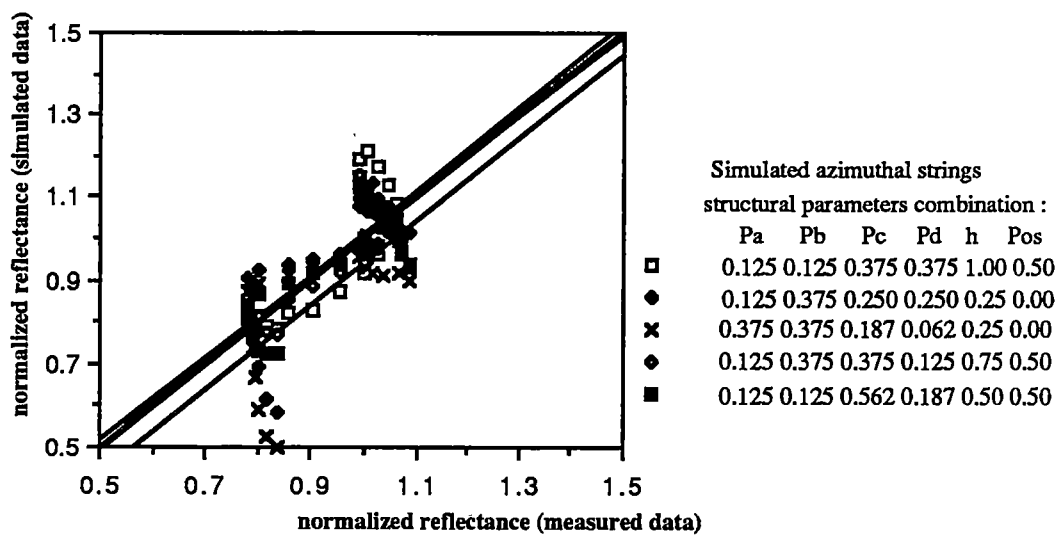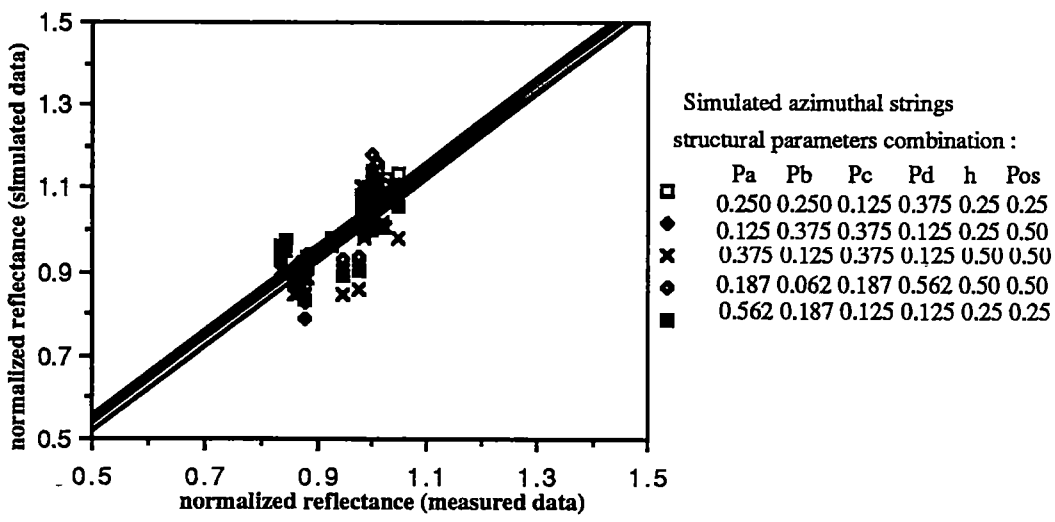

FIGURE 6.9 : The correlation between 5 simulated azimuthal strings and an azimuthal string derived from field measurements of reflected radiance from site 1a of pebbles sparsly arranged on soil at sun zenith of 50^0 and azimuth of 75^0.

between the simulated microstructures and the real ones; and secondly the effect of measurement errors and noise which corrupt the data and complicate the procedures for identification of the underlying microstructures. Most of the scattering appears either near the maximum values or near the minimum values, a fact which suggests that more weight should be given for deviations in those regions of the azimuthal strings in determining equifinal strings. Analysis of the combinations of structural parameters of the simulated microstructures which showed BRDF equifinality with the real azimuthal strings shows that it supports the finding from the simulation that the equifinal pairs exhibit an extensive variation in the underlying microstructures.

The assessment of equifinality in relation to remote sensing applications is difficult as most of the current existing sensor systems do not provide a range of $+/- 65^0$ off nadir viewing angles. Since most of the crucial reflectance information exists in off nadir viewing angles larger than 30^0, there will be an increase in the number of equifinal microstructures. In other words, the derivation of surface microstructures from the currently available satellite data is expected to be difficult.

6.6 Discussion

As discussed in Chapter 2 the similarity of BRDF of different microstructures was assumed previously in remote sensing: for many years many surfaces were assumed to be isotropic reflectors despite the fact that they were obviously different in their microstructure. In view of the increased attention given to the BRDF of terrain surfaces in relation to their roughness, the lack of wide investigation of BRDF equifinality and its potential effect on albedo and remote sensing applications (specially for bare terrain), then equifinality needed to be assessed. This chapter has defined BRDF equifinality and tested its existence on the basis of simulated data and BRDF measurements of bare terrain surfaces. It was found that there is a significant number of equifinal azimuthal strings of significantly different microstructures for the simulated and measured strings. This result is important as it seriously limits the quality of structural information that can be derived from remotely sensed data . This finding strongly supports the second research hypothesis which suggested that there

is not one to one correspondence between the surface BRDF and its roughness microstructure. As the range of viewing angles demonstrated here is not available in current satellite systems, the number of potential equifinal sets should increase,thus further reducing the quality of information derived from the satellite data of off-nadir reflected radiance.

In this chapter we highlighted the problem of BRDF equifinality , but there is a need for further investigation of correlation methods for determining the similarity between azimuthal strings, of potential structural combinations which may lead to equifinality and of the roughness information which may be derived from the surface BRDF. These three areas of further investigation will be given attention in the following two chapters.

CHAPTER 7 : THE ROUGHNESS SIMILARITY OF EQUIFINAL MICROSTRUCTURES

In the last chapter it was suggested that BRDF equifinality is associated with some combinations of structural properties rather than with similarity in structure. In this chapter, the formalization of such combinations is carried out on the basis of observations made of equifinal microstructures and on considerations of reflectance - structure relations. It is anticipated that the roughness parameters which are formed on the basis of these combinations firstly will show some sensitivity to the structure, and secondly that equifinal microstructures will show similarity in their roughness. Both sensitivity and similarity are tested on the basis of the simulation model presented in the last chapter, as this simulation provides an efficient framework for linking the reflectance field to a wide range of microstructures.

The work is divided into two parts: firstly the characteristic roughness properties are formalized in relation to reflectance; and in the second stage an assessment of the roughness sensitivity and similarity is carried out .

7.1 The formalisation of two dimensional roughness description of microstructures

Reflectance / roughness relations for electromagnetic radiation have been the subject of numerous works in remote sensing. However, most of the research has been done in the radar / microwave spectral region where the radiation wavelength is of the scale of the surface roughness, thus giving major weight to specular reflection in explaining the scattering properties. The Rayleigh criterion (section 2.1.2.1) was utilized for studying roughness / scattering relations as indicated by Backmann and Spitzzino (1963), Schaber et al. (1976) and Schultijan (1986). The main roughness parameter used in these studies was the height or the diameter of the scattering elements (particles on the surface).

In the shortwave and near infrared spectral region most of the existing studies utilize the

Minnaert constant (section 2.2.3.2) which was frequently claimed to be an expression of the surface roughness. This constant (dimensionless) was primarily a correction factor to account for the anisotropic reflection of the surface and was not linked to the surface properties using morphometric measurements. A more recent work by Norman et al. (1985) bridges the gap by suggesting the following roughness measure for calculating the roughness of the soil :

$$\sigma = [\,H\,L\,(\,1 - W\,)]^{1/3} \qquad\qquad [7.1]$$

where H, L and W are the height , length and width of the soil aggregates (see Figure 2.6).

However, the roughness measure σ in that form is completely insensitive to the surface structure as it allows a 'trade-off' of the three major structural properties and it does not account for the change in roughness due to the sloping facets (facets c and d in our simulation). This situation is not desirable where the objective is to determine surface properties from reflectance data. The omission of the role of the sloping facets in changing the elements reflection pattern is another limitation set on applying σ. In fact, that most of the existing roughness measures are statistical parameters of either height or area measurements (Hobson ,1973) and are not sensitive to reflectance (see Figure 7.1) .

As described earlier in Chapter 2, the reflectance is closely related to the amount of shadow occurring within the microstructure. The cavity as the concave part of the microstructure (between two protruding elements along the direction of the sun) defines the amount of shadow and its proportion in any viewing direction. For this reason, it will serve as the basis for formalizing the roughness parameters in this work . The cavity may be defined in three dimensions: height , length (along the sun azimuth) and width; alternatively it can be defined on the basis of its relative surface area and height. In the following discussion we use the microstructure terminology which was introduced in Chapter 6 (Figure 6.1). It is believed that any real surface roughness element can be generalized to fit one of our 432 microstructures.
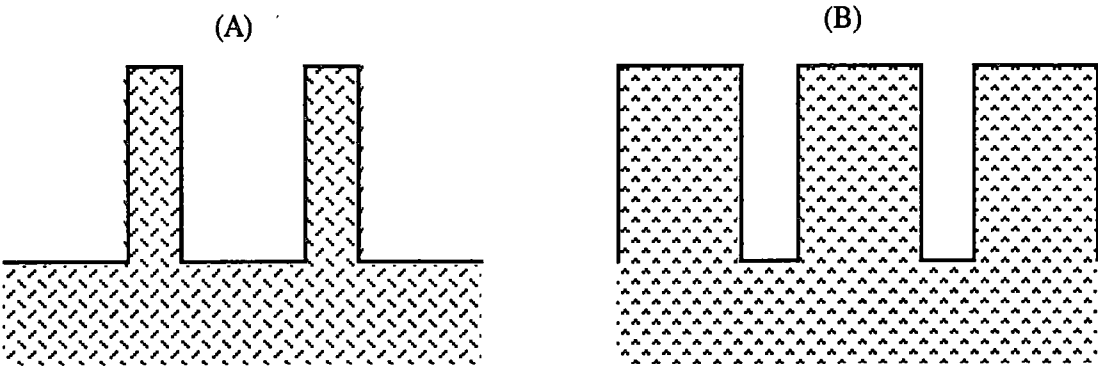
FIGURE 7.1 : Two surface structures which are characterized as having the same roughness in methods based on elevation and surface area calculations but having a completely different reflectance properties: while structure A will have a major shadow effect , in B it will be only limited.
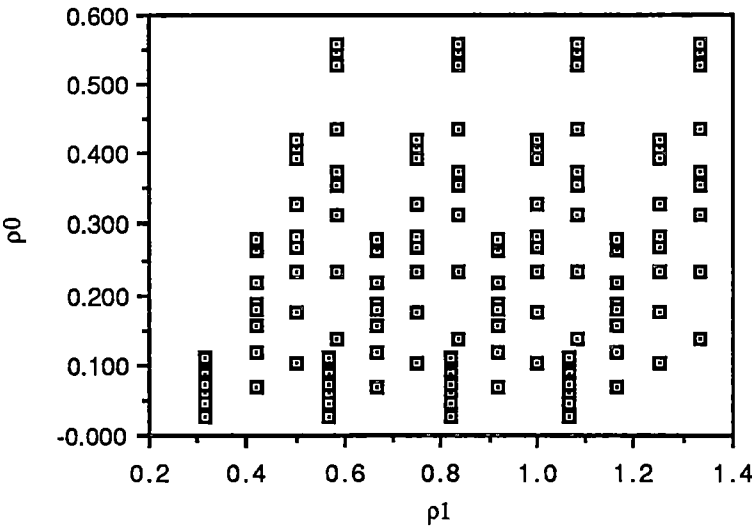
FIGURE 7.2 : Mapping of the roughness derived for simulated microstructures in the two dimensional roughness plane formed by ρ_0 and ρ_1 (it is not possible to see all the 432 roughness points as a result of the resolution of the diagram).

The first roughness parameter is given by:

$$\rho_0 = [1-\rho_{0A}]\ \rho_{0B} \qquad\qquad [7.2]$$

where:

$$\rho_{0A} = [Pos + Pa\ (1 - Pos)]$$

$$\rho_{0B} = [\ Pb + (Pc + Pd)/2]$$

ρ_{0A} is the total proportion of unobstructed flat areas (areas outside of the cavity which can be viewed from any direction along the sun azimuthal plane) while ρ_{0B} accounts for the presence of the sloping facets in the cavity.

The effect of the sloping facets on the ρ_0 can be demonstrated as follows: if the microstructure is built of parallel thin walls (with Pa --> 0) where $[1-\rho_{0A}]$ is virtually 1, then ρ_0 approaches 1 as well , while if the cavity is built of a V shaped valley with $[1-\rho_{0A}]$ still equals 1 but with Pb=0 then $\rho_0 = 0.5$. There is therefore a certain amount of insensitivity of ρ_0 to the exact form of the cavity. A smaller cavity with steep walls will get the same roughness value as a wide V shaped cavity. It is this insensitivity which partly explains the equifinality.

The second roughness parameter is the height of the elements (= the depth of the cavity). Observations regarding equifinal sets suggest that microelement height and side facet may interact to produce equifinality. An increase in one can be compensated by an increase in the other. Two strings can be equifinal if the height and the side facet size in one of them are both increased relative to the second microstructure. As the height of the microelements is an important roughness property, as Pos is accounted partly in ρ_0 and as it is important to minimize the dependency between the two roughness parameters , the weight given to Pos in balancing the height has to be limited. The second roughness parameter is therefore given by:

$$\rho_1 = h + (1\text{-Pos}) / 3 \qquad\qquad [7.3]$$

The effect of Pos in determining ρ_1 can be demonstrated as follows : if h of a microstructure is 0.50 and its Pos is 0 then it will get a value of 0.833 while if another microstructure has h of 0.75 and Pos of 0.8 it will get a value of 0.816 which is a

small deviation relative to a value of 1.0833 given to a microstructure with h = 0.75 and Pos= 0.0 .

Figure 7.2 maps the roughness values of each of the simulated microstructures (described in Chapter 2) in the two dimensional space formed by ρ_0 and ρ_1, the values along the ρ_0 axis ranges from 0.688 (when Pos=0 and Pa=0.1875) to 0.0273 (when Pos=0.8 and Pa=0.562). The two extreme values in the ρ_1 axis are 0.3166 and 1.333. The two dimensional plane (Figure 7.2) represents maximum directional roughness at the top right corner and a decrease in roughness along both directions (with decrease in h and with increase in Pos+Pa). For a specific illumination direction there will be maximum shadow, and therefore maximum roughness, when the microstructure exhibits maximum height differences in the illumination direction and minimum in the perpendicular direction (the situation in the top right corner). However, maximum overall roughness occurs when the sum of the shadowed area is maximum for all possible illumination directions. This occurs when the microelements are equally distributed (i.e. when Pos=Pb+(Pc+Pd)/2 and when Pc+Pd approaches 0).

The sensitivity of the proposed roughness parameters to differences in microstructure can be discussed on the basis of the simulation data. The wide scatter of points in Figure 7.2 indicates sensitivity to the two roughness scales chosen here. It is possible also to observe that there is an increase in point density at low roughness values of ρ_0 which suggests that this is a major source for BRDF equifinality. Another way to look at relations of roughness sensitivity versus BRDF equifinality is given in Figure 7.3. In the simulation model, 432 microstructures are formed in a nesting order of six loops, one loop for each of the six structural parameters. Thus, a certain sequence of roughness patterns is formed following the sequence of simulated microstructures. Figures 7.3a and 7.3b provide another indication that the roughness values are well spread within the set range of data. Note that ρ_1 shows a decrease in the range of values following an increase in the sequential order of the microstructures. That phenomenon is mainly explained by the increase in the proportion of the 'top facet' (Pa) occurring through the simulation process.
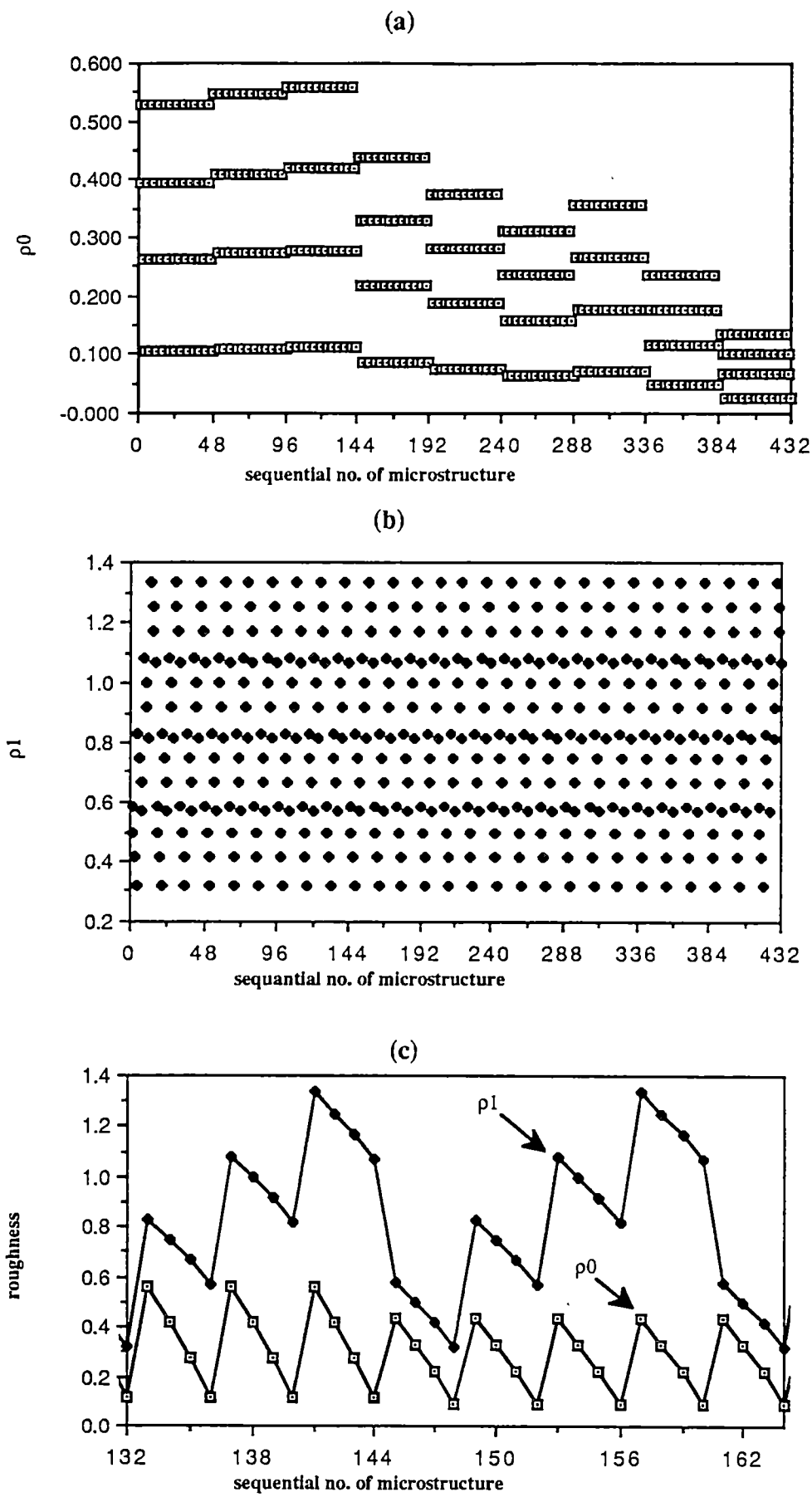
(a)

(b)

(c)

FIGURE 7.3 : Roughness variation and pattern following the sequence of microstructures formed in the simulation process .

A close look at a section of the roughness series (Figure 7.3c) shows the effect of the side facet (Pos) on the pattern of change of the two roughness elements expressed by the primary cyclic pattern of ρ_0 and by the secondary cyclic pattern of ρ_1. Those cyclic patterns demonstrate the level of equifinality which occurs in the data.

To summarize, the proposed roughness parameters characterize the cavity of the surface microstructure while allowing some level of equifinalty. Each of the parameters describes a different property of the surface: while ρ_0 is proportional to the area of the cavity (and to the flat unobstructed areas $(1- \rho_0)$), the second parameter ρ_1 is mainly proportional to the height of the microelements. The surface is flat when either or both of the two parameters is equal to 0. It should be mentioned that ρ_0 is a function of the cavity in two directions where Pos describes the cavity area in the direction perpendicular to the illumination. Thus, if the roughness pattern is directional , then ρ_0 in a specific direction is a function of the cavity in the two major directions of the pattern, otherwise ρ_0 is equal in all directions.

7.2 Four strategies for analysing the similarity between azimuthal strings

In the previous chapter, equifinality between two azimuthal strings was examined according to their linear correlation . The method applied was that equal weight is given to all viewing directions, thus emphasizing the role of the maximum and minimum reflectance data. However, it is possible that some viewing directions or some properties of the reflectance curves might be of major importance when analysing the similarity / dissimilarity between two strings even though their effect on the trend is minor. In other words, there could be some viewing directions which are more sensitive than others to the effect of structure / roughness ,but the magnitude of the effects in absolute terms (of normalised reflectance) is low relative to the general trends. Consequently, in order to ensure that all possible equifinal microstructures are selected, it is necessary to apply some other methods which will give emphasis to deviations in several important regions of the azimuthal strings. These regions are the region of maximum reflectance, the region of minimum reflectance and the region of forward

specular reflection. When comparing curves, attention had also to be given to the area under the curve in addition to the normalized values. One of the methods used is based therefore on the transformation of the azimuthal strings into curves of cumulative values. · The four methods which were formalised are as follows:

strategy 1: simple linear correlation as used in the previous section:

$$R'_1(\theta_i , \theta_v) \, W \, (\theta_v) = c \, [R'_s(\theta_i , \theta_v) \, W \, (\theta_v)] + a_0 \qquad [7.4]$$

where $R'(\theta_i , \theta_v)$ is the normalized reflectance viewed from direction θ_v due to direct beam irradiance from direction θ_i ; the subscript 1 refers to a measured or modelled azimuthal string while the subscript s denotes simulated azimuthal strings whose equifinality to azimuthal string 1 is being examined, $W(\theta_v)$ is the weighting function used (in this method $W (\theta_v)=1$), c is the correlation 'slope' and a_0 is the intercept. The equifinality is determined as in [6.14] according to c and the correlation coefficient (r'). The term 'viewing direction' used in this text is an angular measure along one azimuthal plane with 0° value on the horizon in the direction into the sun (backward direction) with 180° value on the horizon with the direction of the sun (forward direction) and with 90° value in the nadir direction.

strategy 2: linear correlation as in [7.4] applied after equalizing the weight given to deviations in the region of forward viewing direction to deviations in the region of backward viewing direction. The weighting function is given by the following expression:

$$W (\theta_v)=1 \qquad \text{for} \qquad 25^o \leq \theta_v \leq 90^o$$

and

$$W (\theta_v)=V \qquad \text{for} \qquad 90^o < \theta_v \leq 155^o$$

where

$$V = \frac{\sum\limits_{\theta_v=90^\circ}^{155^\circ} R'_1(\theta_i, \theta_v)}{\sum\limits_{\theta_v=25^\circ}^{90^\circ} R'_1(\theta_i, \theta_v)}$$

[7.5]

Since the maximum values of the backward region ($25^\circ < \theta_r \le 90^\circ$) tend to have larger deviation from the nadir value (1.0) than the minimum values of the forward region, the equalization process involves stretching the deviations in that region . The stretching value (V) used is the one calculated for $R'_1(\theta_i, \theta_v)$ and then applied to the two azimuthal strings(1 and s in 7.4); thus it is expected to amplify the deviations in the region of forward reflection and equalize the relative contribution that forward scatter and backscatter make in the correlation.

strategy 3: linear correlation applied after stretching the azimuthal strings in the narrow regions of backward and forward specular reflection . The stretching was done according to the following equation:

$$W(\theta_v) = \exp(1-\sin^2(|\theta_v - \theta_b|) \quad \text{for} \quad 25^\circ \le \theta_v \le 90^\circ$$

[7.6]

$$W(\theta_v) = \exp(1-\sin^2(|\theta_v - \theta_f|) \quad \text{for} \quad 90^\circ \le \theta_v \le 155^\circ$$

where θ_b is the backward direction corresponding to the vector parallel to the direct rays of the sun, and θ_f is the forward direction ($\theta_f =180^\circ - \theta_b$). The multiplication value for a normalized reflectance value is e (natural log) when it is exactly at the specular direction and decreases very rapidly to 1 as the viewing angle deviates from that direction. Using this procedure the deviations between two azimuthal curves in the specular regions get much more weight than those in the other regions.

strategy 4: linear correlation applied after transforming the two azimuthal strings to cumulative curves of the original normalized reflectance values squared:

$$R_1^c(\theta_i, \theta_v) = \sum_{\theta_j=25^\circ}^{\theta_v} [R'_1(\theta_i, \theta_j)]^2 \qquad [7.7]$$

This procedure emphasizes differences in the rate of change of normalized reflectance and the differences between the forward and backward regions of the strings. Note that no further transformation is done on the modified azimuthal strings and W (θ_r) =1 for all viewing directions.

The following procedure was applied to obtain a data base for the analysis of roughness similarity. As described in the last chapter, it is possible to generate 432 microstructures as an ordered set by varying each of six structural parameters. These microstructures in turn generate 432 azimuthal strings which are labelled "S_i" in Figure 7.4. These 432 strings ordered into contiguous groups of 9 and a random number generator selected one string from each group. Thus a smaller set, set B, was formed composed of 50 azimuthal strings (Figure 7.4). Each azimuthal string in B was correlated with each element of set A according to the four strategies listed above. Thus a new set $E_1, .. E_{15}$ was formed from the 15 highest ranking equifinal strings corresponding to one element of B and one correlation strategy. This gave a total of 200 sets of $\{E_i\}$. That data served for examining both the roughness sensitivity and similarity in the following two sections.

7.3 The assessment of roughness similarity of equifinal microstructures.

Using the simulation data it is possible to examine the variation in roughness similarity within and between equifinal sets since the true roughness values can be derived for each microstructure from [7.2] and [7.3]. The analysis of these data sets considered the following :

1. The roughness similarity between each of the microstructures in set B and the microstructures in its four equifinal sets (one for each method).
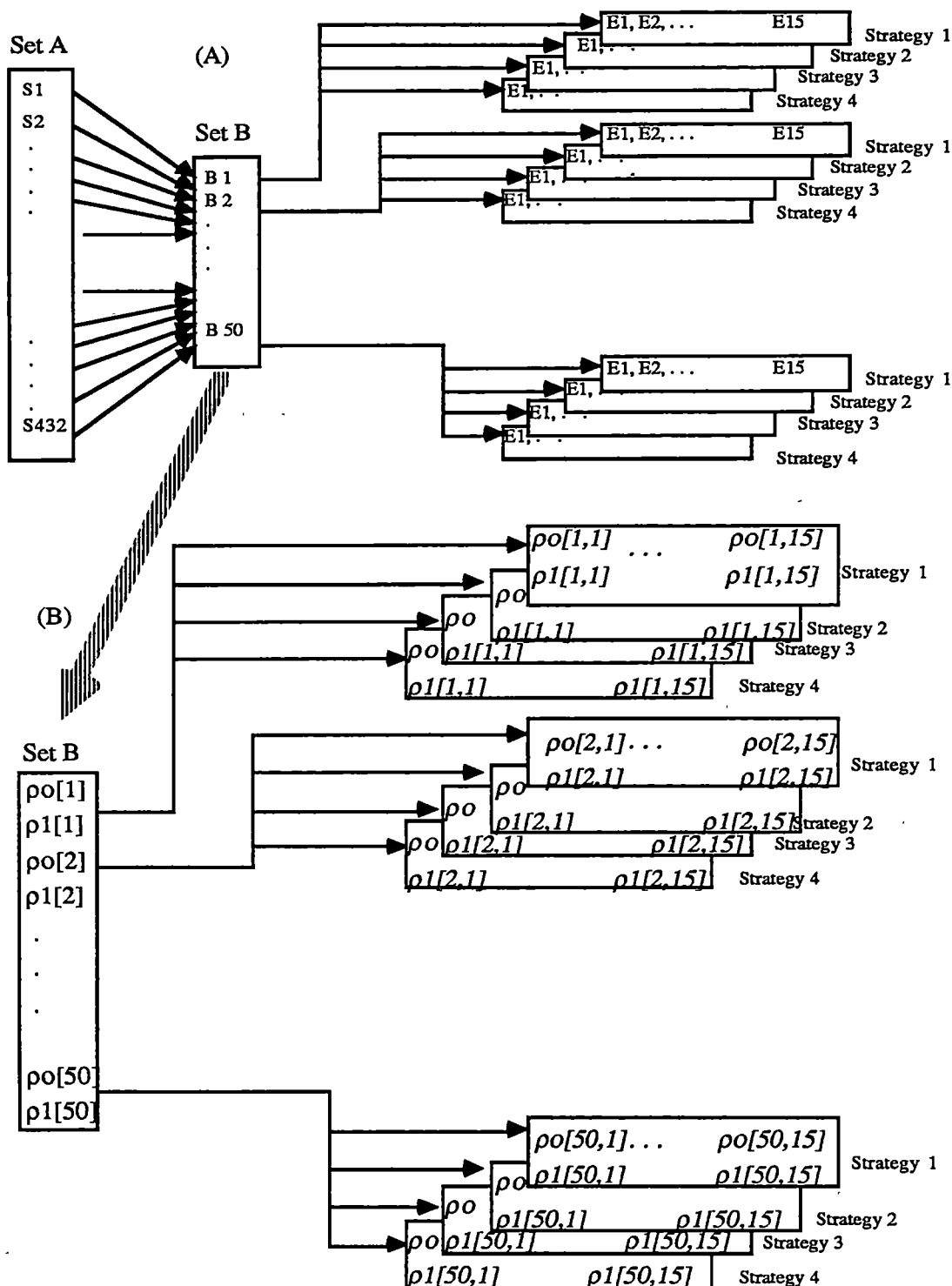
FIGURE7.4 : Diagram to illustrate the process of selecting a data base to analyse the roughness similarity of equifinal microstructures. Set B is a subset of A and contains 50 azimuthal strings. The four correlation strategies are applied to each element of B and each of the 432 elements of A. The 15 strings (of A) exhibiting the highest correlation form the {E_i} set. Section 2 of the diagram presents the roughness variables associated with each element of set B and each element of E_i.

$$\Delta\rho o[I,K] = \rho o[I,K] - \rho o[I,K]$$

$$\Delta\rho 1[I,K] = \rho 1[I,K] - \rho 1[I,K]$$

I - index no. of sample microstructure[1...50]

K- order of equifinality [1...15]

FIGURE 7.5 : Roughness deviations between original (set B) and values predicted by equifinal microstructures grouped according to the order of equifinality.

2. The accuracy that can be attached to the roughness values given by equifinal microstructures (sets E) in predicting the roughness of the 'true microstructures' (set B).

3. The change of accuracy in predicting roughness values for different sun elevation angles.

Roughness similarity of equifinal microstructures can be tested from the deviations between the known roughness values (set B) and those predicted by the equifinal microstructures (Figure 7.5): the smaller the deviations are, the larger the similarity. The use of a semi-random sampling procedure for selecting set B ensured that the maximum range of roughness values will be present in the sample. This was checked by comparing the average and standard deviation of ρ_0 and ρ_1 in the original set (set A) and that of the sample set. It was found that the statistics of both distributions are similar. This step was necessary to 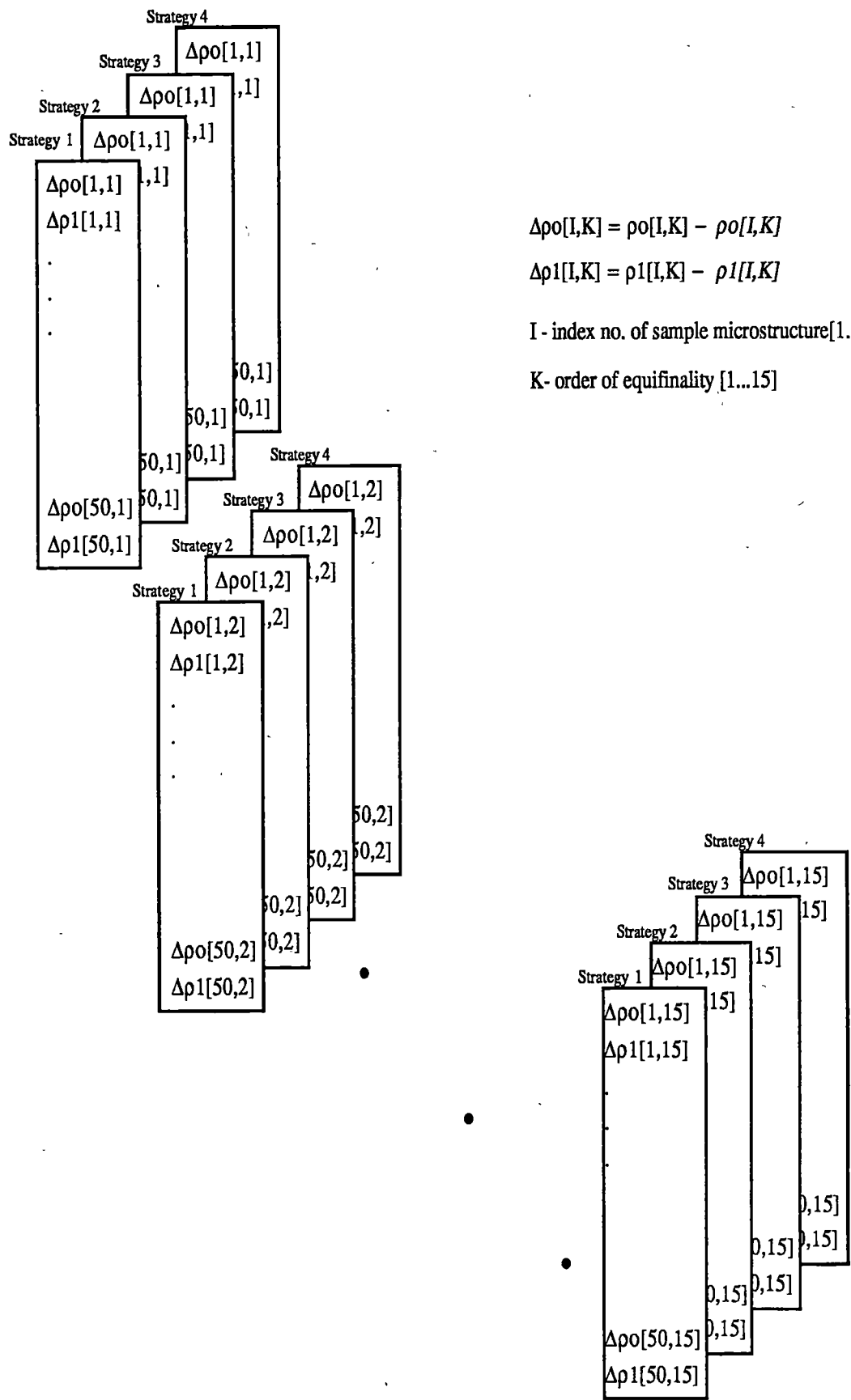prevent a case where the sampled data is clustered and therefore limit the validity of the results . Denoting the deviations as prediction errors, the root mean square error (RMSE) was chosen to be a representative statistic for analysing the roughness similarity. The roughness RMSE was stratified according to the roughness parameter (ρ_0 or ρ_1), the correlation approach followed, and the order of equifinality (see Figure 7.5). Thus, all the RMS errors of first order predictions (those of the best equifinal microstructures) are grouped together (for example : $\Delta\rho_0[1,1]$ . . . $\Delta\rho_0[50,1]$) , then the second order errors ($\Delta\rho_0[1,2]$ . . . $\Delta\rho_0[50,2]$) and the procedure is followed until the errors of the 15th order predictions are grouped (see Figure 7.5). The RMSE of each group is then calculated and plotted against the order of equifinality (Figures 7.6 and 7.7).

Interpretation of the RMSE levels is difficult as there has been little work in this area. However, it is possible to treat the problem as one of contouring where there is a need to define the appropriate interval. The contouring intervals then can be used to divide the two dimensional roughness space into regions of characteristic roughness. An empirical method for deriving contouring intervals is described for elevation mapping applications in Gustafson and Loon (1982) and given by:

$$\text{Interval} / 2 = 1.645 * \text{RMSE} \qquad [7.8]$$

where 1.645 is a conversion factor which describes the number of standard deviations needed to account for 90% of the errors, provided that the error distribution is normal. The factor 2 is included since 90% of the errors account only for half of the interval.

Thus, knowing the intervals for both p_0 and p_1, it is possible to group the entire data set into roughness categories that are physically meaningful. All microstructures with roughness values within one category may be expected to exhibit BRDF equifinality. In other words, all these microstructures can be held as similar in terms of their roughness.

Comparison between the roughness similarity given in the different methods shows that the fourth method is significantly less accurate than the three others. The same level of similarity is produced by the first, second and third methods, while their RMSE fluctuate in relation to each other as each method determines a slightly different equifinal set.

Analysis of roughness similarity for equifinal microstructures of lower order reveals a decreased level of similarity (increasing RMSE) with increasing order of equifinality . The decreasing level of roughness similarity was found to be parallel in both roughness components. The first order equifinal microstructures provide the most accurate combined prediction for both roughness components, even though there are a few cases where a single parameter is predicted more accurately by a lower order equifinal microstructure.

Substantial differences were obtained in roughness similarity of equifinal microstructures for different sun elevation angles. The result is important since it suggests that there is a range of sun elevation angles which is optimal for characterising the surface roughness from reflectance data. The p_1 roughness parameter shows a general decrease in RMSE while the second parameter p_0 shows an increase of RMSE with increasing sun elevation angle.The optimal sun elevation angles in terms of the combined accuracy of both roughness components are then between 40^0 and 60^0 .

In this range of sun elevation angles, the roughness RMSE derived for the first order equifinal microstructures provides a roughness interval of 0.20 for p_0 (equation 7.8) which means a division into three roughness categories (regions) in the simulated range

FIGURE 7.6 : Roughness RMSE for ρ_0 according to the order of equifinality as determined for equifinal microstructures in four methods and at six sun elevation angles.
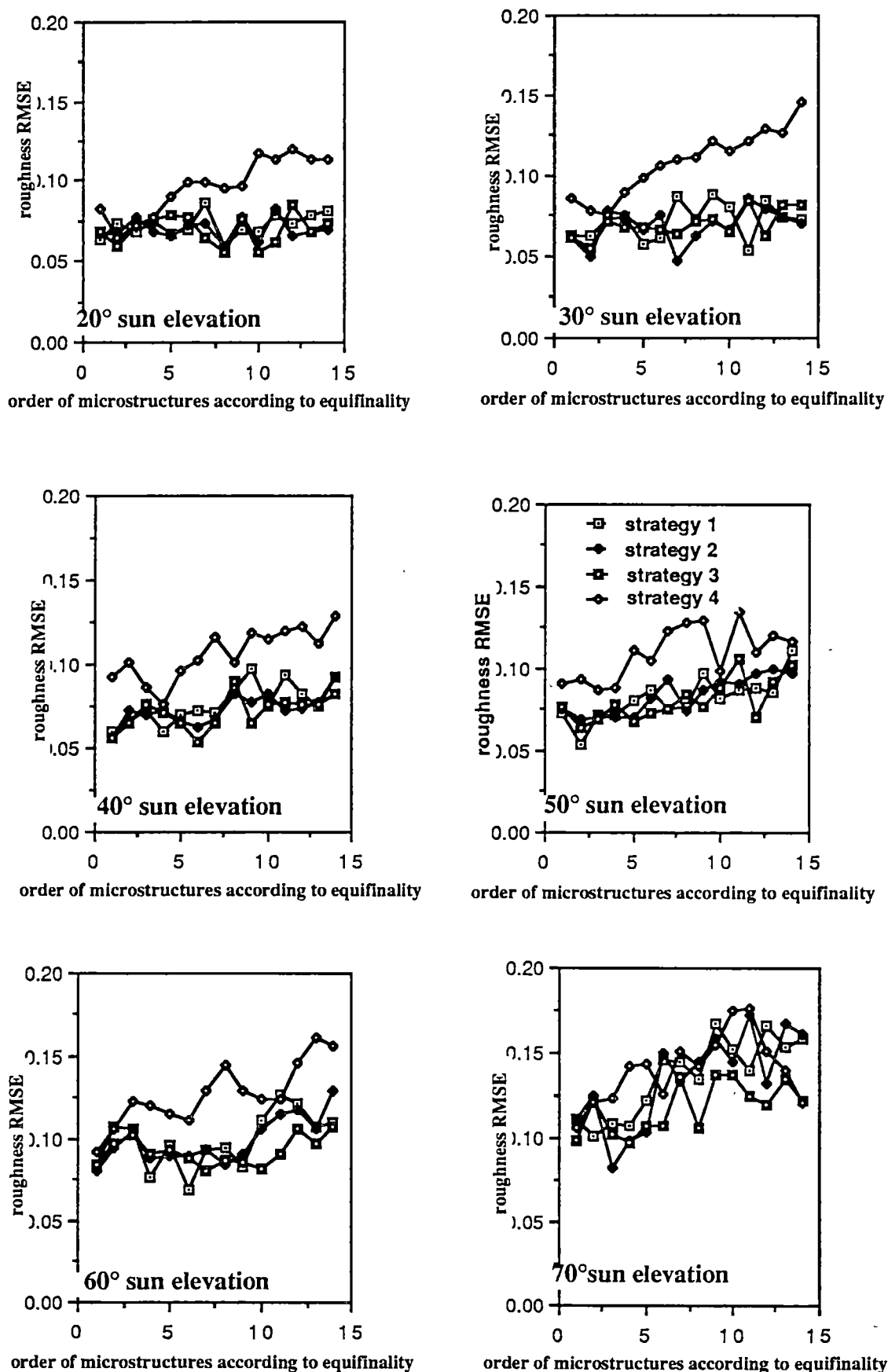
FIGURE 7.7 : Roughness RMSE for ρ_1 according to the order of equifinality as determined for equifinal microstructures in four methods and at six sun elevation angles.
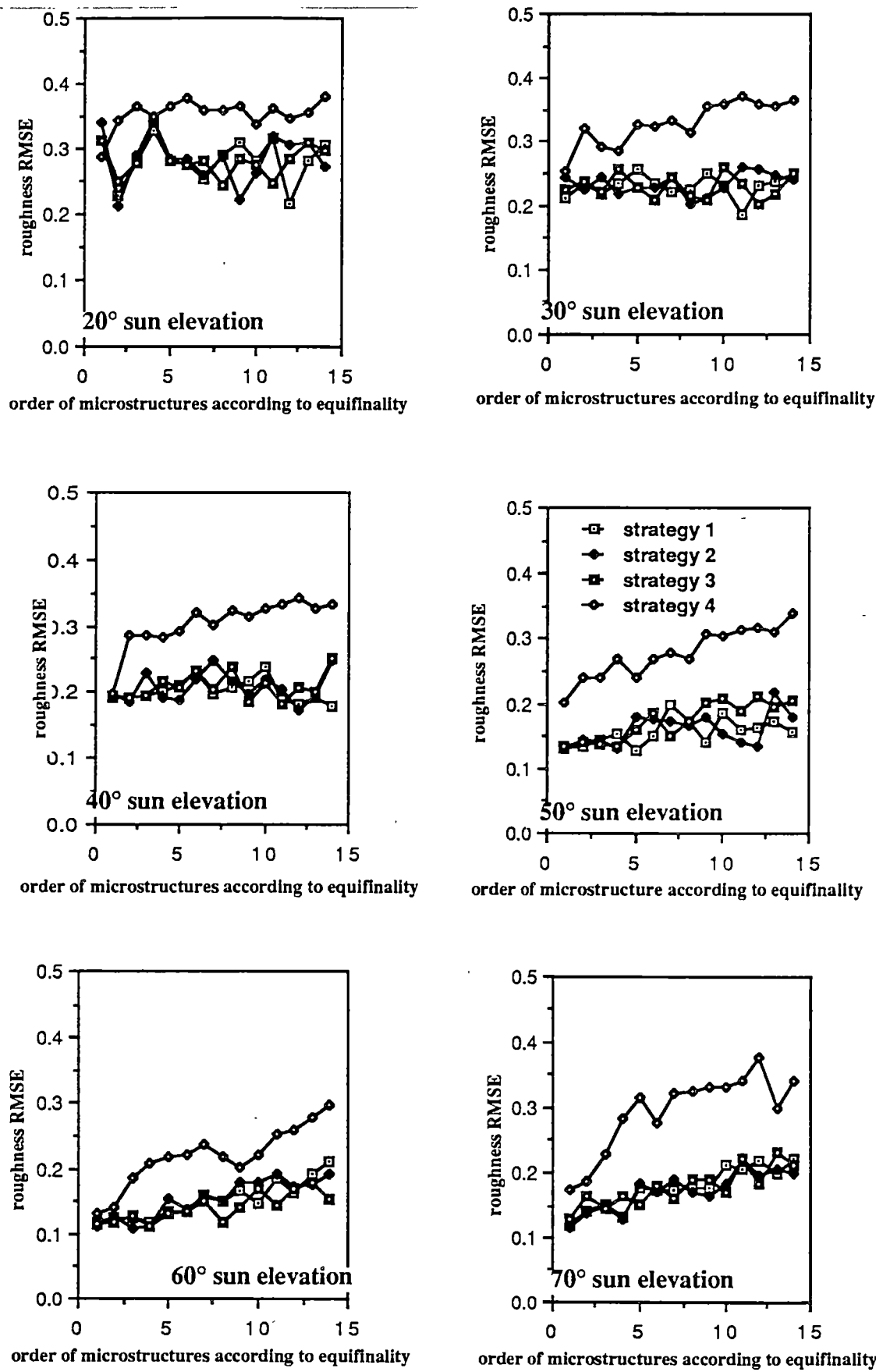
(between 0 and 0.68) and an interval of 0.4 for ρ_1 which again allows the division of the simulated roughness range (between 0 and 1.4) into three categories (regions).

7.4 Discussion

In this chapter we formalized a two dimensional roughness description of surface microstructures in order to assess the sensitivity of the reflectance distribution to roughness. It was pointed out that the cavities formed between surface elements along the illumination direction are important in terms of roughness / reflectance relations. The two roughness parameters, ρ_0 and ρ_1 represent the cavities' relative area and relative depth (which is also the relative height of the elements). The proposed roughness parameters were found sensitive to the microstructure in the sense that there was no clustering of the values. At the same time it was shown that those parameters allow for equifinality. Analysis of roughness similarity between equifinal microstructures showed that the two dimensional roughness plane can be divided into nine regions following the roughness RMSE levels found. The significance of these results regarding the research hypotheses given in Chapter 2 is that the roughness intervals represent limits on the equifinality of BRDF for different surface conditions.

The method applied in section 7.3 for analysing the roughness similarity can serve as an inversion process where surface properties are defined by determining the best equifinal microstructures. However this method requires relatively large amounts of computer CPU   time. Better inversion options are explored in the following chapter .

CHAPTER 8 : THE DETERMINATION OF SURFACE ROUGHNESS PARAMETERS FROM REFLECTANCE DATA: AN INVERSION PROCESS

In Chapter 6 it was shown that a simple microstructure requires a lengthy and non-linear function (Equation [6.12]) for modelling its reflectance. The complexity of those causal relations between the microstructure and the BRDF makes it difficult to develop an inversion procedure which will enable microstructure parameters to be determined from reflectance data. In the last chapter two roughness parameters were found to represent well the similarity between equifinal microstructures. In this chapter, two simplified functional relationships between the reflectance field and parameters describing the viewing / illuminating geometry and the roughness properties of the surface are formalized and assessed. A study of inversion techniques is then carried out for each of these functions. The techniques are then assessed using both the simulation data and the combination of reflectance and roughness data collected in the field. In a similar way to that described in the last chapter, the roughness RMSE of the azimuthal strings is calculated and utilised for identifying optimal off-nadir viewing angles.

This chapter is divided into four sections: the first section describes the development of two parametric models for reflectance; section two describes their inversion; section three examines the inversion results; and section four discusses their implictions for remote sensing applications.

8.1 The development of parametric reflectance models for rough surfaces

A review of some of the parametric and empirical reflectance models is given in Chapter 2 (section 2.2.3.2). The importance of these model types is in two related areas: firstly, as an empirical or semi-empirical tool for describing the surface BRDF, and secondly, as a tool for linking surface properties to its reflectance. The parameters

used in these models can be divided into two groups, those describing the geometry of the illumination / viewing angle and those representing the surface properties. In this section two parametric models are formalized and assessed using the simulation data.

As described in Chapter 5 most of the bare surfaces exhibit a certain level of anisotropy. This is exhibited in the reflected radiance field which changes with off-nadir angles. Most of the existing models use angular viewing parameters to simulate the general form of anisotropy and surface parameters to determine the level (or range) of anisotropy. This approach can be demonstrated in models related to the Minnaert formulae (equations [2.37] , [2.38] and [2.39]). When k =0 (the Minnaert constant) the reflectance is proportional to the cosine of the viewing angle while when k=1 the reflectance is Lambertian. The angular parameters used for determining the rate of change in reflectace are usually the off-nadir viewing angle or the phase angle. Combining these two angles can produce an asymmetric directional pattern with a nonlinear decrease of reflectance similar to that found in field data. As attempts to accommodate the two roughness parameters in the existing formulae were not successful, it was necessary to develop new forms of parametric models which follow principles similar to those described earlier. The first model was formalized as follows:

$$f'_r = 1-\rho_0 + \rho_0 \, e^{\rho_1 \, \cos \, [0.5 \, (\Omega + \theta_v)]} \qquad\qquad [8.1]$$

where f'_r is the bidirectional reflectance into direction r normalized by the nadir reflectance, θr is the viewing angle measured from the horizon in the azimuth of the sun , Ω is the phase angle between the direction of incoming direct beams and the viewing direction , and ρ_1 and ρ_0 are the roughness components. The use of θ_v instead of the off-nadir viewing angle was firstly a result of the consideration that it provides a better link of the reflectance (reflected radiance) to the change of the surface roughness properties while the off-nadir angles are symmetric around the nadir, unlike the shadowing for example (and it is wrong to assume that the shadowing is fully accounted for by the phase angle). The second reason was that in its present combination with Ω, it causes the reflectance to stabilize for directions between the

horizon and the illumination direction. Such a pattern of change in the reflectance field is reported in the existing literature (see discussion in section 2.2.2.2), in the simulation process (equation [6.12]) and in field measurements. Nevertheless, it is important to point out that in the process of developing [8.1] other forms of models with other combinations of viewing and phase angles were assessed and found to have a lower level of correlation with the simulated azimuthal strings.

The assessment of the appropriateness of [8.1] in representing the reflectance field concerns its ability to converge to a Lambertian reflection pattern and its ability to exhibit an asymetric pattern with a nonlinear change of reflectance. The ability of the model to represent Lambertian reflectance is demonstrated by assuming that either $\rho_1=0$ or $\rho_0=0$ or when both equals zero. In all these cases [8.1] provides the expected normalised reflectance of 1. The asymmetry of the model can be shown by following the decrease of the cosine term from a value close to 1 in the illumination direction to a value close to zero when the sum $\Omega + \theta r$ approaches 180°. The nonlinearity of the directional change of reflectance is given by the exponential form of [8.1].

The above model cannot not be expected to produce the exact normalized reflectance values since it is not a process based model. Its final form depends on the type of regression model which best fits real data to the model. In view of this limitation on the applicability of the model in its idealized form and the wish to widen the inversion options, a slightly different model was formalized by changing the form of the exponential term:

$$f_r' = 1-\rho_0 + \rho_0 \, e^{\rho 1 + \cos [0.5 \, (\Omega + \theta_v)]} \qquad\qquad [8.2]$$

This model differs from [8.1] by not converging to Lambertian reflectance when $\rho 1$ equals 0 in its idealized form.

The performance of the two models in predicting the real reflectance patterns was assessed using the simulation data. The roughness parameters ($\rho 0$ and $\rho 1$) and the azimuthal strings were calculated for each of the 432 microstructures used in this study. Equations 8.1 and 8.2 were compared with the calculated azimuthal strings. This

procedure was followed for eight sun elevation angles between 20° and 90°. Table 8.1 represents the quality of the correlations found between the strings as a percentage of the 432 correlations calculated with the correlation coefficient (r) greater than 0.9 which indicate a very high and significant level of similarity. For the range of sun elevation angles from 20° up to and including 60°, the proposed models performed very well with r>0.9 for more than 98% of the cases. As explained in the last chapter, the roughness parameters describe the cavity that is formed by the microstructure and is linked to the amount of shadowing occurring with the change in the sun elevation angle. The drastic decrease in the level of performance for sun elevation angles greater than 70° was expected as there is a decrease in the shadow component and its importance in determining the reflectance field.

To summarize: two parametric models were introduced in this section on the basis of their ability to follow the trends in reflectance found in real azimuthal strings, but more for their ability to link the surface roughness properties to its reflectance field. Since the two models were found to correlate well with the reflectance patterns determined by the simulation it is possible to consider inverting them in order to determine the surface roughness.

8.3   The development of inversion techniques for the two parametric models

A review of existing inversion techniques is given in section 2.3.1 (Chapter 2). Two of the techniques introduced by Smith et al. (1980) and by Li and Strahler (1986) are based on parametric models, while Goel and Greir (1986) developed theirs as process based models.The two last inversion techniques were applied to vegetated surfaces and emphasized the role of spectral reflectance differences between the vegetation and the background in determining the scene's properties. Bare terrain surfaces cannot be generally characterized by such spectral contrast. As demonstrated in the stony areas near Fowlers Gap , when there are spectral differences between the quartz pebbles, the quartzite pebbles and the soil for example, they are mixed spatially and cannot be utilized to derive the surface properties.

TABLE 8.1 : The correlation between model predictions and simulated data for 432 azimuthal strings calculated for eight sun elevation angles. Numbers represent the percentage of the data set (432 strings) with r greater than 0.9

Sun elevation	20^0	30^0	40^0	50^0	60^0	70^0	80^0	90^0
model 1								
precentage of cases								
with $r > 0.9$	98	98	100	100	100	94	47	17
model 2								
precentage of cases								
with $r > 0.9$	100	100	100	100	100	93	44	16

r : correlation coefficient

TABLE 8.2 : The correlation between the regression coefficients Co and C1 of the empirical form of model 2 (given by equation [8.5]) and the roughness component ρ_0 as changed following the computation of [8.5] for 432 azimuthal strings at eight sun elevation angles.

Sun elevation	20^0	30^0	40^0	50^0	60^0	70^0	80^0	90^0
r for								
$1-\rho_0$ and C_0	0.924	0.904	0.878	0.847	0.808	0.739	0.612	0.414
r for								
ρ_0 and C_1	0.933	0.920	0.903	0.882	0.840	0.750	0.575	0.214

r : correlation coefficient

This limitation is also demonstrated by the fact that for most of our field sites, no trend existed in band ratio values in relation to viewing angle. Instead, it is the shadowing or the irradiance distribution as a function of the surface microstructure and roughness which is the main reason for the anisotropic reflection patterns. The objective of the inversion technique in this thesis is to determine both surface roughness parameters ρ_1 and ρ_0 from normalized reflectance (or reflected radiance) data. In the last chapter it was found possible to estimate the roughness properties following the roughness similarity of equifinal azimuthal strings. However, the method is time consuming as there is a need to determine the correlation for 432 pairs of azimuthal strings. In this section we will explore more efficient ways by trying to invert the parametric models.

A) Model 1

For relating the first model in its parametric or empirical form to a family of numerical problems it is necessary first to generalize its form ; thus it may be rewritten as follows:

$$f'_r = C_0 + C_1\, e^{a\,x} \qquad\qquad [8.3]$$

where x represents $\cos 0.5\,(\Omega + \theta r)$, a represents ρ_1, C_1 represents ρ_0 and C_0 represents $(1 - \rho_0)$ in [8.1].

Equation [8.3] cannot be the starting point for the inversion as most of its components are usually unknowns. If the unknown coefficients C_1, C_0 and a of [8.3] can be defined from data of x and f'_r, and if those coefficients are proven to be expressions of the roughness parameters then the model can be inverted. The problem of determining C_1, C_0 and a of [8.3] from the dependent variable f(x) and the independent variable x is part of the general solution of exponential approximations of the form (Hildebrand, 1956):

$$f(x) = C_0\, e^{a0\,x} + C_1\, e^{a1\,x} + C_3\, e^{a3\,x} + \ldots + C_n\, e^{an\,x} \qquad\qquad [8.4]$$

When the number of the data points exceeds n, the unknown parameters of this equation can be solved using Prony's method. In our case a0=0 , n=1 and the number

of the data points is 27, thus it provides a possible form for inverting model 1 and defining the roughness components from azimuthal strings. A procedure for solving [8.4] using Prony's method is readily available in the IMSL library of mathematical routines. Applying this routine to the simulated azimuthal strings provides three coefficients (C0,C1,a) which were then compared to the real roughness parameters. Results showed that the coefficient **a** from the exponential approximation did not resemble ρ_1 and therefore it is concluded that the inversion of model 1 is not suitable for defining the roughness parameters. Thus, despite the facts that model 1 (described by [8.1]) and its equivalent form (equation [8.3]) have the same general form and both fit the simulated data well, they were not identical. This is explained firstly by the differences in the mathematical procedures used to fit the models to the simulated data: fitting [8.1] to the azimuthal strings is a simple linear regression problem since the non-linearity of f'_r is accounted for by the exponential term in [8.3]. By contrast, Prony's method solves [8.4] by an exponential (non-linear) procedure. Secondly, since for many of the simulated microstructures the reflectance data provide only a limited range of values (limited range of anisotropy), the normalized reflectance predictions by the two models can be similar in this range but diverge substantially outside this range. This explanation is supported by the fact that where there was a wide range of reflectance values (for example for microstructures with low ρ_0 and high ρ_1) the coefficient a of [8.3] as defined by Prony's method was nearly identical to the roughness parameter ρ_1 .

B) Model 2

Unlike the procedure described above, the development of an inversion technique for model 2 will start by exploring the relations between ρ_0 and the coefficients determined for its empirical form. Assuming that ρ_1 is known, Model 2 can be expressed by the following empirical equation:

$$f'_r = C_0 + C_1 e^{\rho_1 + \cos [0.5 (\Omega + \theta_v)]} \tag{8.5}$$

In this form the coefficients C_0 and C_1 can be determined using a regression procedure between the normalized reflectance values given by f'_τ and the independent variable given by the exponential term ($e^{\rho 1 + \cos [0.5 (\Omega + \theta_v]}$). Thus, calculating the two coefficients for the 432 azimuthal strings it is possible to assess the empirical relations between those 432 pairs of coefficients and the corresponding roughness parameter ρ_0 determined for each of the 432 microstructures. The assessment of those relations was done by calculating the correlation between C_0 and (1- ρ_0) and between C_1 and ρ_0 as their values varied following the sequence of 432 azimuthal strings and their corresponding microstructures. The procedure was followed for eight sun elevation angles and the results are given in Table 8.2 . Considering the large number of cases and the fluctuations of ρ_0 following the sequence of the simulated microstructures (see Figure 7.3), both coefficients were found to correlate very well with the changes of the roughness parameter ρ_0 (and its transformation (1- ρ_0)) for sun elevation angles between 20 and 70°. The reasons for the decline in correlation for sun elevation angles larger than 70° are basically similar to those given for the similar phenomenon found in Table 8.1.

Following the good correlation found between the roughness parameter ρ_0 and the regression coefficients C_0 and C_1 (of [8.5]) , their relations can be formalized in the following regression equation:

$$C_0 = C_{01} + C_{02} (1- \rho_0)$$
and
$$C_1 = C_{11} + C_{12} \rho_0$$

[8.6]

[8.7]

As C_{01} , C_{02} and C_{11} , C_{12} were calculated separately for each sun elevation angle it was interesting to find that the change in those coefficients corresponds extremely well to the change of the cosine of the elevation angle (Figure 8.1). This important finding means that for generalizing model 2 to a wide range of sun elevation angles it is possible to add terms to [8.2] which link each of the above coefficents to the cosine of the sun elevation angle.
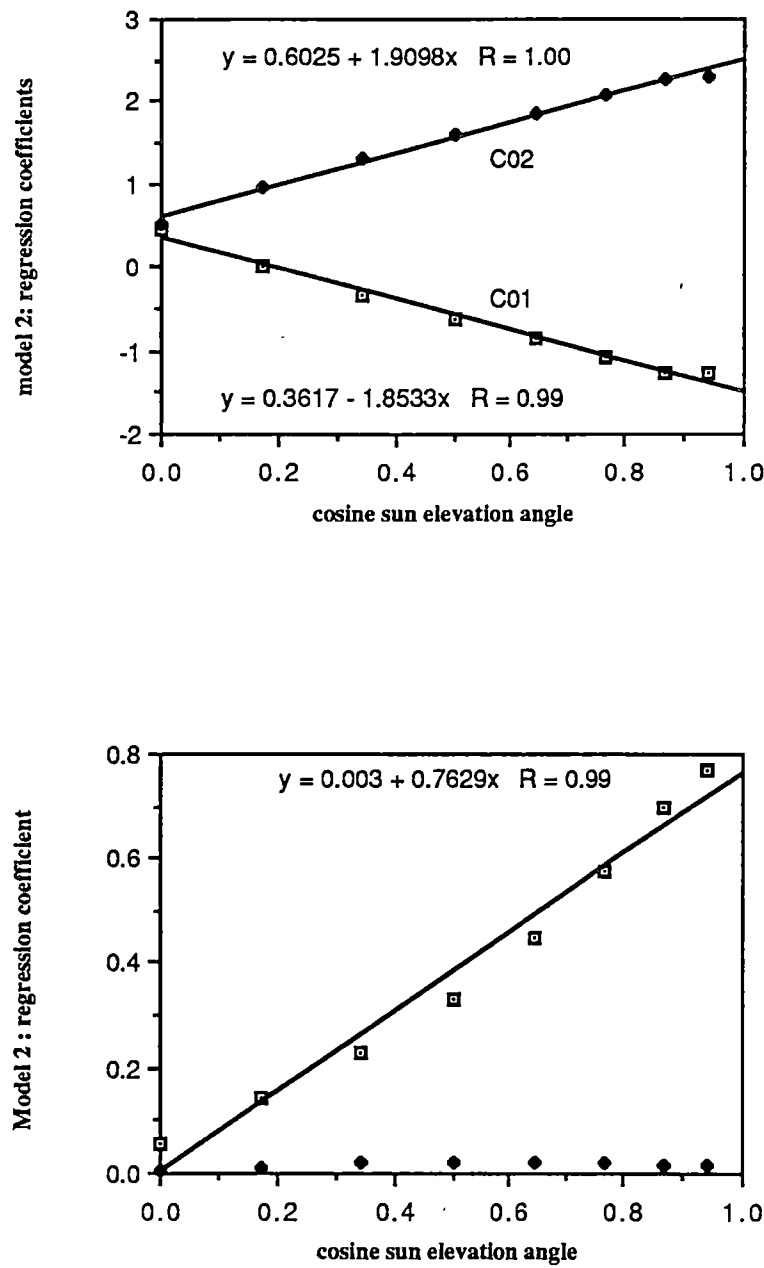
FIGURE 8.1 : The relation between model 2 coefficients and the cosine of the sunelevation angle. The C01, C02, C11 and C12 are the coefficients of equations [8.14] as derived from the regression of [8.6] and [8.7] for the 432 microstructures separately at each sun elevation angle.

The above development established the empirical relations between ρ_0 and the empirical form of [8.2] assuming that ρ_1 is known. In the next step the inversion will be further developed by also determining ρ_1 from a fully empirical version of [8.2] :

$$f_r' = C_0 + C_1 \, e^{\, a+\cos \, [0.5 \, (\Omega + \theta r)]} \qquad [8.8]$$

where C_0, C_1 and a are unknowns.

Since a is a constant for each microstructure and azimuthal string, [8.8] can be rewritten as:

$$f_r' = C_0 + C_2 \, e^{\, \cos \, [0.5 \, (\Omega + \theta r)]} \qquad [8.9]$$

where the exponential term contains only angular parameters describing the illumination / viewing geometry. The phase angle (Ω) can be easily determined knowing the sun and viewing elevation and azimuth angles, while θr can be determined for most of the remote sensing applications from digital terrain models (DTM).

The coefficient C_0 in [8.9] is expected to be identical to the one in [8.5] thus allowing the determination of ρ_0 from their empirical relations as established in Table 8.2 . Once the regression equation of [8.9] is formalized for a set of dependent variables (normalised reflectance data) and a corresponding set of the independent variable (the exponential term of [8.9]), ρ_0 can be derived using the coefficients C_{01} and C_{02} in [8.6]. This is done in the following form:

$$\rho_0 = 1 - (C_0 - C_{01})/C_{02} \qquad [8.10]$$

In the next stage we derive ρ_1 on the basis of the relations between C_1 in [8.5] and C_2 in [8.9] . It can be claimed according to simple mathematical relations between the two coefficients that :

$$C_2 = C_1 \, e^a \qquad [8.11]$$

where both C_1 and e^a are not known.

However, as ρ_0 can be derived using [8.10] and as ρ_0 and C_1 were found to correlate well (as presented in Table 8.2) it is possible to estimate C_1 using the coefficients C_{11} and C_{12} of [8.7]:

$$C'_1 = \rho_0 \, C_{12} + C_{11} \qquad\qquad [8.12]$$

where C'_1 is the estimated C_1.

Then, $e^a = C_2 / C'_1$ and a can be therefore derived by:

$$a = \ln (C_2 / C'_1) \qquad\qquad [8.13]$$

where a is the estimate for ρ_1.

Thus, the inversion procedure for model 2 is based on the mathematical relations which were established between the azimuthal strings (of normalized BRDF), the roughness parameters ρ_1, ρ_0 and independent exponential term ($e^{\cos 0.5 (\Omega + \theta_v)}$) using the simulation data .

As discussed earlier in this section, the coefficients C_{01}, C_{02} and C_{12} defined at each bin of sun elevation angle found to form a linear function with the cosine of the sun's elevation (Figure 8.1). The coefficient C_{11} appears to be of very small magnitude with only a slight variation with a change in the sun elevation angle . On the basis of these findings it is possible to suggest a new general parametric form for model 2 :

$$f'_r = C_{01} + C_{02} (1-\rho_0) + [C_{11} + C_{12} \, \rho_0] \, e^{\rho_1 + \cos 0.5 (\theta_f + \theta_v)} \qquad [8.14]$$

where C_{01}, C_{02} and C_{12} are given by:

$C_{01} = 0.3617 - 1.8533 \cos (\pi/2 - \theta_i)$

$C_{02} = 0.6025 + 1.9098 \cos (\pi/2 - \theta_i)$

$C_{12} = 0.003 + 0.7629 \cos (\pi/2 - \theta_i)$

and C_{11} is negligible.

Equation [8.14] represents the function which is inverted using the technique described above. To summarize the inversion procedure it is developed as follows: we start by calculating the regression coefficients C_0 and C_2 in the fully empirical form of [8.14] given by [8.9], then knowing coefficients C_{01}, C_{02}, C_{11} and C_{12} we derive ρ_0 and C'_1 using equations [8.10] and [8.12] and finally using the empirical coefficient C_2 and C'_1 in equation [8.13] we can derive an estimate for ρ_1.

The assessment of the predictions made for ρ_1 and ρ_0 using the inversion technique of model 2 was carried out firstly on the basis of the simulation data, to be reported in this section, and secondly on the basis of the data collected in the field (to be reported in section 8.4). As presented earlier, the key factor in developing the inversion technique is the strong correlation found between ρ_0 and the empirical coefficient C_0. However as indicated in Table 8.2, this correlation is not perfect and there is a marked decrease in the correlation with increasing sun elevation angle. In this regard it is worth investigating if there are some viewing angles for which the estimate of ρ_0 is more accurate than for other. The coefficient C_0 is the y intercept value of the regression equation [8.9] which can be estimated by the average difference between corresponding values of f_r and $C_2 e^{\cos [0.5 (\Omega + \theta_v)]}$. Thus, relating to the difference given at each viewing angle as an estimate for C_0, it is possible to estimate ρ_0 by :

$$\rho_0 = 1 - (f'_r - C_2\, e^{\cos 0.5 (\Omega + \theta_v)} - C_{01}) / C_{02} \qquad [8.15]$$

where C_0 in [8.10] is replaced by the term $f'_r - C_2\, e^{\cos 0.5 (\Omega + \theta_v)}$ separately for each interval of $(\Omega + \theta_v)$ following the change in the viewing angle .

Since ρ_1 is approximated using [8.12] on the basis of the approximation for ρ_0 the assessment of the accuracy of the inversion predictions for ρ_0 and ρ_1 is done separately for each viewing angle.

Two measures, the average and the root mean square error (RMSE) of the inversion predictions for each of the roughness parameters of the 432 different simulated microstructures, were calculated for each of the viewing angles (Figure 8.2). That

process was repeated for each sun elevation angle and the results are presented in Figure 8.3 .

A typical pattern of change in the error statistics with varying viewing angle was found for each of the four error measures:

-The $\rho 1$ average error is characterized by a U shape: maximum negative error for viewing angles between 60° and 80° and maximum positive errors for viewing angles lower than 50° and higher then 130°. That U shape is flattened as the sun elevation angle increases from 20° to 60° and then turns upsidedown for sun elevation greater than 60°. The accumulated average error for all viewing angles was found to be close to 0 at most of the sun elevation angles.

- $\rho 1$ RMSE is characterized by a W shape with minimum errors approximately at 50° and 130° . That pattern changes to indicate minimum errors for viewing angles between 70° and 90° when the sun elevation is greater than 60°. The average RMSE is around 0.2 for sun elevation angles lower than 70°, and their magnitude increases considerably for higher elevation angles .

-The ρ_0 average error has the opposite pattern to the one found for the average $\rho 1$ error.

—The ρ_0 RMSE has limited variation with viewing angles and its average level changes from 0.08 at 20° sun elevation to 0.15 at 70°.

The above roughness error statistics are similar to those obtained in the last chapter and they indicate that the inversion technique for model 2 is generally successful.

The patterns of roughness error outline two regions (50° for backward and 130° for forward reflection) which provide consistently best inversion results. These directions have a significant low level of errors for all four measures at sun elevation angles of 20° to 60°. While the backward direction shifts from 40° to 65° with increasing sun elevation, the forward direction shifted from 125° to 150°. General expressions which indicate the optimal forward and backward directions as a function of the sun elevation
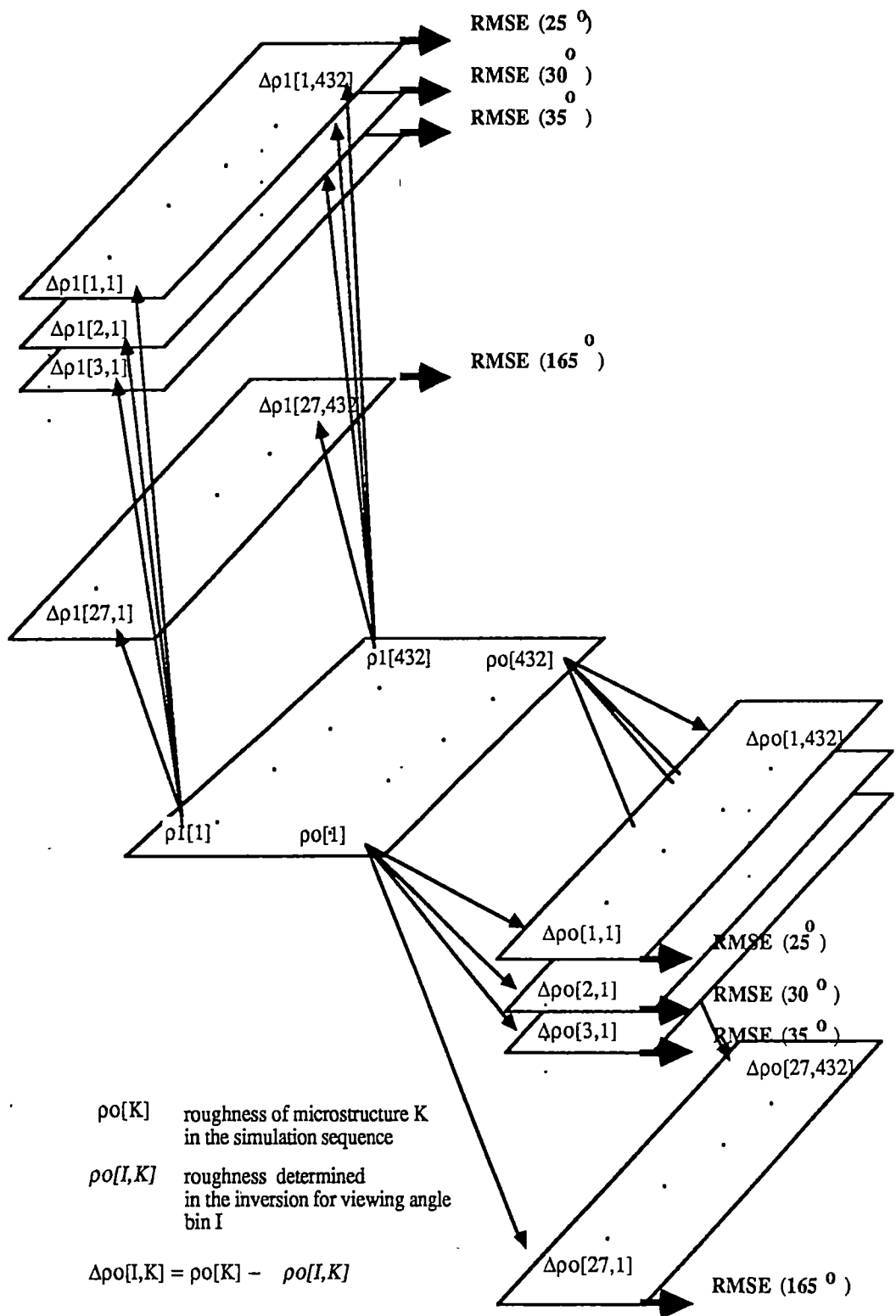
FIGURE 8.2 : Diagram representing the process of organizing the data base for calculating the inversion roughness RMSE at each viewing angle: arrows connect the roughness attached to every of the 432 microstructures with roughness error determined for the corresponding inversion prediction at each of the 27 bins of viewing angles.

angle (θ_h) can be written as:

$$\theta_{opf} = 0.5 \ (\theta_h - 20) + 125^o \qquad\qquad [8.16]$$

$$\theta_{opb} = 0.5 \ (\theta_h - 20) + 40^o \qquad\qquad [8.17]$$

However, these optimal directions may be a general phenomenon or linked to the methodology implemented for inverting the reflectance data. As can be observed in Figure 8.4, the errors of the parametric model 2 in predicting the normalized reflectance are of extremely low level relative to the roughness errors. Assessment of the distribution of model errors in predicting the normalized reflectance values at the different viewing angles shows that there is a high level of cross-correlation between the series of normalized reflectance errors and that of roughness errors (mainly for $\rho 1$ RMSE), especially at sun elevation angles of 20° and 30° . However, it is difficult to judge whether the inversion errors are due to the model errors (in which case those angles are optimal only methodologically) or the model and inversion errors are both due to the insensitivity of the reflectance to the roughness in these regions of high errors. If the second scenario were to apply then the angles exhibiting the lowest RMSE in Figure 8.3 would in fact be the optimum viewing angles.

The hypothetical explanation in support of the generality of the results is that the microstructure components of the surface create their best pronounced effect on the reflectance field in directions where it is either defined by the strong reflectance in the backward reflection or by the shadowing effect in the forward direction, while in the nadir direction the reflectance is an insensitive average of reflectances of the shadowed and highly irradiated facets.

8.3 A comparative study of roughness derived through inversion and through field measurements

For each field site the roughness parameters were derived twice : once by applying the inversion technique for the measured azimuthal strings and secondly by determining
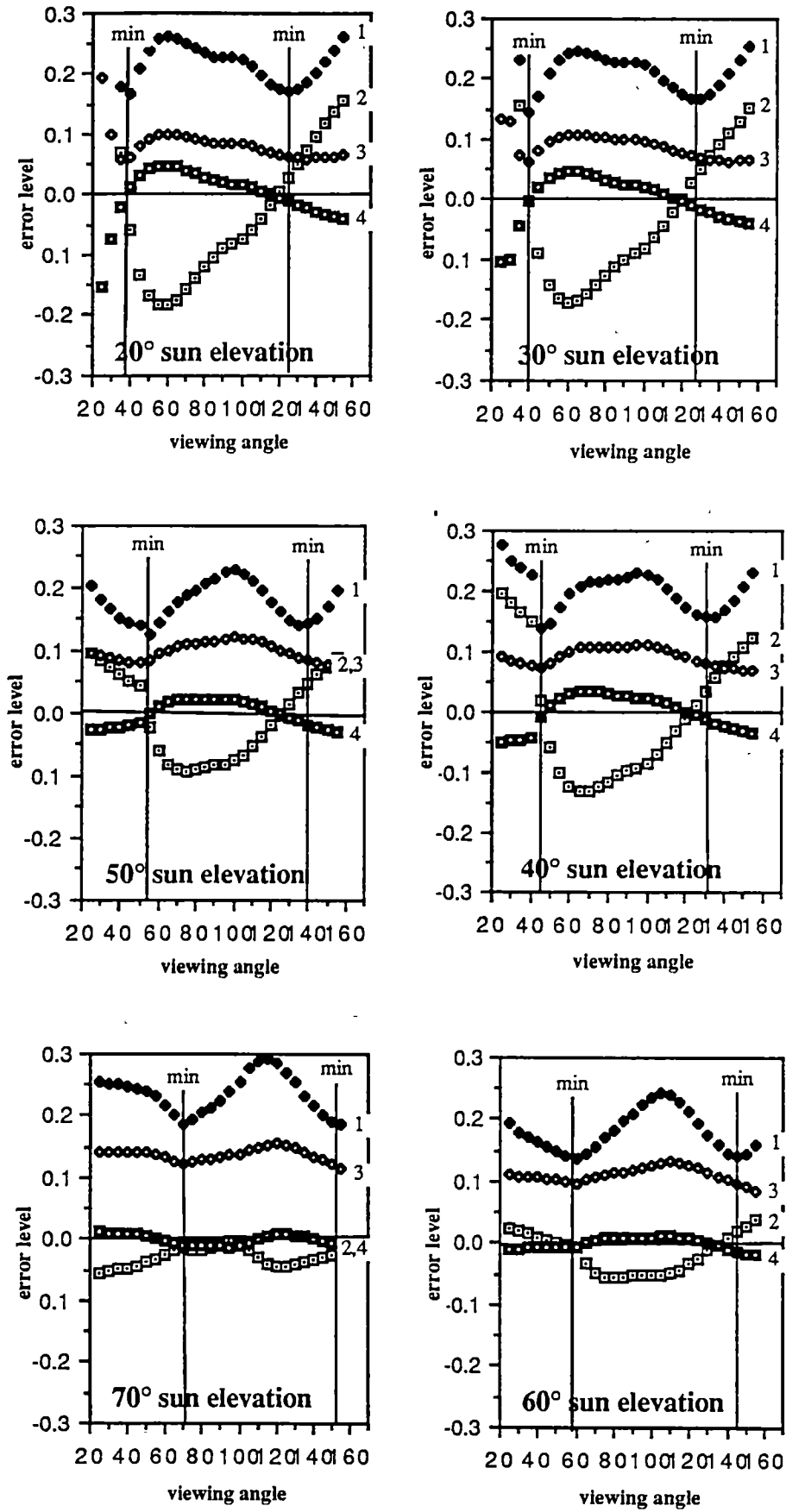
FIGURE 8.3 : Error curves for roughness predicted by the inversion technique: ρ_1 RMSE (1), ρ_1 average error (2), ρ_0 RMSE (3) and ρ_0 average error (4) for 27 viewing angles between 25° to 155°.
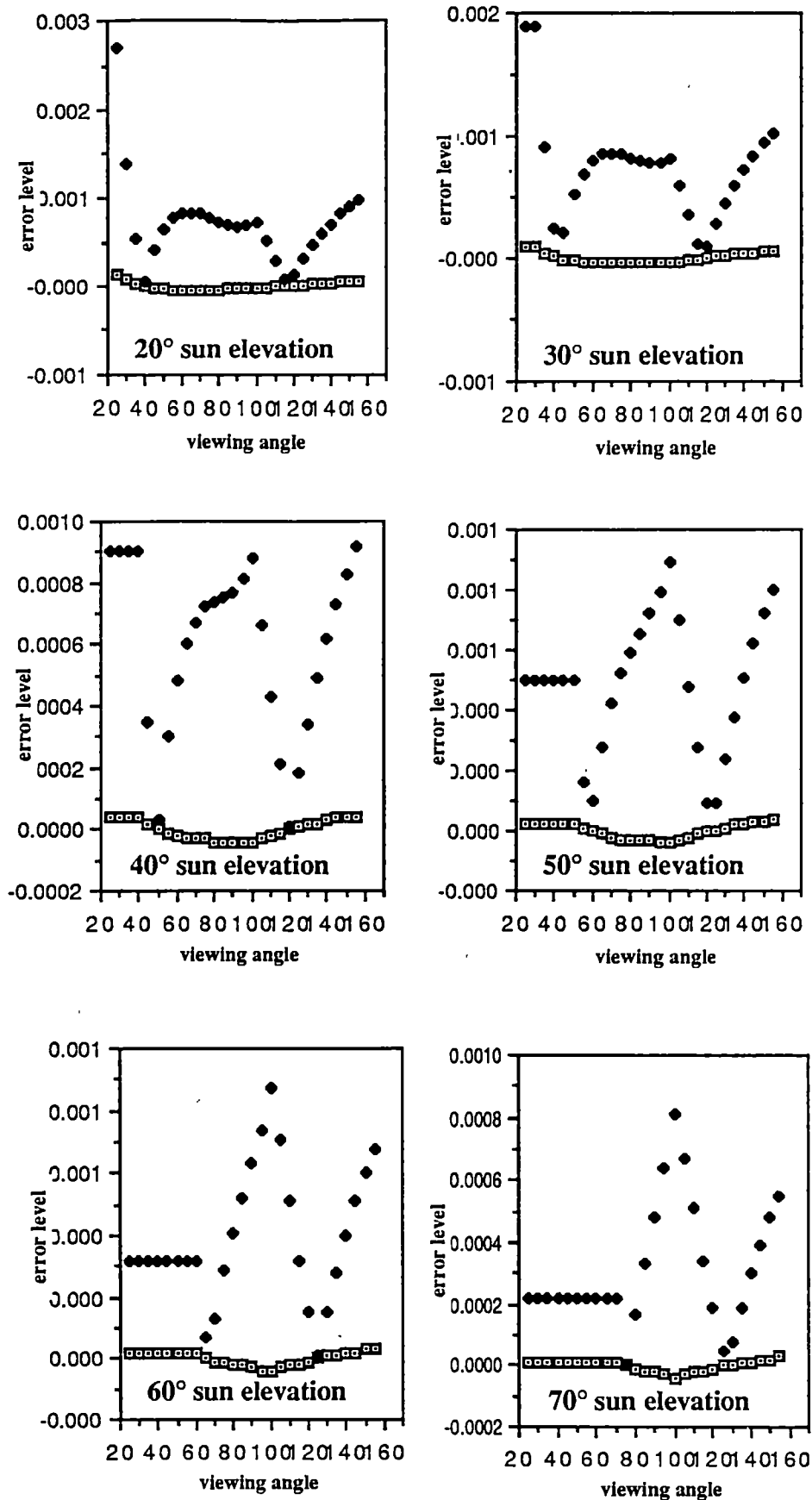
FIGURE 8.4 : Normalized reflectance error of model 2 predictions (equation [8.14]) for the simulated data as derived for 432 azimuthal strings separately at 27 viewing angles between 25° and 155° and repeated at six different sun elevation angles : (1) average error and (2) RMSE.

them from the field measurements of the mean size and sphericity of the pebbles and the mean distance between them in 9 azimuthal directions (which correspond to the 20° azimuthal intervals of the reflected radiance measurements). There are a few limitations set on a comparison between the inversion predictions and the field measurements:

- Whilst the simulation data describes the reflectance distribution for specific structural elements, the real sites exhibit forms which are built of nesting structures where shapes of smaller size appear on larger ones. For example, sand ripples may be built of smaller ripples built of particles assembled on the surface in different forms and with different texture (shape and roundness of the particles themselves). Another implication of this situation is that the reflection for the sites built of smaller forms is not isotropic.

- The accuracy of field measurements is limited by the precision of the observer and the apparatus specifications. For example :

     -the removal of shadows from the HDRM data, specially in the sun's azimuthal plane.

     - the resolution of the roughness digitiser was limited to 3 mm, therefore not representing forms of smaller size.

In view of these limitations it is unrealistic to expect the roughness parameters determined through the inversion to be identical to those defined through field measurements. It is also difficult to determine which set of measurements is more adequate. However, it is important to compare the two data sets as they are independent measures of the same phenomenon. A major requirement of the roughness parameters is to have sensitivity to the microstructure as referring to the largest forms within the field of view; thus, differences between surfaces must be expressed by the parameters defined through the inversion. The four model sites (see Figure 5.12) represent three totally different microstructures : dense raws of pebbles (site 2.1), sparse rows of pebbles (site 1a) and artificially built sand ripples (sites 17 and 18).

The mapping of the roughness values obtained through the inversion process indicates that the three types of surfaces are separable in the 2-D roughness space (Figure 8.5). However, it was apparent that despite the marked directionality of all three patterns the values did not vary with the change of the sun azimuth as much as

would be expected. For example: while the sun azimuth relative to the pattern of ripples of site 18 changed from nearly perpendicular to the ripples to 15° from the ripples direction, it was expected that in the latter position the roughness values would indicate a flat surface but that did not happen. A close examination of the situation showed that at the same time the sun elevation angle decreased to 25° and that the facets away from the sun (only by 15° in azimuth) were receiving a very low irradiance compared to those facing the sun. Thus, a relatively high anisotropy level was apparent in the reflectance data. A similar example occurred for the case where the sun azimuth was in the same direction as the sand ripples with an elevation angle of 50°. There was still a marked level of anisotropic reflection leading again to relatively high predicted roughness values as found for site 17. However, this anomaly might be explained by roughness at the scale of the particles size. It was found that when the sun azimuth was perpendicular to the direction of the structure, the predicted roughness was lower than expected (specially for the ρ_0 parameter). This phenomenon might also be explained by the smaller size forms causing some shadows behind the sun facing facets, thus reducing the level of anisotropy that would be expected if the facets were smooth. To summarize: in the case of directional pattern of the microstructure we observed an overall reduction in the range of predicted roughness values by the inversion relative to the expected range. This is mainly a result of the existing roughness on the facets of the microstructure which causes the reflection from the facets to be anisotropic. That anisotropy on one hand increases the predicted roughness when the sun azimuthal plane is parallel to the direction and on the other hand decreases the level of anisotropy when the sun azimuth is perpendicular to the microstructure direction.

It was found for the artificial experimental sites that the average roughness values determined through the inversion technique were very similar to the average values determined by the direct measurements in the field.

The stony sites presented us with a few additional difficulties. Firstly, it was not possible to derive the 'real' roughness for the stony plains sites since it involves the need to give different weight to each of the spectral classes (the roughnessas there was a mixture of quartz and quartzite pebbles with different reflection characteristics).
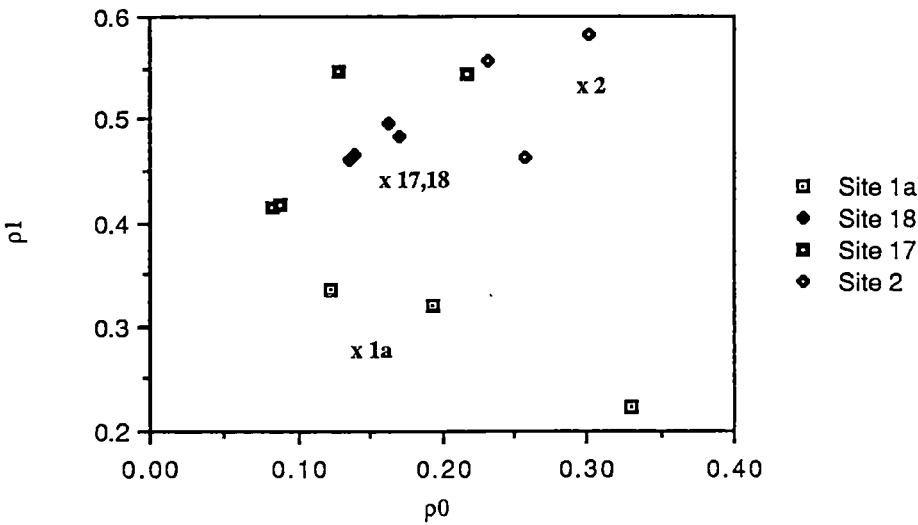
FIGURE 8.5 : Mapping the roughness parameters determined through the inversion for each site at different sun azimuth and zenith angles in the two dimensional roughness space together with the average roughness determined from direct field measurements surface model sites (marked by x).
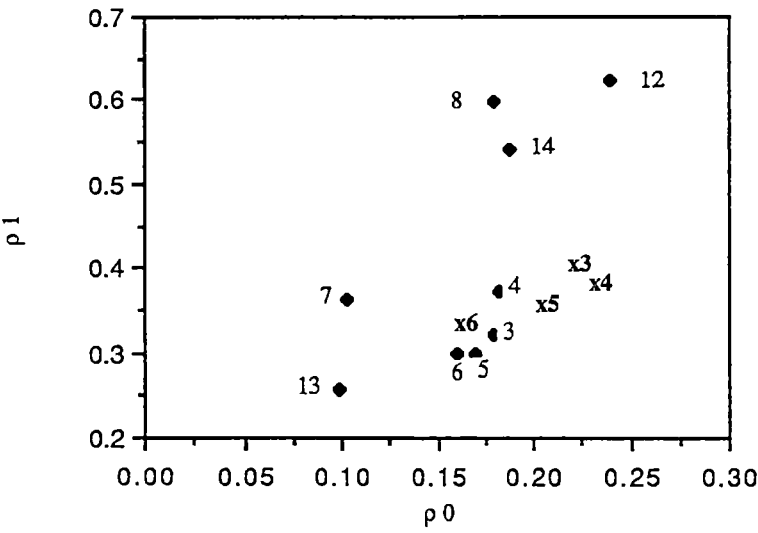

FIGURE 8.6 : Mapping the average roughness parameters determined through the inversion for each site in the two dimensional roughness space together with the average roughness determined from direct field measurements of stony plains sites (marked by x).

Secondly, there was a large variation of sun zenith angles between successive measurements of reflected radiance of each site; consequently some of the angles of incidence were outside of the optimal angles (between 40° and 60°) and the roughness values given by the inversion varied considerably between measurements of each site by 30%. To allow comparison between the sites we therefore again used the average values for all measurements of a site. Figure 8.6 presents the roughness values derived for each of the stony sites. The variation of the values indicates that the stony plains sites split into two groups: one of sites 7 and 13 which represents low level of roughness and the second group of sites 8, 12 and 14 which represents relatively high level of roughness. The stony slopes sites (3,4,5 and 6) presented a cluster of values in an intermediate level of roughness . A comparison to the roughness values derived from the field measurements indicated that there is good similarity between the two sets. The values derived from the field measurements showed a slightly higher level of roughness than those derived using the inversion technique.

8.4 The assessment of the inversion process with a limited range of viewing angles

As most of the remote sensing systems provide a much limited range of viewing angles (usually less than +/- 65° off-nadir angles), there is a need to assess the applicability of the inversion process to the existing viewing geometries. In this section the best roughness accuracy that can be achieved in three ranges will be explored. These ranges are: +/- 30°, +/- 40° and +/- 50° as measured relative to the nadir direction. Following the identification of the two optimal regions of viewing angles, the accuracy of the inversion will be assessed at the extreme angles in both the backward and forward directions.

The procedure applied was identical to that described for deriving the roughness RMSE for model 2 predictions at each viewing angle separately (in section 8.3). The differences were firstly that the regression developed to define coefficients C_0 and C_2 of [8.9] was based on the part of the azimuthal strings which corresponds to the

TABLE 8.3 : Roughness (ρ1) RMSE at optimal viewing angles for four viewing configurations

Sun zenith Viewing configuration	20°	30°	40°	50°	60°
+ / - 65°					
backward	0.16752	0.14563	0.13702	0.12529	0.13712
forward	0.17159	0.16794	0.15712	0.14244	0.14101
+ / - 50°					
backward	0.16799	0.16024	0.14537	0.13250	0.14396
forward	0.17303	0.16147	0.14435	0.13060	0.13816
+ / - 40°					
backward	0.17700	0.16672	0.15012	0.13872	0.15444
forward	0.18147	0.16893	0.14816	0.13017	0.14208
+ / - 30°					
backward	0.21233	0.20310	0.17962	0.15766	0.16788
forward	0.20075	0.19300	0.17117	0.15084	0.16265

range of viewing angles under assessment and secondly that the roughness RMSE calculations were limited to the extreme angles in each range.

The roughness RMSEs found for ρ_1 at each of the assessed ranges of viewing angles (once for the backward and once for the forward extreme angles) are presented in Table 8.3 for sun elevation angles between 20° and 50° (data for ρ_0 exhibit identical trends and therefore are not included in Table 8.3). There is an increase in predicted roughness error level with reducing the range of viewing angles and it is particularly noticeable in the $+/-30^o$ configuration. The magnitude of predicted roughness error for the $+/-50^o$ and $+/-40^o$ is not large enought to suggest that the range $+/-65^o$ is much preferable to the other ones in terms of costs involved in increasing the range of viewing angles relative to

the increase in efficiency.

These results are therefore very useful since they provide a clear indication of the reduction in accuracy involved in reducing the range of viewing angles.

8.5 Discussion

This chapter presented the development of two parametric models for describing the directional distribution of normalized reflectance (or normalized reflected radiance) along the sun azimuthal plane and their inversion . We included the description of model 1 despite the fact that the inversion technique developed was not successful since it is believed that this model and its inversion could be further developed in future work. The importance of the inversion technique developed for model 2 is in two areas: firstly by providing a method for deriving average surface roughness from its reflectance distribution, and secondly by suggesting a possible way to extrapolate for reflectances at other viewing angles and sun azimuth and elevation angles on the basis of a limited range of directional reflectance data. Once the roughness parameters of the surface are determined through the inversion of one or a few azimuthal strings, it is possible to use these values in the parametric model to predict the normalized reflectances for other azimuthal strings. The errors that would be associated with those predictions may be expected to be low because of the BRDF equifinality phenomenon.

More work is required for extending the model to viewing angles outside the sun azimuthal plane. Such development involves the study of the change in normalized reflectance as a function of the viewing angle (θ_v), the phase angle (Ω) and the surface roughness properties.

The analysis of the roughness predicted by inversion relative to that derived from direct measurements exemplified how limited direct measurements are in providing data adequate for reflectance modelling. Consequently, it may be suggested that the roughness measures derived from reflectance distribution represent well the integration of the roughness with scale, where smaller shapes are superimposed on larger ones at a range of scales.

CHAPTER 9 : SUMMARY AND CONCLUSION

This chapter summarizes the study in three sections : the first section discusses the methodologies and apparatus developed for providing suitable data. The second section summarizes the results of the analysis within the framework of the research objectives, hypotheses and questions stated in Chapters 1 and 2. The third part assesses the results within the larger framework of present and future research needs.

9.1 Methodologies and apparatus developed

The following experimental designs and related methodologies were developed as part of this thesis:

- A methodology and apparatus for measuring the external secondary reflection effect (described in Chapter 3 and in Shoshany (1989A)) was designed. It provided, for the first time, an objective assessment of the effect of multiple reflections between facets on the upwelling radiance. The difficulty in measuring the secondary reflection effect (SRE) stems from the inseparability of the primary and secondary components of the reflected radiance. In this study, a method was devised to block the external type of secondary reflection without changing the geometry of the scene. This procedure made it possible to measure the radiance both with and without the effect.

- A methodology and apparatus was designed for measuring the directional distribution of reflected radiance from a target of limited area in field conditions. Most of the existing apparatus is built for measurements over homogeneous terrain (Deering and Leon, 1986), which is not particularly suitable for the heterogeneous environment of bare stony surfaces and stony slopes. The apparatus built in this study for conducting Hemispherical Directions Radiance Measurements (HDRM) is capable of limiting the spread of the sensor field of view to an area of 2.5 m radius while changing the viewing angle from nadir to 65°. A full hemispherical set of measurements including data over 235 directions in four different spectral bands can be accomplished within less than 3 minutes. The HDRM used a Delphi radiometer developed by the DSIR of New Zealand

(Ellis and Nankeville, 1985) with an interface developed in the Central Science Laboratory of the University of Tasmania to enable the logging of large amount of data within a short span of time. A comparison between the HDRM and the PARABOLA system developed in NASA (Deering and Leon, 1986) showed that the latter is superior in term of the speed of data collection but inferior to the HDRM in terms of the target configuration, the amount of hemispherical data collected and the simplicity of design.

The HDRM provided the only economical way, dictated by research budget constraints, to gather the necessary amount of data. The total costs involved in constructing the apparatus using the existing radiometer and data logger, together with the field work expenses, were less than the costs involved in purchasing two SPOT images.

- A methodology and apparatus were developed for measuring surface roughness properties in field conditions. The roughness digitiser (described in Chapter 4 and in Shoshany (1989 B)) proved to be an efficient tool for collecting data regarding the shape and density of pebbles on the surface within a short time interval. The field digitizer has since been found useful for field measurements in sedimentology , geomorphology , and even in biogeography / botany for field measurements of vegetation growth rates (of Sphagnum moss for example).

- A simulation model has been designed to calculate the BRDF of a large number of microstructures (432) exhibiting different forms and roughness conditions. The method (described in Chapter 6 and in Shoshany (1989 C)) is based on a set of simple equations developed for estimating the irradiance, shadowing and obstruction for each facet of a particular microstructure . Most of the existing methods were developed for specific microstructures and therefore are limited in providing data suitable for the assessment of equifinality. The method is also much more efficient in terms of processing time than equivalent techniques using a Monte Carlo simulation method.

9.2 Roughness and BRDF relations: pre- and post-equifinality

The two primary research objectives are not independent and they were both developed in two separate stages in this work. The first stage is the pre-equifinality one

which takes the deterministic view of roughness microstructure as a starting point, with the accumulation of evidence suggesting that roughness microstructure and BRDF do not have a one to one correspondence. The second stage is the post-equifinality one which attempts to determine surface roughness parameters which are reflectance oriented and therefore relate mainly to the amount of shadowing occurring within the cavity between two roughness elements . In other words, the two major research hypotheses are tested twice during the research, firstly with a deterministic roughness approach and secondly with roughness cavity parameterisation approach.

First objective

The first objective concerns the assessment and modelling of the effect of roughness on the reflected radiance field. Following the review of the literature in Chapter 2, two alternative hypotheses were established. They suggested that there is either a one to one correspondence between the roughness microstructure and the BRDF or that more than one microstructure can produce the same BRDF. Three questions were formalised in an attempt to resolve the contradictions between the two hypotheses. Our discussion is focused on these three questions:

1. What is the role of multiple reflections in determining the reflectance field?

It was important to assess the role of multiple reflections (secondary reflection effect) since potentially it may mask the effect of the microstructure on the distribution of reflected radiance. This work provided the first empirical assessment of the phenomenon and the results suggested the following:

- Secondary reflection effect depends on the surface roughness, the valley planes' slope and aspect, the sun angle of incidence and the surface anisotropy level. Certain combinations of these factors may result in a relatively high SRE.

- An assessment of the secondary reflection effect on a facet in the meso and macro scales must consider its roughness (or particulate nature), as the roughness further attenuates the SRE. In other words, the modelling of the SRE has to be based on at least two levels of roughness: the level of the facet's orientation toward each other and the level of the individual facet roughness. Predictions of the SRE at these scales by

some of the the existing models (Ferencz et al., 1987) were overestimated as a result of considering the facets to be smooth .

- The modelling of the interaction of light with the surface at the microscopic scale (scale equivalent to the incident radiation wavelength) must include the SRE since it may help in explaining the observed isotropic reflection from rough surfaces at low viewing angles where theories based on the assumption that the scattering at this scale depends on the distribution of the specularly reflecting microfacets do not hold.

2. What are the directional and hemispherical characteristics of radiance reflected from bare terrain ?

There is only a limited amount of BRDF measurements reported in the literature for natural bare terrain (Table 2.2) and most of those measurements were not accompanied by a detailed study of surface roughness. The apparatus and methodologies which were developed in this work allowed concurrent study of the radiometry and morphometry of natural bare terrain in a desert environment near the Fowlers Gap Arid Zone Research Station . More than 100 hemispherical data sets were collected for 14 sites, with 9 of the sites being sampled at three different locations, thus providing an average of 3 hemispherical measurements of reflected radiance for sun zenith angles between 65° to 15° for each location. This data set is, to the best of our knowledge, the first of its type in Australia in particular and one of the most detailed measurements of reflected radiance over bare surfaces in general.

Most of the hemisperical data sets (see reflectance maps in appendix A) exhibited a pronounced level of anisotropy with a major component of backscattering and a secondary component of forward scattering (mainly for sites with exposure of quartz particles on the surface). The anisotropy reflection factors (as the ratio between maximum and normal reflection) were found to range from 1.7 at large zenith angles and to nearly 1.0 (isotropic reflection) at sun zenith angles smaller than 20° . An attempt to link the anisotropy level to surface roughness properties such as mean pebble size, mean pebble sphericity or percentage stony cover, indicated that the anisotropy level is not necessarily related to those properties. On the other hand, the directionality of the roughness patterns of the model sites was well expressed in the hemispherical

data.

The hemispherical reflectance factors calculated from the reflected radiance distributions and the irradiance measurements were found to be similar to those measured for desert terrain by Otterman (1981) and others and ranged from 0.16 for band 4 (0.5 to 0.6μ) to 0.50 for band 7 (0.8 to 1.1μ). The hemispherical reflectance was found to increase with an increase in the sun zenith angle, similar to the results provided by Coulson and Reynolds (1972) and Eaton (1976).

Band ratio distributions were found to exhibit a very limited variation between viewing directions and also at different sun zenith angles. However, ratios with band 4 were found sensitive to the percentage of quartz cover as quartz pebbles have the most pronounced contrast to the soil's spectral response. It was also found possible to use band ratio for separating between stony plains and stony slopes thus indicating a potential use of the band ratios for mapping land systems.

A simulation method was developed for extending the scope of the investigation by calculating the BRDF along the sun's azimuthal plane for 432 types of microstructure. The level of anisotropy changed considerably between the microstructrure with anisotropy factors over 3.0 (which were found for microstructures built of thin parallel high walls) and those with relatively flat types of roughness elements.

3. What is the level of sensitivity of the BRDF to changes in the surface microstructure? Existing theory and data together with results from our simulation model indicated that the surface microstructure is an important source of anisotropy. However , there was also evidence suggesting that the BRDF is not sensitive to surface properties such as the shape of the particles and their density on the ground. A full empirical assessment of the question could not be practically achieved on the basis of field measurements because of time limitations, problems involving the search for a representative number of sites which resemble a wide diversity of roughness properties within a reasonable size of area, accuracy limitations set on the collection of both radiometric and morphometric data in field conditions and difficulties due to the logistics of such a large operation. The alternative was the use of the above described methodology for simulating the BRDF along the sun's azimuthal plane for a large number of different microstructures. The

sensitivity of the BRDF to changes in microstructure was tested by examining the similarity between two BRDFs of different microstructures. If the BRDFs (in the sun's azimuthal plane) were found highly similar than they were called equifinal since the situation denoted similar outcome of similar processes acting on different surface conditions. It was found that a relatively large number of microstructures (more than 40 from 432 on average) exhibited BRDF equifinality. An investigation of the equifinal cases revealed that none of the six parameters describing the microstructure can be regarded as a major reason for equifinality. In other words, none of these parameters were found equal for a substantial number of cases of equifinality between pairs of microstructures. Further testing of the equifinality was carried out by searching for simulated microstructures having similar BRDF to those acquired by field measurements. All of the field measured BRDFs (azimuthal strings) were found to have at least ten equifinal microstructures, each representing a marked difference in terms of structural combination. The inevitable conclusion from these findings was that the second hypothesis is accepted.

Second objective

The second objective formalized the roughness parameters which represent properties of the surface irregularities that mostly influence the reflectance. The analysis also developed a reflectance model which linked the roughness parameters with the reflectance distribution. An inversion technique was also developed for determining the roughness from bidirectional reflectance distribution in the sun plane.

The analysis began by recognizing the importance of the cavity of the microstructure in determining the backscattering and shadowing properties of the surface. Two roughness parameters were chosen for describing the cavity : its relative area and depth. Both parameters were formalized in such a way that they account for some of the structural combinations which are responsible for the BRDF equifinality . The representativeness of these roughness parameters was examined by looking at their similarity between microstructures which exhibit BRDF equifinality (equifinal microstructures). An analysis of such similarity revealed that equifinal microstructures

were similar in terms of the two proposed roughness parameters within certain ranges which dictated the classification of each of the parameters to between three and four levels of roughness. .

Following the formalization of the roughness parameters, the work involved development in two phases. In the first phase a model was developed which linked the directional distribution of the reflected radiance to the surface roughness. The second phase formalized an inversion technique for the model. A simple reflectance model was found to represent well the variation of the normalised BRDF along the sun's azimuthal plane for sun zenith angles between 70° to 20° . An empirical expansion of the model to include other viewing directions in other azimuthal planes is a relatively simple numerical task (Kimes et al. ,1987). However future research effort has to be made to expand the model in its parametric form . Such expansion is needed to further improve of hemispherical reflectance factor estimates using satellite data and of the derivation of surface roughness properties from bidirectional reflectance data. The model is invertible and assessment of the roughness predictions from the inversion on the basis of the simulation data revealed the same level of accuracy as found in the analysis of the roughness similarity between equifinal microstructures. Analysis of the inversion prediction with the field data added an insight to the problem since the field sites presented surface irregularities in many scales. It was found that the mean roughness values determined from the inversion in a few different sun zenith and azimuth angles corresponded well to values determined from field roughness measurements.

The above discussion summarises the answer to the fifth research question regarding the substance and quality of the roughness information that can be derived from BRDF data. In the process of developing the inversion and assessing its accuracy, the sixth research question was answered regarding the identification of viewing angles which are most sensitive to the surface roughness . It was clearly demonstrated that the two viewing directions of +/- 50° (on average) from the surface normal direction are more sensitive than others to the roughness effect. This result is important and should be considered in the designing process of future remote sensing systems.

9.3 Implications and contribution to the present and future research

One of the most important results of this study it to show the extent of BRDF equifinality and its effect on the interpretation of surface properties from reflectance data. The possibility of similarity of BRDF for different surface conditions has been noticed previously (see for example, Norman et al.,1985). However, there had been no attempt to study the extent and implications of this phenomenon for albedo studies and remote sensing applications. Equifinality is a result of two combined sources: firstly, the non linearity in the way that different parameters interact and influence the reflectance field and, secondly, as a result of the simplification involved in modelling and measuring complex properties such as leaf distribution, surface roughness, trees structure, their spatial distribution etc. It is also likely that equifinality applies to vegetation surfaces and may have serious implications on the interpretation of inversion results developed for these surfaces. Many inversion techniques (Goel and Grier, 1986, 1988; Nilson and Kuusk, 1989) are based on the minimization of the deviations between sets of predicted and measured reflectances by adjusting the parameters of the reflectance model in a certain way. The problem is then one of how to evaluate different combinations of the model parameters which produce similar bidirectional reflectance distributions.

The confusion in the signals resulting from spectral mixtures (Townshend and Hanson, 1981; Fraser et al.,1987) is also a source of equifinality. Class separability may be achieved by further increasing the spectral resolution of the sensor and the number of bands. However, discrimination will not be achieved when the equifinality is due to roughness differences, as increasing the spatial resolution is not expected to solve the problem in the general case. This is because the same roughness can be obtained by forms of different scale .

A second important outcome of this study is the formalization of roughness parameters which are related to surface reflectance properties, via a parametric model of the roughness / reflectance relations and the development of an inversion technique. The parametric model presented here is very simple in its form and was found to be able to predict accurately the normalised reflectance in the sun's azimuthal plane. Once the

roughness of the surface has been determined, using the proposed parametric model, it becomes possible to predict the normalised distribution of reflected radiance along the sun's azimuthal plane for a range of sun zenith angles and thus assisst in determining the surface albedo and its yearly and daily variation.

In an early work, Eaton (1976) developed indicatrices which account for the anisotropy reflection of the surface when calculating the hemispherical reflectance from the reflected radiance into the nadir direction. It was suggested that there could be groups of " ... surfaces that exhibit similar indicatrix patterns". As surfaces with similar roughness can be expected to have similar indicatrices, this present work provides a framework by which the classification of surfaces into such groups can be achieved.

The determination of surface roughness from the distribution of its reflected radiance may aid in terrain classification and its temporal change. For example, following flooding events, desert surficial deposits may experience roughness changes (Cooke and Warren, 1973; Mabbut, 1977) detectable by inversion techniques. Furthermore, the usefulness of this inversion technique is emphasised by the fact that it is independent of the spectral changes which can be of considerable magnitude between seasons or following rain events in the desert.

The removal of pixel to pixel brightness variations due to changes in roughness, illumination (due to topography) or viewing geometry in satellite or airborne images is an essential step prior to the application of classification techniques. The problem of removal of such variation is even more important in applications for mineral exploration where the mineralogical responses are, according to Fraser et al. (1987), insignificant compared to the above mentioned sources of variation.. Since many mineral exploration projects rely on airborne devices such as the Daedalus 1268 ATM scanner with +/- 37° off-nadir viewing angles, there is the potential to account for some of the brightness variations by estimating the roughness using this inversion procedure. Once the roughness is known, the amount of shadow in the sensor field of view can be obtained from the calculations made for one of the microstructures with the same roughness properties using the equations developed in Chapter 6.

Future improvements in satellite instrumentation, which will provide wide range of viewing angles will have to be accompanied by the development of methods for utilizing off-nadir reflection for improving the determination of surface properties from remote sensing data . It is hoped that this study will help in that direction.

BIBLIOGRAPHY

Ahmad, S.B. , Lockwood, J.G., 1979, Albedo. *Progress in Physical Geography* , 510-543.

Atlas of Australian Resources. Third Series, 1986, Climate, Vol. 4. Div. of National Mapping, Canberra.

Atlas of Australian Resources. Third Series, 1980, Soils and Land Use, Vol. 41 Div. of National Mapping, Canberra.

Barnsley, M. J., 1984 , Effects of off-nadir view angles on the detected spectral response of vegetation canopies . *Int. J. of Remote Sensing*. **5**, 715-728.

Beavis, F.C., and Beavis, J.C., 1984, Geology, engineering geology and hydrogeology of Fowlers Gap Station. *Research Series* No. 6, University of New South Wales.

Becker, F., Ramanantsizehena, P. and Stoll, M., 1985, Angular variation of the bidirectional reflectance of bare soils in the thermal infrared band. *Applied Optics*, **24**(3), 365-375.

Beckmann, P. and Spizzichino, A., 1963 ,*The scattering of electromagnetic waves from rough surfaces*. Oxford: Pergamon Press.

Bell, F.C., 1972, Climate of the Fowlers Gap - Calindary area. In: Lands of the Fowlers Gap - Calindary area, New South Wales. *Research Series* No. 4. The University of New South Wales.

Bellis, S.E., 1986, Remote Sensing in New Zealand: a status report. In: *Remote Sensing Yearbook 1986*, Cracknell, A., and Hayes, L., (Editors). Taylor & Francis, London.

Berry, E.M., 1923, Diffuse reflection of light from matt surface. *J. of the Optical Society of America*. **7**, 627.

Bird, R.E., and Riordan, C., 1986, Simple solar spectral model for direct and diffuse irradiance on horizontal and tilted planes at the Earth's surface for cloudless atmospheres. *J. of Climate and Applied Meteorology*, **25**, 87-97.

Brennan, B., and Bandeen, W.R., 1970, Anisotropic reflectance characteristics of natural Earth surfaces . *Applied Optics* **9**, 405.

Bruhl, C., and Zdunkowski, W., 1983, An approximate calculation method for parallel and diffuse solar irradiances on inclined surfaces in the presence of obstructing mountains or buildings. *Archives for Meteorology Geophysics and Bioclimatology*, **B32**, 111.

Budyko, M.I., 1974, *Climate and Life.*, Academic Press, New York.

Burke, K., and Freeth, S.J., A rapid method for the determination of shape, sphericity and size of gravel fragments. *J. of Sedimentary Petrology*, **39**, 797-798.

Campbell Scientific Inc., 1985, 21 X Micrologger, Utah.

Campbell Scientific Inc., 1982, Met One wind direction sensor, Utah.

Carroll, J.J., 1982, The effect of surface striations on the absorption of shortwave radiation . *J. of Geophysical Research,* **87**(C12), 9647-9652.

Chang, A.T.C., and Shiue, J.C., 1980, A comparative study of microwave radiometer observations over snowfields with radiative transfer model calculations. *Remote Sensing of Environment*, **10**, 215-229.

Chen, H., and Rao, N. ,1968, Polarization of light on reflection by some natural surfaces. *British J. of Applied Physics*, **1**, 1191-1200.

Christian, C.S., and Stewart, G.A., 1953, General report on survey of Katherine-Darwin region, 1946 . *CSIRO Aust. Land Res. Ser.*, **1.**

Christie, A.W., 1953, The luminous directional reflectance of snow . *J. Optical Society of America*, **43**(7), 621-622.

Cierniewski, J. 1989, The influence of the viewing geometry of bare rough soil surfaces on their spectral response in the visible and near-infrared range. *Remote Sensing of Environment* , **27**, 135-142.

Cierniewski, J. 1987, A model for soil roughness influence on the spectral response of bare soils in the visible and Near Infrared range. *Remote Sensing of Environment*, **23**, 97-115.

Cooke, R.U., and Warren, A., 1973, *Geomorphology in Deserts*. B. T. Batsford Ltd, London.

Cooper, K.D., and Smith, J.A., 1985, A Monte Carlo reflectance model for soil surfaces with three-dimensional structure. *IEEE Transactions on Geoscience and Remote Sensing*, **GE-23** (4), 668-673.

Cooper, K.D., Smith, J.A., and Pitts, D., 1982, Reflectance of a vegetation canopy using the Adding method. *Applied Optics*, **21**(22), 4112-4118.

Corbet, J.R., Mabbutt, J.A., Milthorpe, J.C., Ngethe, J.C., and Sullivan, M.E., 1972, Lands systems of the Fowlers Gap - Calindary area. In: Lands of the Fowlers Gap - Calindary area, New South Wales. *Research Series* No. 4. The University of New South Wales.

Corbet, J.R., 1972, Soils of the Fowlers Gap - Calindary area. In: Lands of the Fowlers Gap - Calindary area, New South Wales. *Research Series* No. 4. The University of New South Wales.

Coulson, K.L., and Reynolds, D.W., 1971, Spectral reflectance of natural surfaces . *J. of Applied Meteorology* , **10**, 1285-1295.

Coulson, K., 1966, Effects of reflection properties of natural surfaces in aerial reconnaissance . *Applied Optics* . **5**(6), 905-917.

Coulson, K.L., Bouricius, G.M. and Gray, E.L., 1965, Optical reflection properties of natural surfaces . *J. of Geographical Research* . **70**, 4601-4611.

Cox, C. and Munk, W., 1954 , Measurements of the roughness of the sea surface from photographs of the Sun's glitter. *J. of the Optical Society of America*, **44**(11), 838-850.

Curran, P.J. and Williamson, H.D., 1985, The accuracy of ground data used in remote sensing investigations. *Int. J. of Remote Sensing.* **6**(10), 1637-1651.

Curran, P.J. and Hay, A.M., 1986, The importance of measurement error for certain procedures in remote sensing at optical wavelengths. *Photogrammetric Engineering and Remote Sensing.* **52**(3), 229-241

Danson, F.M., 1988, Remotely sensed response to forest stand structure. *Proceedings of the NERC 1986 Airborne Campaign Workshop* (p. 7-12), 24 February 1988, Institute of Hydrology, Wallingford, UK.

Dave, J.V. and Bernstein, R., 1982, Effect of Terrain orientation and solar position on Satellite- level luminance observations. *Remote Sensing of Environment..* **12**, 331-348.

Davies, J.A. , Robinson, P.J. and Nunez, M., 1970, Radiation measurements over Lake Ontario and the determination of emissivity. Report no. HO 81276 McMaster University.

Davis, C.F., Shuchman, R.A., and Suits, G.A., 1981, The use of remote sensing in the determination of beach sand parameters. *Proceedings of the 15th International Symposium on remote Sensing of Environment*, Ann Arbor MI , 775-789.

Deering, W.D. and Leone, P. A, 1986, Sphere-scanning radiometer for rapid directional measurements of sky and ground radiance. *Remote Sensing of Environment* **19**, 1-24.

Dozier, J., and Strahler, A.H., 1983, Ground investigation in support of remote sensing, 959-986, In: *Manual of Remote Sensing*, Colwell, R.N. (Ed.), American Society of Photogrammetry.

Duggin, M.J., 1986, Review article: factors limiting the discrimination and quantification of terrestrial featues using remotely sensed radiance. *Int. J. of Remote Sensing.* **6**(1), 3-27.

Duggin M.J. and Philipson, W.A., 1982, Field measurement of reflectance: some major considerations. *Applied Optics.* **21**(15), 2833-2840.

Duntley, S.Q., 1942, The optical properties of diffusing materials, *J. of the Optical Society of America.* , **32**, pp,61-70.

Dury, G.H., 1968, An introduction to the geomorphology of Australia, (p. 1-36), In: *Studies in Australian geography*, Dury, G.H., and Logan, M.I., (Editors), Heinemann Educational Australia, Melbourne.

Dymond, J.R. , 1988, Nonparametric modeling of radiance in Hill country. *Remote Sensing of Environment*, **25**, 3-21.

Eaton, F.D., Dirmhirn, I., 1979, Reflected irradiance indicatrices of natural surfaces and their effect of Albedo . *Applied Optics*. **18**(7), 994-1008.

Eaton, F.D., 1976, Albedo of the Earth's surface : a comparison of measurements taken on the ground and from flying platforms. PhD Thesis, Utah State University.

Egan , W.G., 1985, *Photometry and Polarization in remote sensing*, Elsevier, New York.

Egbert, D. and Ulaby, F., 1972, Effects of angles on reflectivity . *Photogrammetric Engineering and Remote Sensing*. **38**(6), 556-564.

Ellis, P.J., and Nankivell, C.T., 1985, *Eight channel hand held radiometer, Users guide*. Delphi Industries Limited, Auckland, New Zealand.

Emslie, A.G., and Aronson, J.R., 1973, Spectral reflectance and emittance of particulate materials.Applied Optics, **12**, 2563.

Eyton, R.J., 1989, Low-relief topographic enhancement in a Landsat snow-cover scene. *Remote Sensing of Environment*, **27**, 105-118.

Ferencz, Cs., Ferencz Arkos, I., Hamar, D., Lichtenberger, J., and Tarcsai, Gy., 1987, Surface models including direct cross-radiation: a simple model of furrowed surfaces. *Int. J. of Remote Sensing*, **8** (3), 449-465.

Forgan, B.W., 1983, Errors resulting from the use of measured albedos to calculate diffuse irradiance. *Solar Energy*, **31**(1), 105-112.

Forshaw, M.R.B., Haskell, A., Miller, P.F., Stanley, D.J., and Townshend, J.R.G., 1983, Spatial resolution of remotely sensed imagery A review paper. *Int. J. of Remote Sensing*, **4**, 497-520.

Fraser, S.J., Horsfall, C.L., Gabell, A.R., Huntington, J.F., and Green, A.A., 1987, Targeting hydrothermal alteration systems in north Queensland using aircraft thematic mapper data. *Proceedings of the 4th AustralAsian Remote Sensing Conference,* September 1987, Adelaide, Volume 1, 340-351.

Gagalowicz, A., and De Ma, S., 1985, Sequential Synthesis of natural textures. *Computer Vision, Graphics and Image Processing,* 30, 289-315.

Garnier, B.J. and Ohmura, A., 1968, A method of calculating the direct short-wave radiation income of slopes . *J. of Applied Meteorology* 7, 796-800.

Gerstl, S.A.W. and Simmer, C., 1986, Radiation physics and modeling for off nadir Satellite sensing of non Lambertian surfaces. *Remote Sensing of Environment.* **20**, 1-29.

Goel, N.S., and Grier, T., 1988, Estimation of canopy parameters for inhomogeneous vegetation canopies from reflectance data: III. TRIM: A model for radiative transfer in heterogeneous three-dimensional canopies. *Remote Sensing of Environment,* **25**, 255-293.

Goel, N.S., and Grier, T., 1986, Estimation of canopy parameters for inhomogeneous vegetation canopies from reflectance data. I. Two-dimensional row canopy. *Int. J. of Remote Sensing,* **7** (5), 665-681.

Grabowski, L., 1914, On the theoretical photometry of diffuse reflection, *Astrophysical J* ., **39**, 299-306.

Grant, L., 1987, Diffuse and specular characteristics of leaf reflectance. *Remote Sensing of Environment,* **22**, 309-322.

Gustafson, G.C., and Loon, J.C., 1982, Cotour accuracy and the National Map Accuracy Standard. *Surveying and Mapping,* 42(4), 385-402.

Haines-Young, R.H., and Petch, J.R., 1983, Multiple working hypotheses: Equifinality and the study of landforms. *Transactions Institute of British Geographers,* N.S. **8** ,458-466.

Hamalainen, P., Nurkkanen, P. and Slaen, T. A, 1985, Multisensor Pyranometer for determination of the direct component and angular distribution of solar radiation. *Solar Energy* . **35**(6), 511-525.

Hapke, B. W., 1963, A theoretical photometric function for the lunar surface . *J. Geophysical Research,* **68**(15), 4571-4586.

Hapke, B. W. and Van Horn, H., 1963, Photometric studies of complex surfaces with applications to the moon . *J. of Geophysical Research* . **68**(15), 4545 - 4570.

Hecht, E. and Zajac, A., 1973, Optics. Addison-Wesley, Publishing Company, Inc. Reading, Massachusetts.

Henderson-Sellers, A., 1980, Albedo changes: surface surveillance from satellites. *Climatic change.* **2**, 275-281.

Henderson-Sellers, A. and Hughes, N.A., 1982, Albedo and its importance in climatic theory. *Progress in Physical Geography.*; **6**, 1-44.

Henderson-Sellers, A., and Wilson, M.F., 1983, Surface albedo data for climatic modelling. *Rev. Geophys.Space Phys.*, **21**, 1743-1778.

Hildebrand, F.B., 1956, *Numerical Analysis.* McGraw Hill, New York.

Hobson, R.D.,1973, Surface roughness in topography: Quantitative approach, in: *Spatial Analysis in Geomorphology* , Chorley, R.J. (editor), 221-246.

Holben, B., and Fraser, R.S., 1984, Red and near-infrared sensor response to off-nadir viewing. *Int. J. of Remote Sensing,* **5**(1), 145-160.

Holben, B.N., and Justice, C.O., 1981, An examination of spectral band ratioing to reduce the topographic effect on remotely sensed data . *Int. J. of Remote Sensing* . **2**, 115.

Horn, B.K.P. and Sjoberg, R.W., 1979, Calculating the reflectance map. *Applied Optics.* **18**(11), 1770-1779.

Horn, B.K.P. and Bachman, B.L., 1978, Using synthetic images to register real images with surface models. *Communications of the ACM.*, **21**(11), 914-924.

Hughes, N.A. and Henderson-Sellers, A., 1982, System albedo as sensed by satellites: its definitions and variability . *Int. J. of Remote Sensing.* **14**, 77-111.

Hugli, H. and Frei, W., 1983, Understanding anisotropic reflectance in mountainous terrain. *Photog. Engi. and Remote Sensing.* **49**(5), 671-683.

Hummel, J.R., and Reck, R. A., 1979, A global surface albedo model. *J. of Applied Meteorology,* **18**, 239-253.

Huntington, J.F., and Raiche, A.P., 1978, A multiattribute method for comparing geological lineament interpretations. *Remote Sensing of Environment*, **7**, 145-161.

Holben, B.N., and Justice, C.O., 1980, The topographic effect on the spectral response of nadir-pointing sensors. *Photogrammetry Engineering and Remote Sensing,* **46**, 1191.

Iqbal, M., 1983, *An introduction to Solar Radiation.* Academic Press, New York.

Jupp, D.L.B., Walker, J., and Penridge, L.K., 1986, Interpretation of vegetation structure in Landsat MSS imagery: a case study in disturbed semi-arid Eucalipt woodlands. Part 2. Model-based analysis. *J. of Environmental Management.,* **23**, 35-57.

Jupp, D.L.B., Strahler, A.H. and Woodcock, C.E., Autocorrelation and regularization in digital images. I. Basic theory. *IEEE Trans. on Geoscience and Remote Sensing*, **26**, 463-473.

Justice, C.O., and Townshend, J.R.G., 1981, The use of Landsat data for land cover inventories of Mediterranean lands. In : *Terrain analysis and remote sensing*, Townshend, J.R.G.(Ed.), George Allen & Unwin, London.

Justice, C.O., Wharton, S.W., and Holben, B.N., 1981, Application of digital terrain data to quantify and reduce the topographic effect on Landsat data. *Int. J. Remote Sensing*, **2**, 213- 230.

Justice, C.O., and Holben, B.N., 1980, *The contribution of the diffuse light component to the topographic effect on remotely sensed data.* Goddard Space Flight Center, Greenbelt, Maryland, USA.: NASA, TM 852900.

Justice, C.O., and Holben, B.N., 1979, *Examination of Lambertian and non-Lambertian models for simulating the topographic effect on remotely sensed data.*: NASA Goddard Space Flight Center, Greenbelt, Maryland, USA, TM 80557.

Justus, C.G., and Paris, M.V., 1985, A model for solar spectral irradiance and radiance at the bottom and top of a cloudless atmosphere. *J. of Climate and Applied Meteorology*, 24(3), 193-205.

Kimes, D.S., Sellers, P.J., and Diner, D.J., 1987, Extraction of spectral hemispherical reflectance (albedo) of surfaces from nadir and directional reflectance data. *Int. J. of Remote Sensing*, 8(12), 1727-1746.

Kimes, D.S., Holben, B. , Tucker, C. and Newcomb, W. , 1984, Optimal directional view angles for remote sensing missions . *Int. J. of Remote Sensing,* 5(6), 877-908.

Kimes, D.S., 1983, Dynamics of directional reflectance factor distributions for vegetation canopies . *Appl. Opt.*. 22, 1364-1372.

Kimes, D.S. and Kirchner, J.A., 1982, Radiative transfer model for heterogeneous 3-D scenes. *Applied Optics*, 21(22), 4119-4129.

Kimes, D.S. and Kirchner, J.A., 1981, Modeling the effects of various radiant transfers in mountainous terrain on sensor response. *IEEE Transactions on Geoscience and Remote Sensing.* 19(2), 100-108.

Kondratyev, K. Ya., 1969, *Radiation in the atmosphere.*, Academic Press, New York.

Kriebel, K.T., 1978, Measured spectral bidirectional reflection properties of vegetated surfaces . *Applied Optics,* 17, 253-259.

Kriebel, K.T., 1976, On the variability of the reflected radiation field due to differing distributions of the irradiation. *Remote Sensing of Environment ,* 4, 257-264.

Lewis, D.W., 1984, *Practical Sedimentology*, Hutchinson Ross, Pennsylvania.

Li, X., 1985, Geometric-Optical modeling of a Coniferous forest canopy. Ph.D Thesis, University of California.

Li, X., and Strahler, A.H., 1986, Geometric-optical bidirectional reflectance modeling of a Conifer forest canopy. *IEEE Transactions on Geoscience and Remote Sensing,* GE-24 (6), 906-919.

Loffler, E., 1977, Landform interpretation with modern remote sensors- examples from Papua New Guinea. *Die Erde .* 108, 202-216.

Mabbutt, J.A., 1977, *Desert Landforms. An Introduction to Systematic Geomorphology*, Vol. 2, Australian National University Press, Canberra.

Mabbutt, J.A., 1972, Geomorphology of the Fowlers Gap - Calindary area,In: Lands of the Fowlers Gap - Calindary area, New South Wales. *Research Series* No. 4. The University of New South Wales.

Markham,B.L., and Townshend, J.R.G., 1981, Land cover classification accuracy as a function of sensor spatial resolution. *Proceedings of the Fifteenth International Symposium on Remote Sensing of Environment*, Ann Arbor, MI., 1075-1091.

Marsh, S.E. , Switzer, P. , Kowalik, W.S. and Lyon, R.J.P., 1980, Resolving the percentage of component terrains within single resolution elements. *Photogrammetric Engineering and Remote Sensing.* 46(8), 1079-1086.

Mather, P, 1976, *Computational methods of multivariate analysis in physical geography.* John Wiley, London.

Mathieu, J.P., 1975, *Optics.* (Translated by: Blaker, W.J.), Pergamon Press, Oxford.

Middleton, W.E. , Mungall, A.G., 1952, The luminous directional reflectance of snow. *J. Optical Society of America ,* 42(6), 572-579.

Milne, A.K., and Zhou, Q., Manipulating geographic information and remotely sensed data for land cover mapping in Arid Australia. *Proceedings of the 4th AustralAsian Remote Sensing Conference*, September 1987, Adelaide, Volume 2, 544-555.

Milthorpe, P.L., 1972, Vegetation of the Fowlers Gap -Calindary area . In: Lands of the Fowlers Gap -Calindary area, New South Wales. *Research Series ,* No. 4. The University of New South Wales.

Minnaert, M., 1941, The reciprocity principle in Lunar Photometry. *J. of Astrophysics,* **93**, 403-410.

Minnis, P. and Harrison, E.F., 1984, Diurnal variability of regional cloud and clear-sky radiative parameters derived from GOES data Part III: radiative parameters. *J. of Climate and Applied Meteorology,* **23**, 1032-1051.

Mitchell, C.W., 1981, Reconnaissance land resource surveys in arid and semi-arid lands. In : *Terrain analysis and remote sensing,* Townshend, J.R.G., (Ed.), George Allen & Unwin, London.

Monteith, J.L., 1962, Attenuation of solar radiation : a climatological study. *Quart. J. Roy. Meteorological Society,* **88**, 508-521.

Nicodemus, F.E., Richmond,J.C., Hsia, J.J., Ginsberg, I.W., and Limperis, T., 1977, *Geometrical considerations and nomenclature for reflectance.* U.S.A: U.S. Dep. of commerce, National Bureau of Standards.

Nilson, T., and Kuusk, A., 1989, A reflectance model for the homogeneous plant canopy and its inversion. *Remote Sensing of Environment,* **27**, 157-167.

Norman, J.M., Welles, J.M., and Walter, E.A., 1985, Contrast among bidirectional reflectance of leaves, canopies and soils. *IEEE Transactions on Geoscience and Remote Sensing.* **GE-23(5)**, 659-667.

Norton, C.C., Mosher, F.R., and Hinton, B., 1979, An investigation of surface albedo variations during the recent Sahel drought. *J. of Applied Meteorology,* **18**, 1252-1262.

Nunez, M., 1985, Modelling daily global radiation at the forest floor. *Boundary Layer Meteorology,* **33**, 379-395.

Nunez, M., 1982, Estimation of solar radiation on slopes in Tasmania. *The papers and Proceedings of the Royal Society of Tasmania,* **117**, 153-159.

Nunez, M., and Oke, T.R., 1980, Modeling the daytime urban surface energy balance. *Geographical Analysis,* **12(4)**, 373-386.

Nunez M., 1980, The calculation of solar and net radiation in mountainous terrain. *J. of Biogeography,* **7**, 173-186.

Nunez, M., Davies, J.A., and Robinson, P.J., 1972, Surface albedo at a tower site in Lake Ontario. *Boundary-Layer Meteorology,* **3**, 77-86.

Nurkkanen, P. and Hamalainen, M. , 1981, A compound Pyranometer . *Proceedings ISES Congress,* 23-28 August Brighton, England, Vol. **3** , 2461-2465.

Ott, W. , Pfeiffer, B. and Quiel, F., 1984, Directional reflectance properties determined by analysis of airborne multispectral scanner data and atmospheric correction . *Remote Sensing of Environment,* **16**,47-54.

Otterman, J., 1985, Bidirectional and hemispheric reflectivities of a bright soil-plane and a sparse dark canopy. *Int. J. Remote Sensing,* **6**, 897-902.

Otterman, J., 1984 ,Albedo of forest modeled as a plane with dense protrusions. *J. Climate Appl. Meteor.*, **23**, 297-307.

Otterman, J., 1984, Atmospheric effects on radiometry from zenith of a plane with dark vertical protrusions. *Int. J. Remote Sensing*, **5**, 909-923.

Otterman, J., 1981, Plane with protrusions as an atmospheric boundary. *J. of Geophysical Research*, **86**, 6627-6630.

Otterman, J., 1977, Anthropogenic impact on the albedo of the Earth. *Climate Changes;* **1**, 137-157.

Otterman, J., 1974, Baring high-albedo soils by overgrazing: Hypothesised desertification mechanism. *Science,* **186**, 530-533.

Otterman, J., and Fraser R.S., 1976, Earth-Atmosphere System and Surface reflectivities in Arid Regions from LANDSAT MSS Data. *Remote Sensing of Environment*, **5**, 247-266.

Otterman, J., and Robinove, C.J., 1981, Effects of the atmosphere on the detection of surface changes from Landsat Multispectral Scanner data. *Int. J. of Remote Sensing*, **2**, 351-360.

Otterman, J., and Tucker, C.J., 1985, Satellite measurements of surface albedo and temperatures in semi-desert. *J. of Climate and Applied meteorology,* **24**, 228-235.

Pain, C.F., 1985, Mapping of Landforms from Landsat Imagery: An Example from Eastern New South Wales, Australia. *Remote Sensing of Environment.*, **17**, 55-65.

Peterson, W.A., Dirmhirn, I. and Hurst, R.L., 1985 , Atheoretical model to determine solar and diffuse irradiance in valleys. *Solar Energy* ,**35**(6), 503- 510.

Peterson, W.A. and Dirmhirn, I., 1981, The ratio of diffuse to direct solar irradiance (perpendicular to the sun's rays)- a conserved quantity throughout the day . *J. of Applied Meteorology*, **20**, 826-828.

Pettijohn, F.J., 1975, *Sedimentary rocks*. Harper & Row, New York.

Pickup, G. and Nelson, D.J., 1984, Use of Landsat radiance parameters to distinguish soil erosion, stability, and deposition in Arid Central Australia. *Remote Sensing of Environment,* **16,**195-209.

Pinty, B. and Ramond, D., 1987, A method for the estimate of broadband directional surface albedo from a Geostationary satellite. *J. of Climate and Applied Meteorology,* **26,** 1709-1722.

Pinty, B. and Ramond, D., 1986, A simple bidirectional reflectance model for terrestrial surfaces. *J. of Geophysical Research,* **91,** 7803 - 7808.

Prior, W.A., 1971, Grain shape, In : *Procedures in sedimentary petrology,* Carver, R.E. (Ed.), John Wiley, New York.

Ranson, K.J., Daughtry, C.S.T., and Biehl, L.L., 1986, Sun angle, view angle, and background effects on spectral response of simulated Balsam Fir canopies. *Photogrammetric Engineering and Remote Sensing,* **52**(5), 649-658.

Ranson, K.J., and Daughtry, C.S.T., 1987, Scene shadow effects on Multispectral response. *IEEE Transactions on Geoscience and Remote Sensing,* **GE-25,** 502-509.

Raschke, E. , Preuss, H.J., 1979, The determination of the solar radiation budget at the Earth surface from satellite measurements. *Meteor. Rundsch.,* **32,** 18-28.

Reifsnyder, W.E., 1967, Radiation geometry in the measurement and interpretation of radiation balance. *Agric. Meteorol.,* **4,** 255-265.

Rense, W.A., 1950, Polarization studies of light diffusely reflected from ground and etched glass surfaces. *J. of the Optical Society of America,* **40**(1), 55- 59.

Revfiem, K.L.A. Solar radiation at a site of known orientation on the earth's surface. *J. Applied Meteorology*; 1976; 15: 651-656.

Rockwood, A.A. and Cox, S.K., 1978, Satellite infrared surface albedo over north western Africa. *J. of the Atmospheric Sciences,* **35,** 513-522.

Salomonson, V.V., and Marlatt, W.E., 1971, Airbourne measurementts of reflected solar radiation. *Remote Sensing and Environment,* **2,** 1-8.

Salomonson, V.V. and Marlatt, W.E., 1968, Anisotropic solar reflectance over white sand, snow and stratus clouds . *J. Applied Meteorology,* **7,** 475-483.

Schaber, G.G. , Berlin, G.L. and Brown, W. E., 1976, Variations in surface roughness within Death Valley, California: Geologic evaluation of 25-cm-wavelength radar images. *Geological Society of America Bulletin*, **87**, 29- 41.

Schiffer, R., 1988, Reflectivity of a slightly rough surface. *Applied Optics*, **26**(4), 704-712.

Schneider, S.R., McGinnis, D.F. and Pritchard, J.A., 1979, Use of Satellite Infra-red data for Geomorphology studies . *Remote Sensing of Environment*, **8**, 313-330.

Schultegann, P.A., 1985, Structural trends in Borrego Valley, California : Interpretation from SIR-A and SEASA SAR . *Photogrammetric Engineering and Remote Sensing*, **51**(10), 1615-1624.

Shibayama, M., Wiegand, C.L., and Richardson, A.J., 1986, Diurnal patterns of bidirectional vegetation indices for wheat canopies. *Int. J. of Remote Sensing*, **7**(2), 233-246.

Shoshany, M.,1989 A, Secondary reflection effect on sensor response for a V shaped valley. *Int. J. of Remote Sensing*, In press.

Shoshany, M.,1989 B, A roughness digitizer for field measurements of roughness elements and their spatial pattern. *J. of Sedimentary Petrology*, In press.

Shoshany, M.,1989 C, The equifinality of Bidirectional Reflectance Distribution Functions (BRDF) of various microstructures. Submitted to the *Int. J. of Remote Sensing*.

Shoshany, M., 1988, The bidirectional reflectance distribution function (BRDF) and the micromorphometry of bare terrain surfaces.Paper presented at the 26th Congress of the International Geographical Union, Sydney, Australia.

Shoshany, M., and Nunez, M., 1987, The effect of surface reflection on the sensor response for a V shaped valley with particulate surfaces, *Proceedings of the 4th AustralAsian Remote Sensing Conference*, September 1987, Adelaide, Volume 1, 107-113.

Shoshany, M., 1986, Surface structure effects on reflected radiance. Paper presented at the 6th Australian Cartographic Conference, October, Melbourne.

Singh, S.M., 1988, Estimation of multiple reflection and lower order adacency effects on remotely-sensed data. *Int. J. of Remote Sensing*, 9(9), 1433-1450.

Singh, S.M., and Cracknell, A.P., 1985, Effect of shadows cast by vertical protrusions on AVHRR data. *Int. J. of Remote Sensing*, 6(11), 1767-1771.

Slaen, T.A., 1983, A method for computing the angular distribution of solar radiation from multipyranometer observations . *Proceedings ISES Congress*, August , Perth, Australia , 2189-2193 .

Slater, P.N., 1980, *Remote Sensing, Optics and Optical Systems.*, Addison-Wesley, London.

Smith, J.A., 1983, Matter-energy interaction in the optical region, 61-113, In: *Manual of Remote Sensing*, Colwell, R.N. (Ed.), American Society of Photogrammetry.

Smith, J.A., Lin, T.L., and Ranson, K.J., 1980, The lambertian assumption and Landsat data. *Photogrammetric Engineering and Remote Sensing*, 46(9), 1183-1189.

Steyn, D.G., 1980, The calculation of View Factors from Fisheye-Lens photographs . *Atmosphere Ocean* . 18(3), 254-258.

Stohr, C.J. and West, R. T., 1985, Terrain and look angle effects upon Multispectral Scanner Response. *Photogrammetric Engineering and Remote Sensing*, 51(2), 229-235.

Strahler, A. H., Woodcock, C.E., and Smith, J. A., 1986, On the nature of models in remote sensing. *Remote Sensing of Environment*, 20, 121-139.

Strebel, D.E., Goel, N.S., and Ranson, K.J., 1985, Two-dimensional leaf orientation distributions. *IEEE Trans. Geoscience an Remote Sensing*, GE-23, 640-647.

Suits, G.H., 1983, The nature of electromagnetic radiation, 37-60, In: *Manual of Remote Sensing*, Colwell, R.N. (Ed.), American Society of Photogrammetry.

Suits, G.H., 1972, The calculation of the directional reflectance of vegetative canopy. *Remote Sensing of Environment.*, 2, 117-125.

Suits, G.H., 1972, The cause of azimuthal variations in directional reflectance of vegetative canopies. *Remote Sensing of Environment.*, 2, 175.

Sullivan, M.E., 1972, Geology of the Fowlers Gap -Calindary area, In: Lands of the Fowlers Gap Calindary area, New South Wales. *Research Series* No. 4. The University of New South Wales.

Swain, P.H., and Davis, S.M., 1978, Remote Sensing the Quantitative Approach. McGraw-Hill, New York.

Teillet, P.M., 1986, Image correction for radiometric effects in remote sensing. *Int. J. of Remote Sensing,* 7(12), 1637- 1651.

Teillet, P.M., Guindon, B. and Goodenough, D.G., 1985, Slope - aspect effects in synthetic aperture radar imagery. *Canadian J. of Remote Sensing.* , 11(1), 39-49.

Teillet, P.M., Guindon, B. and Goodenough, D.G., 1982, On the slope-aspect correction of multispectral scanner data. *Canadian J. of Remote Sensing.* 8(2), 84-106.

Tonelli, A., 1978, Surface texture analysis with thermal and near infrared sensors. *Photogrammetric Engineering and Remote Sensing,* 44(10), 1273-1278.

Torrance, K. E., and Sparrow, E. M., 1967, Theory for off-specular reflection from roughened Surfaces. *J. of the Optical Society of America.,* 57(9), 1105-1114.

Townshend, J.R.G., and Hancock, P., 1981, The role of remote sensing in mapping surficial deposits. In : *Terrain analysis and remote sensing,* Townshend, J.R.G.(Ed.), George Allen & Unwin, London

Trowbridge, T.S. and Reitz, K.P., 1975, Average irregularity representation of a rough surface for ray reflection. *J. of the Optical Soc. of America,* 65(5), 531-536.

Tucker, C.J. and Garret, M.W., 1977, Leaf optical system modeled as a stochastic process. *Applied Optics,* 16, 635-642.

Ulaby, F.T., and McNaughton, J., 1975, Classification of physiography from ERTS imagery. *Photogrammetric Engineering and Remote Sensing,* 41, 1019-1027.

Valko, P., 1983, Empirical study of the angular distribution of sky radeiance and of ground reflected radiation fluxes. Proceedings ISES Congress, 14-19 August, Perth, Australia , 4, 2189-2193.

Van De Hulst, H.C., 1980, *Multiple Light Scattering Tables, Formulas, and Applications, Volume 1* . Academic Press, New York.

Verhoef, W., 1984, Light scattering by leaf layers with application to canopy reflectance modeling: the SAIL model. *Remote Sensing of Environment*, **16**, 125-141.

Walthall, C.L., Norman, J.M., Campbell, G. and Blad, B.L., 1985, Simple equation to approximate the bidirectional reflectance from vegetative canopies and bare soil surfaces. *Applied Optics*, **24**(3), 383-387.

Williams, D.F., 1981, Integrated land survey methods for the prediction of gully erosion. In : *Terrain analysis and remote sensing*, Ed. Townshend, J.R.G., George Allen & Unwin, London.

Woodham, R.J., 1980, Photometric method for determining surface orientation from multiple images. *Optical Engineering*, **19**, 139-144.

Woodham, R.J., and Gray, M.H., 1987, An analytic method for radiometric correction of satellite MSS data. IEEE Transactions on Geoscience and Remote Sensing, **GE-25**, 97-110.

Woodcock, C.E., Strahler, A.H., and Jupp, D.L.B., 1988, The use of variograms in remote sensing: II. real digital images.*Remote Sensing of Environment..* **25**, 349-379.

APPENDIX A : REFLECTED RADIANCE MAPS

In this Appendix we will present maps of the directional distribution of reflected radiance in band 7, as measured in the field using the HDRM apparatus (described in Chapter 4). Each hemispherical set of reflected radiance represents an average of measurements taken at three different locations of each site within 10 min. The measured data of off-nadir angles includes the range of 0° to 65° while the values for angles larger than 65° were extrapolated using the Trend Surface technique. The maps were produced using the contouring routines of the SURFACE II software. The conturing process was involved also smoothing of the contour lines.

Units : $\mu W\ cm^{-2}\ sr^{-1}$

Horizontal axis : azimuth (add 360° to the negative values for getting the real azimuth).

Vertical axis : reflection angle (0° = normal direction to the surface).

Contouring interval : 50 $\mu W\ cm^{-2}\ sr^{-1}$.
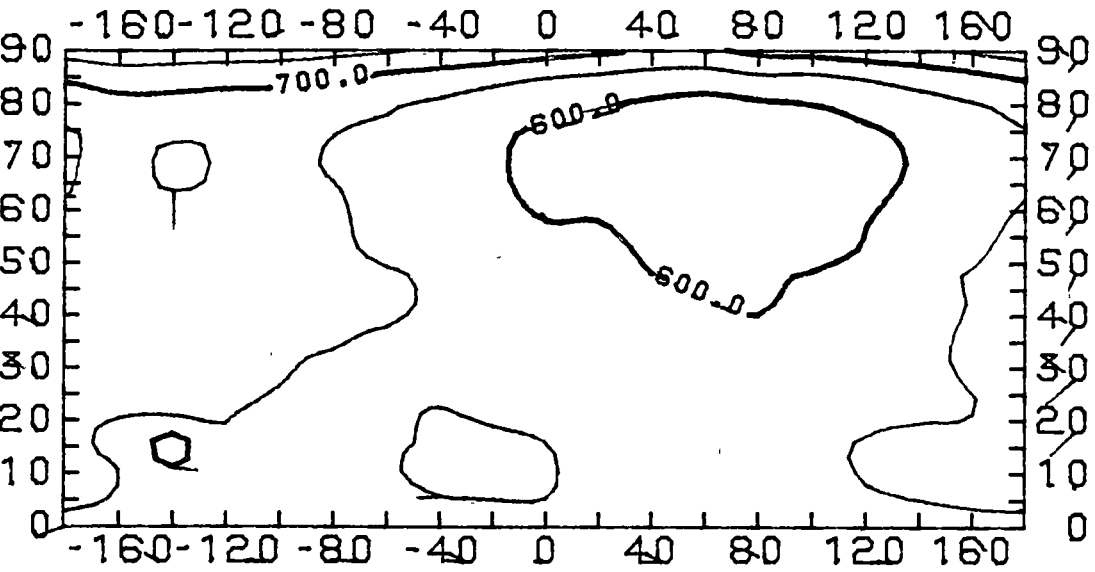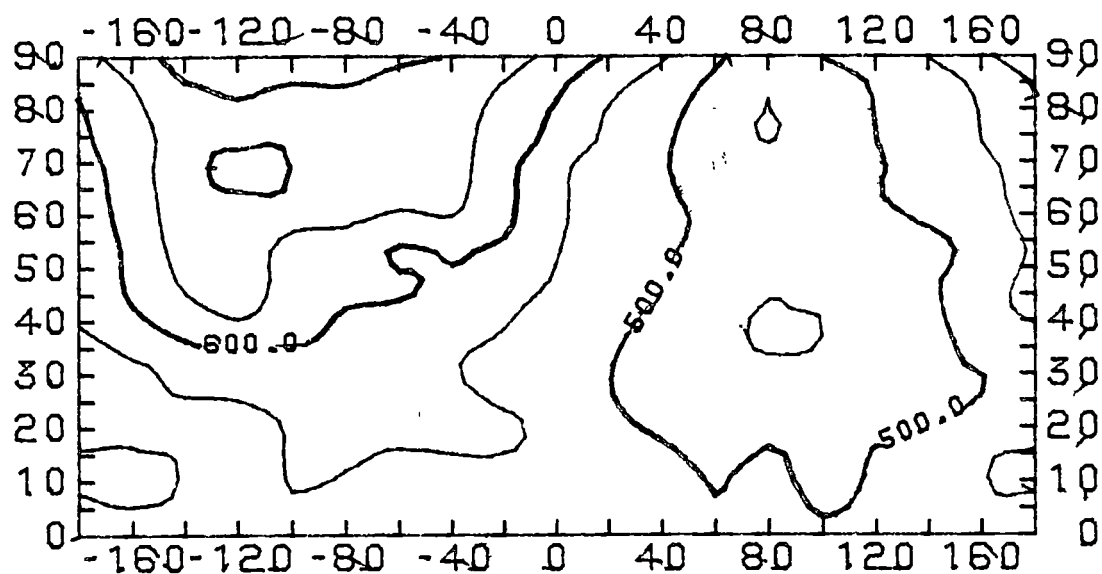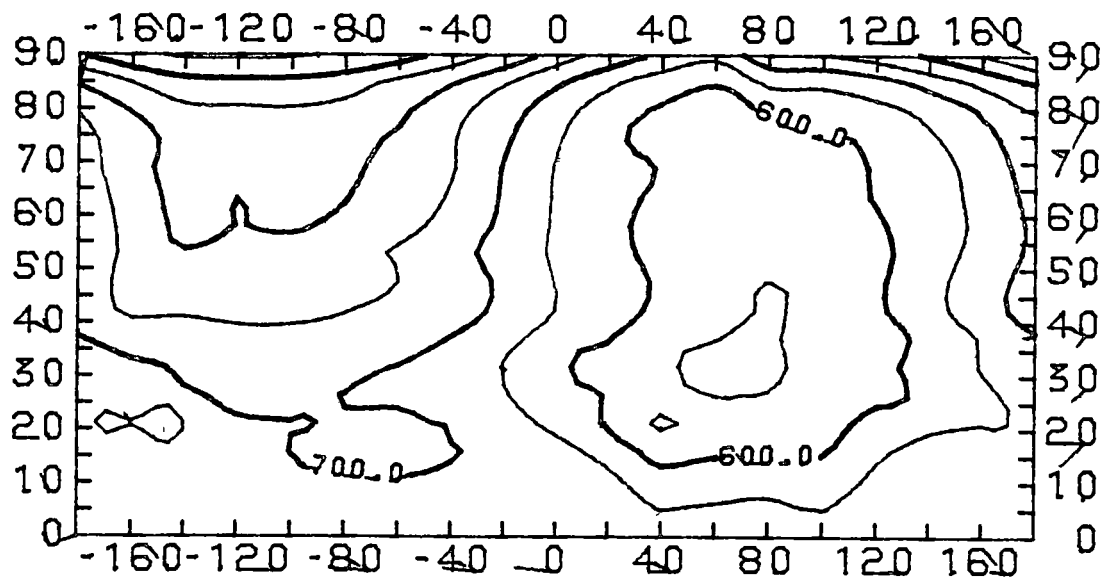
SITE 3

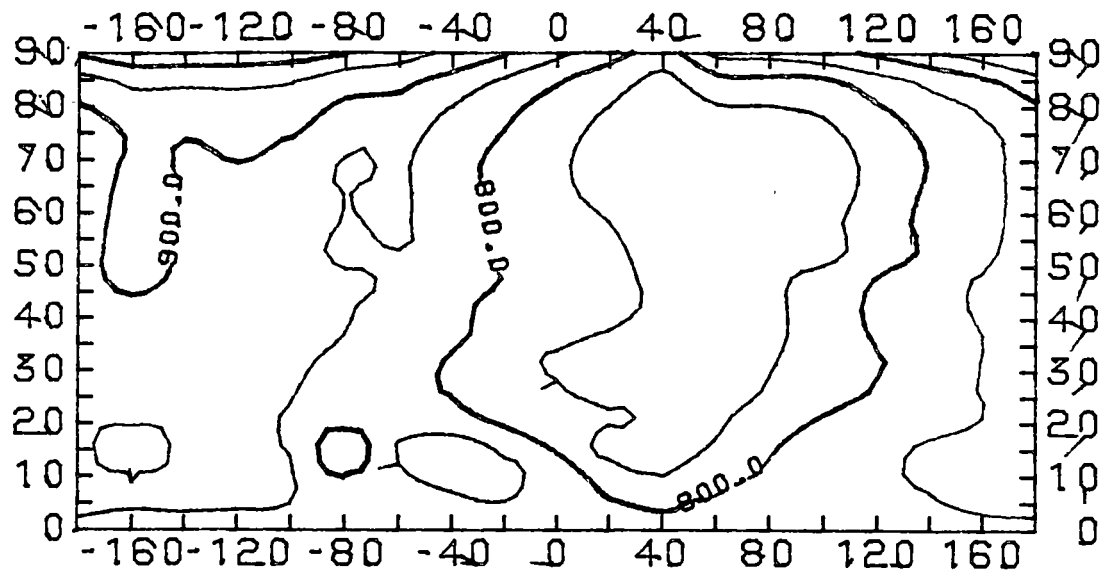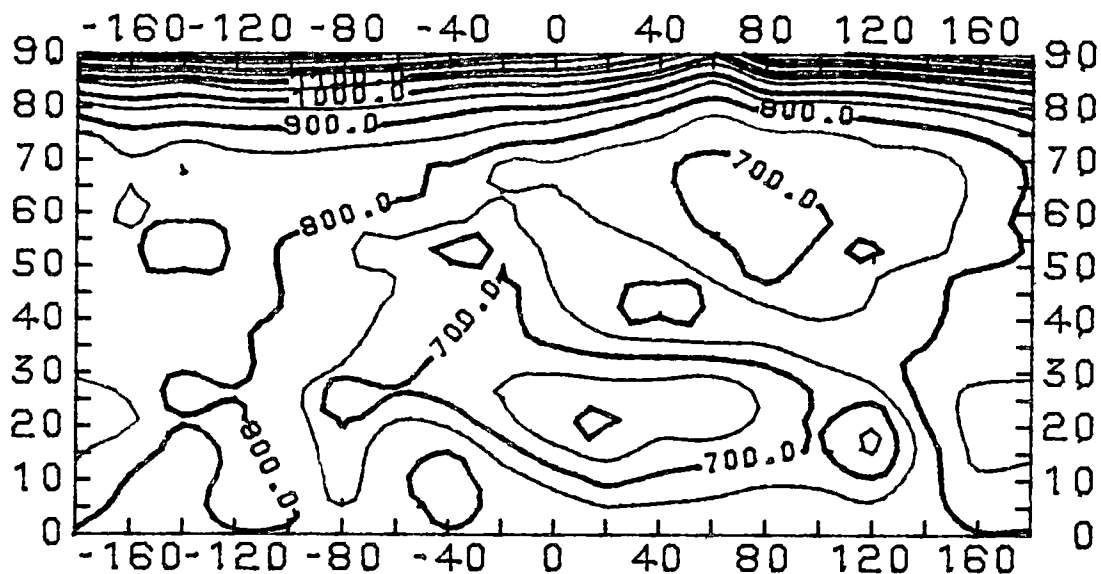sun zenith = 58° and azimuth = 88°
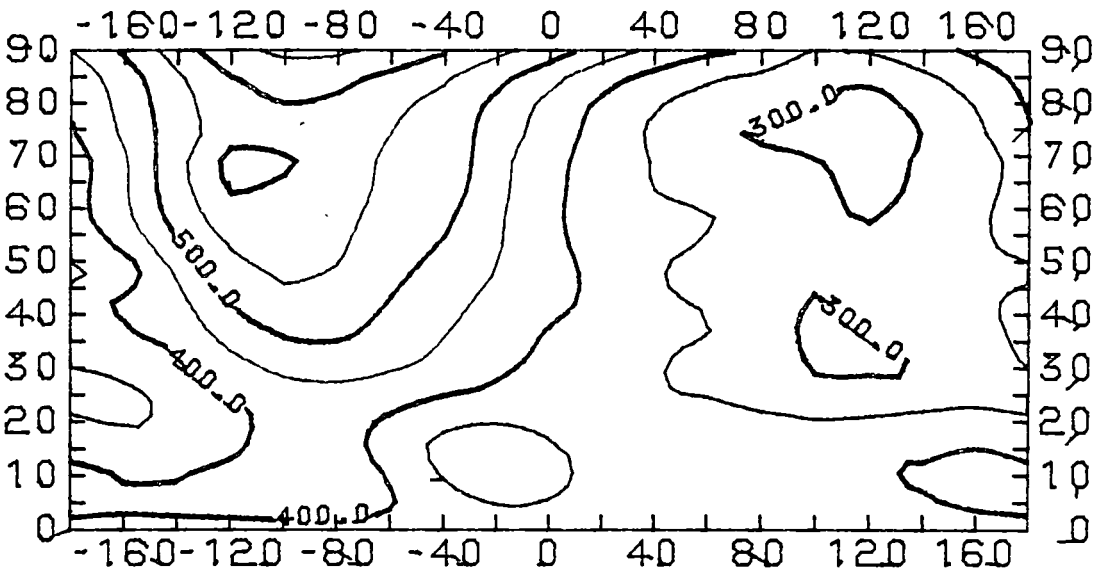
sun zenith = 30° and azimuth = 67°
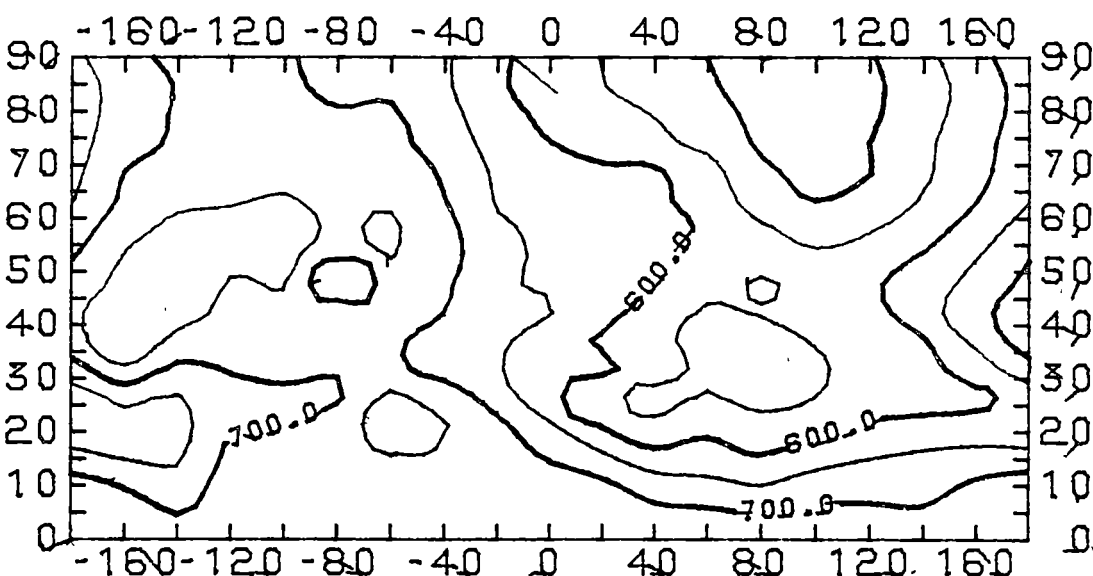
sun zenith = 47° and azimuth = 269°
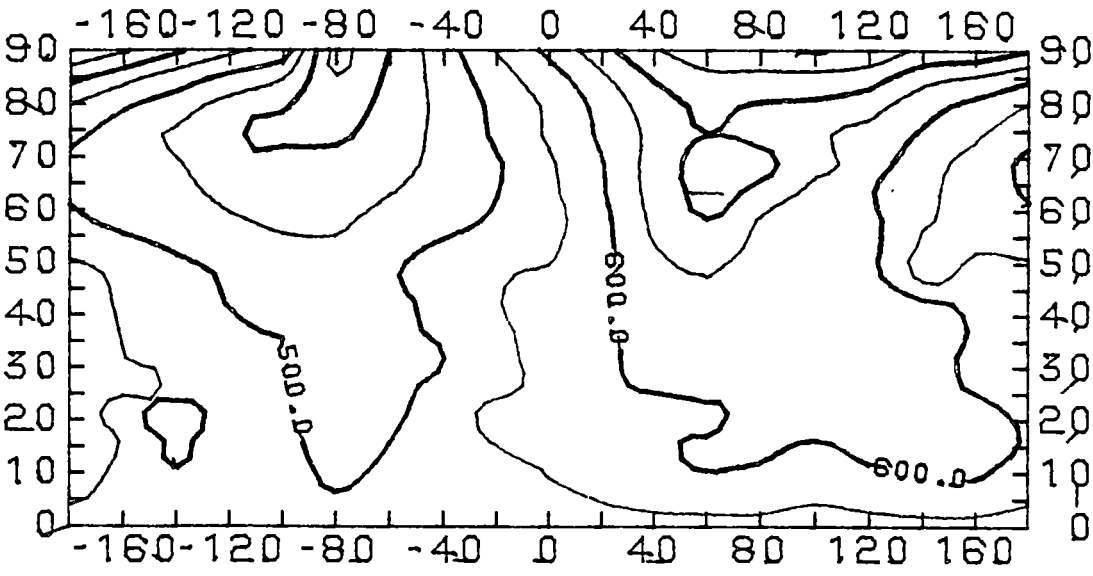
SITE 4

sun zenith = 55° and azimuth = 87°
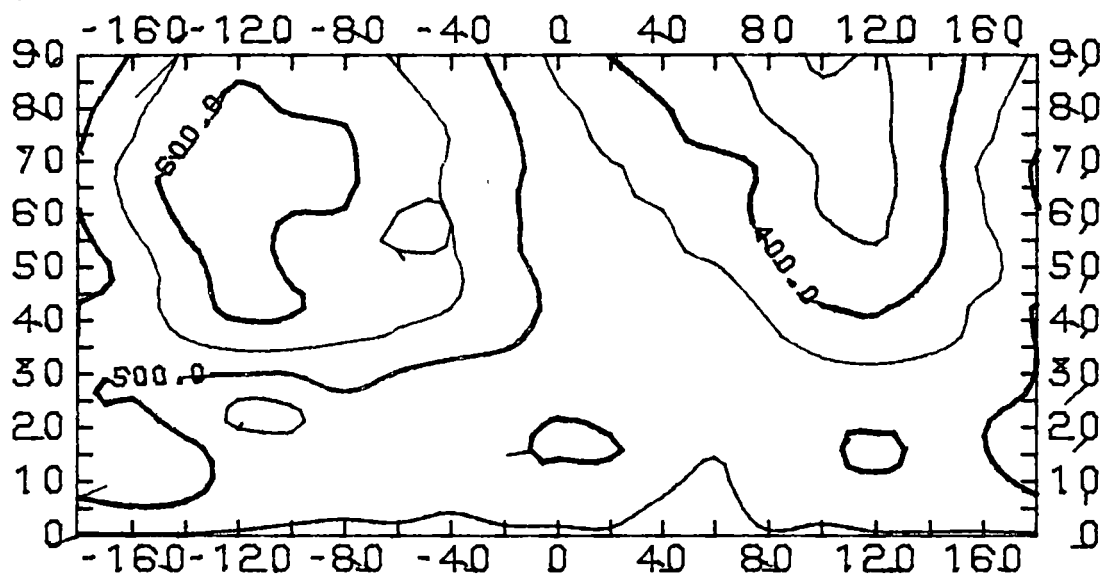
sun zenith = 38° and azimuth = 77°
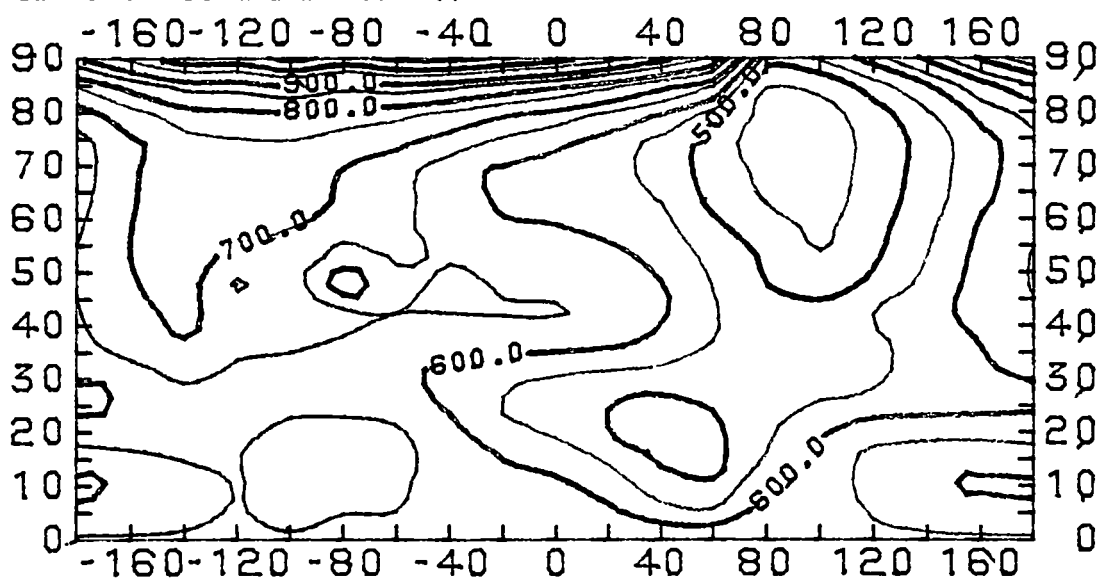
SITE 5

sun zenith = 21$^{\text{O}}$ and azimuth = 52$^{\text{O}}$
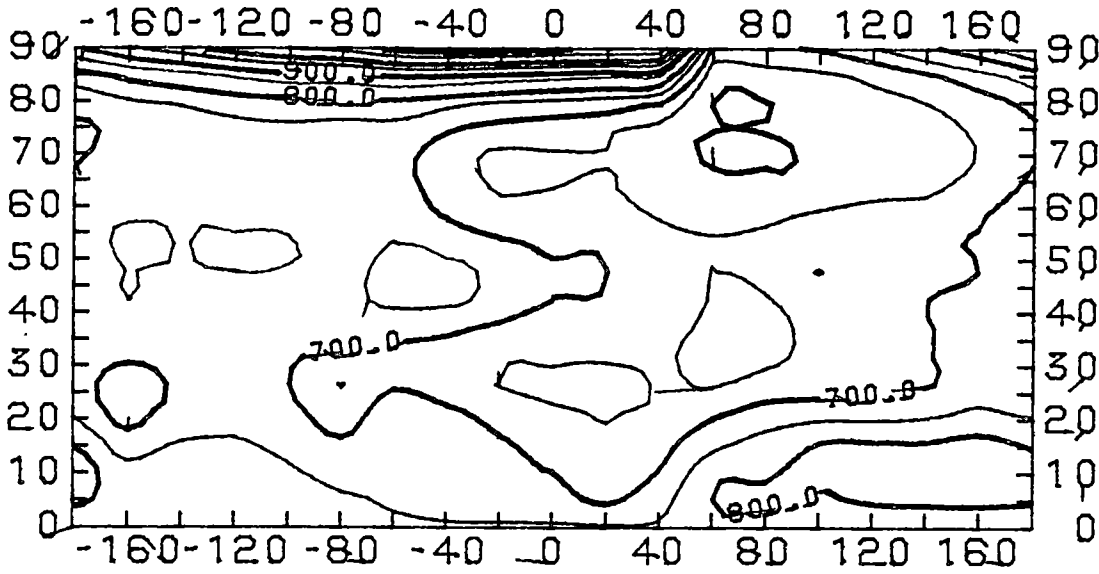
sun zenith = 59$^{\text{O}}$ and azimuth = 263$^{\text{O}}$
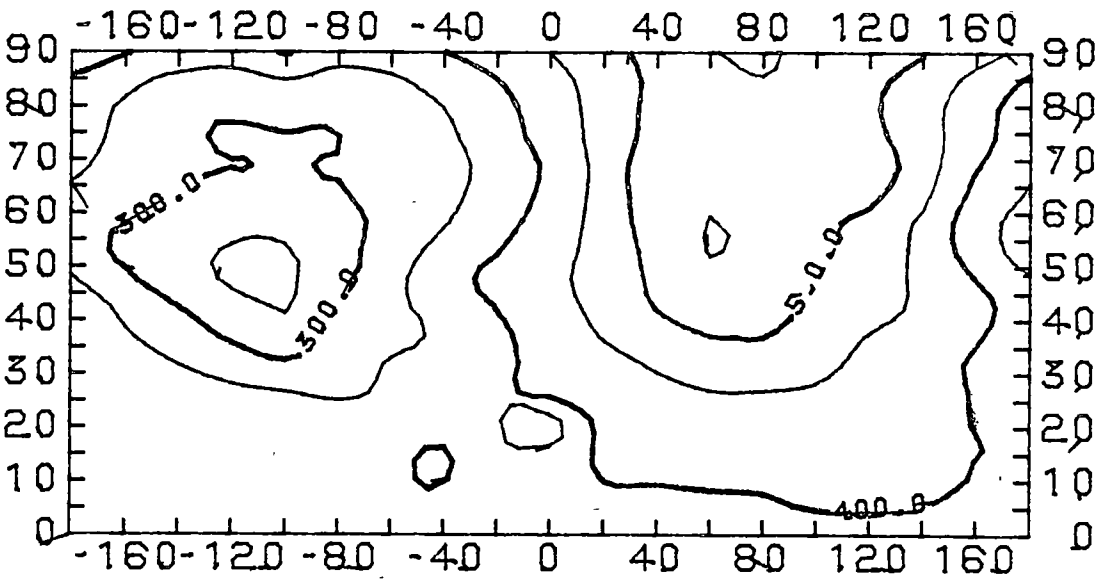
SITE 6

sun zenith = 14° and azimuth = 31°
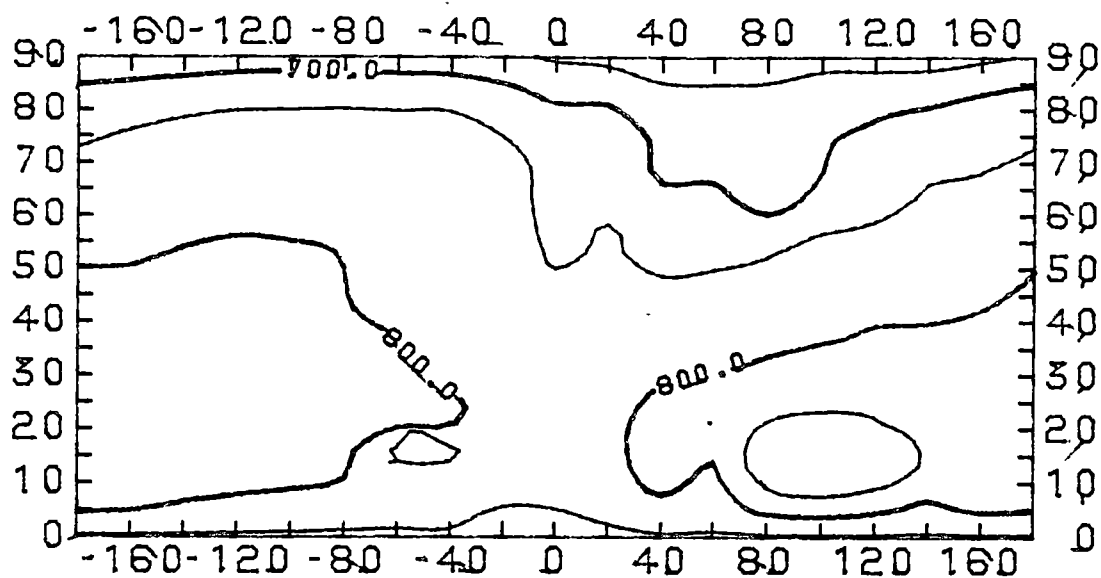
sun zenith = 24° and azimuth = 295°
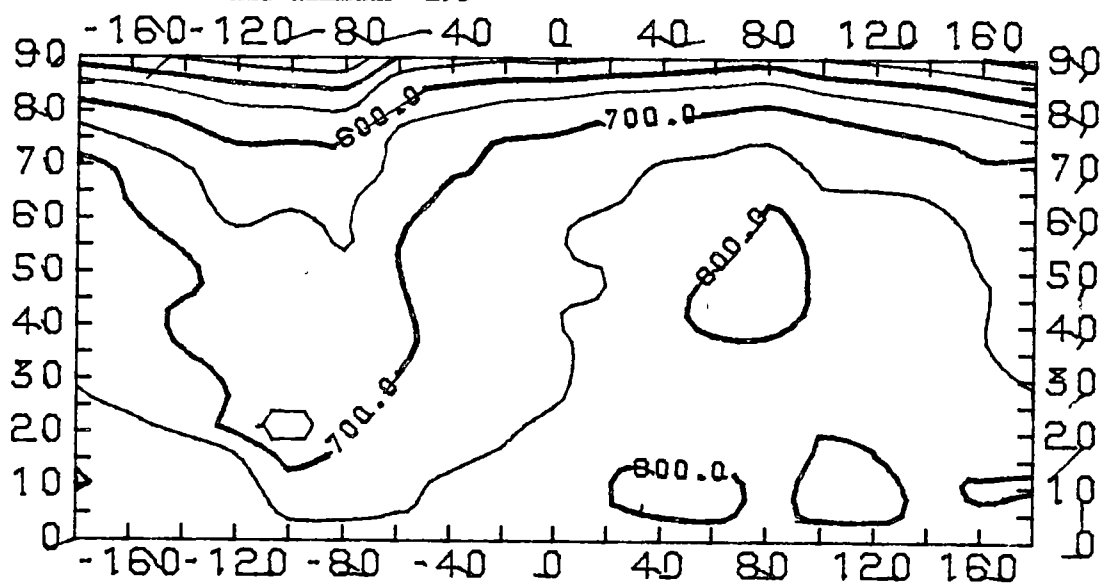
sun zenith = 65° and azimuth = 258°
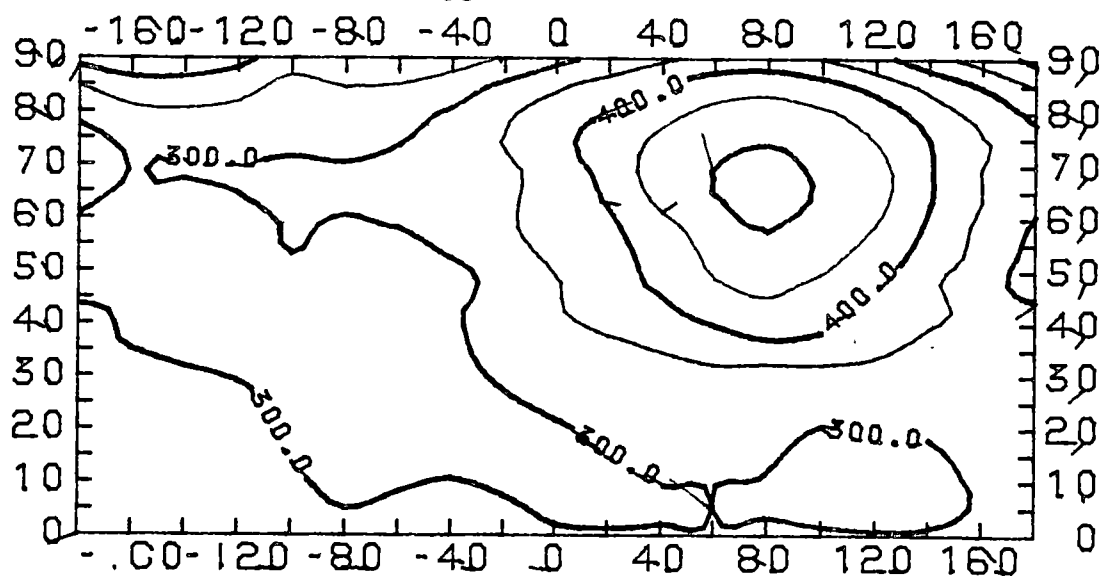
SITE 7

sun zenith = 59⁰ and azimuth = 88⁰
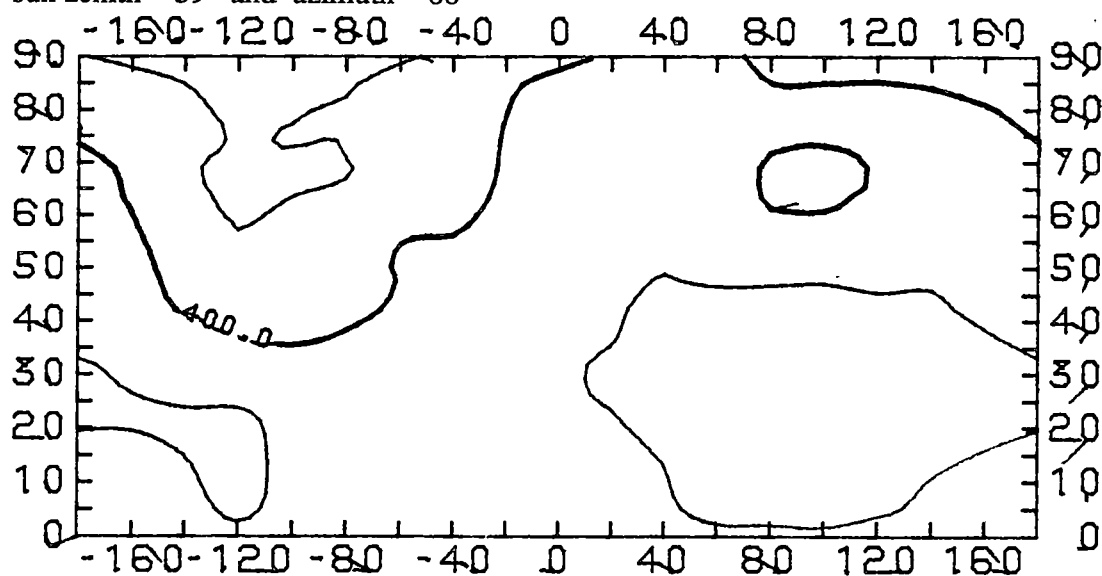
sun zenith = 43⁰ and azimuth = 80⁰
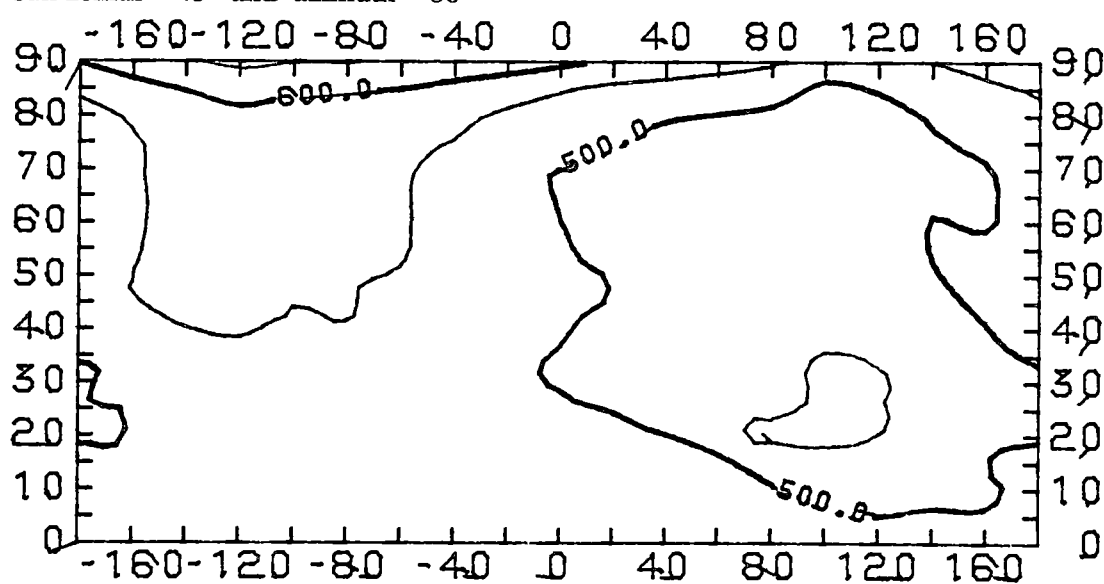
sun zenith = 19⁰ and azimuth = 45⁰
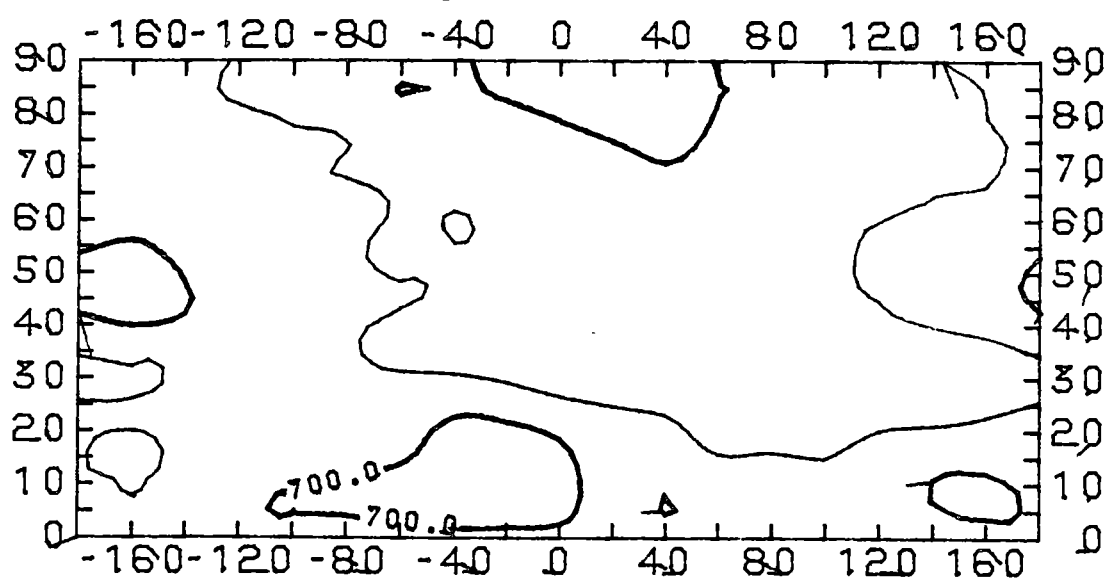
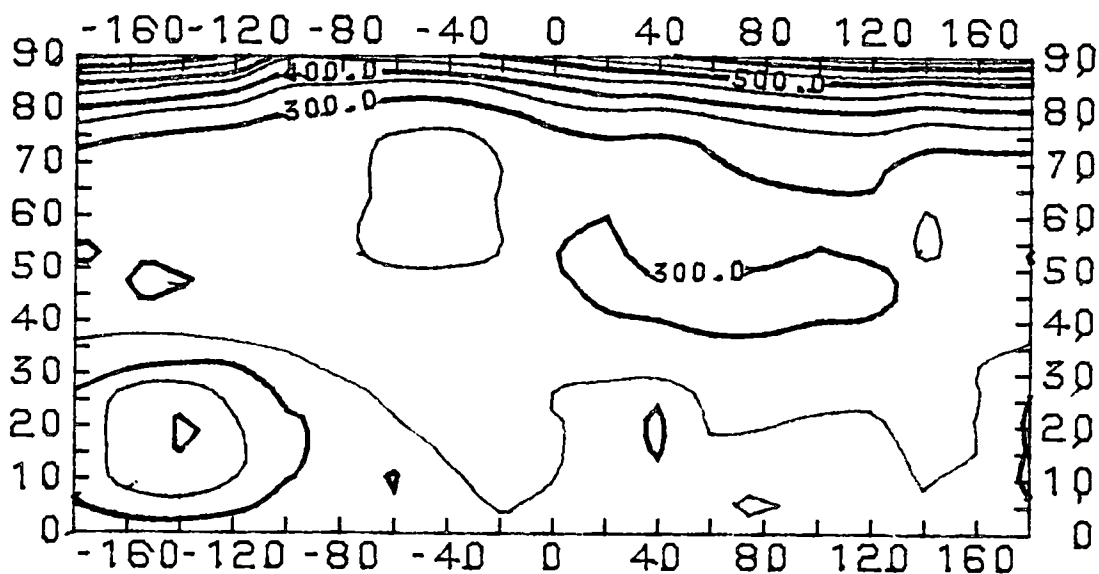**SITE 8**

sun zenith = 69° and azimuth = 93°
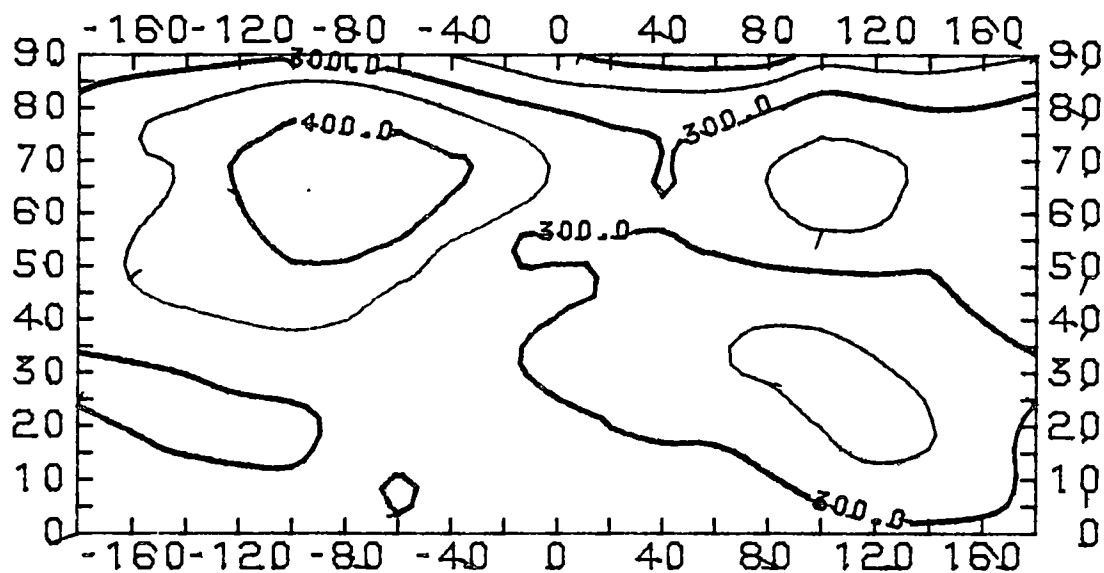
sun zenith = 51° and azimuth = 84°
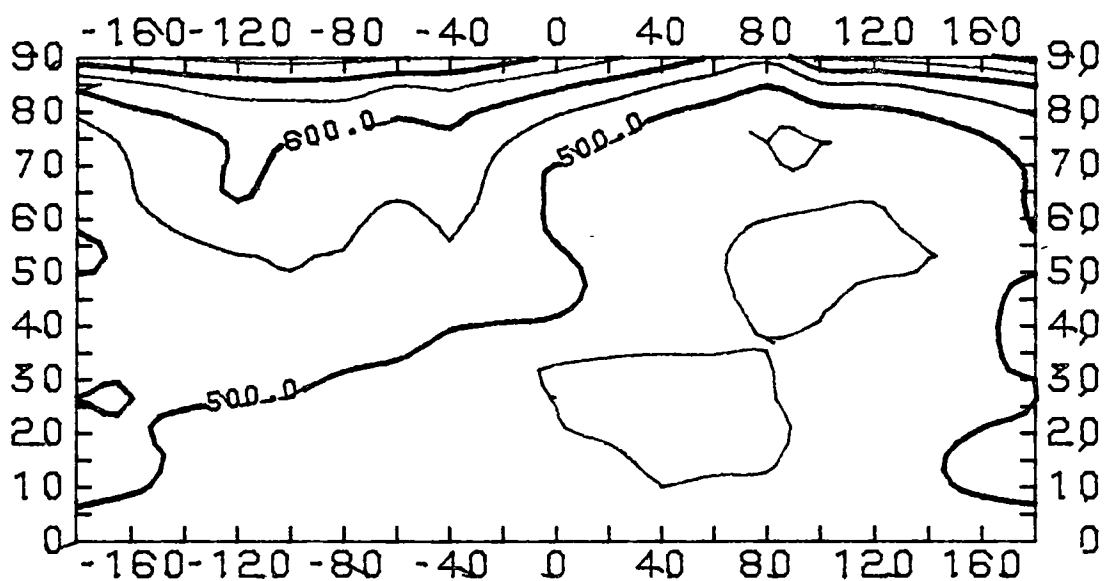
SITE 12
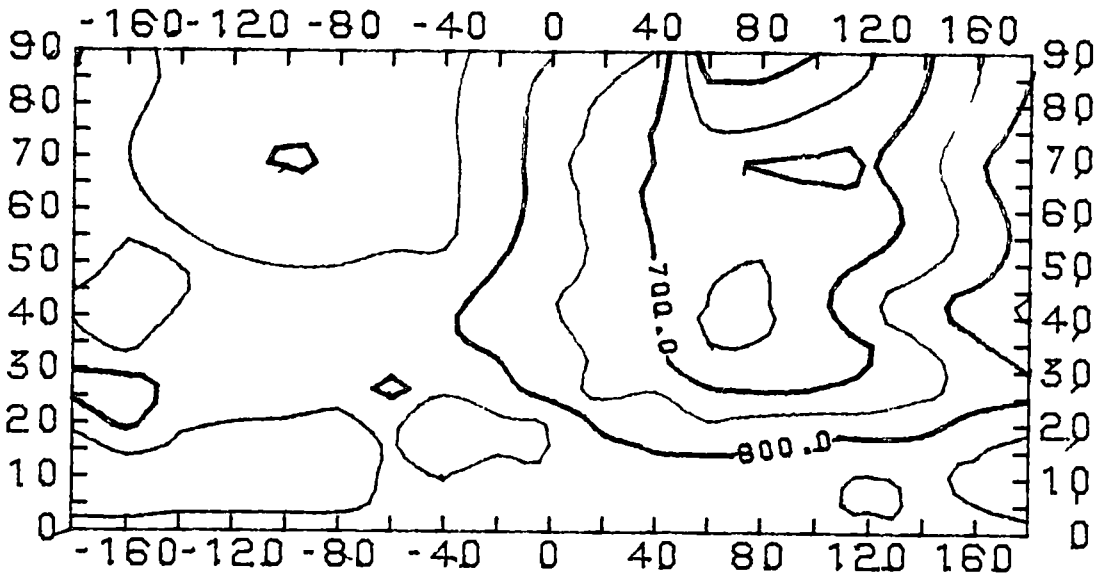
sun zenith = 67° and azimuth = 92°
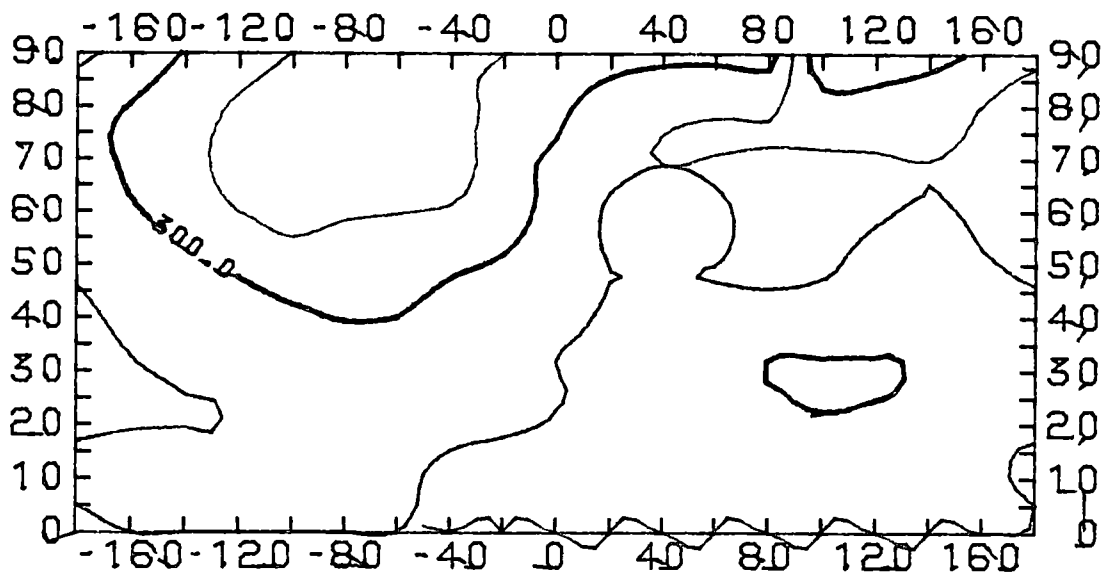
sun zenith = 36° and azimuth = 73°
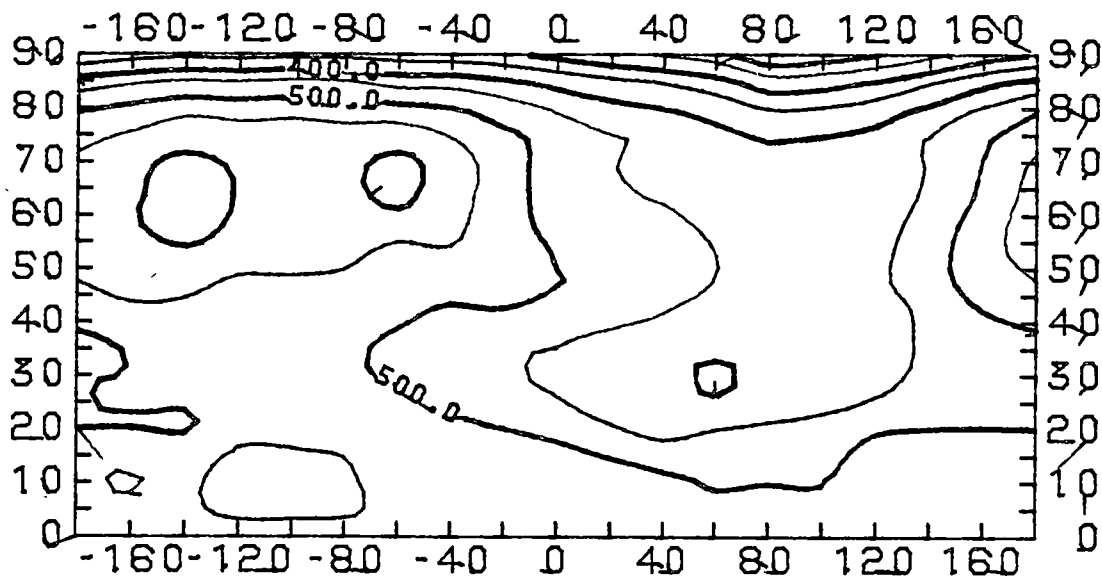
sun zenith = 23° and azimuth = 54°
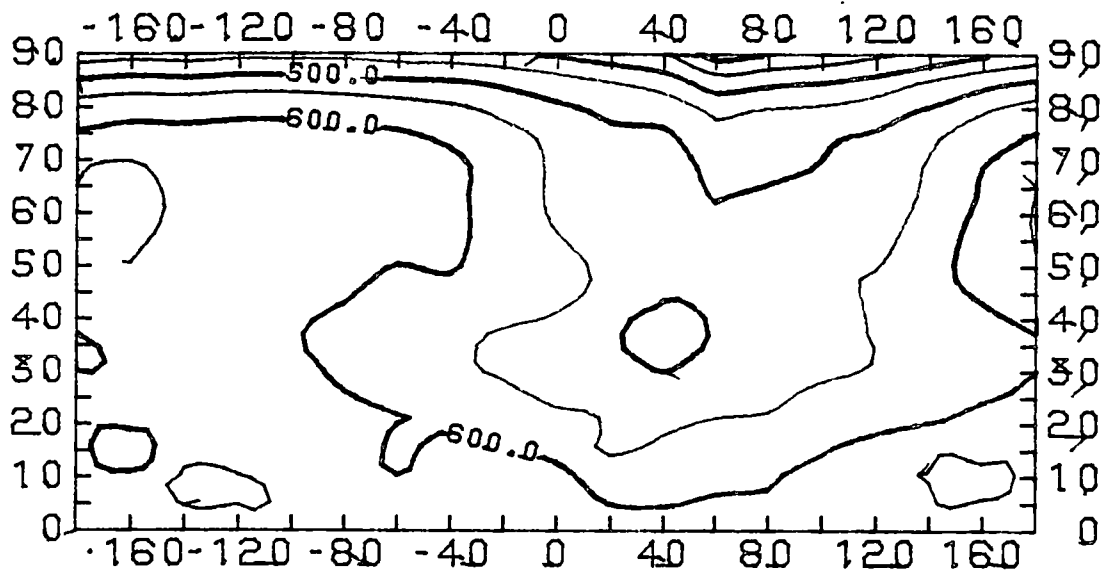
SITE 13

sun zenith = 57° and azimuth = 88°
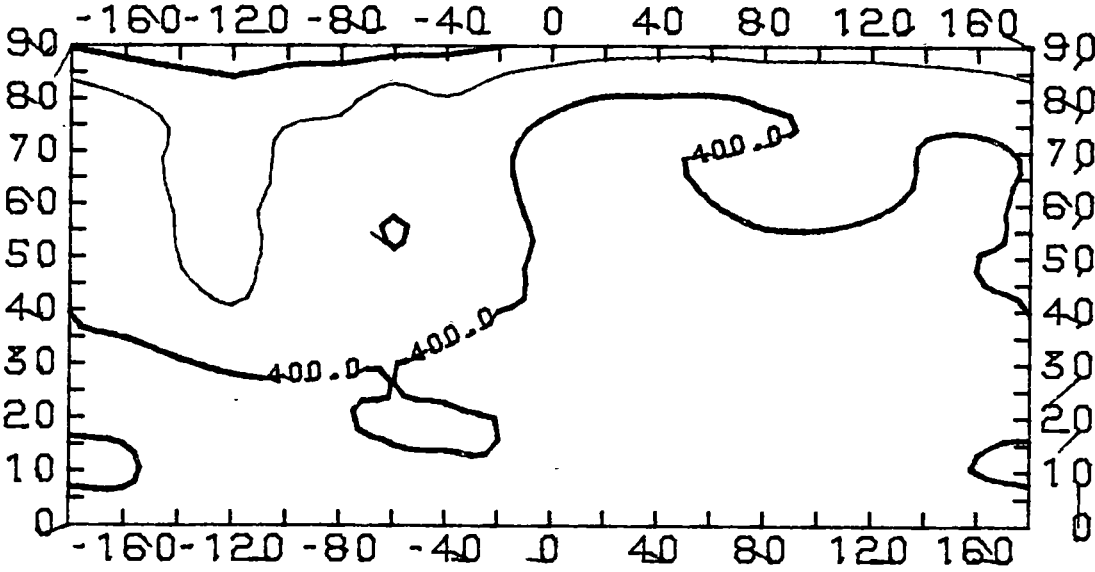
sun zenith = 41° and azimuth = 78°
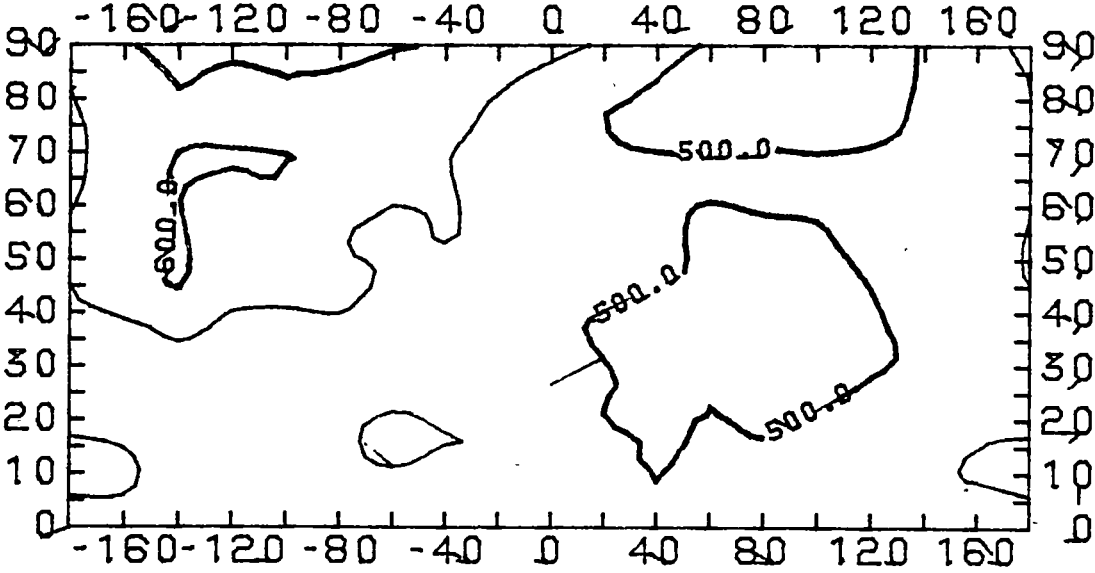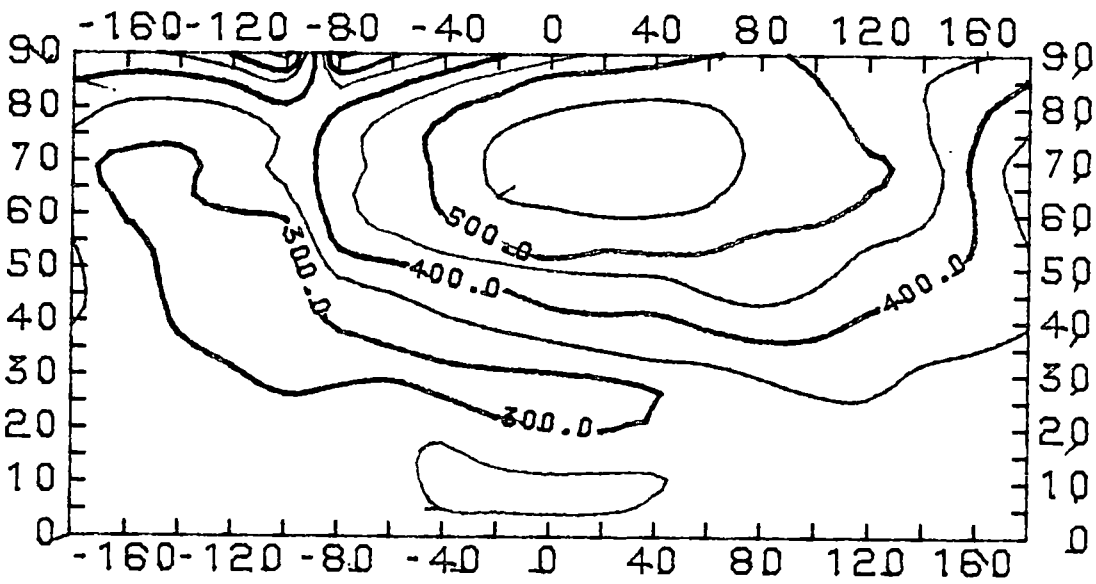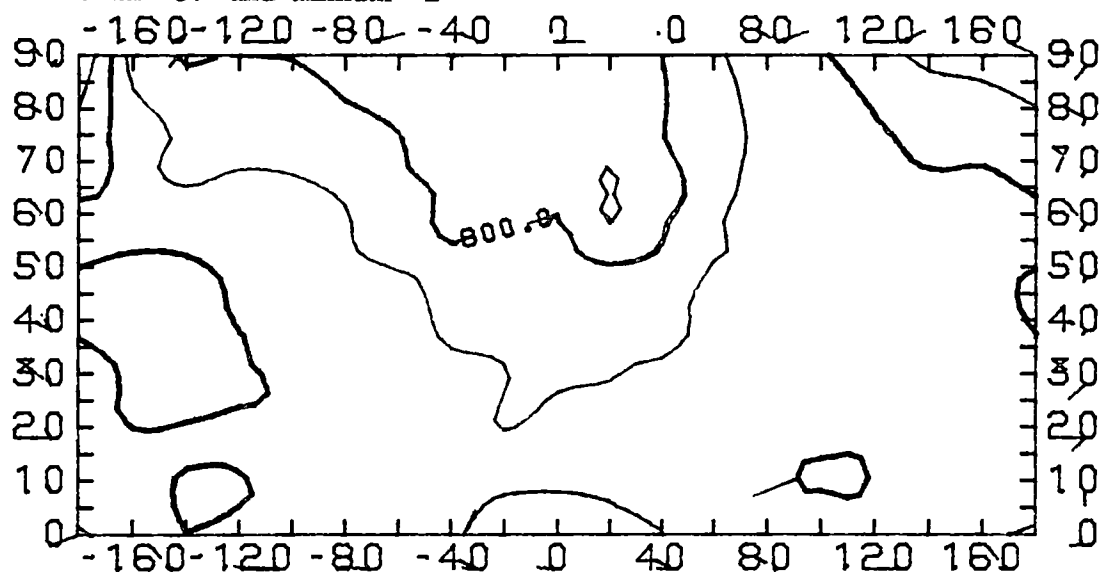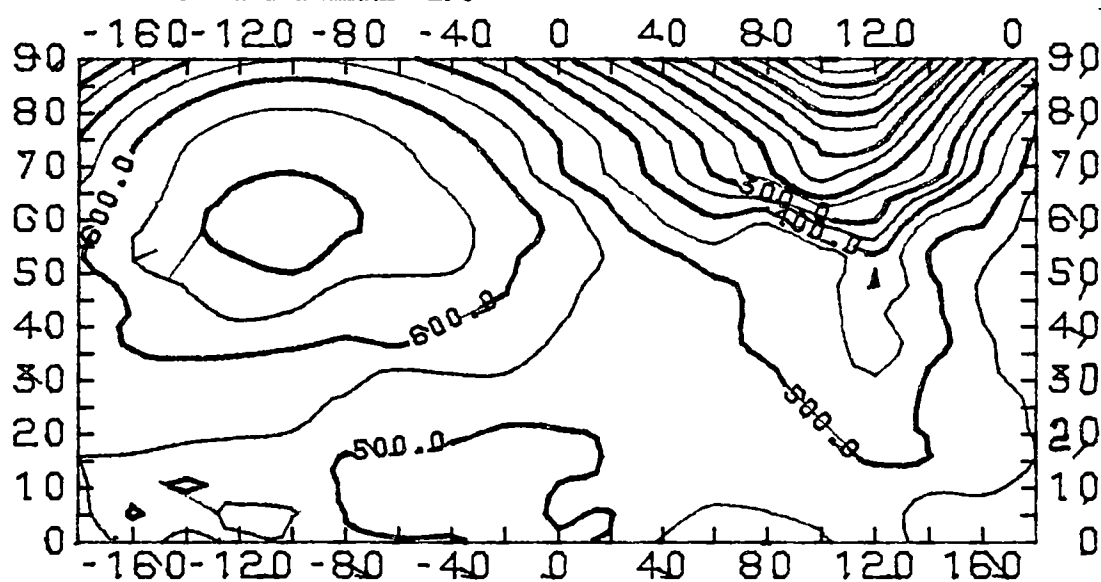

sun zenith = 27° and azimuth = 62°

SITE 14

sun zenith = 54° and azimuth = 82°

sun zenith = 43° and azimuth = 74°

sun zenith = 28° and azimuth = 56°

SITE 1a (model site)

sun zenith = 37° and azimuth = 75°

sun zenith = 62° and azimuth = 264°
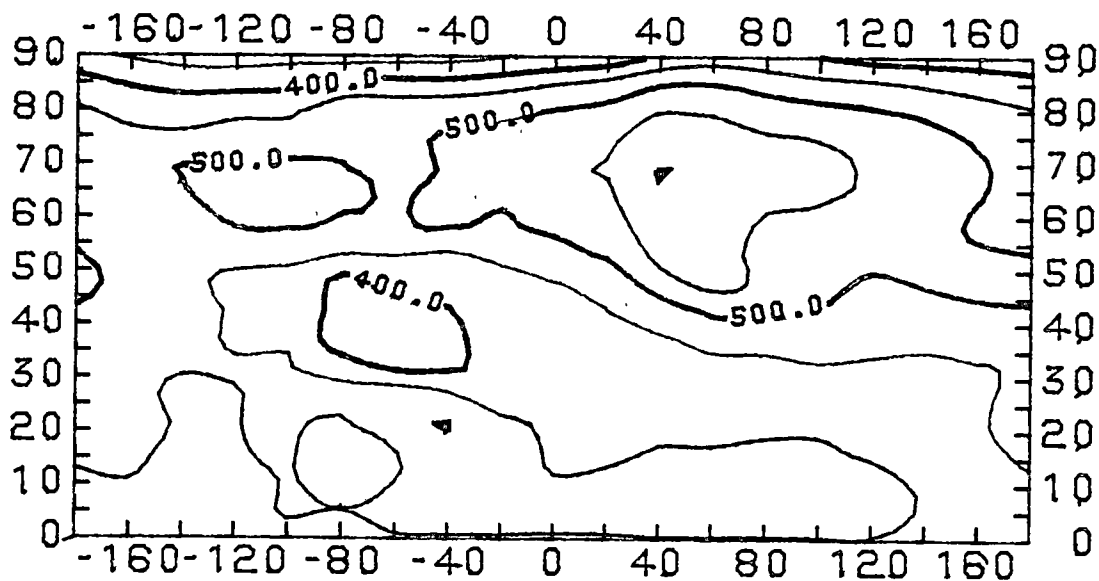
sun zenith = 74° and azimuth = 254°

SITE 2 (model site)

sun zenith = 21$^{\text{O}}$ and azimuth = 51$^{\text{O}}$

sun zenith = 64$^{\text{O}}$ and azimuth = 264$^{\text{O}}$

SITE 17 (model site)

sun zenith = 37° and azimuth = 2^O

sun zenith = 52° and azimuth = 298°

sun zenith = 65° and azimuth = 273°